OFDM Precoding for Filter-Bank based Waveforms

David Demmer

le cnam

École Doctorale Informatique, Télécommunications et Électronique

Centre d'étude et de recherche en informatique et communications

THÉSE présentée par :

David DEMMER

soutenue le: **06 juin 2019**

pour obtenir le grade de : **Docteur du Conservatoire National des Arts et Métiers**

Discipline : **Génie informatique, automatique et traitement du signal**
Spécialité : **Radiocommunications**

OFDM Precoding for Filter-Bank based Waveforms

THÈSE DIRIGÉE PAR :

Pr. Le Ruyet Didier	Professeur des universités, CNAM Paris, directeur de thèse
Dr. Doré Jean-Baptiste	Docteur-Ingénieur de recherche, CEA Grenoble, encadrant

JURY :

Pr. Ciblat Philippe	Professeur à Télécom ParisTech, Paris, rapporteur
Pr. Renfors Markku	Professeur à l'université de Tampere, Finlande, rapporteur
Pr. Douillard Catherine	Professeure à l'IMT Atlantique, Brest, présidente du jury
Dr. Bader Carlos	Professeur associé à CentraleSupelec, Rennes, examinateur
Dr. Ros Laurent	Maître de conférence HDR à Grenoble-INP, Grenoble, examinateur
Dr. Gerzaguet Robin	Maître de conférence à l'université de Rennes 1, Rennes, invité

Acknowledgements

Je souhaite remercier toutes les personnes qui ont contribué au succès de cette thèse.

Je tiens tout d'abord à remercier très chaleureusement Jean-Baptiste Doré d'avoir encadré cette thèse. J'ai beaucoup appris auprès de toi. Merci pour tes précieux conseils et la grande pédagogie que tu as manifesté durant cette thèse. Merci également à Didier Le Ruyet d'avoir dirigé cette thèse. Merci de m'avoir fait confiance et de m'avoir guidé pendant ces trois années.

Je tiens également à remercier les membres du jury. C'est un honneur pour moi d'avoir partagé mes résultats de recherche avec vous. Merci à la présidente du jury Pr. Catherine Douillard, aux rapporteurs Pr. Philippe Ciblat et Pr. Markku Renfors et aux examinateurs Dr. Carlos Bader et Dr. Laurent Ros pour l'intérêt qu'ils ont porté à ce travail de recherche en acceptant d'examiner ce travail et de l'enrichir par leurs nombreuses propositions.

Un grand merci à Robin Gerzaguet. Tu as consacré beaucoup de ton temps sur ce travail et tu l'as rendu meilleur. Je t'en suis très reconnaissant. Je tiens également à remercier Rostom Zakaria d'avoir apporter sa grande expertise à ce travail.

Merci aussi à mes anciens co-bureaux qui ont rendu ces journées de travail conviviales et sympathiques: en commençant par cet exceptionnel premier bureau avec Yoann et Jérem, vous êtes bien plus que de simples collègues mais de véritables amis, Patrick et tes "minutes-culture", Benoit pour ton éternelle bonne humeur. Également merci à Quynh, Ludovic, Simon et Mohammed. Je tiens également à sincèrement remercier les équipes LSHD et LCOI de m'avoir accueilli et facilement intégré parmi vous.

Sans oublier mes parents qui m'ont toujours soutenu et sans qui tout cela n'aurait pas été possible. Merci du fond du cœur! Merci également à mes chers frères, Guillaume et Matthias, pour leur soutien sans faille. Merci à vous, Cyril et Dany (a.k.a. les PainPains), ces années grenobloises auraient été bien plus fades sans votre gentillesse et votre joie de vivre. Cœur sur vous !

Un énorme merci à toi Cloé ! Merci pour la patience que tu as témoigné surtout aux cours de ces derniers mois. Grâce à toi, je voyage et m'évade quotidiennement. Merci < 3 !

Abstract

New use cases for wireless communications recently emerged ranging from massive sensor networks to connected cars. These applications highly differ from typical signals supported by already deployed mobile technologies which are mainly high data rate pipes. The forthcoming generation of mobile technology, 5G New Radio, introduces the new concept of signal numerology so as to properly serve the requirements of the diverse applications it will support. Indeed by considering different numerologies, the time/frequency signal allocation is made more flexible which allows to shape the transmitted signal according to its needs. However, multiplexing signals with different numerologies generates interference and therefore signal distortion. Spatial filtering, such as beamforming, is envisioned for 5G above 6-GHz communications to limit inter-user interference. However, this issue still holds for sub-6 GHz systems where spatial filtering is not considered in 5G.

In this work, we consider side lobe rejection techniques to ease service multiplexing in sub-6 GHz bands. Not only it provides inter-user interference mitigation but it also improves the bandwidth use efficiency. A novel solution, mixing filter-bank for confined spectrum and complex orthogonality for a straightforward re-use of known-how 4G/5G techniques, is proposed. The complex orthogonality is restored thanks to an OFDM precoding substituting the commonly used Offset-QAM signaling which limits the orthogonality to the real field. Moreover, the proposed solution, named Block-Filtered Orthogonal Frequency Division Multiplexing (BF-OFDM), relies on a simple 5G receiver scheme which makes it backward compatible with already deployed technologies.

The BF-OFDM system model is fully described and adapted to cellular standards. Besides, different prototype filter design methods are proposed to either improve the intrinsic interference attenuation or to better confine the spectrum of the transmitted signal. Last but not least, the proposed waveform will be compared with state-of-the-art solutions for both typical and 5G oriented evaluation scenarios such as multi-service coexistence.

Keywords : 5G, physical layer, OFDM, filter banks, BF-OFDM

Résumé

De nouveaux usages des systèmes de communications sans fils, tels que les réseaux de capteurs ou les voitures autonomes, ont émergé au cours des dernières années. Ces usages sont fondamentalement différents des applications haut-débit actuelles des réseaux cellulaires. La future technologie mobile, la 5G New Radio, introduit donc le concept de numérologie du signal afin de pouvoir satisfaire aux besoin hétérogènes des multiples applications supportées. En effet en supportant différentes numérologies de signaux, l'allocation temps/fréquence des signaux devient plus flexible et le signal transmis peut être adapté en conséquence. Cependant, supporte simultanément différentes numérologies génère de l'interférence et donc distord les signaux. Les filtrages spatiaux, comme la formation de faisceaux, est envisagée en 5G pour limiter l'interférence générée mais pour les communications au-dessus de 6 GHz.

Il n'y a cependant pas de solutions proposées pour mes communications en-dessous de 6 GHz. Dans ce travail, des techniques d'atténuation des lobes secondaires sont étudiées pour faciliter le multiplexage des services pour les communications sous 6 GHz. L'interférence entre-utilisateurs est alors contrôlée mais la bande est également mieux utilisée. Une solution innovante, combinant bancs de filtres et orthogonalité complexe, est proposée. L'orthogonalité complexe est garanti grâce à un précodage OFDM qui remplace le précodage OQAM communément utilisé. De plus, le système développé, le Block-Filtered OFDM, utilise un récepteur 5G classique ce qui garantit la retro-compatibilité avec les techniques déjà déployée.

Le modèle du BF-OFDM est entièrement décrit et adapté aux normes des réseaux mobiles. De plus, de multiples méthodes de conception des filtres prototypes sont proposées afin de mieux répondre aux besoins des systèmes. La forme d'onde étudiée est également comparée avec les autres solutions de l'état de l'art sur des scénarios d'étude classiques mais également adaptés aux nouveaux enjeux des technologies sans fils.

Mots-clés: 5G, couche physique, OFDM, bancs de filtres, BF-OFDM

Résumé Étendu

La nouvelle génération de réseaux mobiles, la 5G, ne va pas seulement améliorer les débits du réseau existant mais va également fortement intégrer de nombreuses nouvelles applications comme l'internet des objets (Machine-Type-Communications (MTC) en anglais) avec les réseaux de capteurs ou les maisons connéctées et les communications dites critiques (critical MTC (cMTC) en anglais) avec les applications médicales ou les voitures autonomes.

L'objectif de ce travail est de concevoir et d'étudier une couche physique qui répond efficacement à ces nouveaux enjeux en se focalisant sur les formes d'onde. Nous nous intéresserons notamment aux techniques de confinement de spectre. Dans un premier temps, nous allons étudier la description de la couche physique proposée par la norme 5G.

1 Description de la couche physique 5G

La 5G doit non seulement assurer de meilleurs débits et une plus grande capacité du réseau mais elle doit surtout apporter de nouvelles fonctionnalités comme l'intégration des objets connectés.

Dans ce travail, nous allons surtout nous intéresser à la couche physique des systèmes mobiles, c'est-à-dire la couche responsable de la transmission et la réception effective des signaux radios.

De nouvelles bandes de fréquence sont alors utilisées pour augmenter la capacité du réseau. En effet, les ondes millimétriques, qui sont des ondes de très hautes fréquences (> 30 GHz) et qui peuvent fournir de larges bandes (plusieurs centaines de MHz), seront maintenant utilisées par la nouvelle génération de réseaux mobiles.

Plus de flexibilité est également apportée dans les techniques de partage de la ressource radio. L'unité de base attribuée aux différents utilisateurs du réseau est appelée le bloc de ressource radio (ou Resource Block (RB) en anglais) et correspond à l'allocation temps/fréquence minimale supportée par le réseau. Pour les réseaux 4G, un RB équivaut à une transmission de 1 ms (soit 14 symboles en temps) pour 12 sous-porteuses espacées de 15 kHz comme représenté sur la Figure 1. Cette allocation est fixe et supportée par tous les usagers du réseau 4G. Avec la 5G, il est maintenant possible d'adapter le temps de transmission et l'espacement inter-sous-porteuses comme représenté sur la Figure 1. Cela permet d'adapter la configuration du signal transmis aux besoin de l'utilisateur et du service utilisé. En effet, la numérologie $\mu = 2$ (en orange) sera plus intéressante pour les applications nécessitant une très faible latence alors que la numérologie $\mu = 0$ (en rouge), qui

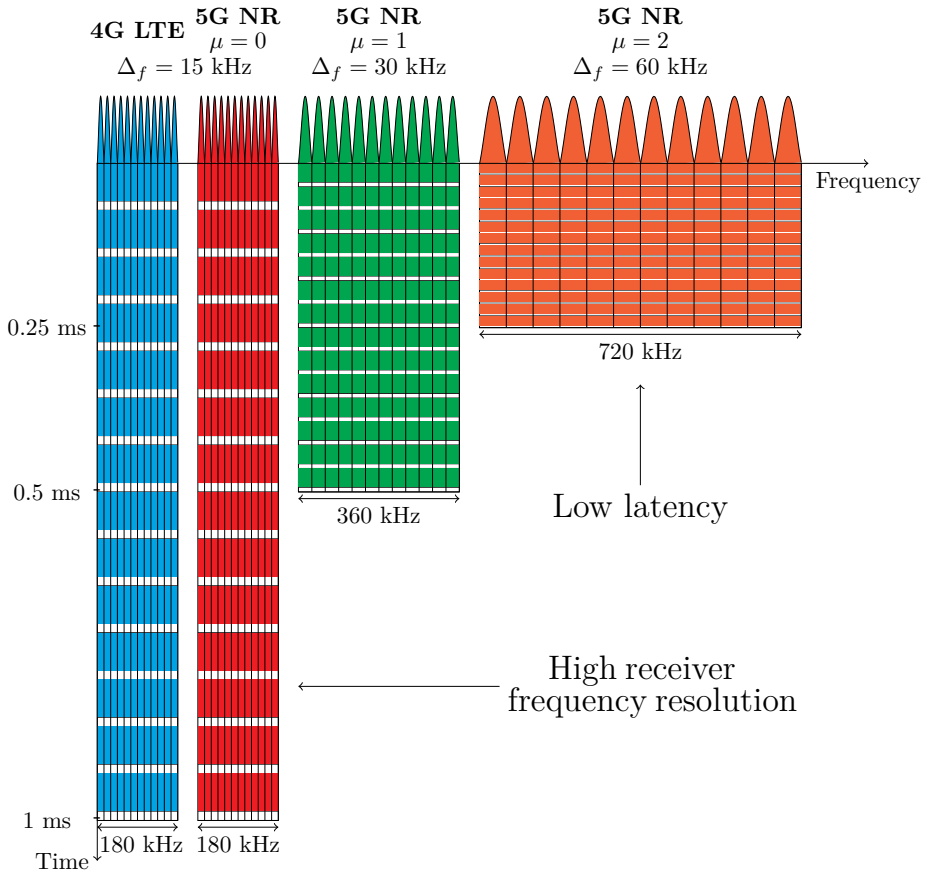

Figure 1: Une allocation des blocs de ressource radio plus flexible en 5G.

d'ailleurs correspond à la configuration 4G pour rétro-compatibilité avec le réseau déployé, sera préférée lorsque le canal de transmission présente une forte sélectivité fréquentielle.

Le choix de la forme d'onde n'a quant à lui pas changé entre la 4G et la 5G. En effet, l'*Orthogonal Frequency Division Multiplexing (OFDM)* est réutilisée pour le futur réseau mobile. Le principe de base de l'OFDM est de décomposer un signal large bande en plusieurs signaux à bande étroite, appelés sous-porteuses, orthogonaux entre eux. Pour se faire, des réponses en sinus cardinal sont utilisées dans le domaine fréquentielle. Le préfixe cyclique, une copie des derniers échantillons de chaque symbole au début de ces derniers, est généralement utilisé avec l'OFDM d'où le nom CP-OFDM. Cette technique permet de lutter contre l'interférence entre symboles, en présence de canaux à fort étalement et donc à simplifier l'égalisation à un unique coefficient complexe par sous-porteuse à condition que lu durée du préfixe cyclique soit supérieure à celle de l'étalement du canal et que l'espacement inter-sous-porteuses soit plus faible que la bande de cohérence du canal.

L'OFDM est donc une forme d'onde à forte efficacité spectrale et qui est par construction très robuste aux effets induits par les canaux multi-trajets. De plus, l'implémentation matérielle de cette forme d'onde est très peu complexe puisqu'elle repose sur des techniques de Transformations de Fourier rapides (ou *Fast Fourier Transform)* (FFT) en anglais). C'est pourquoi cette technique est

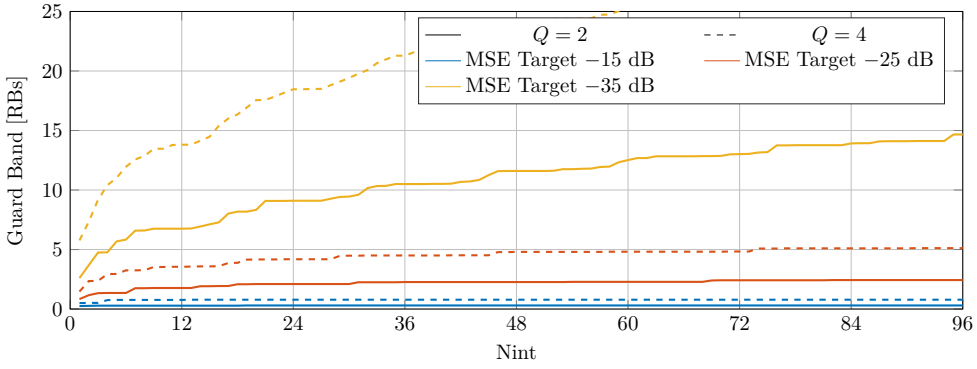

Figure 2: Évaluation de la bande de garde entre deux utilisateurs en fonction de N_{int}.

beaucoup utilisée dans les systèmes de transmissions sans fils, non seulement en 4G et 5G mais également pour la télévision numérique ou le Wifi. Cependant, l'OFDM rayonne beaucoup en dehors de bande et donc admet un faible confinement spectral. Les sous-porteuses situées au bord de la bande du système doivent par conséquent ne pas être utilisées pour éviter d'interférer avec les autres systèmes. De plus, de fortes variations de l'enveloppe du signal transmis apparaissent suite à la forte décomposition du signal en sous-porteuses. Ceci induit une diminution de l'efficacité des schémas amplificateurs.

Nous pouvons maintenant étudier les performances de l'OFDM pour des scénarios d'évaluations type 5G comme la coexistence des différentes numérologies décrites précédemment. En effet en supportant différents espacements inter-sous-porteuses, cela casse l'orthogonalité entre les sous-porteuses ce qui génère de l'interférence. Nous proposons maintenant d'étudier le niveau de distorsion induit par cette coexistence des services 5G.

Pour cela, il est ici proposé d'estimer les bandes de gardes (ou *Guard Band* en anglais) nécessaires pour garantir un niveau de distorsion du signal fixé. Les bandes de garde sont estimées en mesurant l'erreur quadratique moyenne (ou *Mean Square Error* (MSE) en anglais) entre deux utilisateurs de numérologies différentes où N_{int} correspond au nombre de sous-porteuses de l'utilisateur interférant et $Q = 2^{\mu_i - \mu_u}$ avec μ_i la numérologie de l'utilisateur interférant et μ_u la numérologie de l'utilisateur d'intérêt. Les résultats sont indiqués dans la Figure 2.

Nous observons que de bandes de garde importantes doivent être insérées entre les utilisateurs pour garantir des niveaux de distorsion faibles (< -25 dB MSE). Ceci limite grandement l'utilisation de la bande du système. Les faibles performances obtenues par l'OFDM sont essentiellement dues à son faible confinement spectral. C'est pourquoi dans l'état-de-l'art de nombreuses solutions proposant une meilleure atténuation des lobes secondaires ont été étudiées. En effet, garantir un meilleur confinement spectrale permet d'améliorer les taux d'utilisation des bandes du système, et donc sa capacité, tout en préservant la flexibilité de la couche physique proposée par la 5G. Certaines de ces techniques à fort confinement spectral vont être décrites dans la section suivante.

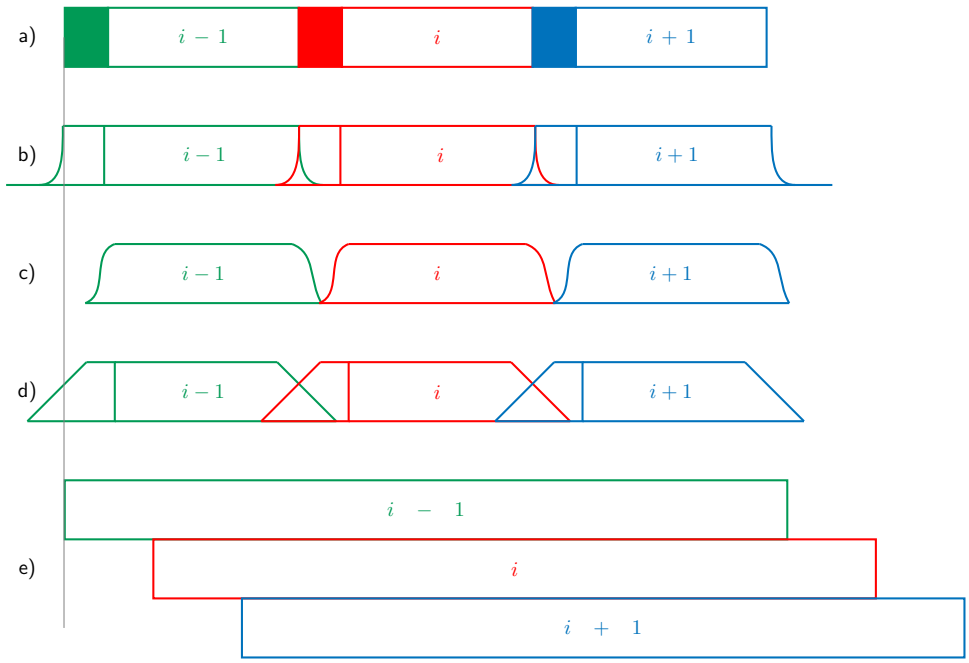

Figure 3: Représentation temporelle des signaux transmis pour a) CP-OFDM b) fOFDM, c) UF-OFDM, d) WOLA-OFDM and e) FBMC-OQAM.

2 Solutions de l'état-de-l'art à fort confinement spectral

Dans cette partie, plusieurs solutions offrant une meilleur localisation fréquentielle que l'OFDM vont être présentées puis comparées.

Une première et pragmatique approche serait simplement filtrer le signal OFDM transmis par un filtre passe-bande. En effet, en faisant cela, nous conservons tous les avantages de l'OFDM tout en améliorant son confinement spectral. Cette technique est appelée l'OFDM filtré (ou *Filtered OFDM* (fOFDM) en anglais). Pour se faire un filtre très long dans le domaine temporel (environ la moitié du temps symbole OFDM) est utilisé ce qui permet de garantir une réponse fréquentielle plate sur la bande filtrée. La même technique peut être utilisée au niveau du récepteur de sorte à se protéger des interférences hors-bande. Une représentation temporelle des signaux transmis est donnée avec la Figure 3. Les symboles OFDM sont donc élargis en temps à cause de la convolution temporelle avec le filtre long mais l'énergie du symbole filtré est néanmoins très confinée. Cette technique est donc très intéressante mais requiert une énorme complexité à cause de la convolution temporel avec le filtre long.

Afin de proposer une implémentation matérielle moins complexe, il est possible d'utiliser des filtres plus court en temps (de la durée du préfixe cyclique par exemple) comme c'est proposé avec l'*Universal Filtered OFDM* (UF-OFDM). Cependant en faisant cela, la réponse fréquentielle du filtre n'est plus plate dans la bande filtrée et donc un étage de pré-distorsion doit être utilisé pour compenser la distorsion induite par le filtrage. De plus, pour éviter une forte interférence entre-symbole, c'est un signal *Zero-Padded* OFDM (ZP-OFDM), et non un signal CP-OFDM, qui est filtré. C'est-à-dire que le préfixe cyclique est remplacé par un simple intervalle de garde vide. La représentation temporelle du signal transmis est donnée dans la Figure 3. Au niveau du récepteur UF-OFDM, le fenêtrage, une

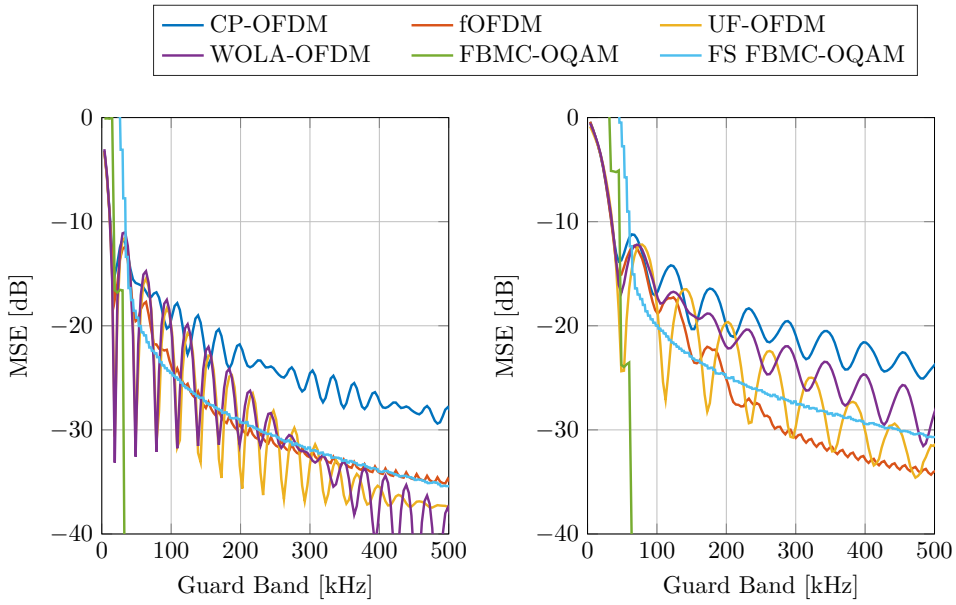

Figure 4: Évaluation de l'erreur quadratique moyenne en fonction de la bande de garde pour les cas $\mu = 1$ sur $\mu = 0$ (gauche) et $\mu = 2$ sur $\mu = 0$ (droite).

pondération du signal en temps, est préféré au filtrage. Cette technique très peu complexe équivaut à un filtrage dans le domaine fréquentiel.

Le fenêtrage peut également être utilisé à l'émetteur comme cela est proposé par le *Weighted OverLap and Add* OFDM (WOLA-OFDM). Avec le WOLA-OFDM, le fenêtrage est également utilisé au récepteur. Cette solution a l'avantage d'être très peu complexe et très flexible.

Il est également possible d'envisager une forme d'onde intrinsèquement différente de l'OFDM comme les formes d'onde multi-porteuses à base de banc de filtres (ou *Filter-Bank MultiCarrier* (FBMC) en anglais). En effet, avec ces dernières, l'impulsion de mise en forme n'est plus une simple réponse rectangulaire en temps (donnant une réponse fréquentielle en sinus cardinal) mais une impulsion de mise en forme offrant une meilleure localisation fréquentielle. Cependant, en faisant cela l'orthogonalité entre sous-porteuses n'est pas garantie comme avec l'OFDM. Par conséquent, des modulations réelles (*Offset QAM*) sont généralement utilisées pour préserver une reconstruction parfaite du signal au récepteur, d'où le nom FBMC-OQAM. Le récepteur effectue la démodulation adaptée. L'avantage du FBMC-OQAM est la possibilité de grandement relâché le localisation temporelle des signaux transmis pour fortement améliorer l'atté- nuation des lobes fréquentiels secondaires. Cependant, le FBMC-OAM garantit une efficacité spectral optimale grâce à une superposition des signaux transmis et l'absence de préfixe cyclique.

Nous pouvons maintenant comparer les performances obtenues par ces différentes formes d'onde sur le scénario de coexistence des services 5G présenté dans la partie précédente. Pour cela, nous allons mesurer les niveaux de distorsion en fonction de la bande de garde entre deux utilisateurs de numérologie différente avec 1 RB par utilisateur. La Figure 4 présente les résultats obtenus.

Nous pouvons observer que les versions filtrées de l'OFDM (fOFDM, UF-OFDM et WOLA-OFDM) sont plus performantes que le CP-OFDM. Cepen-

dant, nous pouvons également constater que le FBMC-OQAM présente de loin les meilleurs résultats. En effet, si la bande de garde entre les utilisateurs est supérieure au plus grand des espacement inter-sous-porteuses des numérologies alors le niveau de distorsion induit par la coexistence des services 5G est négligeable. Le FBMC-OQAM propose donc d'excellents résultats et nous pourrions nous demander pourquoi cette solution n'est pas préférée à l'OFDM pour la 5G.

Comme mentionné précédemment, la reconstruction des symbole FBMC-OQAM est assuré dans le domaine réel et non le domaine complexe comme avec l'OFDM. Ceci implique que les techniques utilisées en traitement du signal numériques (comme l'estimation du canal, l'égalisation ou la conception des schémas multi-antenne) doivent être adaptées à cette orthogonalité réelle et sont par conséquent différente de celle utilisées par les réseaux existants. Il est donc difficile d'assurer la retro-compatibilité avec les réseaux existants.

L'utilisation des formes d'onde FBMC semble néanmoins intéressante pour les applications 5G. Nous proposons donc dans la prochaine partie de concevoir une forme d'onde à base de banc de filtres mais assurant l'orthogonalité dans le domaine complexe de sorte à bénéficier du filtrage des FBMC et d'assurer une rétro-compatibilité avec les systèmes OFDM.

3 Le précodage OFDM appliqué aux formes d'onde à base de banc de filtres

Dans cette partie, nous allons concevoir une forme d'onde à base de banc de filtre assurant la reconstruction de signal dans le domaine complexe afin d'être proposée pour les réseaux post-5G.

Le précodage est une technique simple qui permet de restaurer l'orthogonalité complexe d'une forme d'onde FBMC. Précoder un signal FBMC revient à substituer la modulation OQAM, qui impose l'orthogonalité réelle, par une autre modulation. Le *Fast Fourier Transform* FBMC (FFT-FBMC) utilise des blocs OFDM pour le précodage. Et il a été montré que les techniques couramment utilisées avec l'OFDM, comme l'estimation de canal ou les codes espace-temps des systèmes multi-antennes, peuvent être directement réutilisées avec le FFT-FBMC. Cependant, le récepteur FFT-FBMC effectue le traitement adapté à l'émetteur. Ce qui signifie que le récepteur a besoin de connaître le traitement effectué à l'émetteur pour pouvoir démoduler le signal reçu. Et cela ne valide donc pas la condition de transparence recommandée par la norme 5G. La condition de transparence du récepteur stipule qu'un récepteur doit être capable de démoduler un signal sans aucune connaissance du traitement (filtrage, fenêtrage, ..) effectué en transmission.

Nous proposons donc une nouvelle forme d'onde à base de banc de filtres qui garantit l'orthogonalité complexe et qui valide la condition du transparence de la norme 5G. Cette nouvelle forme d'onde s'appelle le *Block Filtered* OFDM (BF-OFDM). Les schémas de l'émetteur et du récepteur sont donnés avec la Figure 5.

Le BF-OFDM réutilise à l'émission le précodage OFDM utilisé pour le FFT-FBMC. En effet, comme nous pouvons le constater sur la Figure 5, le filtrage du banc de filtre est appliqué par sous-bande, c'est-à-dire un groupe de N_p sous-

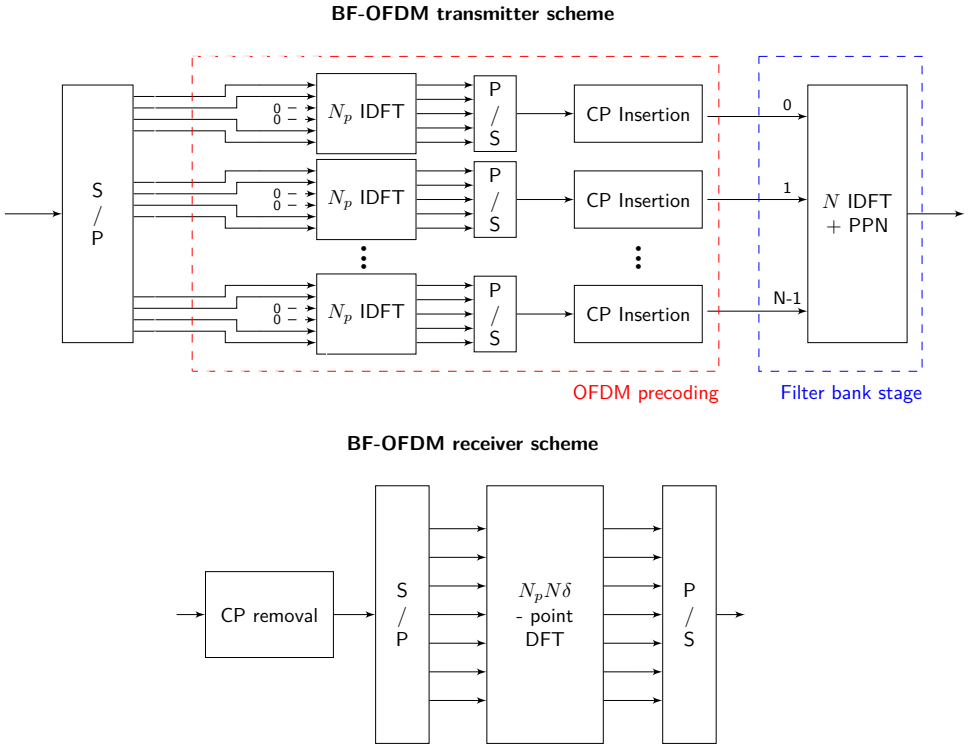

Figure 5: Schémas de l'émetteur et du récepteur BF-OFDM.

porteuse OFDM, comme pour le FFT-FBMC et N sous-bandes sont gérées par le banc de filtre. Néanmoins, vu que la compensation de la distorsion induite par le filtrage ne doit pas être effectué par le récepteur (pour satisfaire la condition de transparence), un étage de pré-distorsion est ajouté sur le schéma de l'émetteur BF-OFDM (non représenté sur la Figure 5. Cette pré-distorsion aplatit la réponse fréquentielle du filtre sur la sous-bande filtrée comme avec l'UF-OFDM.

Le récepteur BF-OFDM est réduit à un simple récepteur OFDM. Cette propriété est très intéressante car d'une part cela signifie que le BF-OFDM satisfait la condition de transparence du récepteur. Mais de plus, un signal BF-OFDM peut être démodulé par n'importe quel récepteur OFDM (comme un récepteur 5G par exemple) et donc que le récepteur BF-OFDM peut également démodulé des signaux OFDM. Cela signifie que le BF-OFDM est rétro-compatible avec l'OFDM et donc que le déploiement d'un réseau BF-OFDM sur un réseau OFDM est facilité.

Le banc de filtre sur-échantillonne donc des signaux à bandé étroite (les sous-bandes) avec un rapport $\times 2N$ où N correspond au nombre de sous-bandes et 2 est un coefficient de sur-échantillonage supplémentaire utilisé en FBMC-OQAM. Or en BF-OFDM, les modulations OQAM ne sont plus utilisées et donc ce coefficient de sur-échantillonage n'est plus nécessaire pour le BF-OFDM. Nous proposons donc d'introduire un nouveau paramètre, appelé le *rate factor* δ, pour rendre le modèle du système plus générique. Nous devons maintenant déterminer les valeurs possibles pour ce nouveau paramètre.

Pour cela, nous devons étudier l'impact de ce nouveau paramètre sur la réponse fréquentielle du signal. Comme observé sur le Figure 6, grâce au précodage OFDM, il est possible de n'utiliser qu'une partie de la sous-bande ce qui évite la superpo-

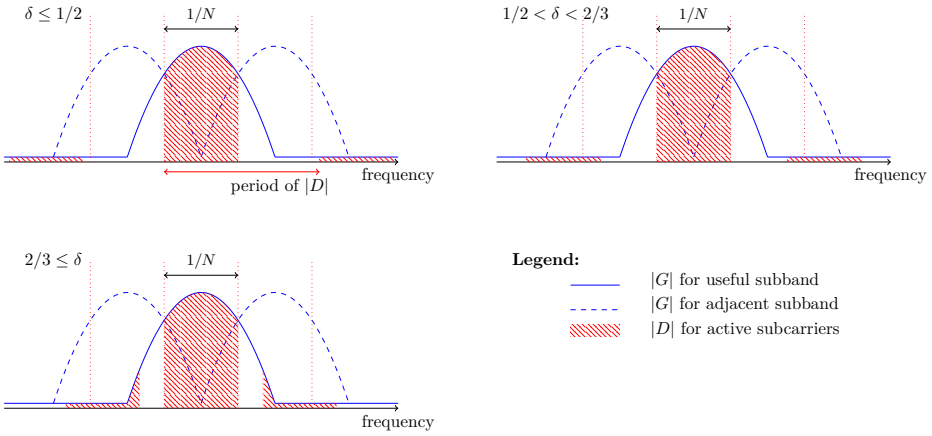

Figure 6: Représentation de l'interférence générée dans le domaine fréquentielle en fonction de *rate factor* δ.

sition des sous-bandes et donc de l'interférence entre sous-bandes. Cependant en sur-échantillonnant les signaux sous-bandes, des images, ou *aliases* en anglais, sont générées dans le domaine fréquentiel. Ces images sont de l'interférence et doivent être suffisamment atténuées pour ne pas compromettre la bonne reconstruction du signal. La distance entre le signal utile et les images dépendent, entre autre, du nouveau paramètre le *rate factor*. Ce qui va limiter l'intervalle des valeurs possibles de ce paramètre. En effet, si nous considérons des valeurs faibles, les images sont générées loin du signal utile et sont donc suffisamment atténuées par le filtre de mise en forme. Cependant, si des valeurs élevées sont utilisées, les images sont proches du signal utile et peuvent être générées dans la bande effective du filtre de mise en forme (cas $\delta \geq 2/3$). Dans ce cas, une interférence de forte énergie est générée ce qui compromet la parfaite reconstruction du signal. Des valeurs supérieures à $2/3$ ne seront donc pas utilisées pour garantir une orthogonalité dans le domaine complexe quasi-parfaite.

Dans le domaine temporel, il faut maintenant se prévenir de l'interférence entre-symbole dûe à la superposition des symboles transmis (cf Figure 3). Pour cela, les symboles transmis doivent être séparé et c'est pourquoi un préfixe cyclique est inséré entre chaque symbole. A partir du modèle du système, il est possible de déterminer la taille minimum de ce préfixe cyclique N_{CP}:

$$N_{\mathrm{CP}} \geq \frac{K}{\delta} - 1 \tag{1}$$

La durée minimale du préfixe cyclique dépend du coefficient d'entrelacement K propre au banc de filtre et du *rate factor*. A noter que même si le préfixe cyclique est nécessaire au BF-OFDM pour assurer une bonne reconstruction du signal même en cas de propagation idéale (c'est-à-dire avec un canal de propagation sans étalement), le préfixe cyclique va aussi servir à se prémunir de l'interférence induite par un canal de propagation à fort étalement comme en CP-ODFM.

La forme d'onde BF-OFDM génère donc de l'interférence intrinsèque, c'est-à-dire de l'interférence qui n'est pas induite par la propagation du signal mais par la technique de modulation elle-même. Le BF-OFDM ne peut donc pas être parfaitement orthogonal complexe comme l'est OFDM. Il est donc intéressant

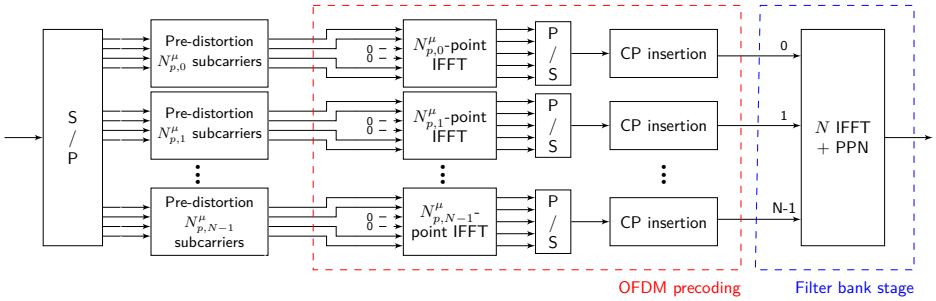

Figure 7: Schéma de l'émetteur multi-service du BF-OFDM.

d'étudier la métrique du rapport signal sur interférence (ou *Signal-to-Interference Ratio* (SIR) en anglais). L'expression du rapport signal sur interférence donnée en (2) dépend fortement de la réponse fréquentielle du filtre de mise en forme G.

$$\mathrm{SIR} = \frac{1}{N_p \delta} \sum_{k \in \Omega} \frac{|G(k)|^2}{\sum_{\Delta_p \neq 0} |G(k + \Delta_p N_p \delta)|^2} \tag{2}$$

Dans ce travail, nous proposons donc deux méthodes pour optimiser le filtre de mise en forme BF-OFDM. La première méthode consiste à maximiser le rapport signal sur interférence ce qui maximise la condition d'orthogonalité de la forme d'onde. La deuxième méthode qui est proposée est d'optimiser le filtre de mise en forme en fonction du niveau d'atténuation des lobes secondaires avec une contrainte sur le niveau de rapport signal sur interférence. Cette dernière permet de concevoir un filtre assurant une bonne localisation fréquentielle tout en garantissant une orthogonalité dans le domaine complexe quasi-parfaite.

Le BF-OFDM est donc une forme d'onde offrant un excellent confinement spectral tout en assurant une reconstruction du signal quasi-parfaite dans le domaine complexe et en satisfaisant la condition de transparence du récepteur voulu par la norme 5G. Le BF-OFDM semble donc être une alternative intéressante à l'OFDM pour les technologies mobiles. La forme d'onde proposée va donc être adaptée aux réseaux mobiles et comparée aux formes d'onde de l'état-de-l'art précédemment étudiées dans la prochaine partie.

4 Adaptation à la norme 5G

Dans cette partie, la forme d'onde proposée, le BF-OFDM, va être adaptée et paramétrer pour satisfaire la norme 5G. Puis dans un deuxième temps, la paramétrisation retenue de la forme d'onde sera comparé aux autres formes d'onde précédemment étudiées.

Avant de déterminer le jeu de paramètres optimal pour le BF-OFDM, nous proposons une configuration de l'émetteur spécialement conçue pour les transmissions multi-service 5G comme représenté avec la Figure 7.

Le principe est d'utiliser une unique paramétrisation du banc de filtre qui sera valide pour tous les numérologies, c'est-à-dire tous les services, et d'utiliser les paramètres de l'étage de précodage OFDM pour s'adapter à la numérologie à utiliser. Cela permet par exemple à une station de base, de pouvoir directement

émettre des signaux des différents services dans sa bande avec une complexité matérielle limitée.

Dans un second temps, il faut déterminer la meilleure paramétrisation de la forme d'onde. Pour cela, une étude paramétrique a été effectuée en se basant sur deux métriques: la condition d'orthogonalité (estimée en mesurant le niveau du rapport signal-sur-interférence) et la complexité de l'émetteur (estimée en évaluant le nombre de multiplications réelles nécessaires à la transmission d'un symbole). La complexité est normalisée par rapport à la configuration 5G équivalente. Il semble intéressant de noter que la complexité du récepteur BF-OFDM est la même que celle d'un récepteur 5G vu que les schémas de réception sont identiques.

Cette étude paramétrique nous a permis de conserver trois configuration pour le BF-OFDM:

- Configuration 1: SIR très élevé (75 dB) et une faible complexité normaliser ($\times 2.6$)
- Configuration 2: SIR élevé (40 dB), une faible complexité ($\times 2.6$) et un filtre de mise en forme optimiser pour améliorer la localisation fréquentielle du signal transmis.
- Configuration 3: Une configuration supportant des sous-bandes plus étroites (4 sous-porteuses plutôt que les 32 sous-porteuses supportées par les deux configurations précédentes), mais un SIR plus faible (26 dB) et une complexité accrue ($\times 5.5$)

Nous pouvons maintenant comparer le BF-OFDM avec l'OFDM et d'autres formes d'onde de l'état-de-l'art en commençant par l'étude du confinement spectral présenté sur la Figure 8. Nous pouvons observer que seul la configuration 2 offre un bon confinement spectral. En effet, pour les configurations 1 et 3 le filtre de mise en forme est contraint à être mieux localisé en temps ce qui empêche une bonne localisation fréquentielle.

Nous pouvons maintenant observer les performances obtenues pour le scénario de coexistence multi-service 5G. Comme observé précédemment la configuration 1 n'apporte qu'un faible gain par rapport à l'OFDM et n'est par conséquent par intéressante. Cependant, les configurations 2 et 3 offrent de bonnes performances respectivement grâce à l'optimisation du filtre de mise en forme et au filtrage en bande étroite. En effet, les niveaux de performances de ces deux paramétrisation sont proches des niveaux obtenus par fOFDM ce qui est très intéressant puisque la complexité du BF-OFDM est bien moindre comparé au fOFDM.

Cependant il semble intéressant de remarquer que le BF-OFDM ne peut pas égaler le FBMC-OQAM. En effet, en restaurant l'orthogonalité dans le domaine complexe, la localisation fréquentielle de la forme d'onde à due être relâchée, ce qui est une conséquence direct du théorème de Balian-Low. Néanmoins, le BF-OFDM est plus intéressant que le FBMC-OQAM malgré ses plus faibles performances grâce à l'orthogonalité complexe et le respect de la condition de transparence.

Conclusion

Trouver une alternative intéressante à l'OFDM n'est pas tâche facile. En effet, il faudrait pour cela trouver une solution plus performante que l'OFDM sur ces

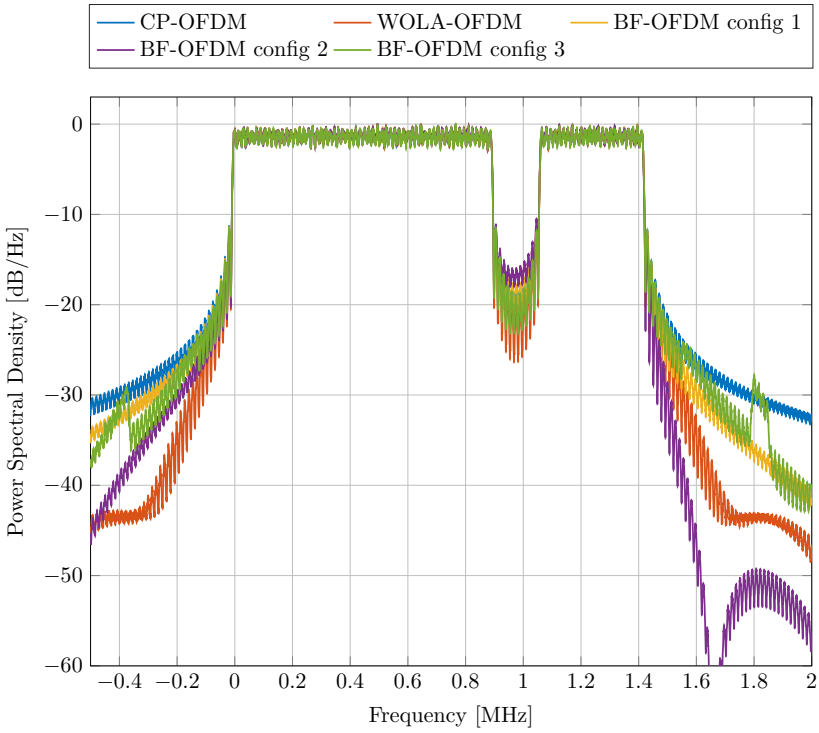

Figure 8: Étude du confinement spectral du BF-OFDM.

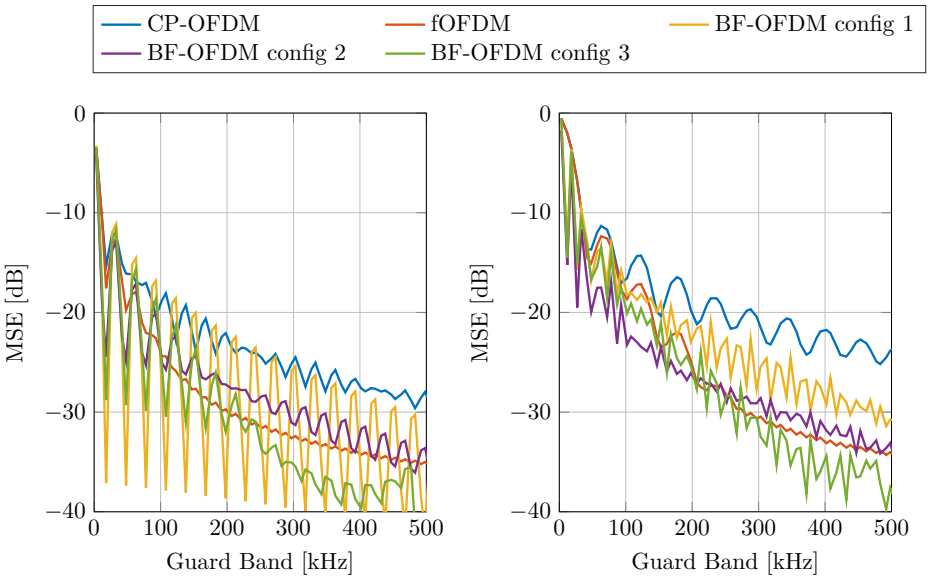

Figure 9: Évaluation de l'erreur quadratique moyenne en fonction de la bande de garde pour $\mu = 1$ sur $\mu = 0$ (gauche) et $\mu = 2$ sur $\mu = 0$ (droite).

points faibles tout en préservant ses points forts.

Une solution pragmatique est d'améliorer directement l'OFDM en y ajoutant des techniques d'atténuation de lobes secondaires ce qui a donné suite aux versions filtrées de l'OFDM. Cependant pour ces formes d'onde, le gain de performance est souvent faible et leur flexibilité est généralement limitée. Il est également possible de considérer des formes d'onde intrinsèquement différente comme les formes d'onde à base de bancs de filtre. Ces dernières, à l'image du FBMC-OQAM, offrent d'excellents gains de performances. Cependant, elles ne sont pas compatibles avec les techniques couramment utilisées avec l'OFDM ce qui rend leur déploiement sur un système OFDM très compliqué.

Il semble donc qu'une forme d'onde offrant un meilleur équilibre entre les gains de performance, le niveau de complexité et la compatibilité avec les systèmes OFDM puisse être conçue. C'est ce que nous proposons avec le Block-Filtered OFDM. C'est une forme d'onde à base de banc de filtre qui opère la reconstruction du signal dans le domaine complexe comme avec l'OFDM et dont le récepteur est un simple récepteur OFDM. Cela signifie que le BF-OFDM est entièrement compatible avec les techniques OFDM et que son déploiement sur un réseau OFDM est par conséquent facilité. Le BF-OFDM offre de bons gains de performances avec une paramétrisation 5G malgré de fortes contraintes sur la complexité de l'émetteur et le niveau d'interférence intrinsèque. De meilleurs gains pourraient être obtenus en relâchant ces contraintes. De plus, la forme d'onde est par construction conçue pour satisfaire les enjeux de la 5G et des réseaux post-5G. Le BF-OFDM présente donc de forts atouts pour être envisagé pour les systèmes sans fils de demain.

Contents

List of Acronyms **xxiii**

Introduction **1**

1 Overview of 5G Physical Layer **3**

1.1 From human-to-human communications to heterogeneous networks. 3

1.2 Physical layer and system model 4

1.3 From 4G LTE to 5G NR 5

1.4 OFDM, the most predominant waveform in wireless standards . . 10

1.5 Limitations to meet 5G challenges 16

1.6 Analysis 25

1.7 Conclusion 28

2 State-of-the-art solutions with enhanced spectral confinement **29**

2.1 Filtered-OFDM 29

2.2 UF-OFDM 33

2.3 WOLA 34

2.4 FBMC-OQAM 39

2.5 Performance Evaluation 49

2.6 Conclusion 60

3 OFDM-based precoding for FBMC waveforms **63**

3.1 CDMA-FBMC/OQAM 63

3.2 FFT-FBMC 64

3.3 FFT-FBMC with a flexible rate factor of δ 71

3.4 BF-OFDM 73
3.5 Prototype Filter design 77
3.6 Filter Predistortion 84
3.7 Conclusion 85

4 Compatibility with 5G NR and analysis 87
4.1 Waveform configuration 87
4.2 Performance evaluation 94
4.3 Conclusion 101

5 Lattice Reduction aided MIMO receivers 105
5.1 Introduction to lattice reduction 105
5.2 Application to MIMO systems 109
5.3 Extension to coded systems 116
5.4 Conclusion 119

6 Conclusion 121

Appendices 129

A Nyquist relation applied to frequency-sampling prototype filters 131

List of Acronyms

3GPP	third Generation Partnership Project
4G LTE	fourth Generation - Long Term Evolution
5G NR	fifth Generation - New Radio
APP	A Posteriori Probabilities
AWGN	Additive White Gaussian Noise
BER	Bit Error Rate
BF-OFDM	Block-Filtered Orthogonal Frequency Division Multiplexing
BLT	Balian Low Theorem
BS	Base Station
BT	Bandwidth-Time (Gaussian filter parameter)
CBER	Code Block Error Rate
CIR	Channel Impulse Response
cMTC	critical Machine-Type-Communication
CP	Cyclic Prefix
CP-OFDM	Cyclic-Prefix Orthogonal Frequency Division Multiplexing
CS	Cyclic Suffix
CSI	Channel State Information
DFT	Discrete Fourier Transform
DL	DownLink
eMBB	enhanced Mobile BroadBand
FBMC	Filter-Bank MultiCarrier
FIR	Filter Impulse Response
FFT	Fast Fourier Transform
FFT-FBMC	Fast Fourier Transform - Filter-Bank MultiCarrier
fOFDM	filtered Orthogonal Frequency Division Multiplexing
FR	Frequency Range
FS-FBMC	Frequency-Spreading Filter-Bank MultiCarrier
IAI	Inter-Antenna Interference
ICI	Inter-Carrier Interference
IFFT	Inverse Fast Fourier Transform
IoT	Internet of Things
ISI	Inter-Symbol Interference
LD	Linear Detection

LDPC	Low Density Parity Check
LLL	Lenstra-Lenstra-Lovász
LLR	Logarithmic Likelihood Ratio
LR	Lattice Reduction
MAP	Maximum A Posteriori
MCS	Modulation Coding Scheme
MIMO	Multiple Input Multiple Output
ML	Maximum Likelihood
MMSE	Minimum Mean Square Error
mMTC	massive Machine-Type-Communication
MSE	Mean Square Error
MTC	Machine-Type-Communication
NPR	Near Perfect Reconstruction
OFDM	Orthogonal Frequency Division Multiplexing
OFDMA	Orthogonal Frequency Division Multiple Access
OOB	Out Of Band
OSI	Open Systems Interconnection
OQAM	Offset Quadrature Amplitude Modulations
QAM	Quadrature Amplitude Modulations
PAM	Pulse Amplitude Modulations
PPN	PolyPhase Network
PSD	Power Spectral Density
RB	Resource Block
RF	Radio Frequency
Rx	Receiver
SCS	SubCarrier Spacing
SIC	Successive Interference Cancellation
SIR	Signal-to-Interference Ratio
SNR	Signal-to-Noise Ratio
STBC	Space Time Block Code
TDL	Tap Delay Line
Tx	Transmitter
UE	User Equipment
UF-OFDM	Universal Filtered OFDM
UoI	User of Interest
UL	Uplink
URLCC	Ultra Reliable Low Latency Communications
WOLA-OFDM	Weighted OverLap and Add OFDM
ZF	Zero Forcing

Introduction

5G enables a fully connected society with a highly heterogeneous network thanks to its improved signal flexibility. However, multiple access is made more difficult because of the diverse services that 5G supports. Enhanced spectral confinement is considered in this work to ease service multiplexing especially in sub-6 GHz communications. The considered option in the proposed work is to properly combine filter-bank with complex orthogonality so that both improved side lobe rejection and direct re-use of 4G/5G techniques can be simultaneously achieved.

The **first chapter** gives the context of mobile technology development and introduces the 5G New Radio standard by highlighting the differences with 4G LTE from the physical layer perspectives. The system model of the Orthogonal Frequency Division Multiplexing (OFDM), waveform in use in 4G LTE and 5G NR, is fully described and its performance is evaluated focusing on 5G-oriented scenarios. Two 5G scenarios are considered in this work: relaxed time synchronization and multi-service coexistence. The study shows that the high out-of-band emissions of OFDM are responsible for the poor performance in those 5G scenarios.

In the **second chapter**, different state-of-the-art solutions that were proposed as an alternative of OFDM for 5G are described. The waveforms rely on diverse techniques to improve their spectral confinement from time convolution to windowing via filter-banks processing. A performance evaluation is then provided to compare the considered alternatives with OFDM on typical scenarios (spectral confinement, complexity, channel performance for both uncoded and coded systems) and 5G specific scenarios (asynchronous multi-user uplink and multi-service coexistence). It is shown that Filter-Bank MultiCarrier with Offset QAM (FBMC-OQAM) provides the best trade-off between performance and system complexity. However, the orthogonality condition is restricted to the real field which prevents a straightforward re-use of known-how 4G/5G techniques. Besides, the system is fundamentally different from legacy OFDM which prevents backward compatibility with already deployed technologies.

A precoding scheme for filter-bank based transmission scheme is described in **chapter 3**. The proposed precoding scheme is based on OFDM modulators and can be used instead of the commonly used OQAM signaling. It allows the use of filter-bank while ensuring the orthogonality in the complex field and therefore it alleviates the drawbacks induced by the OQAM signaling used in FBMC-OQAM. Two waveforms using the OFDM-based precoding are studied. The first one is a state-of-the-art solution named Fast Fourier Transform FBMC (FFT-FBMC). Its receiver scheme performs the reverse transmitter processing. The second one is a novel solution developed in this work named Block-Filtered OFDM. The main difference with FFT-FBMC is the receiver scheme which is reduced to a simple

FFT receiver (*i.e.* similar to a 4G/5G receiver scheme). BF-OFDM thus provides a good trade-off between spectrum confinement and backward compatibility with former mobile technologies. In this chapter, two prototype filter design methods are provided as well. A first method optimises the intrinsic interference rejection (*i.e.* complex orthogonality condition) and the other the side lobe rejection (*i.e.* spectrum confinement).

In the **fourth chapter**, the waveform models provided in the third chapter are adapted to 5G NR systems. Different configurations are selected for the performance evaluation to be able to analyze the potential benefits of each one of them. The selected configurations are then compared with OFDM and the state-of-the-art solutions presented in the second chapter by considering the same evaluation scenarios as in the second chapter. Both FFT-FBMC and BF-OFDM provide excellent results in 5G specific scenarios while maintaining a low complexity increase compared to legacy OFDM.

In the **fifth chapter**, some results on multi-antenna receivers are presented. Lattice reduction techniques are used to improve the performance of linear receivers. However, the adaptation with advanced channel coding and reliability information estimation is not straightforward. This work presents a new demapping technique named Successive Interference Cancellation improving the performance for uncoded systems and allowing the use of channel coding. OFDM systems are used for the performance evaluation but the techniques developed in this chapter are thought to improve the interference cancellation for FBMC/OQAM MIMO receiver. Unfortunately, the adaption with FBMC/OQAM is not addressed in this study and is left for future works. The chapter not only proposes a solution to efficiently support large MIMO configurations (interesting for mobile above 6 GHz communications and for the schemes studied on the previous chapters), but it also introduces a novel solution for FBMC/OQAM to efficiently support MIMO schemes.

Concluding comments are given in the **last chapter** where the major contributions of the presented works are summed up and study perspectives are proposed.

1 Overview of 5G Physical Layer

The first chapter is dedicated to the introduction of cellular networks. A brief review of the major changes brought by the new standard is provided. Then, the system model of the resulting physical layer is described and analysed by considering 5G oriented scenarios.

1.1 From human-to-human communications to heterogeneous networks.

Technological advancements have often shown a substantial impact in human life and communication was no exception. In the second half of the 19^{th} century, wireline telegraphy and telephony allowed information to move from speed of people to speed of light. A century later with the emergence of radio communications, wires were no longer required and wireless communications came into sight. Since, the mobile technologies successively broke technological limitations enabling new applications with voice communications with 1G, data services like text and multimedia messages with 2G, TV broadcasting and video on demand enabled by 3G and full internet access supported by 4G.

Internet has permanently changed the way people communicate with other. The use of images and videos as support of messages has become common with the rise of social networks. Besides, mobile phones became entertainment devices with 4G which allows gaming and supports high definition video streaming. As a consequence, 4G mainly supports high data rate downlink traffic.

With the newly proposed fifth generation (5G), the enhanced mobile broadband service (eMBB) will be further improved and enhanced allowing for instance the support of latest video standards (4K, 8K). But the new technolgoy also aims at supporting Machine Type Communications (MTC) communications. MTC can be very diverse. Among possible use cases, one can mention sensor networks (smart homes, agriculture), connected cars, healthcare devices (with remote surgery) or smart grids. MTC are thus basically different from typical 4G communications and can be categorized into two groups. A first group rallies all applications with a huge number of low data rate devices and is known as massive MTC (mMTC). Sensor networks and Internet of Thing (IoT) are two typical applications of mMTC. The second group gathers critical applications like connected cars, remote control of industry machineries or healthcare devices. Critical communications means that

the information must be exchanged with an extremely high reliability to ensure a proper working of the applications. Besides, ensuring low latency is imperative for most of the targeted applications. That is why this second group is also known as Ultra Reliable Low Latency Communications (URLLC) and sometimes denoted by critical MTC (cMTC).

MTC are currently served by mostly by non-3GPP networks (Bluetooth, Wifi, NFC, Lora, Sigfox, ...). Nonetheless, 3GPP already paved the way to MTC support with the development of Narrow-Band IoT (NB-IoT) (4G release 13). 5G aims at extending this concept of heterogeneous network by providing a unified solution with adaptable features. The three services (namely eMBB, mMTC and URLLC) and their diverse requirements will be supported inside the same network. The network thus becomes device-centric. Indeed with 5G, the radio link has also to be adapted to the node specifications and requirements.

With 5G, technological locks imposed by 4G network must be broken which results in significant changes in the air interface design. However on the other hand, backward compatibility with already deployed systems must be ensured which limits the modifications to bring.

1.2 Physical layer and system model

Transmitting and receiving information are complex operations that depend on the network and the use case. The Open Systems Interconnection model (OSI model) is a conceptual framework that is commonly used to describe the functions of a networking communication system. The processes of transmission and reception of a message are described into seven independent layers. Each layer is dedicated to a special feature which thus eases the design and the standardization of communication systems. The three upper layers (application (7), presentation (6) and session (5)) are data-related layers ensuring the interaction with the user, the encryption/decryption and data compression and authentication processes. The transport layer (4) controls the reliability of the link through flow control, (de)segmentation and error control. The transport layer provides the acknowledgement of successful transmissions and re-transmission of failed ones. The network layer (3) ensures host addressing and message forwarding (inter-network routing). The data link layer (2) ensures the link and data transfer between connected nodes. It arbitrates the access of the transmission medium among the nodes and specifies how nodes detect and recover from message collisions occurring when multiple nodes use the medium simultaneously. The physical layer (1) directly interacts with the transmission medium. It converts the raw bitstream coming from the upper layer into a signal (*i.e.* modulation stage) to be transmitted over the medium and ensures a proper reception and demodulation of the signal.

The physical-layer system model can be represented as depicted in Figure 1.1. It is composed of three parts: the transmitter, the propagation channel and the receiver. The modulation and demodulation are respectively the operations of varying the properties of a periodic waveform according to the bitstream to be transmitted and extracting the bitstream from the received signal variations. In mobile systems, the conversion from binary to waveform is performed with digital modulations. At the transmitter side, groups of bits are mapped into complex symbols drawn from a known constellation (Quadrature Amplitude Modulations

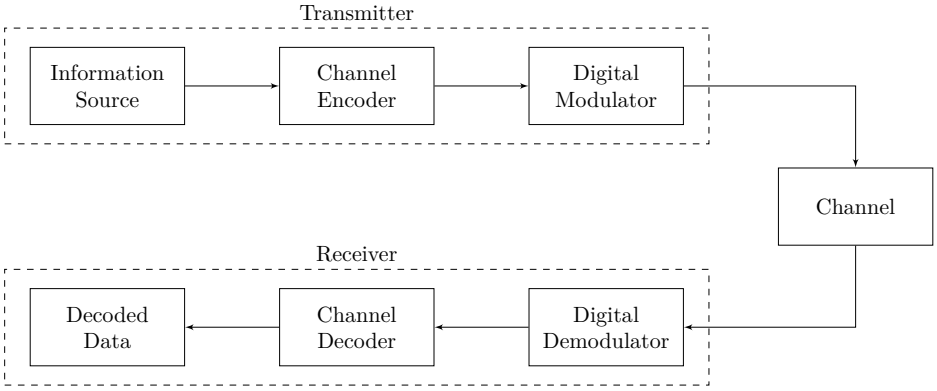

Figure 1.1: The physical-layer system model.

(QAM) are commonly used in mobile systems). The signal waveform is then modulated according to the incoming symbol stream (in phase and amplitude for QAM symbols). The receiver estimates the symbols sequence from the received signal parameters (phase and amplitude for QAM modulations) and then the transmitted bitstream.

However the propagation channel alters the signal which makes its reconstruction more difficult. In wireless systems, the channel response (channel strength over time and frequency) can be described through two phenomena: large-scale fading which is due to path loss and shadowing by large obstacles and small-scale fading which is induced by the constructive and destructive interference of multiple delayed echoes of the transmitted signal. The channel response can thus not be predicted and needs to be estimated in real time by the communication systems. In addition to that, the signal is corrupted by various noise sources such as thermal noise intrinsic to any communications systems.

The encoder and decoder schemes aim at improving the robustness of the communication against propagation-induced distortion. Redundancy can be added to the bitstream at the transmitter side so that the decoder can correct some errors. It seems interesting to notice that the waveform design plays a predominant role in channel robustness as well. Indeed, redundancy can be added as well at the modualtion stage like for instance the Cyclic Prefix (CP) technique which prepends a copy of the tail of the each transmitted symbol to it.

The Radio Frequency (RF) front ends could be considered as well in the system model. Indeed, the amplification of the signal and the upconversion or downconversion to RF bands are other sources of signal distortion (probably non linear). However in this work, the RF front end is assumed to be ideal and thus will not be considered.

1.3 From 4G LTE to 5G NR

To ensure a world-wide deployment of mobile technologies, standardization is a mandatory step. That is why the 3rd Generation Partnership Project (3GPP), a collaboration of telecommunications standard organizations was formed in 1998. It produces technical reports and specifications for mobile technologies. The initial scope of 3GPP was to find a global consensus for the third generation of

mobile technology (3G). Since, the project has been extended to the maintenance and the development of post-3G technologies. The project covers both cellular telecommunication networks (*i.e.* radio access and transport network) and service capabilities (*i.e.* quality of service, security, ..).

3GPP uses a system of incremental "releases" which provides industry and developers with a stable system for the implementation of new features. Releases from 8 to 14 were dedicated to 4G Long Term Evolution (4G LTE) and since release 15 to 5G New Radio (5G NR) and beyond.

1.3.1 LTE structure

4G LTE was introduced with release 8 to get higher data rate with 100 Mbps peak for downlink (DL) and 50 Mbps peak for uplink (UL). Those speeds have been brought to 1000 Mbps peak for DL and 500 Mbps peak for UL for LTE advance (release 10). This performance could be achieved thanks to a flexible air interface technology which is described in this section.

The Orthogonal Frequency Division Multiplexing (OFDM) is the core of the LTE radio transmission. In OFDM transmissions, the data is transmitted over a large number of parallel narrow-band subcarriers. Moreover, CP can be inserted between OFDM symbols in time which makes the OFDM transmission robust to time dispersion of the propagation channel[1]. Moreover, OFDM is used as a multiple access scheme (OFDMA) which enables the allocation of the available bandwidth between several connected nodes without collision. Duplexing can be performed both in the time domain with the Time Division Duplexing (TDD) or in the frequency domain with the Frequency Domain Duplexing (FDD). Nonetheless, both schemes rely on the same radio frame.

The LTE radio frame is composed of ten subframes of 1 ms duration each. Each subframes is composed of two slots of 0.5 ms duration which corresponds to the transmission of 7 OFDM symbols with normal CP as depicted in Figure 1.2. In FDD, both Downlink (DL) and Uplink (UL) share the same time structure but use different bands. In TDD, the subframes can be dedicated either to DL transmissions, UL transmissions or pilots (for both UL and DL) according to seven available patterns.

In LTE, the subcarrier spacing is fixed 15 kHz for most transmissions. The smallest unit that can be scheduled is a group of twelve subcarriers for a slot duration (0.5 ms for 180 kHz of band), also known as a Resource Block (RB). Depending on the data to transmit, each nodes can allocate multiple RBs over time and/or frequency. Nonetheless, LTE also supports a more robust configuration to very high delay spreads with 7.5 kHz of subcarrier spacing and therefore symbols with doubled duration. Besides, this configuration also allows the use of an extended CP with 6 symbols per slot (instead of 7). This configuration is used for multimedia broadcast over single frequency network (MBSFN).

LTE can be deployed for different frequency bandwidths in order to be able to operate in available spectrum of different size. It supports six different bandwidths ranging from 1.4 MHz to 20 MHz. The RB dimension (0.5 ms for 180 kHz of band) remain the same for all the bandwidth configurations. However, the OFDM

[1] A detailed description of the OFDM transmission is given in Section 1.4

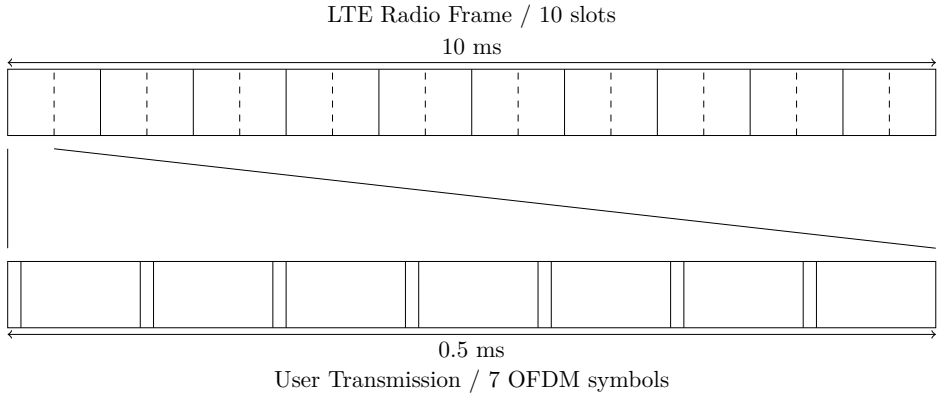

Figure 1.2: Slot structure for the normal cyclic prefix case

.

Table 1.1: 5G NR numerologies.

μ	SCS [kHz]	Symbol duration (with CP) [μs / in sples]	Support
0	15.0	71.35 / 4096 + 288	Data & Sync FR1
1	30.0	35.68 / 2048 + 144	Data & Sync FR1
2	60.0	17.84 / 1024 + 72	Data FR1, Data FR2
3	120.0	8.92 / 512 + 36	Data & Sync FR2
4	240.0	4.46 / 256 + 18	Sync FR2
5	480.0	2.23 / 128 + 9	only specified

symbol duration (with the CP) and the chip rate is adapted from one configuration to another. LTE-Advanced (release 10) can exploit bandwidth allocations up to 100 MHz thanks to Carrier Aggregation. It consists in combining different spectrum fragments (contiguous or not) to enlarge the allocated bandwidth.

LTE provides a strong spectrum flexibility and can adapt the radio spectrum to local regulations.

1.3.2 Release 15 overview

Release 15 is dedicated to the specifications of the fifth generation of mobile technology, named 5G New Radio (5G NR). In 5G NR, the spectrum flexibility is further improved with respect to 4G LTE. Indeed, new bandwidths up to 100 MHz are specified. To obtain such available bandwidths, millimeter waves (mmWave) are now used. Besides, dynamic TDD is supported. But 5G NR is not reduced to a simple mobile technology. Besides, it also aims at integrating a wide range of communication types including massive IoT and vehicular communications as well as non terrestrial networks (*e.g.* satellite networks). To this end, 5G NR also integrates signal flexibility by introducing scalable waveform numerologies. Release 15 only addresses eMBB and URLCC services for carrier frequencies below 52.6 GHz. Study items for release 16 are dedicated to mMTC service, Vehicle-to-Everything (V2X), satellite communications, non orthogonal multiple access (NOMA) and even backhaul. Those features may nonetheless not be included in release 16 depending on the maturity of those techniques at the end of the study period.

With 5G NR, scalable SubCarrier Spacing (SCS) and symbol duration are supported. Thanks to this new feature it is possible to support the extreme variation of requirements target services. Numerologies are identified by a numerology index μ ranging from 0 to 5 as shown in Table 1.1 [1]. The three first numerologies, $\mu = \{0, 1, 2\}$, are used for sub-6GHz frequency (Frequency Range (FR) 1), $\mu = \{2, 3, 4\}$ addresses mmWave ($<$ 52.6 GHz, FR2) and $\mu = 5$ is not supported yet[2, 1]. The SCS Δ_f^μ and the symbol duration T^μ are determined by the numerology index μ: $\Delta_f^\mu = 15 \times 2^\mu$ kHz, $T^\mu = 71.35/2^\mu$ μs. For each numerology, the CP duration is adapted so that all numerologies still provide the same symbol density as in LTE. Sub-6GHz numerologies ensures a good robustness to multipath propagation (thanks to long CP and high receiver frequency resolution) while mmWave numerologies have enhanced frequency offset and phase noise resilience (thanks to enlarged SCS).

The possible values of SCS and symbol durations still guarantee a straightforward multiple access scheme. Indeed, in the time domain, 5G still relies on a frame system. 5G frame lasts 10 ms and is decomposed of ten subframes of 1 ms as in LTE. However in 5G NR, the scheduling can be either slot-based or non-slot-based (or mini-slot-based). A slot is defined as a group of 14 OFDM symbols with normal Cyclic Prefix (CP) length (except for $\mu = 4$ where 28 symbols per slots are assumed). The slot duration thus depends on the numerology with $1/2^\mu$ ms. It implies that the number of slots per subframe thus varies according the numerology which is a difference with respect to LTE. Mini-slots can span less waveform symbols as small as one symbol [2] and represent the minimum time scheduling unit in 5G. Mini-slots give more flexibility and allow to support very low latency requirements. This finer time domain granularity can be used for beam sweeping (*i.e.* pairs of transmit and receive beams are measured so as to determine the best beam pair) in mmWave and paves the way to forward compatibility with unlicensed communications.

In the frequency domain, the scheduling unit is still a group of 12 subcarriers. But now, the RB bandwidth depends on its numerology from 180 kHz with $\mu = 0$ to 5.76 MHz for $\mu = 5$. Moreover, the symbol duration is halved when the SCS is doubled. It makes the 5G resource grids flexible in terms of allocation while ensuring a high use efficiency as illustrated in Figure 1.3.

Regarding duplexing, dynamic TDD patterns are supported in release 15. Mixed slots replace LTE special slots. In such slots, the assignment between UL and DL loads is defined at the symbol level as described in [3] (in LTE assignment is done at the subframe level). Different slot formats are described where each of the 14 symbols can be dedicated to DL transmissions, UL transmissions or flexible. The mixed-slots can thus be statically (no flexible symbol), semi-statically (presence of both DL and/or UL and flexible symbols) or dynamically (only flexible symbols) configured.

When it comes to the frequency domain, Bandwidth Parts (BP) are a new concept introduced in release 15 as well. BPs are defined as a set of contiguous RBs sharing the same numerology. An User Equipment (UE) can be configured with up to four BPs with at least one BP for DL and one BP for UL. The first use case of BPs is to support UE with reduced bandwidth capabilities. Indeed, some UEs are not able to operate over the large bandwidths considered for 5G NR with a single RF chain. By introducing such concept, 5G NR UEs are not

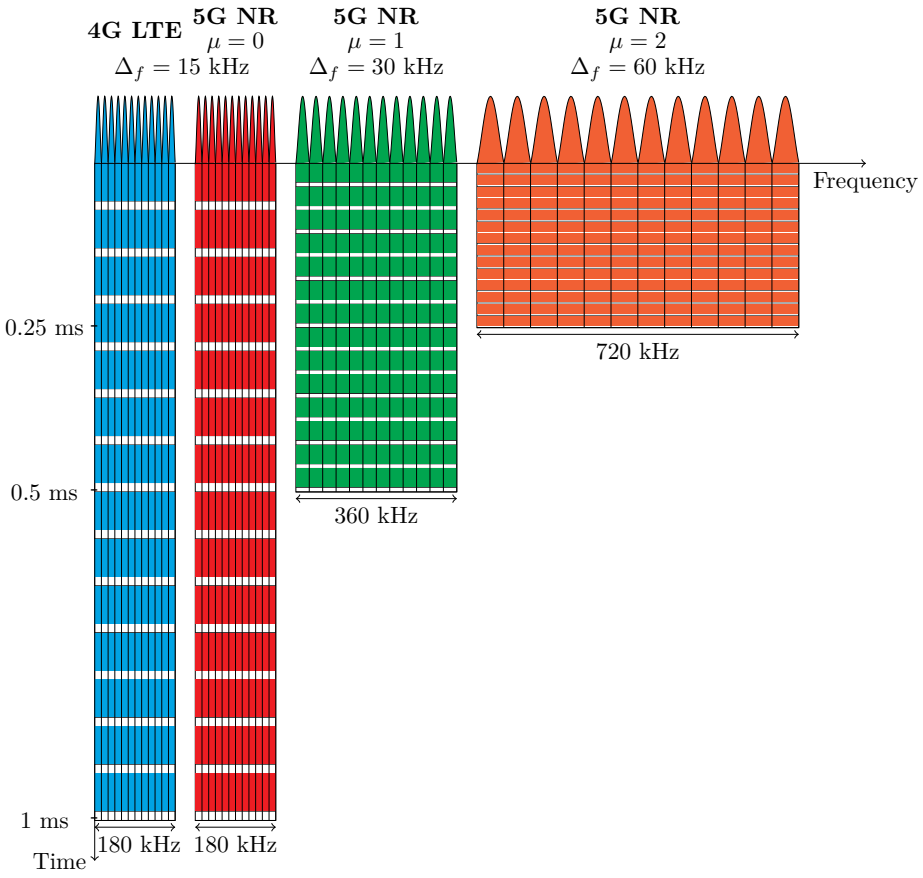

Figure 1.3: Scalable RB allocation.

forced to support the overall cell bandwidth to be assigned to it. It also enables power saving as a low data-rate UE can be associated with a narrow-band BPs (*i.e.* at least a RB) to avoid idling power consumption. Thanks to BPs, it is possible to support different numerologies inside the same cell. Indeed, even if a BP is dedicated to a service, adjacent BPs can provide distinct numerologies. The support of non-contiguous spectrum is also straightforward thanks to this new feature and it also paves the way to forward compatibility as the BPs can work without any knowledge on the activities of adjacent BPs.

Regarding channel coding, it has been only defined for the eMBB service. The channel coding for mMTC and URLLC will be addressed in further releases. For eMBB, turbo coding used in LTE has been replaced by Low Density Parity Check (LDPC) codes for data channels and Polar coding for control channels and the Physical Broadcast CHannel (PBCH). Moreover, the Code Block Group (CBG) retransmission is introduced in release 15. It enables retransmissions with a codeblock granularity to improve latency.

Big changes are also considered about multiple antennas (MIMO) techniques for 5G NR. 5G NR will support both Single-User MIMO (SU-MIMO) and Multi-User MIMO (MU-MIMO). However, the use cases depend on the used FR. Sub-6GHz MIMO configurations are dedicated to spectral efficiency enhancement. Large MIMO configurations are specified (up to 8×8) working with spatial multiplexing. MIMO for mmWave aims at ensuring the Line of Sight (LoS) with

the UEs by means of beamforming techniques (beam sweeping and monitoring). MIMO mmWave transceivers are expected to include analog components.

As a conclusion, 5G NR is designed to be even more flexible than LTE especially at the signal level. Strong efforts have been taken to support very low latency requirements while still ensuring a high spectral efficiency. The system has significantly improved its capacity with more than 20 GHz of bandwidth specified in mmWave (about 10 GHz for each UL and DL)[4] and maximum channel bandwidth is increased to 100 MHz for FR1 and 400 MHz for FR2[2].

Once this overall description of these new 5G NR features is made, we can move to the study of the selected waveform (for the considered services and FRs in release 15) which brings us to the next section.

1.4 OFDM, the most predominant waveform in wireless standards

1.4.1 Brief history of OFDM

In multicarrier systems, the total bandwidth is divided into multiple subbands. Each subband is modulated by its own symbol sequence and then they are all multiplexed. Dividing large bandwidth offers the possibility to rely on a simple equalization scheme. Indeed, as long as each subband is narrower than the coherence bandwidth of the channel, the flat channel approximation holds. Consequently, a 1-tap equalisation per subband is sufficient to counteract the channel response. Besides, if the transmitter knows the channel response, it is possible to optimize the power allocation among the subbands to cope with the frequency selectivity of the channel[5].

Subband separation can be achieved in two ways: i)using filters to completely separate non-overlapping subbands or ii)using overlapping but non-interfering subbands. The first method refers to conventional Frequency Division Multiplexing (FDM). This method exhibits an inefficient bandwidth use induced by the roll-off of the shaping filters. However with the second method, 100% bandwidth use can be ensured by relying on orthogonal basis functions. The harmonic sinusoids are a simple choice as they are orthogonal on their period if the subband spacing equal to the reciprocal of the useful symbol duration as shown in Figure 1.4. This technique is known as Orthogonal FDM (OFDM). OFDM is usually designed with rectangular shaping pulse and the subbands are reduced to simple subcarriers.

In OFDM, the baseband modulation/demodulation can be performed by means of (Inverse) Discrete Fourier Transform ((I)DFT) which replaces the banks of subband oscillators[6]. Besides the OFDM transceiver implementation can be made even more efficient when the number of subcarrier is a power of 2 by relying on the Cooley-Turkey Fast Fourier Transform (FFT)[7], a low-complexity DFT algorithm. Another important contribution is the use of Cyclic Prefix (CP) to guarantee the orthogonality in time over dispersive channels [8]. It simulates a cyclic convolution between the transmitted signal and the channel as long as the CP length is longer than the delay spread of the channel. As a conclusion, OFDM has been designed to guarantee high spectral efficiency while being robust to frequency-selective channels. Moreover, it benefits from an efficient hardware implementation.

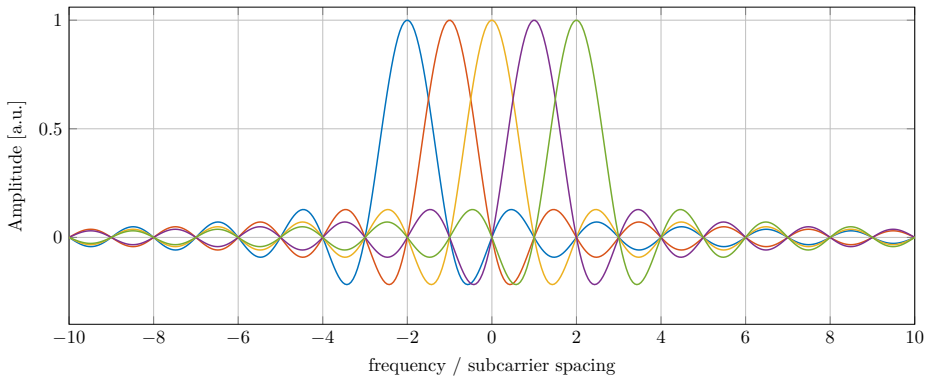

Figure 1.4: OFDM frequency response for a few subcarriers.

The aforementioned advantages has made the OFDM the most used multicarrier waveforms in wireless standards: mobile broadband LTE[9], Wireless LAN IEEE 802.11 (a, g, n, ac, ax)[10], digital radio and TV[11][12], etc. The waveform is also used in wired systems but under the term Discrete MultiTone (DMT): ADSL and VDSL, power line communications, digital cable TV [13], optical communications, etc.

1.4.2 System model

This section aims at introducing the mathematical framework for signal modelling. The baseband OFDM transmitted signal can be expressed as in (1.1). The subcarrier (*i.e.* subband) frequencies are spaced by $\Delta_f = 1/T_u$ where T_u is the useful symbol duration. A CP of length T_{CP} is prepended to each useful symbol which brings to the total symbol duration to T. Let us denote by N the maximum number of subcarriers and $a_k[n]$ the data symbol (with mean energy $E_{k,n}\left[|a_k[n]|^2\right] = \sigma_a^2$) transmitted over the k^{th} subcarrier at time instant n. The data symbol can be drawn from any complex constellation such as M-QAM. Π_T is the gate function of length T: $\Pi_T = 1$ if $0 \leq t < T$ and null otherwise.

$$s(t) = \frac{1}{\sqrt{N}} \sum_{n} \sum_{k=0}^{N-1} a_k[n] \Pi_T(t - nT) e^{j2\pi k \Delta_f (t - T_{\text{CP}} - nT)} \tag{1.1}$$

Perfect orthogonality is ensured when (1.2) is verified. $\delta_{x,x'}$ is the Kronecker product between x and x' which returns 1 if the two parameters are equal and null otherwise.

$$\int_{-\infty}^{+\infty} \Pi_{T_u}(t - n_o T - T_{\text{CP}}) \Pi_T(t - nT) e^{j2\pi \frac{(k-k_o)t}{T_u}} dt = N \delta_{k,k_o} \delta_{n,n_o} \tag{1.2}$$

At the receiver side, the signal is sampled according to Nyquist sampling theorem with a period $T_s = M/T_u$. Let $f[n] = f(nT_s)$, N_{CP} be the length of the CP (in samples) and $N_{\text{ext}} = N + N_{\text{CP}}$. Assuming an ideal propagation channel, a noiseless communication and ideal synchronization, the baseband received signal over the ${k_o}^{\text{th}}$ subcarrier at time instant n_o can be written as follows.

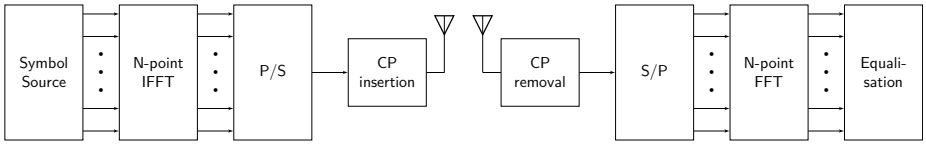

Figure 1.5: CP-OFDM Tx and Rx schemes.

$$\begin{aligned} r_{k_o}[n_o] &= \frac{1}{\sqrt{N}} \sum_{m=0}^{N-1} s[m + n_o N_{\text{ext}} + N_{\text{CP}}] e^{-\frac{j2\pi k_0 m}{N}} \\ &= \frac{1}{N} a_{k_o}[n_o] \underbrace{\sum_{m=0}^{N-1} e^{j2\pi \frac{m(k_o - k_o)}{N}}}_{=N} + \underbrace{\sum_{k \neq k_o} a_k[n_o] \sum_{m=0}^{N-1} e^{j2\pi \frac{m(k-k_o)}{N}}}_{=0} \\ &= a_{k_o}[n_o] \end{aligned} \tag{1.3}$$

The CP-OFDM Tx and Rx schemes are depicted in Figure 1.5. The symbol source represents the bitstream coming from upper layers and mapping into conventional symbol constellations. The IFFT generates the temporal signal and then the CP is inserted for every OFDM symbols. Finally, the signal is transmitted over the Radio Frequency (RF) front end performing the up conversion to the RF carrier frequency, the amplification, passband filtering and transmission over the antenna unit.

At the receiver side, the RF front end ensures low noise amplification, passband filtering to remove the spurious and the down conversion to baseband where some pre-processing may occur as well (like hardware-induced distortion compensation). The CP are removed and the useful OFDM symbols are transposed in the frequency domain via the FFT. The received symbols are then forwarded to the equalisation stage to cancel the propagation channel effect. The presented schemes could be more detailed by taking into account the channel estimation that provides the real-time estimation of the propagation channel response, the synchronisation stage which detects the beginning of frames, hardware impairment compensation and so forth...

Realistic transmissions are affected by many impairments and frequency-selective channels is one the most critical impairments for sub 6 GHz communications. The signal arrives at the receiver by different paths, *i.e.* with different attenuations and delays, and can partially cancel itself. A multi-path channel can be represented by a Finite Impulse Response (FIR) filter $h[m]$. The baseband received signal $y[m]$ can be expressed as follows:

$$y[m] = h[m] * s[m] = \sum_{l=0}^{L-1} h[l] s[m-l] \tag{1.4}$$

The L echoes of the signal are collected by the receiver. However, one can observe that as long as the delay spread of the channel is shorter than the CP length, *i.e.* $L \leq N_{\text{CP}}$, InterSymbol Interference (ISI) is avoided as shown in (1.5). The channel coefficient $H[k_o]$ (defined in (1.5)) is then compensated by the

equalization stage. A one-tap equalization performs well if the response channel is constant over the subcarrier band. In (1.5), the channel is assumed constant in time. This condition can be relaxed as long as the channel is constant over at least an extended symbol duration T.

$$\begin{aligned} r_{k_o}[n_o] &= \frac{1}{\sqrt{N}} \sum_{m=0}^{N-1} \sum_{l=0}^{L-1} h[l] s[m + n_o N_{\text{ext}} + N_{\text{CP}} - l] e^{-j2\pi \frac{m k_0}{N}} \\ &= \frac{1}{\sqrt{N}} \sum_{l=0}^{L-1} h[l] \sum_{m=0}^{N-1} s[m + n_o N_{\text{ext}} + N_{\text{CP}} - l] e^{-j2\pi \frac{m k_0}{N}} \\ &= a_{k_o}[n_o] \underbrace{\sum_{l=0}^{L-1} h[l] e^{-j2\pi \frac{k_o l}{N}}}_{H[k_o]} \end{aligned} \tag{1.5}$$

It is one of the main reasons why OFDM has been widely preferred for sub-6GHz communications. Indeed the CP length can be adapted to the measured channel delay spread which ensures a good robustness against fading while maximizing the spectral efficiency.

A more realistic model also takes into consideration Additive White Gaussian Noise (AWGN) which represents the thermal noise intrinsic to any electronic device. The noise ν is usually modeled with circularly-symmetric normally distributed random variable with zero mean and variance σ_ν^2. The received signal can thus be expressed as shown in (1.6).

$$r_{k_o}[n_o] = a_{k_o}[n_o] H[k_o] + \nu_{k_o}[n_o] \tag{1.6}$$

1.4.3 Demodulation

The received signal may thus be highly altered which makes the recovery of the information difficult. A demodulator aims at estimating the received symbol from the observation of the received signal (1.6).

The optimal solution to minimize the symbol error rate consists in evaluating the A Posteriori Probabilities (APP) for each possible symbol drawn from the constellation given the observation of the received signal. The symbol with the highest APP is then selected according to the Maximum A Posteriori (MAP) criterion. By assuming the constellation symbols are equiprobable (*i.e.* same probability of being transmitted), the MAP method can be reduced to the Maximum Likehood (ML) estimation.

ML estimation therefore requires a full search process in order to obtain the estimation of the transmitted symbols. Despite the optimal performance it provides, this method is not appealing for high data rate applications employing large constellations.

Hence in practice, linear equalization is considered to obtain an estimation of transmitted symbol sequence with low-complexity. Linear equalizer mainly aims at counteracting the distortion induced by the propagation channel and two algorithms are usually used: Zero Forcing (ZF) (1.7) and Minimum Mean Square

Error (MMSE) (1.8). The Zero-Forcing may result in noise enhancement so that is why MMSE limits signal amplification for low Signal-to-Noise Ratio (SNR) levels.

$$w_{\mathrm{ZF}}[k_o] = H^*[k_o] / \left|H[k_o]\right|^2 \tag{1.7}$$

$$w_{\mathrm{MMSE}}[k_o] = H^*[k_o] / (\left|H[k_o]\right|^2 + \sigma_\nu^2/\sigma_a^2) \tag{1.8}$$

The estimated signal expressions are given in (1.21) for ZF and (1.22) for MMSE. The MMSE estimator is biased so as to avoid noise enhancement as mentioned above.

$$\tilde{r}_{k_o,\mathrm{ZF}}[n_o] = a_{k_o}[n_o] + w_{\mathrm{ZF}}[k_o]\nu_{k_o}[n_o] \tag{1.9}$$

$$\tilde{r}_{k_o,\mathrm{MMSE}}[n_o] = w_{\mathrm{MMSE}}[k_o]a_{k_o}[n_o]H[k_o] + w_{\mathrm{MMSE}}[k_o]\nu_{k_o}[n_o] \tag{1.10}$$

However, errors may still occur because of noise, channel estimation errors, imperfect synchronization and so on. Redundancy is thus added in the bitstream to limit errors. The decoding can be made even more efficient by relying of soft-input expressing the reliability of recevied bits. Such decoders are known as soft-decision decoders and the reliability metric is named the likelihood ratio. The likelihood ratio of a bit b, $\mathrm{LR}(b)$ corresponds to the ratio of the probability this bit being 1 and the probability of being 0 from the observation of the received signal as expressed in (1.11). If b is the i$^{\mathrm{th}}$ bit of the ${n_o}^{\mathrm{th}}$ symbol transmitted over the subcarrier k_o, the likelihood ratio corresponds the ratio of the probability of transmitting $a_{k_o}[n_o]$ drawn from the sub-set of the constellation with symbols having their i^{th} bit being 1 $\mathcal{S}_i^1$ over the probability of transmitting $a_{k_o}[n_o]$ drawn from the sub-set of the constellation with symbols having their i^{th} bit being 0 $\mathcal{S}_i^0$ as shown in (1.12). By applying Bayes rule and assuming equally distributed symbols, the expression (1.13) yields.

$$\mathrm{LR}(b) = \frac{P(b=1|r)}{P(b=0|\tilde{r})} \tag{1.11}$$

$$= \frac{\sum_{s\in\mathcal{S}_i^1} P(a_{k_o}[n_o]=s|\tilde{r})}{\sum_{s\in\mathcal{S}_i^0} P(a_{k_o}[n_o]=s|\tilde{r})} \tag{1.12}$$

$$= \frac{\sum_{s\in\mathcal{S}_i^1} P(\tilde{r}|a_{k_o}[n_o]=s)}{\sum_{s\in\mathcal{S}_i^0} P(\tilde{r}|a_{k_o}[n_o]=s)} \tag{1.13}$$

The conditional probability density function of $\tilde{r}$ is Gaussian therefore by defining the variance of the estimation $\sigma_{\tilde{\nu}}^2$ as in (1.14) we obtain (1.15).

$$\sigma_{\tilde{\nu}}^2 = \left|w_{\mathrm{ZF}}[k_o]\right|^2 \sigma_\nu^2 \tag{1.14}$$

$$P(\tilde{r}|a_{k_o}[n_o]=s) = \frac{1}{\sqrt{2\pi\sigma_{\tilde{\nu}}^2}} e^{-\frac{\left|\tilde{r}-a_{k_o}[n_o]\right|^2}{2\sigma_{\tilde{\nu}}^2}} \tag{1.15}$$

The expression is derived for ZF but it is valid for MMSE as well. Indeed as the MMSE estimator is biased, (1.8) should be normalised by $(w_{\text{MSSE}}[k_o]H[k_o])^* / |w_{\text{MSSE}}[k_o]H[k_o]|^2$ which is equivalent to directly apply ZF.

As a consequence to compute the optimal LLR, M distances/probabilities have to be evaluated for a M-QAM which is equivalent to the complexity of the ML demapping. Sub optimal algorithms can simplify the LR computation. First, the logarithm of the LR is commonly computed and the metric is named Log LR (LLR). While the sign of LLR(b) indicates the corresponding hard decision (*i.e.* b=1 for positive LLR(b) and vice-versa), the absolute value is proportional to the reliability (*i.e.* the higher the most reliable). The log-sum approximation (1.16) can thus be considered. It states that the logarithm of a sum of normally distributed random variable is dominated by its largest term which is valid in high SNR regions for our applications.

$$\log \sum x_i \approx \max_i \log(x_i) \tag{1.16}$$

The sub-optimal LLR expression is given in (1.17).

$$\begin{aligned} \text{LLR}(b) &\approx \max \left(\log \sum_{s \in \mathcal{S}_i^1} P(\tilde{r}|a_{k_o}[n_o] = s) - \log \sum_{s \in \mathcal{S}_i^0} P(\tilde{r}|a_{k_o}[n_o] = s) \right) \\ &\approx \frac{1}{2\sigma_{\tilde{\nu}}^2} \left(\min_{s \in \mathcal{S}_i^0} \left(|\tilde{r}_{k_o}[n_o] - s|^2 \right) - \min_{s \in \mathcal{S}_i^1} \left(|\tilde{r}_{k_o}[n_o] - s|^2 \right) \right) \end{aligned} \tag{1.17}$$

The simplified LLR expressions still require the evaluation of M distance for a M-QAM. It is shown in [14] that the distances can be calculated with linear approximations by using the real and imaginary part of $\tilde{r}$ and some thresholds. Thanks to this approximation, likelihood metrics can be obtained with low-complexity. This technique will be considered and used for coded systems during numerical simulations.

Extension to MIMO systems

In MIMO systems, the demodulation is more complex as receivers must deal with Inter-Antenna Interference (IAI) as well. The system model (1.6) can be extended to multiple antenna systems as shown in (1.18) for the i^{th} receive antenna. The system is composed of N_T transmit antennas and N_R receive antennas. $\mathbf{H}_{i,j}[k_o]$ denotes the frequency response of the propagation channel between the j^{th} transmit antenna and i^{th} receive antenna for the subcarrier k_o and $(\nu_{k_o}[n_o])_i$ the AWGN noise for the i $^{\text{th}}$ receive layer.

$$(r_{k_o}[n_o])_i = \sum_{j=0}^{N_T-1} (a_{k_o}[n_o][j]\mathbf{H}_{i,j}[k_o]) + (\nu[k_o, n_o])_i \tag{1.18}$$

As for the single antenna systems, linear receivers ensure a low-complex implementation suitable for high data rate systems. In MIMO linear systems, the receive signal $\mathbf{r}_{k_o}[n_o] = [(r_{k_o}[n_o])_i]_{0 \leq i \leq N_R-1}$ is processed by a matrix (assuming

$N_R \geq N_T$) which expression depends on the criterion in use either ZF (1.19) or MMSE (1.20) where $\mathbf{I}_{N_R}$ denotes the identity matrix of size $N_R \times N_R$.

$$\mathbf{W}_{\mathrm{ZF}}[k_o] = \left(\mathbf{H}^H[k_o]\mathbf{H}[k_o]\right)^{-1}\mathbf{H}^H[k_o] \tag{1.19}$$

$$\mathbf{W}_{\mathrm{MMSE}}[k_o] = \left(\mathbf{H}^H[k_o]\mathbf{H}[k_o] + \sigma_\nu^2/\sigma_a^2\mathbf{I}_{N_R}\right)^{-1}\mathbf{H}^H[k_o] \tag{1.20}$$

The estimated signals can thus be expressed as shown below by letting $\beta[k_o] = \mathbf{W}_{\mathrm{MMSE}}[k_o]\mathbf{H}[k_o]$. As for the single antenna case, one can observe that ZF completely compensate the channel-induced distortion (no IAI interference) while the MMSE operates a trade-off between channel compensation and noise enhancement.

$$(\tilde{r}_{k_o,\mathrm{ZF}}[n_o])_i = a_{k_o}[n_o][i] + \sum_{j=0}^{N_R-1}(\mathbf{W}_{\mathrm{ZF}}[k_o])_{i,j}\,(\nu_{k_o}[n_o])_j \tag{1.21}$$

$$(\tilde{r}_{k_o,\mathrm{MMSE}}[n_o])_i = \sum_{j=0}^{N_R-1}(\beta[k_o])_{i,j}\,(a_{k_o}[n_o])_j + \sum_{j=0}^{N_R-1}(\mathbf{W}_{\mathrm{ZF}}[k_o])_{i,j}\,(\nu_{k_o}[n_o])_j \tag{1.22}$$

The computation of the LLR can processed as for single antenna systems and the linear approximation of the distances still holds. However, the variance of the noise $\sigma_{\tilde{\nu}}^2$ has to take into consideration the IAI term. It thus becomes

$$\begin{aligned}\sigma_{\mathrm{ZF}}^2[i] &= \sigma_\nu^2\sum_{j=0}^{N_R-1}\left|(\mathbf{W}_{\mathrm{ZF}}[k_o])_{i,j}\right|^2 \\ \sigma_{\mathrm{MMSE}}^2[i] &= \left(\sigma_\nu^2\sum_{j=0}^{N_R-1}\left|(\mathbf{W}_{\mathrm{MMSE}}[k_o])_{i,j}\right|^2 + \sigma_a^2\sum_{j\neq i}\left|(\beta[k_o])_{i,j}\right|^2\right)/\,(\beta[k_o])_{i,i}^2\end{aligned} \tag{1.23}$$

This section sums up the main advantages of CP-OFDM. With a well dimensioned SCS, it is possible to experience a flat frequency channel response at the subcarrier level which allows a simple 1-tap linear equalisation. Moreover, it is possible with QAM constellations to derive computation-effective likelihood metric which allows the use of state-of-the-art channel coding schemes and likelihood sequence decoders.

In the next section, a performance evaluation focusing on 5G-oriented evaluation scenarios is provided.

1.5 Limitations to meet 5G challenges

In this section, the performance of CP-OFDM in original 5G scenarios will be analyzed and then evaluated with numerical simulations. The two scenarios to

be studied will be the asynchronous multi-user uplink and the multi-service coexistence.

As the main purpose of this study is to analyze the interference induced by these specific scenarios, other sources of distortion such as frequency-selectivity of the channel or effects of additive noise are omitted.

From now and for the rest of the manuscript, two conventions will be taken. First, for the derivation of the analytical expression, only two users are considered in a first time: a User of Interest (UoI) which is the user the receiver demodulates and an interfering user which distorts the UoI signal. Indeed thanks to the linearity of the Fourier Transform and the independence of the transmitted symbols, the obtained expressions can be easily extended to multiple interfering users. Then regarding power control, useful and interfering signals are compared with same maximum power spectral density. Indeed because of the numerology system introduced in 5G, useful and interfering bands may significantly differ and therefore it seems not relevant to study the scenario for same transmitted power. Besides, it is straightforward to consider different power gains from this model.

1.5.1 Asynchronous multi-user uplink scenario: the synchronization issue

In LTE, the uplink users have to be synchronized to avoid time misalignment of the received signals at the Base Station (BS) side. It is ensured by the time advance mechanism. Each UE delays its transmission depending on its line of sight distance to the BS. Such process ensures perfect orthogonality between the uplink users so that they do not interfere with each other. However, this process is not appealing for massive MTC scenarios. Indeed, the time advance mechanism may induce a large overhead at the BS side because of the very high number of devices. Moreover, most of those devices are battery-powered and thus it would be interesting to dedicate their power consumption to the payload transmission rather than accessing the network. As a consequence, relaxed synchronization scenarios have been envisionned for those use cases.

First, the asynchronous-induced interference is analytically expressed. For this section, $s_u(t)$ (1.24) refers to the UoI and $s_i(t)$ (1.25) the interfering user. The two users share the same numerology. A disjoint allocation is assumed with $\Omega_u \cap \Omega_i = \{0\}$ where Ω_u, Ω_i are contiguous subsets of $[0, N-1]$. The BS is properly synchronized with the signal s_u.

$$s_u(t) = \frac{1}{\sqrt{N}} \sum_n \sum_{k \in \Omega_u} a_k[n] \Pi_T(t - nT) e^{j2\pi k \Delta_k (t - T_{\mathrm{CP}} - nT)} \tag{1.24}$$

$$s_i(t) = \frac{1}{\sqrt{N}} \sum_n \sum_{k \in \Omega_i} b_k[n] \Pi_T(t - \tau - nT) e^{j2\pi k \Delta_k (t - \tau - T_{\mathrm{CP}} - nT)} \tag{1.25}$$

The received signal, for the subcarriers of interest Ω_u, can therefore be expressed, as shown in (1.26), as the sum of a useful symbol a_{k_0,n_o} and an interfering term from the second user.

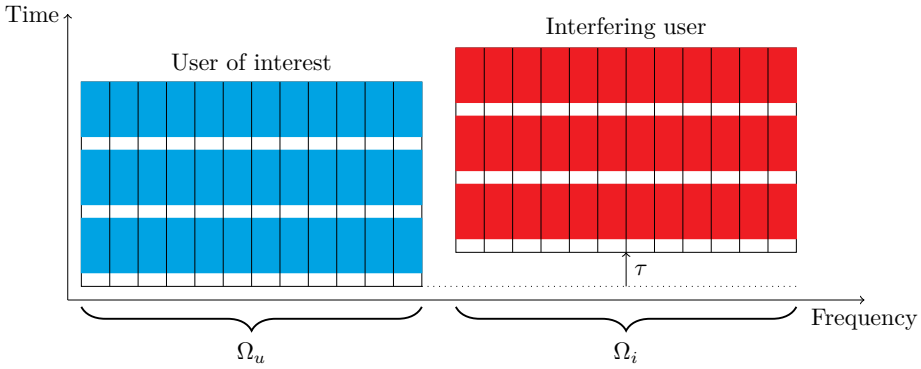

Figure 1.6: Asynchronous multi-user uplink scenario with two users.

$\forall k_o \in \Omega_u$

$$\begin{aligned}\hat{a}_{k_o}[n_o] &= \frac{1}{\sqrt{N}} \sum_{m=0}^{N-1} s[m + n_o N_{\text{ext}} + N_{\text{CP}}] e^{-j2\pi \frac{k_0 m}{N}} \\ &= a_{k_o}[n_o] + \frac{1}{N} \sum_{m=0}^{N-1} \left(\sum_i \sum_{l \in \Omega_i} b_l[i] \Pi_T(mT_s - \tau + (n_o - n)T + T_{\text{CP}}) \right. \\ &\quad \left. \times e^{j2\pi l \frac{(mT_s - \tau + (n_o - n)T)}{T_u}} \right) e^{-j2\pi \frac{k_0 m}{N}} \end{aligned} \tag{1.26}$$

However, as long as the delay is shorter than the CP, the asynchronous user does not generate any interference over the user of interest. The CP provides a perfect interference cancellation over all the bands for delays shorter than its length (with a null-delay-spread channel).

$$\begin{aligned}\hat{a}_{k_o}[n_o]\hat{a} &= a_{k_o}[n_o] + \frac{1}{N} \sum_{m=0}^{\lfloor \frac{\tau}{T_s} \rfloor} \left(\sum_{l \in \Omega_i} b_l[n_o] e^{j2\pi l \frac{(mT_s - \tau)}{T_u}} \right) e^{-j2\pi \frac{k_0 m}{N}} \\ &\quad + \frac{1}{N} \sum_{m=\lfloor \frac{\tau}{T_s} \rfloor + 1}^{N-1} \left(\sum_{l \in \Omega_i} b_l[n_o] e^{j2\pi l \frac{(mT_s - \tau)}{T_u}} \right) e^{-j2\pi \frac{k_0 m}{N}} \\ &= a_{k_o}[n_o] + \frac{1}{N} \sum_{l \in \Omega_i} b_l[n_o] e^{-j2\pi l \Delta_f \tau} \sum_{m=0}^{N-1} e^{j2\pi m \frac{l - k_o}{N}} \\ &= a_{k_o}[n_o] \end{aligned} \tag{1.27}$$

If the delay exceeds the CP length, interference terms are not cancelled anymore. Let define the Dirichlet kernel as in (1.28) and $\Theta_\tau = \lfloor \frac{\tau - T_{CP}}{T_s} \rfloor$, we obtain:

$$D_N^L(x) = \sum_{k=0}^{L-1} e^{j2\pi \frac{x}{N}} \tag{1.28}$$

$$\begin{aligned}\hat{a}_{k_o}[n_o] &= a_{k_o}[n_o] + \frac{1}{N}\sum_{m=0}^{\lfloor\frac{\tau-T_{CP}}{T_s}\rfloor}\sum_{l\in\Omega_i} b_l[n_o-1]e^{j2\pi l\Delta_f(mT_s-\tau+T)}e^{-j2\pi\frac{k_0 m}{N}} \\ &+ \frac{1}{N}\sum_{m=\lfloor\frac{\tau-T_{CP}}{T_s}\rfloor+1}^{N-1}\sum_{l\in\Omega_i} b_l[n_o]e^{j2\pi l\Delta_f(mT_s-\tau)}e^{-j2\pi\frac{k_0 m}{N}} \\ &= a_{k_o}[n_o] + \frac{1}{N}\sum_{l\in\Omega_i} b_l[n_o-1]e^{j2\pi l\Delta_f(T-\tau)}D_N^{\Theta_\tau+1}(l-k_o) \\ &+ \frac{1}{N}\sum_{l\in\Omega_i} b_l[n_o]e^{-j2\pi l\Delta_k\tau}e^{j2\pi(l-k_o)(\Theta_\tau+1)}D_N^{N-\Theta_\tau-1}(l-k_o) \end{aligned} \tag{1.29}$$

The interference appears with two terms which correspond to the interference from the tail of one symbol and the beginning of another from the interfering user as illustrated in Figure 1.6.

The amount of distortion can be expressed by the Mean Square Error (MSE) which leads to (1.30) where $E_n[.]$ is the expectation operator applied in time. $(l-k_0)$ somehow denotes the normalized guard band. The guard band expressed in frequency units can be expressed as follows $\Delta_{\text{gb}} = (|l-k_o|-1)\Delta_k$. As a reminder, the data symbols are assumed to be independent in both time and frequency domains.

$$\begin{aligned}\text{MSE}[l-k_o] &= \frac{E_n[|\hat{a}_{k_o}[n]-a_{k_o}[n]|^2]}{\sigma_a^2} \\ &= \left(\sum_{l\in\Omega_i}\left|D_N^{\Theta_\tau+1}(l-k_o)\right|^2 + \sum_{l\in\Omega_i}\left|D_N^{N-\Theta_\tau-1}(l-k_o)\right|^2\right)/N^2 \end{aligned} \tag{1.30}$$

The expression can be generalized for a multi interfering users (with allocated subband Ω_{i_l} and timing offset with respect to the UoI τ_l) scenarios.

$$\begin{aligned}\text{MSE} &= \frac{E_n[|\hat{a}_{k_o}[n]-a_{k_o}[n]|^2]}{\sigma_a^2} \\ &= \sum_{l=0}^{\substack{\text{number interfering}\\ \text{user}-1}}\left(\sum_{k\in\Omega_{i_l}}\left(\left|D_N^{\Theta_{\tau_l}+1}(l-k_o)\right|^2 + \left|D_N^{N-\Theta_{\tau_l}-1}(l-k_o)\right|^2\right)\right) \end{aligned} \tag{1.31}$$

The performance is now evaluated with two 3-RB interfering user and a one-subcarrier UoI (with the same numerology). The distortion is assessed at the subcarrier level (instead of a mean MSE over the useful subband). The results are depicted in Figure 1.7. The four 2-D images on the left gives the level of MSE (in dB) depending on the timing offset (in μs) between the two users and the guard band between the subcarrier of interest and the closest interfering subcarrier (in kHz). The comparison between analytical (1.30) and simulation results is highlighted with the plots on the right. One can observe that the analytical expression

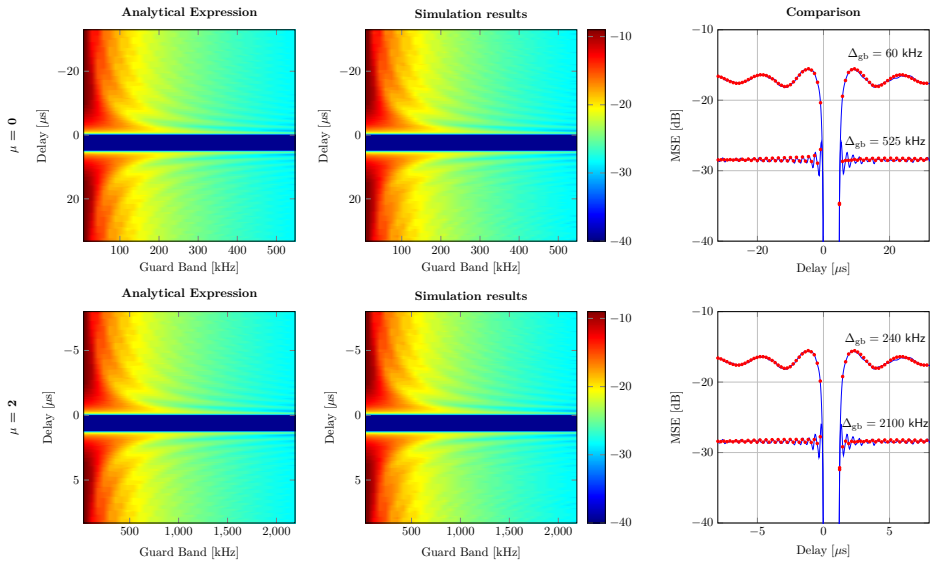

Figure 1.7: Performance of OFDM in the uplink asynchronous multi-user scenario for $\mu = 0$ (top) and $\mu = 2$ (bottom) (right) and comparison between analytical and simulations results (left).

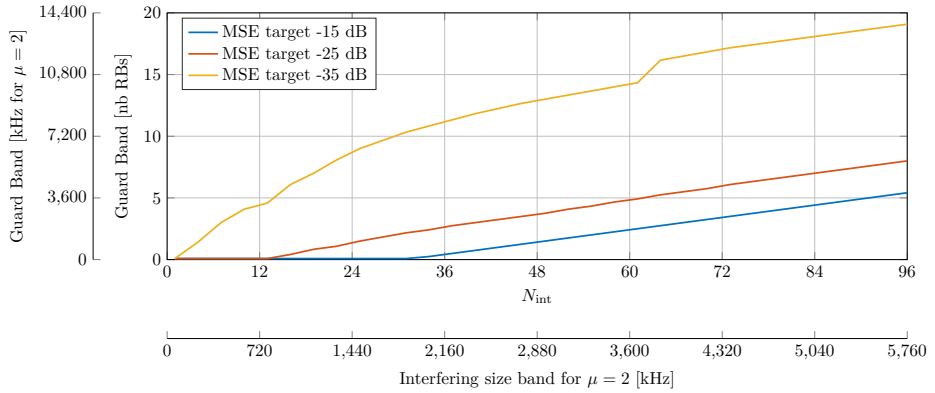

Figure 1.8: Guard band evaluation as function on interfering size band.

perfectly matches with the simulation results (no approximations were considered for the derivation). Regarding the performance results, as aforementioned if the delay is shorter than the CP length there is no distortion (for a null delay spread channel). It corresponds to the dark blue area on Figure 1.7. Beside, there is a strong distortion for small guard band values ($\Delta_{\text{gb}} < 10\Delta_f$) and further the MSE slightly decreases.

It seems worth pointing out that a given MSE level is reached for a guard band four times greater for $\mu = 2$ than for $\mu = 0$. Indeed with $\mu = 2$, the subcarrier spacing is 60 kHz w.r.t 15 kHz for $\mu = 0$ which explains this performance difference. It means than larger guard band must be considered for greater numerologies to ensure a given quality of signal. It seems worth reminding that this scenario has been proposed for M2M and low latency communications which are likely to use large SCS. The given performance illustrates that for such scenarios the bandwidth use may be significantly inefficient.

However, the interfering band size (*i.e.* the number of interfering subcarriers N_{int}) highly impacts on the results. It is therefore proposed to evaluate the guard band required to ensure a target MSE for the UoI for a given interfering band size whatever the timing offset is (worst case). Sub-6GHz MTC numerology, $\mu = 2$, has been taken for both users. The results are depicted in Figure 1.8 for a few MSE targets. They expose the poor bandwidth use efficiency occurring for high MSE targets: more than 3 MHz guard band for 1-RB interferer @ MSE= -35 dB.

1.5.2 Multi-service multiplexing scenario: the multi-signal coexistence issue

This second scenario we consider is the multi-service multiplexing induced by the proposed numerology system presented in 5G NR release 15 [15]. Indeed with release 15, 5G users can have different numerologies (*i.e.* waveform configurations). However, it breaks the orthogonality condition of the OFDM because of different SCS (see Figure 1.4) even when time synchronization is ensured. It thus rises the problem of service co-existence.

The system model given in Section 1.4.2 must be slightly updated to properly address the multi-numerology configurations. The following notations to respectively express the useful symbol N^μ, the cyclic prefix (CP) N^μ_{CP} and entire symbol lengths N^μ_e as function of the numerology index μ are now used to include the numerology index μ in the expressions.

$$N^\mu = N^0 \times 2^{-\mu} = 4096 \times 2^{-\mu} \tag{1.32}$$

$$N^\mu_{\text{CP}} = N^0_{\text{CP}} \times 2^{-\mu} = 288 \times 2^{-\mu} \tag{1.33}$$

$$N^\mu_{\text{ext}} = N^\mu + N^\mu_{\text{CP}} \tag{1.34}$$

The transmitted signal (1.1) can thus be extended to multi-numerology model as defined in (1.35) where $a^\mu_k[n]$ denotes the transmitted constellation symbol over the k^{th} subcarrier at time instant n with numerology μ, Ω the set of the active subcarriers, $T^\mu = (N^\mu + N^\mu_{\text{CP}})T_s$ the length of one complete symbol where T_s denotes the sampling period, $T^\mu_{\text{CP}} = N^\mu_{\text{CP}} T_s$ the CP duration and $\Delta^\mu_f = (T_s N^\mu)^{-1}$ the subcarrier spacing for numerology μ.

$$s_\mu(t) = \frac{1}{\sqrt{N^\mu}} \sum_n \sum_{k\in\Omega} a^\mu_k[n] \Pi_{T^\mu}(t - nT^\mu) e^{j2\pi(t - T^\mu_{\text{CP}} - nT^\mu)k\Delta^\mu_f} \tag{1.35}$$

As before, two users are considered: $s_{\mu_u}(t)$ the UoI (numerology index μ_u and active subcarrier set Ω_1) and $s_{\mu_i}(t)$ the interfering user (numerology index μ_i and active subcarrier set Ω_2). The two users are assumed to be synchronized[2] and the sets of active subcarriers Ω_u and Ω_i are assumed to be disjoint. The sum of the two signals is denoted by $s(t)$. The scenario is depicted in Figure 1.9. The corresponding estimated symbols can be expressed as in (1.36).

[2] In 5G NR, signals are synchronized with respect to the beginning of the CP to satisfy symbol alignment.

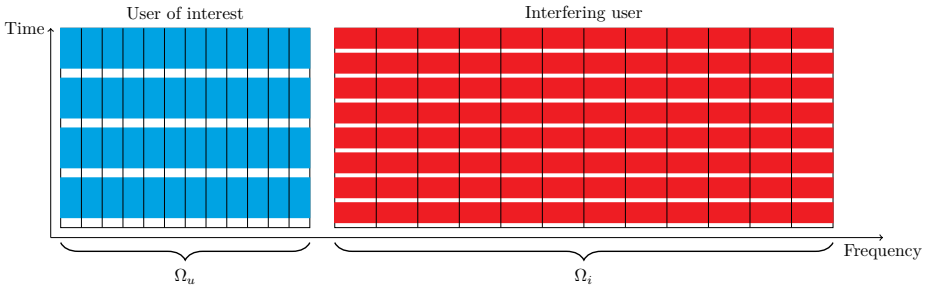

Figure 1.9: Multi-service scenario for two 1-RB users.

$\forall k_o \in \Omega_1$

$$\hat{a}_{k_0}^{\mu_u}[n] = \frac{1}{\sqrt{N^{\mu}}} \sum_{f=0}^{N^{\mu_u}-1} s\left[nN_{\text{ext}}^{\mu_u} + N_{\text{CP}}^{\mu_u} + f\right] e^{-j\frac{2\pi}{N^{\mu_u}}k_0 f} \tag{1.36}$$

The resulting MSE is defined in (1.37) and developed in (1.38). The development of the expression (1.38) relies on the independence in time of the transmitted data symbols and the separation of the distinct interfering OFDM symbols. Regarding the notations, $Q = 2^{\mu_i - \mu_u}$ denotes the numerology index ratio and $\lceil . \rceil$ is the ceiling operator. $\Delta_{\text{gb}_n} = l2^{\mu_i} - k2^{\mu_u}$ corresponds to the normalized guard band and $\Delta_{\text{gb}} = \frac{F_s}{N}(|l2^{\mu_i} - k2^{\mu_u}| - 1)$ the guard band expressed in frequency units.

$$\text{MSE}^{\mu_i \to \mu_u}[\Delta_{\text{gb}_n}] = \frac{E_n\left[\left|\hat{a}_{k_o}^{\mu_u}[n] - a_{k_o}^{\mu_u}[n]\right|^2\right]}{\sigma_a^2} \tag{1.37}$$

$$\begin{aligned}
\text{MSE}^{\mu_i \to \mu_u}[\Delta_{\text{gb}_n}] &= \frac{1}{N^{\mu_u}\sigma_a^2} E_n\left[\left|\sum_{m=0}^{N^{\mu_u}-1} s_{\mu_i}[m + N_{\text{CP}}^{\mu_u} + nN_e^{\mu_u}] e^{-j\frac{2\pi}{N^{\mu_u}}mk_o}\right|^2\right] \\
&= \frac{1}{N^{\mu_u}N^{\mu_i}}\left[\left|\sum_{m=0}^{N_e^{\mu_i}-N_{\text{CP}}^{\mu_u}-1} e^{j\frac{2\pi}{N}m\Delta_{\text{gb}_n}}\right|^2\right. \\
&\quad \left. + \sum_{k=0}^{\lceil Q\rceil-2}\left|\sum_{m=N_e^{\mu_i}-N_{\text{CP}}^{\mu_u}+kN_e^{\mu_i}}^{N_e^{\mu_i}-N_{\text{CP}}^{\mu_u}+(k+1)N_e^{\mu_i}-1} e^{j\frac{2\pi}{N}m\Delta_{\text{gb}_n}}\right|^2\right] \\
&= \frac{1}{N^{\mu_i+\mu_u}}\left[\left|D_N^{N_e^{\mu_i}-N_{\text{CP}}^{\mu_u}}(\Delta_{\text{gb}_n})\right|^2 + (\lceil Q\rceil - 1)\left|D_N^{N_e^{\mu_i}}(\Delta_{\text{gb}_n})\right|^2\right]
\end{aligned} \tag{1.38}$$

The MSE expression (1.38) expresses the distortion level induced by a one-tone interferer over a unique-subcarrier band of interest with a guard band $\Delta_{\text{gb,n}}$. One can observe that the distortion can be decomposed into $\lceil Q \rceil$ terms corresponding to the $\lceil Q \rceil$ interfering symbols overlapping with each symbol of interest. The expression (1.38) can be extended to express the level of distortion induced by N_{int} subcarriers over a sub-carrier spaced by a guard band $\Delta_{\text{gb,n}} = \min|k2^{\mu_u} - l2\mu_i|$, the contributions of each interfering sub-carrier can be summed (assuming that

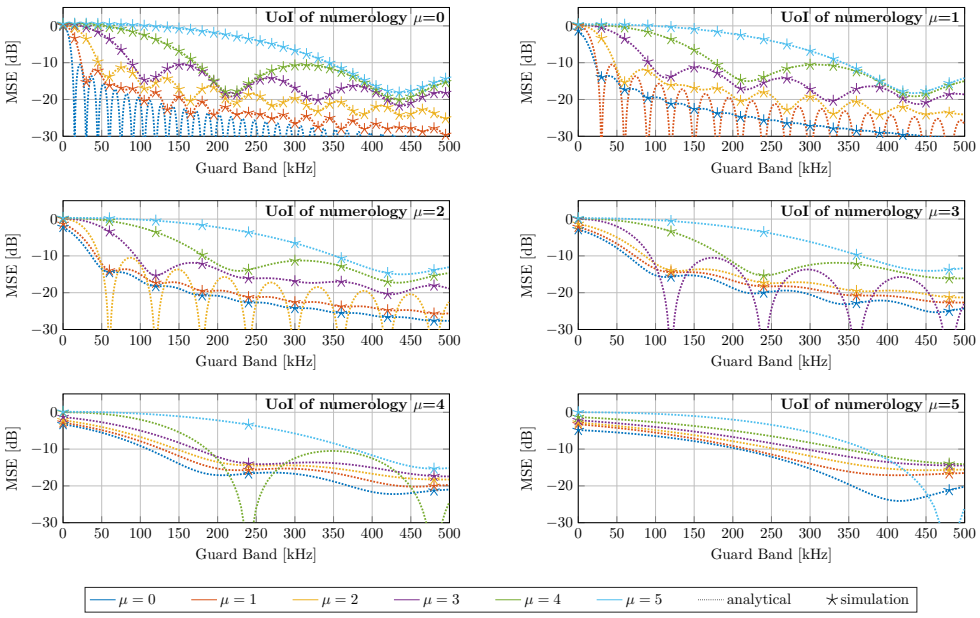

Figure 1.10: Level of distortion induced by 1-RB interferer over 1 sub-carrier user of interest according to guard band spacing the two users for $\mu = \{0, 1, 2, 3, 4, 5\}$.

constellation symbols are independent). The resulting expression is given in (1.39).

$$\mathrm{MSE}_{N_{\mathrm{int}}}^{\mu_i \to \mu_u}[\Delta_{\mathrm{gb}_n}] = \sum_{l=0}^{N_{\mathrm{int}}-1} \mathrm{MSE}^{\mu_i \to \mu_u}[\Delta_{\mathrm{gb}_n} + l2^{\mu_i}] \tag{1.39}$$

The MSE expression developed in (1.39) is first verified and compared to simulation results for a whole RB ($N_{\mathrm{int}} = 12$) as shown in Figure 1.10.

To begin with, one can observe that the analytical expression perfectly matches to the simulation results. Besides, when the interferer and the user of interest share the same numerology (whatever it is), it exists a guard band (and all its multiple) which guarantees the orthogonality between the two users. It is a well-known result used in LTE and OFDMA to multiplex several users. The minimum guard band that ensures the orthogonality is defined by the ratio between the sampling frequency and the total number of sub-carriers (*i.e* the subcarrier spacing).

As expected, the result no longer holds when different numerologies are considered. Users may even significantly interfere from each other even when large guard bands are used. It is worth pointing out that the distortion induced by lower numerologies ($Q < 1$) impacts less than higher numerologies. Moreover, for higher numerologies, the bigger Q is, the more distortion occurs.

Besides for a fixed value of Q, the distortion level increases with the numerology index μ. Indeed, we can observe that for an increment of the numerology index μ, the same level of distortion is observed for a guard band twice as large. The distortion model can thus be simplifyied by using this observation. Indeed by looking at Figure 1.10, one can observe that the approximation (1.40) can be considered for any $\alpha \in \mathbb{N}$ such as $(\mu_i + \alpha) \times (\mu_u + \alpha) \in [0, 4]^2$.

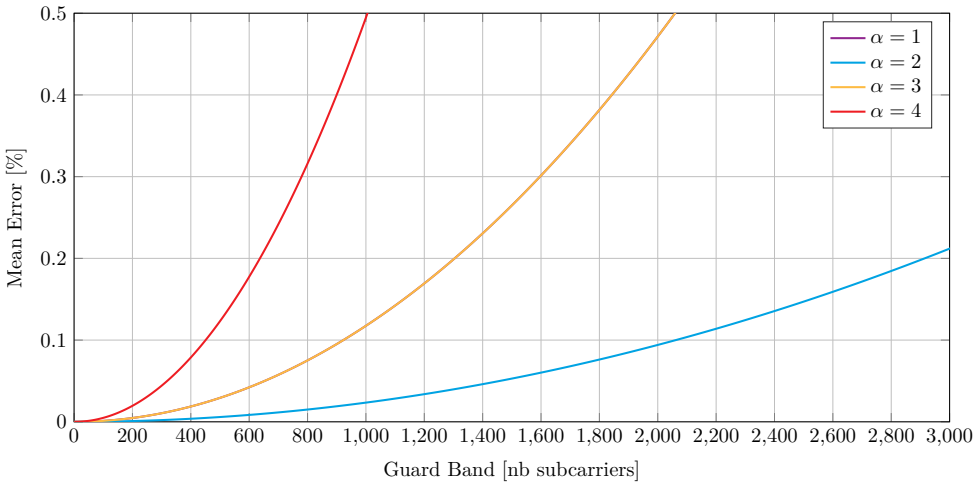

Figure 1.11: Verification of the approximation (1.40) (curve $\alpha = 1$ is confounded with x-axis).

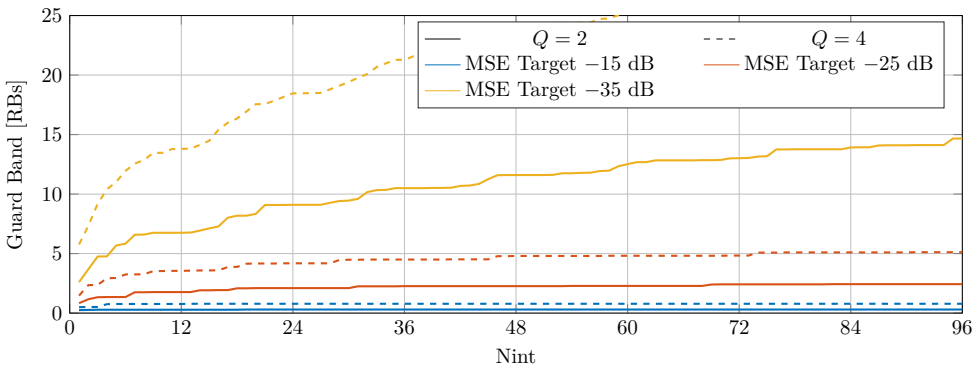

Figure 1.12: Guard band of function of N_{int}

$$\text{MSE}^{\mu_i+\alpha\to\mu_u+\alpha}[2^{\alpha}\Delta_{\text{gb}_n}] \approx \text{MSE}^{\mu_i\to\mu_u}[\Delta_{\text{gb}_n}] \tag{1.40}$$

It means that the distortion model becomes independent of the numerology indices (and only dependent on the ratio Q) when normalized frequencies are used. The approximation is numerically verified by taking $N_{\text{int}} = 1$, $(\mu_u, \mu_i) = (0, 1)$ as reference configuration and for $\alpha \in [1, 3]$ in figure 1.11. The x-axis is expressed in number of subcarriers for UoI instead of in frequency units. The equivalent guard band in frequency units can be determined by multiplying the number of subcarriers by $2^{\mu_u} \times 15$ kHz. One may observe that the approximation is valid for small guard bands (in the neighbourhood of the useful user) which is enough for our scenario involving a few subcarriers (interfering number of subcarriers and guard band). Other reference configurations have been tested as well and provide similar results. They are not depicted for sake of conciseness.

As done in the previous section, it seems interesting to determine the guard band size in order to ensure a given MSE target. The results are depicted in Figure 1.12 for $Q = \{2, 4\}$.

As expected, the required guard band for $Q = 4$ is larger than for $Q = 2$. One

can observe that the required guard band length quickly levels off for low MSE targets (around $N_{\text{int}} = 50$ for MSE target $= -25$ dB for both $Q = 2$ and $Q = 4$) but much later for higher MSE targets. It means that a 3-RB-long guard band is enough to ensure 25 dB MSE for any interferer band with $Q = 2$. However, the required guard band to ensure higher quality becomes significant even for a few RBs of interferer. Indeed, a 9-RB guard band ensures a MSE of -35 dB for 2 RB of interferer with $Q = 2$ while only -30 dB MSE for $Q = 4$. It means that ensuring low level of interference (high MSE target) is possible only at a significant bandwidth band efficiency compromise even for $Q = 2$.

1.6 Analysis

As we observe with the two previous examples, 5G has to cope with scenarios where the orthogonality between users and/or subbands is compromised. Indeed, signal misalignment in the first scenario and multiplexing different numerologies in the second break the orthogonality and are thus source of interference.

In addition to that, dealing with high mobility (V2I, V2V or high speed train scenario) and the use of mmWaves also weaken the orthogonality condition because of potentially high Doppler shifts. As a consequence, 5G is somehow about multiplexing signals that interfere with each others wich is a radical change w.r.t. already deployed mobile technologies.

1.6.1 Spectral confinement study

With a closer look to the interference expressions given in (1.30) and (1.38), one can observe the presence of Dirichlet kernels. This function is related to the Fourier transform and expresses the Out-Of-Band (OOB) power of an OFDM signal in the frequency domain. In other words, the obtained performance for OFDM in the two scenarios we studied, are induced by its OOB radiations.

Indeed, CP-OFDM is by construction not bandlimited and therefore emits large OOB emissions. OOB emissions are unwanted power emissions outside of the allocated band. They are generated by the waveform and non-linearity of the RF front end (only the waveform-induced part is taken into consideration in the proposed analysis). Such emissions interfere with adjacent bands which impacts system performance. That is why OOB are limited in standard specifications by two indicators the Spectrum Emission Mask (SEM) or the Adjacent Channel Leakage Ratio (ACLR). The SEM for 5G FR1 UE is given in Table 1.2[1]. The SEM specifies power in different bands outside of the allocated bandwidth. It allows to control both the high energy side lobes (near the allocated band) and the spurious (further from the allocated band).

In mobile technologies, edges of bands are not allocated to satisfy the SEM (especially the restrictions on high energy side lobes). Maximum transmission bandwidth can therefore be determined and specified in standard as well. They are reminded in Table 1.3[3]. It is an easy way to limit the OOB radiations but it compromises the spectral efficiency especially for small bands. For illustration, the OOB response of some 5G OFDM configuration is depicted in Figure 1.13. For all the configurations, the maximum transmission band and power (*i.e.* 23

[3] N/A means Non Assigned.

Table 1.2: NR General spectrum emission mask for 1-Hz measurement bandwidth [1, Table 6.5.2.2-1]

$\Delta_{f_{OOB}}$ MHz	5 MHz	10 MHz	20 MHz	50 MHz	100 MHz
± 0-1	-59.77	-62.77	-65.77	-68.77	-68.77
± 1-5	-70.00	-70.00	-70	-70.00	-70.00
± 5-6	-73.00	-73.00	-73.00	-73.00	-73.00
± 6-10	-85.00				
± 10-15		-85.00			
± 15-50			-85.00		
± 50-55				-85.00	
± 55-100					
± 100-105					-85.00

dBm) are considered. One may realize that the higher the SCS, the slower the decay rate is. It explains the larger guard bands used in 5G for high SCS numerologies. The OFDM spectrum is compared to 5G 10-MHz SEM (black horizontal lines). However, this comparison is just for illustration as no RF filtering and amplification/RF induced spectral regrowth are considered here.

Table 1.3: Maximum Transmission bandwidth with 5G FR1 UE[1, Tables 5.3.2-1/2]

SCS (kHz)		5 MHz	10 MHz	20 MHz	50 MHz	100 MHz
15	nb max. RBs	25	52	106	270	N/A
	Band use (%)	90	93.6	95.4	97.2	N/A
30	nb max. RBs	11	24	51	133	273
	Band use (%)	79.2	86.4	91.8	95.7	98.3
60	nb max. RBs	N/A	11	24	65	135
	Band use (%)	N/A	79.2	86.4	93.6	97.2

In 5G, in addition to the guard bands at the edges of the bandwidth, guard bands are required as well inside the band between interfering subbands as it has been observed earlier. The bandwidth use efficiency can therefore be severely compromised. However, a better band use could help limiting the device complexity and simplifying the radio resource management mechanism. This aspect is therefore not good to be neglected for future wireless technologies. Improving the bandwidth can be achieved by means of co-subband interference mitigation techniques. Smart antenna arrays and beamforming [16, 17] can be use to this end. However, waveforms can already provide a better co-subband interference rejection simply by lowering the side lobe energy. It is the main subject of this thesis.

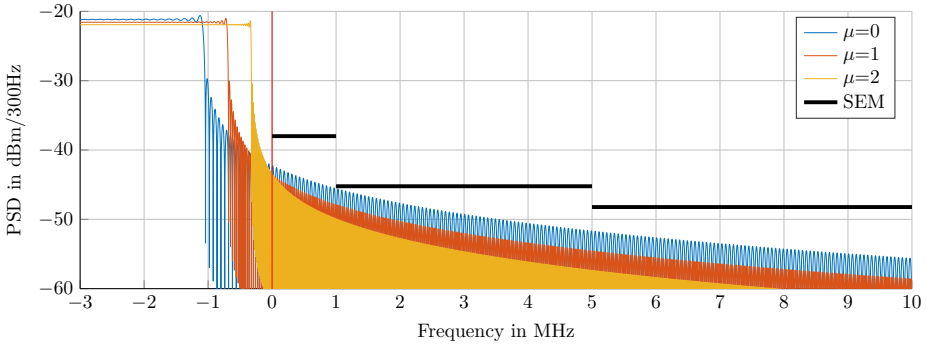

Figure 1.13: Frequency response of the three numerologies of 10-MHz FR1 5G OFDM.

1.6.2 Waveform design and Balian Low Theorem

Designing a waveform is about making trade-offs according to the Balian Law Theorem (BLT)[18, 19]. It states that a trade-off must be established between three properties which are

- being orthogonal
- being well localized in both time and frequency domains
- ensuring maximum spectral efficiency.

From a waveform perspective, the orthogonality is the capacity to cancel intrinsic interference (induced by the waveform itself and not by any propagation and/or RF impairments). The second point corresponds to the ratio between symbol duration and spectral confinement. When it comes to the spectral efficiency, it combines bandwidth use efficiency (frequency) and symbol density (time) and corresponds to the maximum useful rate per band. Obviously, those three properties are all desired but however can't be fully satisfied simultaneously.

A first way to deal with BLT is to greatly relax one of the properties to maximize the two others. That is why happens for CP-OFDM. Indeed, OFDM is built to perfectly satisfy the orthogonality condition and provides high waveform density (efficient bandwidth use and slight symbol density reduction induced by the CP insertion). Consequently, the spectral confinement is relaxed and CP-OFDM emits high OOB emissions.

This way of dealing with BLT (by relaxing one condition) proves to be not fully compatible with the purpose of future wireless technologies. The idea is therefore to find a better trade-off between the three conditions where none of them is neglected. Side lobe rejection techniques and enhanced receiver schemes will be therefore studied and compared to CP-OFDM. However, the comparison can not be reduced to the three properties of the BLT. Indeed, others performance indicators remain crucial and will be considered as well, as multi-path channel and/or frequency offset robustness and transceiver complexity analysis. Comparing the different solutions with maximum fairness is a key aspect of the proposed study.

As the OFDM performs very well on most scenarios but the spectral confinement, it seems interesting to use it as the core waveform with extra spectral confinement techniques applied on it. This idea led to the development of some

waveforms that are studied in the following chapter.

1.7 Conclusion

In this chapter, the role of the physical layer has been described and detailed for mobile systems with a recall of the 4G LTE specifications. In a second time, the 5G NR technology has been introduced focusing on its differences with 4G LTE.

With 5G, the flexibility of the mobile network is further enhanced, especially at the signal level. Indeed, the transmitted signals will be adapted to service to be provided so that the network can satisfy the requirements of the supported applications. However in such scenarios, the capacity of the network is weakened because of CP-OFDM. Indeed, although CP-OFDM is interesting as a multiple access technology and to combat fast fading, it hinders the co-existence of multiple numerologies because of its relaxed spectrum confinement.

Hence, considering a waveform with better confined spectrum would help ensuring higher bandwidth use efficiency. But, according to the BLT, maximizing the spectral confinement can be achieved only at the expense of a orthogonality and/or spectral efficiency which are essential as well respectively for backward compatibility and high data rate applications. The design of a waveform for beyond 5G networks is thus a critical issue.

In the next part of this thesis, several filtering approaches applied on CP-OFDM will be investigated to improve the side lobe rejection. It leads to the description and analysis of so-called ”post-OFDM” waveforms.

1.7.1 Contribution

The multi-service system model for CP-OFDM that is described in Section 1.5.2 has been published in [20]: D. Demmer, R. Gerzaguet, J.-B. Doré, and D. Le Ruyet, “Analytical study of 5G NR eMBB co-existence,” in *Proc. IEEE International Conference on Telecommunications (ICT)*, pp. 186–190, June 2018.

2 State-of-the-art solutions with enhanced spectral confinement

Several waveforms have been proposed as an alternative to CP-OFDM in the context of 5G but only a few of them will be addressed in this work, namely filtered OFDM, Universal Filtered OFDM, Weighted Overlap and Add OFDM and Filter-Bank MutliCarrier with Offset QAM modulations. The selection is based on the spectrum confinement technique they rely on and the impact they have produced in research literature. A technical description is given for the considered solutions focusing on the side lobe rejection technique.

Better confining the transmitted spectrum leads a significant performance gain in 5G specific scenarios. Indeed, the interference generated by multiplexing non-orthogonal subband is considerably attenuated especially when signal processing is considered at the receiver side as well. The guard bands between non-orthogonal subbands can thus be lowered which improves the bandwidth use efficiency. Nonetheless, the obtained results must be nuanced according to error rate penalty and complexity increase induced by the side lobe rejection techniques.

2.1 Filtered-OFDM

2.1.1 Overall description

Filtering an OFDM signal through a pass-band filter is a pragmatic solution to reduce its large OOB radiations. This technique is known as filtered-OFDM (fOFDM)[21, 22]. Not only the spectral confinement of the transmitted signal is improved, but fOFDM also performs a passband filtering at the receiver side (not necessarily matched filter), prior to the OFDM demodulation stage, to remove OOB spurious.

The fOFDM Tx and Rx schemes are depicted in Figure 2.1. The fOFDM transceiver scheme is very similar to the OFDM scheme with just an extra filtering stage between the OFDM scheme and the RF front end at both Tx and

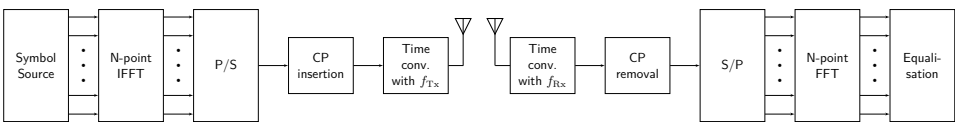

Figure 2.1: Filtered-OFDM Tx and Rx schemes (conv. denotes time convolution).

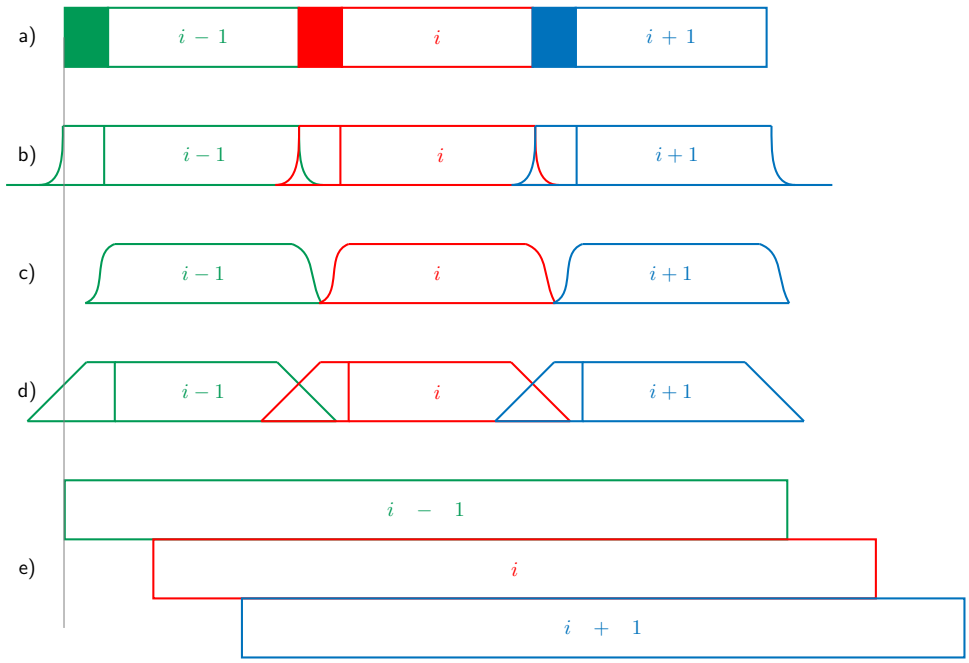

Figure 2.2: TX signals for a) CP-OFDM b) fOFDM, c) UF-OFDM, d) WOLA-OFDM and e) FBMC-OQAM

Rx sides. The transmitted signal is represented in Figure 2.2 and compared with CP-OFDM (and other waveforms that will be defined and described later). The time convolution with the transmit filter significantly enlarge the symbol duration w.r.t. a typical OFDM signal. However, the symbols overlap in time to avoid symbol density penalty.

The baseband fOFDM transmitted signal can be expressed as in (2.1) where $*$ stands dor the time convolution operator and the received signal as in (2.2) where f_{Tx} (length L_{Tx}) and f_{Rx} (length L_{Rx}) respectively denote the transmit and receive filter impulse responses.

$$\begin{aligned} s_{\mathrm{OFDM}}(t) &= \frac{1}{\sqrt{N}} \sum_{n} \sum_{k=0}^{N-1} a_k[n] \Pi_T(t-nT) e^{j2\pi k \Delta_k (t - T_{\mathrm{CP}} - nT)} \\ s(t) &= \left(s_{\mathrm{OFDM}} * f_{\mathrm{Tx}}\right)(t) \end{aligned} \tag{2.1}$$

$$r_{k_o}[n_o] = \frac{1}{\sqrt{N}} \sum_{m=0}^{N-1} (f_{\mathrm{Rx}} * s)[m + n_o N_{\mathrm{ext}} + N_{\mathrm{CP}} + (L_{\mathrm{Tx}} + L_{\mathrm{Rx}})/2] e^{-\frac{j2\pi k_0 m}{N}} \tag{2.2}$$

One major advantage of fOFDM is to keep CP-OFDM as the core waveform. Besides, the filtering performed at the transmitter and receiver sides are independent. fOFDM thus satisfies the transparency condition and ensures backward compatibility with LTE systems.

2.1.2 Filter design

To efficiently reject the main side lobes, the transition band (from pass-band to stop-band) of the filter response should be as sharp as possible with a high

stop-band attenuation to minimize the leakage on adjacent bands. Nonetheless, a suitable filtering for fOFDM satisfies the two following properties: i) the filter frequency response should be as flat as possible in its pass-band to limit the in-band distortion ii) the symbol energy spreading induced by the time convolution should be limited to avoid ISI.

To perform the flat in-band filtering, cardinal sine (sinc) based filters can be considered [23, 21]. However, an ideal sinc impulse response is infinite. However for practical implementation, the sinc impulse response is truncated (2.3) and its edges are made smoother by applying a window pulse $w[n]$ (2.4). At the end, the filter has an impulse response of length $L+1$ (samples), a pass-band of $W+2\delta_W$ subcarriers where W is the number of active sucarriers and δ_W is the excess bandwidth. Finally, the filter is shifted around the frequency f_w which is the central frequency of the active subcarriers block (2.5).

$$p[n] = \text{sinc}\left(\frac{W+2\delta_W}{N}n\right) \tag{2.3}$$

$$p_w[n] = \frac{p[n]w[n]}{\sum_n |p[n]w[n]|} \tag{2.4}$$

$$f[n] = p_w[n]e^{j2\pi n f_w/(N\Delta_k)} \tag{2.5}$$

The window pulse to apply can be any classical window shape such as raised cosine, Hamming or Blackman [24]. The window pulse can also be determined by optimisation as presented in [21] (the optimisation process is not detailed). The latter window pulse is denoted as the Huawei window for the rest of the manuscript.

Because of the filter truncation, the pass-band is not perfectly flat (*i.e.* Gibbs effect). The subcarriers located at the edges of the pass-band are more impacted and suffer from larger distortion level. The excess bandwidth δ_W enlarges the filtered subband so that the fluctuations at the edges of the pass-band do not impact allocated subcarriers as shown in figure 2.3-a. The figure represents the Carrier-to-Interference Ratio in dB (CIR, *i.e.* a SIR measured at a subcarrier level) for different excess bandwidths δ_W (expressed in number of subcarriers). For this example, a broadband configuration ($\mu = 0$, 4096 subcarriers with 15 kHz SCS) has been considered with 12 active RBs (*i.e.* 2.16 MHz bandwidth), a filter impulse response of 2048 samples (50% of useful symbol duration) based on the Blackman window for both the transmitter and the receiver. Only half the active bandwidth is depicted as the situation is perfectly symmetric w.r.t. the central frequency f_w. The inband distortion around the central frequency f_w is approximately the same, about 40 dB of CIR, for all the considered excess bandwidths. However, differences appear at the edges of active bandwidth from 12 dB of CIR for $\delta_w = 2.5$ to 35 dB of CIR for $\delta_w = 10$.

Figure 2.3-b depicts the performance obtained for different windows with the same configuration as Figure 2.3-a and $\delta_w = 2.5$. The Blackman window provides the worst performance and the Huawei window the best with about 25 dB of CIR for the edge subcarriers. As for the excess bandwidth, the difference performance is mainly noticeable at the band edges.

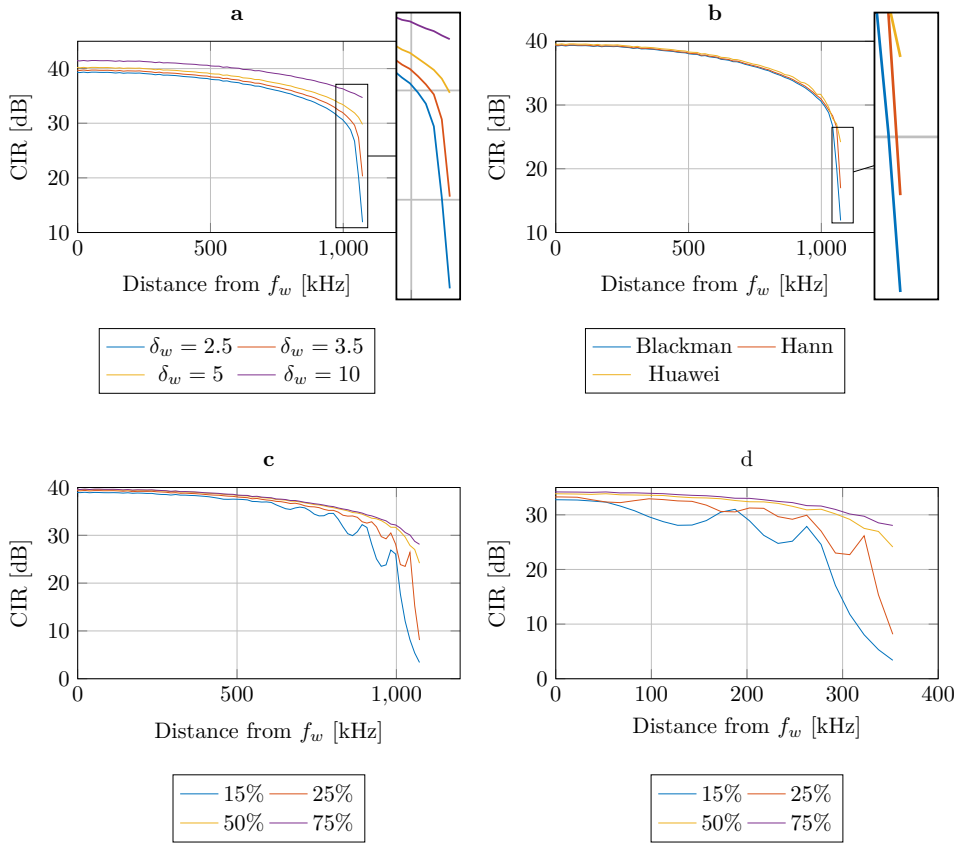

Figure 2.3: Impact of fOFDM filter parameters on the inband flatness filter frequency response a)the excess bandwidth δ_w b)the window pulse, c)the filter impulse length for 12 active RBs and d)the filter impulse length for 4 active RBs.

Last but not least, figures 2.3-c and d, illustrate the trade off between time and frequency localisation. The in-band distortion is measured for different impulse response lengths expressed as a percent of the useful symbol duration for active bandwidth of 12 RBs for figure c and 4 RBs for figure d ($\mu = 0$ configuration, with Huawei window and $\delta_w = 2.5$). The results show that a low level of distortion implies a longer impulse response to limit the effects of filter truncation. The effects induced by filter truncation (*i.e.* fluctuations of the inband frequency response of the filter) are more appreciable when the band to be filtered is narrow.

The typical subband bandwidth that is targeted by fOFDM is a few RBs (*i.e.* the user allocation). The results presented in Figure 2.3 demonstrate that a proper filter design can provide both a near-flat inband frequency response and limited ISI. Indeed, even if a long impulse response ($> 50\%$ of useful symbol duration) is usually preferred [21], most of the filter energy is concentrated in small portion of time. As a consequence, even if fOFDM is not orthogonal (presence of ISI even with zero-delay spread channel and in-band distortion due to filter truncation), it ensures Near-Perfect Reconstruction (NPR).

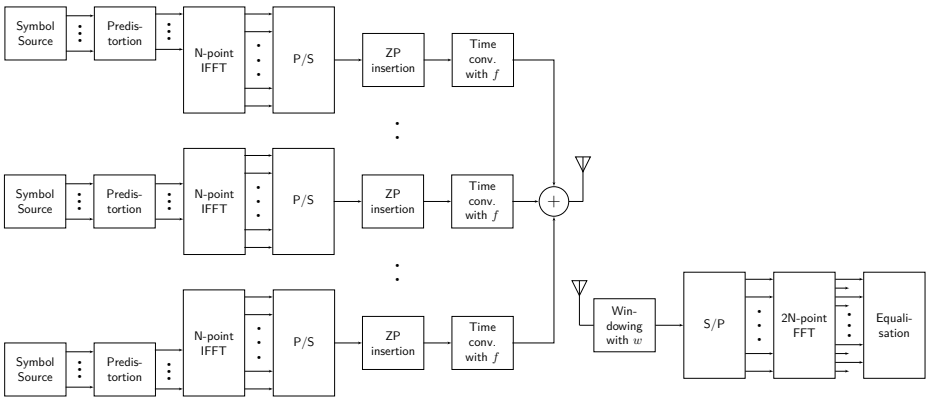

Figure 2.4: UF-OFDM Tx and Rx schemes.

2.2 UF-OFDM

Universal-Filtered OFDM (UF-OFDM) (also known as Universal-Filtered Multi-Carrier (UFMC)) also aims at mitigating the OOB emissions of an OFDM signal by filtering it with a passband filter[25, 26]. However, the process is different than for fOFDM for several reasons.

First, the filtering does not adapt to the allocated bandwidth. Indeed, UF-OFDM filters fixed subband of 12 subcarriers (*i.e.* a RB). All the filtered signals are then summed together and transmited as one. Then, the same baseband filter impulse response is used for all the subband but modulated at the proper frequency (center of filtered subband). The length L of the filter impulse response is determined so as to avoid ISI (with ideal propagation conditions) induced by the time convolution. To do so, the core-waveform in UF-OFDM is no longer CP-OFDM (as in fOFDM) but Zero-Padded OFDM (ZP-OFDM). ZP-OFDM is an OFDM signal with guard interval prepended to each symbol (instead of the tail of the symbol) and $L = N_{\text{CP}} + 1$. The transmitted signal is represented in Figure 2.2. However according to the results presented in the previous section, a flat in-band filter frequency response can be not ensured because of the short filter impulse response. That is why in UF-OFDM a predistortion stage is added so as to compensate the in-band distortion induced by the passband filter. Finally, UF-OFDM does not embed any filtering by convolution at the receiver side but by windowing[27].

The transmitter and receiver schemes are depicted in Figure 2.4. The Tx scheme is rather different than for CP-OFDM and fOFDM because of the subband processing. At the receiver side as the transmit filtering spreads the symbols in time, a double-size FFT is used for the transposition to the frequency domain. However, only one every two outputs is used which brings back to N the number of possible frequency tones. The equalisation scheme is strictly the same as the one used in CP-OFDM or fOFDM.

The baseband UF-OFDM transmitted signal can be expressed as in (2.7) where f_p denotes the transmit filter f impulse modulated around the subcarrier k_p (*i.e.* mean of subccarier index of subband p) $f_p[n] = f[n]e^{j2\pi k_p n/N}$. The transmitted signal is the sum of subband signals with disjoint frequency allocations Ω_p. Besides, a predistortion coefficient is applied to each constellation symbol prior the

OFDM stage (2.6). This coefficient depends on the filter impulse response f, the subband p and the subcarrier index k. The receive UF-OFDM signal is expressed in (2.8) where w denotes the receive window of length $N + L$.

$$\forall k \in \Omega_p \quad a'_k[n] = a_k[n]./\left(\sum_{l=0}^{N-1} f_p[l]e^{-j2\pi lk/N}\right) \tag{2.6}$$

$$s_{\text{OFDM},p}(t) = \frac{1}{\sqrt{N}} \sum_n \sum_{k=\Omega_p} a'_k[n]\Pi_T(t - nT_u)e^{j2\pi k\Delta_k(t-T_{\text{CP}}-nT)}$$

$$s(t) = \sum_{p=0}^{N_{\text{RB}}-1} \left(\left(s_{\text{OFDM},p} * f_p\right)(t)\right) \tag{2.7}$$

$$r_{k_o}[n_o] = \frac{1}{\sqrt{N}} \sum_{m=0}^{2N-1} w[m]s[m + n_o N_{\text{ext}}]e^{-\frac{j2\pi(2k_o)m}{2N}} \tag{2.8}$$

Chebyshev filter has been used for the transmit filter f since [25] thanks to its time limited impulse response. However it is also possible to optimise the filter shapes w.r.t. some criteria such as OOB emissions [28] or propagation impairments [27, 29].

When it comes to the receive window w, a rectangular window with raised-cosine edges is used [28]. The expression of the window is reminded in (2.9). As the proposed window satisfies the Nyquist criterion (preventing ISI and distortion), UFMC is perfectly complex orthogonal as CP-OFDM.

$$w[n] = \begin{cases} \frac{1}{2}\left(1 - \cos\left(\frac{n\pi}{L/2-1}\right)\right) & n \in [0, L/2-1] \\ 1 & n \in [L/2, L/2+N] \\ \frac{1}{2}\left(1 + \cos\left(\frac{n-N-L/2+1}{L/2-1}\pi\right)\right) & n \in [L/2+N+1, L+N-1] \end{cases} \tag{2.9}$$

2.3 WOLA

2.3.1 Overall description

In Weighted-OverLap-and-Add OFDM (WOLA-OFDM), a pulse shape with soft edges is preferred over the rectangular one used in CP-OFDM[30]. Slightly longer symbols are also used. Indeed, the window shape is applied on cyclic extended OFDM symbols (with both cyclic prefix and suffix) of length $N + N_{\text{CP}} + W_{\text{Tx}}$ where W_{Tx} corresponds to time excess induced by the transmit window (*i.e.* the rising/falling length of the window). Nonetheless, consecutive symbols overlap in time to ensure a given symbol density (same as in CP-OFDM for this work). The corresponding transmitted signal is represented in Figure 2.2. At the receiver side, a window of length $N + W_{\text{Rx}}$ is also applied on the received signal. The receive processing is not the same but nonetheless perfectly equivalent to what is done with UF-OFDM. In WOLA-OFDM, the tails of the windowed received symbols are cut and added to the opposite edges of the useful symbols as depicted Figure 2.6. By doing so, the receive WOLA-OFDM scheme relies on a simple N-point FFT. The transmitter and receiver schemes are depicted in Figure 2.5.

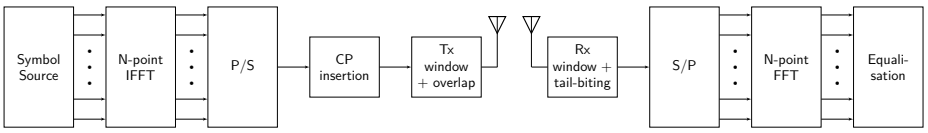

Figure 2.5: WOLA-OFDM Tx and Rx schemes.

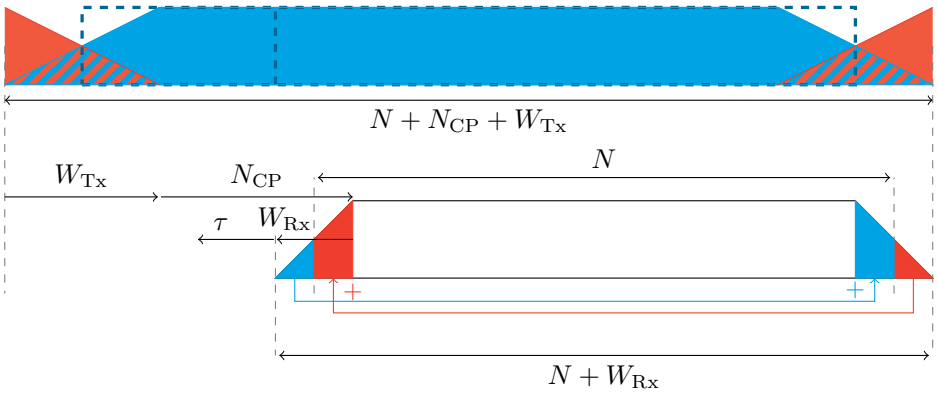

Figure 2.6: WOLA reception scheme.

The baseband WOLA-OFDM transmitted signal can be expressed as in (2.10) and the received signal as in (2.11) where g_{Tx} is the transmit window of length $N+N_{\mathrm{CP}}+W_{\mathrm{Tx}}$ samples and g_{Rx} is the receive window of length $N+W_{\mathrm{Rx}}$ samples. In [30], the receive window is centered with respect to the useful part of the symbol. However, when windows with a large time excess value are considered, it may be interesting to center the window with respect to the OFDM symbol (CP + useful part). That is why a time shift (w.r.t to [30]) τ (assumed positive) is introduced in (2.11). The time shift is compensated by a phase offset as expressed in (2.11). The receive window positioning is illustrated in Figure 2.6.

$$s(t) = \frac{1}{\sqrt{N}} \sum_{n} \sum_{k=0}^{N-1} a_k[n] g_{\mathrm{Tx}}(t - nT) e^{j2\pi k \Delta_k (t - T_{\mathrm{CP}} - nT)} \tag{2.10}$$

$$\begin{aligned} r_{k_o}[n_o] = \frac{e^{-j2\pi \frac{\tau k_o}{N}}}{\sqrt{N}} \sum_{m=0}^{N-1} \sum_{l \in \mathbb{Z}} \Bigg(& g_{\mathrm{Rx}} \left[\frac{W_{\mathrm{Rx}}}{2} + lN + m \right] \\ & \times s \left[lN + m - \tau + W_{\mathrm{Tx}} - \frac{W_{\mathrm{Rx}}}{2} + N_{\mathrm{CP}} + n_o N_{\mathrm{ext}} \right] \Bigg) e^{-\frac{j2\pi k_0 m}{N}} \end{aligned} \tag{2.11}$$

2.3.2 Pulse design

WOLA-OFDM can be designed to be perfectly complex orthogonal. Indeed, if the transmit and receive shaping pulses satisfy the orthogonality condition of the OFDM (1.2) generalized in (2.12), no intrinsic interference is generated. $\Delta_t(\tau) = (N_{\mathrm{CP}} + W_{\mathrm{Tx}} - W_{\mathrm{Rx}} - \tau)\, T_s$ denotes the placement of the receive window. In such case, the shaping pulses are said to be Nyquist.

$$\int_{-\infty}^{+\infty} g_{\mathrm{Tx}}(t - n_o T) g_{\mathrm{Rx}}(t - nT + \Delta_t(\tau)) e^{j2\pi \frac{(k-k_o)t}{T_u}} dt = N\delta_{k,k_o}\delta_{n,n_o} \tag{2.12}$$

The Better Than Raised Cosine (BTRC) introduced in [31] and defined in (2.13) (where α is the roll-off factor) provides a good trade-off between ICI mitigation (induced by frequency offset) and robustness to multi-path effect [32]. The time impulse and frequency responses of the BTRC is depicted in Figure 2.7 and compared with the rectangular pulse (CP-OFDM) and the other WOLA pulse that is described next.

$$g(t) = \begin{cases} 1 & 0 \leq |t| \leq (1-\alpha)T_u/2 \\ e^{(-2\ln 2/\alpha T_u)(|t| - T_u(1-\alpha)/2)} & (1-\alpha)T_u/2 \leq |t| \leq T_u/2 \\ 1 - e^{(-2\ln 2/\alpha T_u)(T_u(1-\alpha)/2 - |t|)} & T_u/2 \leq |t| \leq (1+\alpha)T_u/2 \\ 0 & \text{otherwise} \end{cases} \tag{2.13}$$

The Meyer window has also been considered for WOLA-OFDM especially for 5G scenarios [30]. It is obtained from a raise cosine pulse (2.14) combined with the Meyer auxiliary function (2.15). The time impulse and frequency responses of the Meyer pulse are added to Figure 2.7 and compared with the rectangular window and the BTRC pulse.

$$g(t) = \begin{cases} 1 & 0 \leq |t| \leq (1-\alpha)T_u/2 \\ \sqrt{\frac{1}{2}\left[1 + \cos\left(\pi v\left(\frac{|t| - (1-\alpha)T_u/2}{\alpha T_u}\right)\right)\right]} & (1-\alpha)T_u/2 \leq |t| \leq (1+\alpha)T_u/2 \\ 0 & \text{otherwise} \end{cases} \tag{2.14}$$

$$v(t) = t^4\left(35 - 84t + 70t^2 - 20t^3\right) \tag{2.15}$$

By looking at Figure 2.7, one can observe that in the time domain the energy is better confined with the Meyer window than with BTRC. Indeed, the impulse response of the Meyer pulse somehow looks like the impulse response of the rectangular pulse with rounded corners. However, in the frequency domain, the BTRC benefits from its longer impulse response to better reject its side lobes. The rejection of the second lobe is even significant with $\alpha = 0.50$ providing an attenuation about 10 dB stronger with respect to the other considered pulses.

For the two window pulses, the impact of the positioning of the receive window (by varying τ) on the orthogonality of the waveform is studied. The orthogonality condition is evaluated with the SIR function defined in (2.16) derived from the condition (2.12) evaluated in $(n, k) = (n_o, k_o)$.

$$\mathrm{SIR}(\tau) = \frac{N}{\left|\sum_{n\to-\infty}^{+\infty}\left(g_{\mathrm{Tx}}[n] g_{\mathrm{Rx}}[n + N_{\mathrm{CP}} + W_{\mathrm{Tx}} - W_{\mathrm{Rx}} - \tau]\right) - N\right|} \tag{2.16}$$

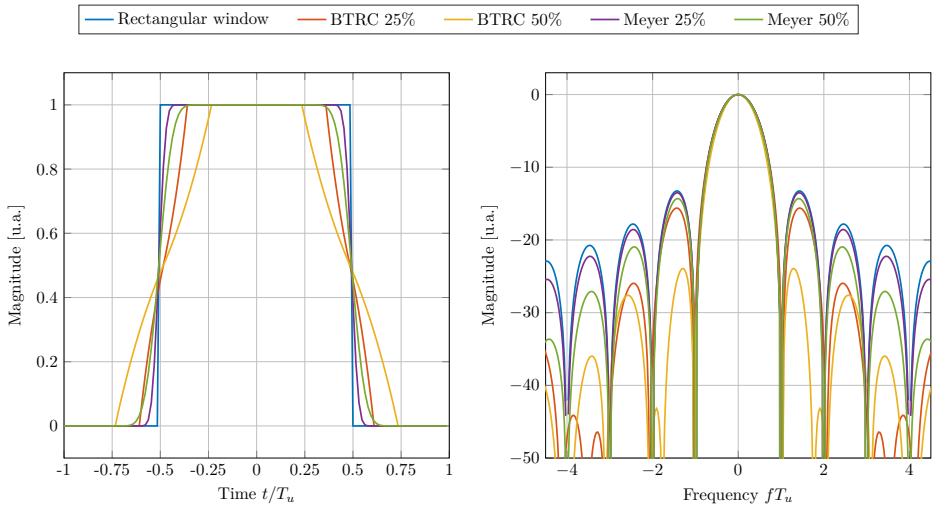

Figure 2.7: Time impulse and frequency responses of rectangular window, BTRC pulse and Meyer pulse for roll-off factors $\alpha = 0.25$ and $\alpha = 0.50$.

For each window pulse, five different configurations have been considered depending on the time excess value (*i.e.* the roll-off coefficient) of the pulse. It is assumed here that both the transmit and the receive windows share the same time excess. The relation between the time excess W_{Tx}, W_{Rx} of the pulse and the roll-off α_{Tx},α_{Rx} is explicated in (2.17). In practice, the time excess of the pulses is fixed as a percentage of the CP length. Indeed, by doing so the pulse configuration for the different 5G NR numerologies is straightforward. As the time excess of the two pulses is the same, the roll-off coefficient differs between the transmit and the receive pulse.

$$\begin{cases} \alpha_{\mathrm{Tx}} = W_{\mathrm{Tx}} / (N + N_{\mathrm{CP}}) & \text{for transmit pulse} \\ \alpha_{\mathrm{Rx}} = W_{\mathrm{Rx}} / (N) & \text{for receive pulse} \end{cases} \tag{2.17}$$

The results are depicted in Figure 2.8 for $\tau \in [0, N_{\mathrm{CP}} + W_{\mathrm{Tx}} - W_{\mathrm{Rx}}]$ and for $W_{\mathrm{Tx}} = W_{\mathrm{Rx}} = \{25\%, 50\%, 100\%, 200\%, 500\%\}$. As a first observation, the complex orthogonality of WOLA-OFDM does not only depends on the Nyquist property of the Tx and Rx pulses but on the time excess and the receive window placement as well. Indeed, the waveform appears to be perfect orthogonal (SIR $>$ 150 dB) when the receive window is centered with respect to the transmit symbol ($\tau = (N_{\mathrm{CP}} + W_{\mathrm{Tx}} - W_{\mathrm{Rx}})/2$) and small time excess ($< 50\%$ N_{CP}) are considered[1]. $\tau = (N_{\mathrm{CP}} + W_{\mathrm{Tx}} - W_{\mathrm{Rx}})/2$ is thus the optimal receive window shift for the orthogonality criterion. Nonetheless, even with the ideal pulse placement, the orthogonality condition may be severely compromised when long window pulses are considered. However, longer window impulse responses are expected to provide enhanced spectral confinement and thus may be more interesting for the considered scenarios in this thesis. Generally speaking, the Meyer window provides better intrinsic interference mitigation than BTRC thanks its time limited impulse response.

[1]We can show that when $W_{\mathrm{Tx}} + W_{\mathrm{Rx}} > N_{\mathrm{CP}}$ WOLA-OFDM can no longer be perfectly complex orthogonal.

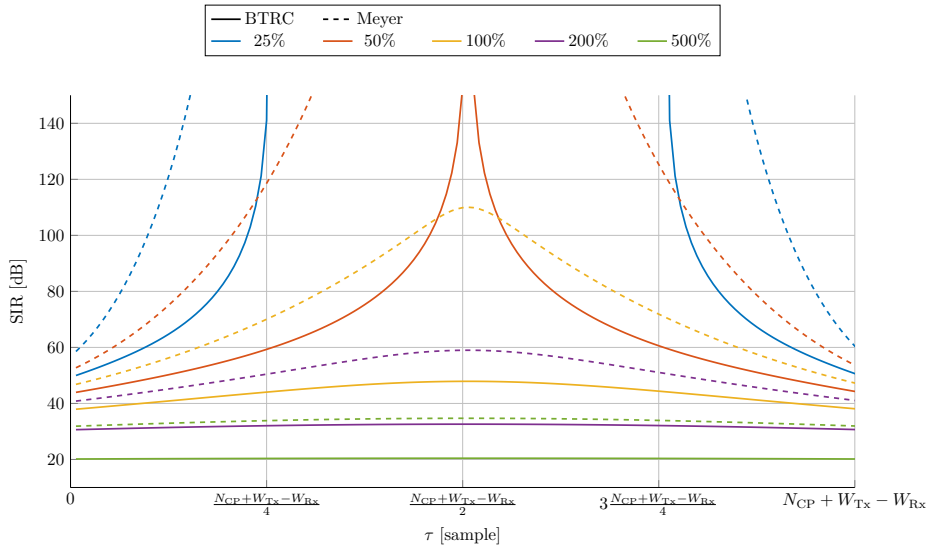

Figure 2.8: Evaluation of the orthogonality condition depending on the placement of the receive window pulse and the Tx/Rx time excess.

Table 2.1: Simulation parameters for Figure 2.9.

Numerology	$\mu = 0$ (CP duration = 4.7μs
Band	9 MHz (50 RBs)
Channel	Perfect CSI
	Constant
Simulation	1000 channel realisations

However, the placement of the receive window is expected to have an impact on multi-path robustness as shifting the window (increasing τ) reduces the available CP length. To evaluate the performance penalty induced by window placement, the Bit Error Rate (BER) is assessed for a transmission over a two-path channel (without additive noise). The channel model is given in (2.18) where α_0 and α_1 are the path gains associated to the two echoes (Rayleigh distributed with 0 dB mean power for α_0 and 2 dB average attenuation for α_1) and n_{DS} corresponds to the delay spread of the channel (varying for the simulation). The simulation parameters are given in Table 2.1.

$$h[n] = \alpha_0 + \alpha_1 \delta[n - n_{\mathrm{DS}}] \tag{2.18}$$

The performance results are depicted in Figure 2.9 for uncoded bit stream so as to emphasize on the impact of the window placement. The evaluation is performed for the two window pulses (BTRC and Meyer) for a fixed time excess ($W_{\mathrm{Tx}} = W_{\mathrm{Rx}} = 0.5N_{\mathrm{CP}}$). The results show that the receive window placement has indeed a significant impact on multi-path resilience. Even when intrinsic interference is generated ($\tau = 0$), the waveform better behaves against fast-fading. According to Figure 2.8, the power of the intrinsic interference is low enough (greater than 40 dB SIR) to have a limited impact on channel performance which explains the obtained results. Regarding the difference between the two window pulses, one

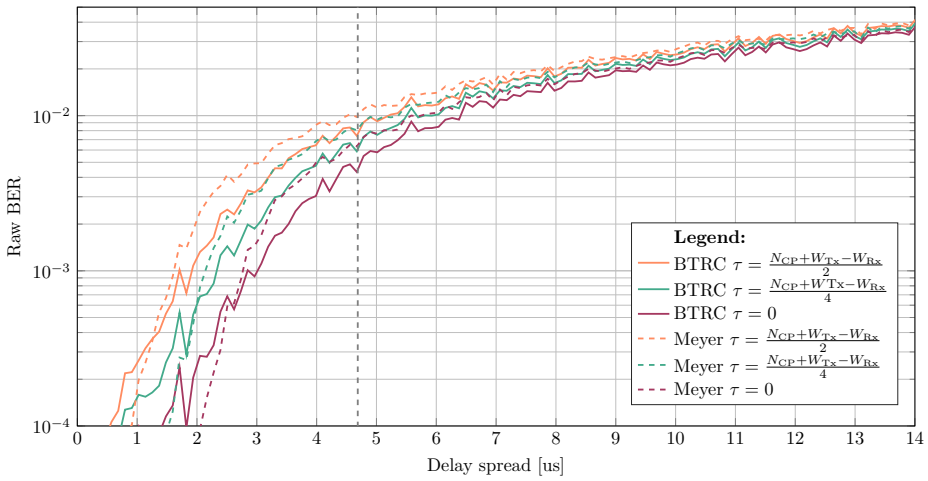

Figure 2.9: Channel performance over a two-ray channel for different receive window placements.

can observe that for high delay spreads (more than twice the CP-OFDM CP length) there is not performance difference between the different configurations. However, the Meyer pulse outperforms BTRC for very small delay spreads (less than half the CP length) while for medium delay spreads BTRC demonstrates a noticeable performance gain. Nonetheless, one can observe that the robustness of WOLA-OFDM against small delay spread channels is significantly reduced w.r.t CP-OFDM as errors occur for delay spread shorter than the CP duration. A performance comparison with the CP-OFDM and other considered waveforms is given in Section 2.5.

The presented results illustrate the trade-off between spectral confinement, orthogonality and channel robustness to operate in WOLA-OFDM window design. In the framework of 5G NR cellular communications, enhanced spectral confinements is wanted while still providing a good robustness against fast fading (to still rely on a simple 1-tap equalization scheme). Given that the obtained results, the BTRC window pulse will be preferred with $W_{\text{Tx}} = \text{Rx} = 0.5N_{\text{CP}}$ and $\tau = 0$.

2.4 FBMC-OQAM

2.4.1 Basic concept and system model

Unlike the aforementioned waveforms, Filter-Bank Multicarrier (FBMC) is not an OFDM-like waveform. In FBMC, the data is transmitted over a bank of modulated band-limited filters. Subcarriers are however not orthogonal which leads to the need of an alternative design for the transmission scheme.

Chang [33] and Saltzberg [34] in the late 60's derived the conditions to perform such a transmission. Indeed, if the roll-off of the prototype filter is small enough (≤ 1), a subband only interfere with its adjacent subbands[2]. In this case, a square-Nyquist prototype filter combined with an Offset-QAM (OQAM) transmission can cancel the induced interference. However, the scheme is not complex orthogonal but real orthogonal because of the OQAM signaling. Besides, in order to preserve

[2]Here, as in CP-OFDM, the subbands are reduced to unique subcarriers.

the spectral efficiency, the in-phase and quadrature components are time staggered by half a symbol duration. This technique is known as FBMC-OQAM (sometimes also called OFDM-OQAM).

The subband signals $s_k(t)$ are therefore generated as shown in (2.19), carried by the pulse $g_{\mathrm{Tx},k}(t) = g_{\mathrm{Tx}} e^{j2\pi f_k t}$ where g_{Tx} is the transmit prototype filter and $s_{k,n}$ the transmit symbols. Then the subband signals are summed together as shown in (2.20). According to the OQAM transmission, $c_k[n] = b_{k,n} e^{j\frac{\pi}{2}(k+n)}$ where $b_k[n]$ are real symbols (with mean energy $\sigma_b^2 = \sigma_a^2/2$). The phase offset depending on the time and frequency position ensures that adjacent symbols in the time-frequency grid are in quadrature which each others. The subbands center frequency f_k are equally spaced, *i.e.* $f_k = k\Delta_k$ and $1/\sqrt{N}$ is the N-point IFFT normalisation coefficient. The phase $\varphi_{k,n}$ results from the OQAM transmission and the overlapping frame structure of the filter bank. The FBMC/OQAM transmitter scheme is thus a synthesis filter bank composed of modulated filters $g_{\mathrm{Tx}}(t - nT/2)e^{j2\pi k\Delta_k t}$ [35].

$$
\begin{aligned}
s_k(t) &= \sum_n c_k[n] g_{Tx,k}(t - nT/2) \\
&= \sum_n c_k[n] g_{Tx}(t - nT/2) e^{j2\pi f_k (t - nT/2)} \qquad (2.19) \\
s(t) &= \sum_{k=0}^{N-1} s_k(t) \\
&= \frac{1}{\sqrt{N}} \sum_n \sum_{k=0}^{N-1} b_k[n] e^{j\frac{\pi}{2}(k+n)} g_{\mathrm{Tx}}(t - nT/2) e^{j2\pi k\Delta_k (t - nT/2)} \\
&= \frac{1}{\sqrt{N}} \sum_n \sum_{k=0}^{N-1} b_k[n] \underbrace{e^{j\pi\left(\frac{k+n}{2} - kn\right)}}_{e^{j\varphi_{k,n}}} g_{\mathrm{Tx}}(t - nT/2) e^{j2\pi k\Delta_k t} \qquad (2.20)
\end{aligned}
$$

The time localisation of the transmit pulse is relaxed to ensure an efficient filtering in the frequency domain. The overlapping factor K is therefore introduced. It is defined as the ratio between the filter impulse response and the useful symbol T. Typical values for FBMC/OQAM are $\{2, 3, 4\}$. A graphical representation of a transmitted FBMC/OQAM signal with $K = 4$ is given in Figure 2.2.

At the receiver side, the subband separation is achieved by applying the matched (conjugate reverse) receive pulse g_{Rx} modulated at frequency $f_{k_o} = k_o\Delta_k$ as shown in (2.21). The normalisation coefficient is added as well for sake of coherence with previously studied waveforms. After the analysis filter-bank stage, the phase offset (induced by the OQAM transmission and the filter-bank) is compensated and the real part of the resulting symbol is taken to remove the intrinsic interference (2.22).

$$
\begin{aligned}
y_{k_o}[n_o] &= \frac{1}{\sqrt{N}} \sum_{m=0}^{KN-1} s[m + n_0 N/2] \left(g_{\mathrm{Rx}}[m] e^{j2\pi \frac{k_0 m}{N}} \right)^* \qquad (2.21) \\
r_{k_o}[n_o] &= \mathcal{R}\left(y_{k_o}[n_o] e^{-j\varphi_{k_o,n_o}} \right) \qquad (2.22)
\end{aligned}
$$

In practice, the transmit and receive prototype filters are the same and the pulse is real-valued and symmetric. For this reason, the subscripts Tx and Rx are dropped from notations from now and for the rest of the manuscript.

2.4.2 Orthogonality condition and prototype filter design

In FBMC/OQAM, the orthogonality is ensured thus by both the phase offset $\varphi_{k,n}$ and the prototype filter properties. The ambiguity function defined in (2.23) can be used to analyse the orthogonality condition [36] with Δ_n the time instant difference and Δ_k the subcarrier index difference.

$$A_g(\Delta_n, \Delta_k) = \sum_{t=0}^{KN-1} g[t]g^*[t - \Delta_n N/2]e^{-j\frac{2\pi}{N}\Delta_k t}dt \tag{2.23}$$

However, the ambiguity function as defined in (2.23) only takes into account the prototype filter. By also considering the OQAM-induced phase offset[3], the orthogonality condition can be expressed as in (2.24)[35].

$$\mathcal{R}\left(e^{-j\frac{\pi}{2}(\Delta_n+\Delta_k)}A_g(\Delta_n, \Delta_k)\right) = \begin{cases} 1 & \text{if } \Delta_n = \Delta_k = 0 \\ 0 & \text{otherwise} \end{cases} \tag{2.24}$$

Gaussian pulses have first been considered to satisfy the orthogonality condition. Alard[37] and Le Floch[38] presented a method to convert Gaussian pulses into orthogonal basis. An optimisation of orthogonal Gaussian prototype filters is proposed in [39, 40] so as to ensure Near Perfect Reconstruction. Those filters are named Isotropic Orthogonal Transform Algorithm (IOTA) filters. However, given that filter responses are usually long (K times the number of subcarriers), traditional optimisation processes applied on filter coefficients become highly complex. That is why Frequency Sampling (FS) technique has also been widely used to design filter-bank prototype filter [41]. Such filters are defined by a few frequency coefficients and their impulse can be derived from them as shown in (2.25) where G_k is the set of frequency coefficients. Usually K distinct coefficients are considered for such prototype filters.

$$g[n] = \left(G_0 + 2\sum_{k=1}^{K-1}(-1)^k G_k \cos\left(\frac{2\pi}{KN}kn\right)\right) \tag{2.25}$$

In Appendix A, (2.24) is used to determine the relations that must satisfy the frequency coefficients H_k to ensure perfect real orthogonality [41, 42]. The expressions are reminded in Table 2.2. For small values of K, all the coefficients are determined with the Nyquist relation. However when $K \geq 3$, at least one coefficient is left undetermined. The undetermined value(s) can thus be determined via optimisation based for instance on side lobe rejection as proposed in [42] and added in Table 2.2. Those filters are named Phydyas filters.

The response of (2.23) and (2.24) are depicted in Figure 2.10 for IOTA and PHYDYAS prototype filters with $K = 4$. (2.24) illustrates the real orthogonality condition but (2.23) is nonetheless important as it gives a representation of the

[3] the term $(-1)^{kn}$ can be omitted in orthogonality study because it has no impact

Table 2.2: Nyquist criterion relation and typical values for the filter coefficients.

K	G_0	G_1	G_2	G_3	G_1 in [42]
1	1				
2	1	$1/\sqrt{2}$			
3	1	G_1	$\sqrt{1-G_1^2}$		0.911
4	1	G_1	$1/\sqrt{2}$	$\sqrt{1-G_1^2}$	0.972

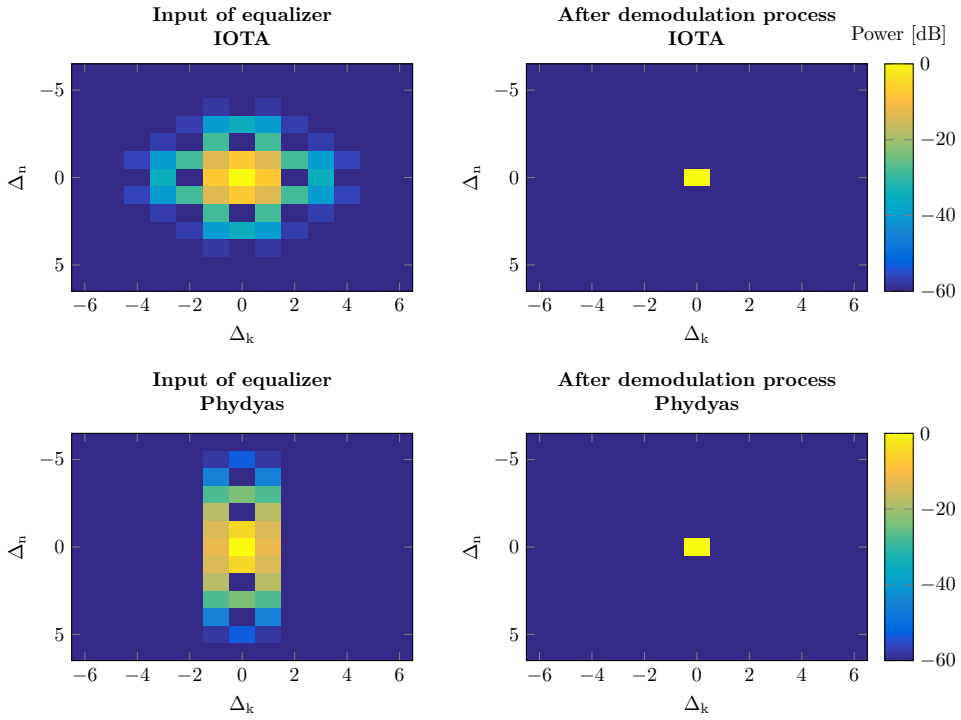

Figure 2.10: Transmultiplexer response of (2.23) (left) and (2.24) (right) for IOTA (top) and PHYDYAS (bottom).

level and the distribution of the intrinsic interference at the input of the equalization/detection stage and thus has to be considered in the channel estimation process.

One can observe that at the input of equalizer (just after applying the receive prototype filter) each symbols are spread over the adjacent time and frequency slots. The intrinsic interference power equals the usefull data power [43]. The distribution of intrinsic interference depends on the prototype filter. Indeed, the distribution is isotropic in both time and frequency domain with the IOTA filter while for the PHYDYAS filter it is limited to directly adjacent slots in the frequency domain and is more spread in the time domain. As we can observe, the intrinsic interference is entirely canceled by applying the receive phase offset and by removing the imaginary part of the demodulated signal.

2.4.3 Polyphase Implementation

The decomposition of the signal into a few components is the core concept of the polyphase representation of a filter-bank structure. Indeed, the response of a finite impulse filter of length KN can be decomposed into N polyphase components $E_n[z^N]$ as shown in (2.26).

$$\begin{aligned} G(z) &= \sum_{l=0}^{KN-1} g[l] z^{-l} \\ &= \sum_{n=0}^{N-1} \underbrace{\left(\sum_{k=0}^{K-1} g[kN+n] z^{-kN} \right)}_{=E_n[z^N]} z^{-n} \end{aligned} \tag{2.26}$$

It seems worth noticing that the polyphase decomposition of the modulated prototype filter corresponds to N-point inverse Fourier Transform of delayed polyphase components of the prototype filter as shown in (2.27).

$$\begin{aligned} G_k(z) &= \sum_{l=0}^{KN-1} g[l] e^{j2\pi \frac{lk}{N}} z^{-l} \\ &= \sum_{n=0}^{N-1} \left(e^{j2\pi \frac{nk}{N}} E_n[z^N] \right) z^{-n} \\ &= \sum_{n=0}^{N-1} \left(E_n[z^N] z^{-n} \right) e^{j2\pi \frac{nk}{N}} \end{aligned} \tag{2.27}$$

Last but not least, $E_n[z^N]$ denotes the filtering applied on a upsampled signal. However, it is equivalent to filtering with $E_n[z]$ followed up by an upsampling (*i.e.* multirate identities [44, section 2.4]). It implies that the filtering can be applied on down sampled signal that is then up sampled for the synthesis. Respectively at the receiver side, the analysis filter-bank, the signal passes through the delay chain, is down sampled, filtered by $E_n[z]$ and is then transposed in the frequency domain. The PolyPhase Network (PPN) is a filter-bank implementation that is based on this principle and has been formalised in the 70's by Bellanger [45]. The structures of the synthesis and analysis PPN-based filter-bank are reminded in Figure 2.11.

The overall Tx and Rx schemes are depicted in Figure 2.12. The symbol source still denotes a complex symbol source from a QAM constellation while the TX OQAM stage represents the splitting of the real and imaginary parts of the complex constellation to generate a PAM constellation. The synthesis filter bank stage corresponds to the scheme depicted in Figure 2.11 top. When it comes to the receiver scheme, the signal is first processed by the analysis filter-bank depicted in Figure 2.11 bottom. The channel distortion is then counteracted before removing the intrinsic interference and reconstituting the complex symbol performed by the Rx OQAM stage.

The PPN enables an efficient filter-bank implementation based on simple N-point (I)DFT. In most cases, the DFT are implemented with the splix radix algo-

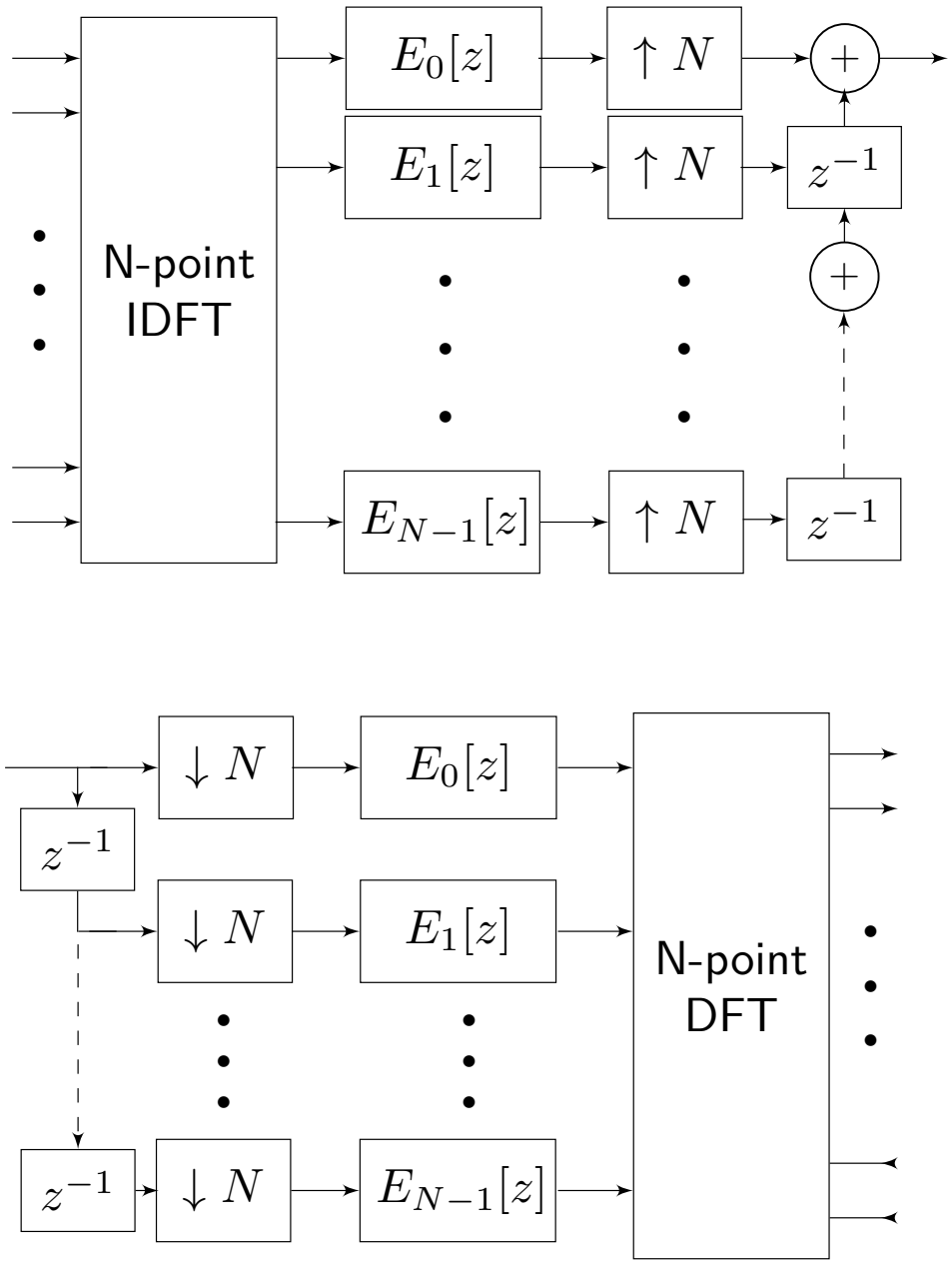

Figure 2.11: Synthesis (top) and analysis (bottom) polyphase-based implementation of filter-banks.

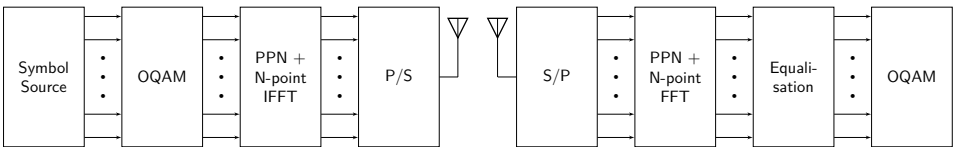

Figure 2.12: PPN-implemented FBMC/QAM Tx and Rx schemes.

rithm of the (I)FFT which is low-complex. The implementation can be even more simplified by considering pruned-IFFT [46, 47].

2.4.4 Frequency-Spreading Implementation

The Frequency-Spreading (FS) structure has also been introduced for FBMC/OQAM [48, 49]. The structure has been introduced as a generalisation of the PPN implementation but more flexible with the possibility of dynamic changes of the overlapping factor K and more robust to fading channels thanks to an improved frequency resolution of the receivers. However with this structure, the number of non-zero frequency taps of the prototype filter must be limited. The frequency-sampling filters are thus well suitable for FS architecture.

$$\begin{aligned} s[l] &= \sum_{n} \sum_{k=0}^{N-1} c_k[n] \left(\sum_{p=-K+1}^{K-1} G_p e^{j\frac{2\pi}{KN}p(l-nN/2)} \right) e^{j\frac{2\pi}{N}kl} \\ &= \sum_{n} \sum_{k=0}^{N-1} \sum_{p=-K+1}^{K-1} c_k[n] G_p e^{j\frac{2\pi}{KN}l(p+Kk)} e^{-j\frac{\pi}{K}pn} \\ &= \sum_{\substack{i=-K+1 \\ i=p+Kk}}^{KN-1} \left(\sum_{n} e^{-j\frac{\pi}{K}in} \sum_{k=0}^{N-1} c_k[n] G_{i-Kk} \right) e^{j\frac{2\pi}{KN}il} \\ &= \sum_{n} \sum_{i=0}^{KN-1} e^{-j\frac{\pi}{K}in} \left(\sum_{k=\lfloor \frac{i}{K} \rfloor}^{\lceil \frac{i}{K} \rceil \pmod{KN}} c_k[n] G_{i-Kk} \right) e^{j\frac{2\pi}{KN}il} \end{aligned} \tag{2.28}$$

The transmitted signal expression is given in (2.28) where $c_k[n] = b_k[n]e^{\varphi_{k,n}}$ is the real symbol with phase-offset. The signal can thus be generated by a KN-point IDFT and a point-wise weighting applied in the frequency domain. This expression stresses the subband overlap with the summation over the subcarrier indices k. The receiver performs the matched processing. An interesting aspect of this architecture is to benefit from the enhanced frequency resolution of the receiver (with the KN-point DFT) and to insert the equalization/detection stage between the transposition in the frequency domain and the matched filtering. Nonetheless, it poses a few challenges to overcome. Indeed, as the equalization/detection stage is applied before the filtering, the symbols are spread over larger areas as depicted in Figure 2.13.

2.4.5 Challenges induced by OQAM signaling

Derivation of likelihood metrics

Unlike the solutions presented in this chapter, the computation of the LLR, introduced for CP-OFDM in Section 1.4.3, must be adapted to the OQAM signaling.

Because of the reduction of the orthogonality in the real field, intrinsic interference terms have to be considered in the symbol estimation. The signal expression at the input of the equalizer is given in (2.29) for the PPN receiver scheme.

$$r_{k_o}[n_o] = H[k_o]\left(b_{k_o}[n_o] + ju_{k_o}[n_o]\right) + \nu_{k_o}[n_o] \tag{2.29}$$

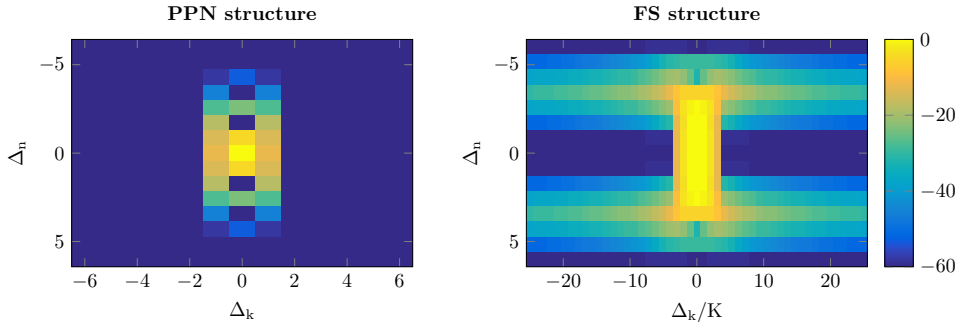

Figure 2.13: Transmultiplexer response comparison between PPN and FS schemes for PHYDYAS $K = 4$ prototype filter.

When virtually complex symbols, composed of the real useful symbol and the purely imaginary interference term, are considered the model is equivalent to CP-OFDM (1.6) because $\sigma_b^2 = \sigma_u^2 = \sigma_a^2/2$ [43]. Hence, the determination of the estimation variance $\sigma_{\tilde{\nu}}^2$ can be performed as (1.14). However, this estimation variance is only valid for real symbols $\sigma_{\tilde{\nu}_r}^2$. By assuming independent noise realisations over different time/frequency position, the variance of the estimation of the complex symbol corresponds to the sum of the two aforementioned variances. The linear approximation [14] can be used for PPN once the complex symbol is reconstructed.

When it comes to the FS receiver, the filtering must be taken into consideration. The channel estimation and the equalisation is applied at the oversampled subcarrier level (*i.e.* subband of $F_s/(KM)$) but the expressions for ZF (1.7) and MMSE (1.8) are still valid. A linear combination weighted by frequency filter coefficients of the oversampled subcarrier estimation variances $\tilde{\sigma}_{\tilde{\nu}}^2[m]$ results in the variance of the estimation of real symbols (obtained after receive filtering) $\sigma_{\tilde{\nu}_r}^2$. The estimation of the complex symbol can be done as decribed for the PPN structure.

$$\sigma_{\tilde{\nu}_r}^2[k_o] = \sum_{m=Kk_o-K+1}^{kK_o+K-1} G_{m-Kk_o}^2 \tilde{\sigma}_{\tilde{\nu}}^2[m] \tag{2.30}$$

The adaptation to MIMO systems is straightforward and is similar to the procedure detailed in Section 1.4.3 [50].

Channel estimation

The transmultiplexer response of the FBMC/OQAM prevents the straightforward use of scattered pilots like in OFDM. One solution is therefore to rely on preamble-based channel estimation techniques which are suitable for slowly-varying channels. Nonetheless, the preamble schemes must take into consideration the intrinsic interference and the real orthogonality.

Indeed, because of the real orthogonality it is not possible to obtain a complex estimation of the channel with a unique pilot. A pragmatic solution is proposed in [51] where a Pair of Pilots (POP) is used instead. If the channel exhibits a low frequency selectivity, pilots at adjacent time instants experience the same channel

distortion. Therefore, a system of two equations with two unknowns (the in-phase and quadrature components of the channel frequency response) is obtained and can be easily solved. However, the presence of noise or intrinsic interference (coming from unknown data) can severely compromise the performance of the estimator [51].

Another approach consists in avoiding canceling the intrinsic interference by removing the imaginary part of the received symbols. To do so, pilots symbols can be surrounded by guard symbols (*i.e.* zero symbols) which cancels the first-tier subcarrier-induced interference. In addition to that, the symmetric response of the transmultiplexer response can be used to cancel the intrinsic interference coming from second-tier subcarriers. As a consequence, the intrinsic interference is cancelled at the pilot position and the complex channel response can thus be easily determined with a Least-Square (LS) estimate. This technique is known as Interference Cancellation Method (ICM) [52]. However, the intrinsic interference can also be used to improve the estimation accuracy. Indeed, if the adjacent positions of the pilot are known, an estimation of the intrinsic interference can be computed. This technique is known as Interference Approximation Method (IAM). Different pilot sequences can be considered: pseudo-random sequence which is interesting to limit Peak-to-Average-Power-Ratio (PAPR), real pilots (IAM-R) [53] or complex pilots (IAM-C) [52] which provide optimal channel estimation performance (according to Mean Square Error (MSE) indicator) and non maximum-magnitude complex pilot sequence (IAM-I) [52, 54] which demonstrates a good trade-off between PAPR behavior and channel estimation performance.

For higher frequency selectivity, the channel response can be modeled with for instance the MUltiple SIgnal Classification (MUSIC) [55]. The Channel Impulse Response (CIR) can also be directly estimated without any further assumptions by using the exact FBMC/OQAM system model [56]. Another possibility is to consider the FS scheme and its high receiver resolution. The adaptation of channel estimation to FS scheme is different because it has to be done before the match filtering. In [57], it is proposed to first use IAM techniques to get a gross estimation of channel coefficients and then to combine successive channel observations (maximum ratio combining) to obtain a more accurate estimation.

For fast-varying channels (varying at a burst level), scattered pilot based channel estimation must be employed. However, the estimation of the channel coefficients is polluted by intrinsic interference induced by adjacent unknown data. Single-scattered pilot schemes (as in OFDM) are thus inefficient. However, scattered cluster structures can considerably reduce the impact of the intrinsic interference. This techniques are known as "pilot-aided" or "Help-Pilot" (HP) estimation schemes [58].

Channel equalization

For low/midly selective channels, an one-tap equalizer per subcarrier can be used. Such equalizers rely on channel estimation and generally just invert the channel. They can be applied in a similar way than in OFDM by considering virtual symbols as shown in (2.31). For the example, the channel is assumed to be invariant over a FBMC/OQAM symbol and a coherence bandwidth larger than the subcarrier spacing. The virtual symbol $x_k[n]$ is composed of the useful real symbol $b_k[n]$ and the intrinsic interference term $u_k[n]$ (real-valued).

$$y_k[n] = H[k,n]\underbrace{(b_k[n] + ju_k[n])}_{x_k[n]} + w_k[n] \tag{2.31}$$

The channel coefficient can then be compensated, as in OFDM, with conventional linear equalizers such as the Zero-Forcing (ZF) which applies the pseudo-Moore inverse of the channel coefficient (2.32) and Minimum Mean Square Error (MMSE) which avoids noise amplification (2.33). For the MMSE, the intrinsic interference energy equals the real symbol energy (*i.e.* $\sigma_u^2 = \sigma_b^2$) and thus the energy of the virtual symbol can be determined from the mean energy of the real constellation: $\sigma_x^2 = 2\sigma_b^2$.

$$W_{\mathrm{ZF}}[k,n] = H^*[k,n] / \left|H[k,n]\right|^2 \tag{2.32}$$

$$W_{\mathrm{MMSE}}[k,n] = H^*[k,n] / \left(\left|H[k,n]\right|^2 + \sigma_w^2/\sigma_x^2\right) \tag{2.33}$$

For channels with strong channel selectivity, multi-tap equalizers provide better performance. A simple approach is to apply equalization coefficients in the frequency domain which allows to equalize the channel response at a number of frequency bins equal to the number of equalizer coefficients. The receive FS scheme can be used to easily simulate multitap equalization with linear single-equalizers on each frequency bins [59, 60]. In the time domain, multitap equalizers are represented as FIR filters. In this category, the classical MMSE solution can be easily adapted to staggered signals [61].

Extension to MIMO schemes

The challenge is intensified in MIMO systems as the inter-antenna interference has to be also taken into account. However, SISO channel estimation techniques can still be easily adapted to multiple-antenna systems. For instance, a MIMO IAM preamble can be constructed by repeating each SISO IAM training sequence as many as times as there are transmit antennas and inserting sign changes to ensure orthogonality between the transmit training sequences (*i.e.* orthogonal preamble training as in MIMO-OFDM)[62]. The disposition of HPs can also be adapted to MIMO systems [63].

Regarding channel equalization, linear techniques can still be used by considering the virtual symbols. More advanced linear-based equalizers can also be adapted exactely as in OFDM [64].

However, because of the intrinsic interference, the Maximum Likelihood (ML) detection is not feasible. Interference cancellation techniques have been developped to be able to apply ML detection to FBMC/OQAM receivers [65]. Linear detection with MMSE is used to estimate the transmitted virtual symbol. The intrinsic interference can thus be estimated by taking the imaginary part. The obtained estimation of the intrinsic interference can then be subtracted from the received symbol. By assuming perfect interference estimation, we may consider than the received symbol after interference cancellation is free of intrinsic interference. A ML detection can thus be performed as in OFDM. However, due to the high energy of the intrinsic interference, the interference estimation is imperfect. The proposed interference-cancellation receiver can thus be improved to a partial

Table 2.3: Waveform configurations

	CP-OFDM	fOFDM	UF-OFDM
Tx		Cardinal Sine with Huawei window $L = 0.5 \times N$	Chebyshev filter $L = N_{\text{CP}} + 1$ RB-wide subband
Rx		$\delta_W = 2.5$ Allocated-RBs subband	Raised-cosine window $L = N + L$ $W_{\text{Rx}} = L/2 - 1$

	WOLA-OFDM	FBMC-OQAM
Tx	BTRC window $L = N + N_{\text{CP}} + W_{\text{Tx}}$ $W_{\text{Tx}} = 0.5 \times N_{\text{CP}}$	PHYDYAS filter $L = K \times N$
Rx	BTRC window $L = N + W_{\text{Rx}}$ $W_{\text{Rx}} = 0.5 \times N_{\text{CP}}$	with $K = 4$ subcarrier-wise

interference cancellation scheme. A tentative detector is first used to give an estimation of the interference that is subtracted followed by Viterbi detector is used to cancel the residual interference [66].

MIMO systems can also be used to improve the reliability of transmission. Spatial diversity can be exploited with Space Time Block Code (STBC). Many works have been dedicated to the Alamouti scheme that is a simple STBC for two transmit antennas. Indeed, because of the intrinsic interference, the Alamouti scheme can not be directly applied to FBMC/OQAM. A pseudo-Alamouti scheme is presented in [67] that requires in CP insertion and a block Alamouti scheme is introduced in [68] which also leads to a spectral efficiency reduction so as to ensure block isolation. Moreover for the latter scheme, the channel should remain static during the block duration which makes this scheme difficult to implement in time varying environment.

2.5 Performance Evaluation

Once the state-of-the-art solutions have been described, they are compared on some scenarios of interest. The considered configurations for the waveforms are reminded in Table 2.3.

2.5.1 Spectral confinement

In a first time, the spectral confinement of the proposed waveforms is evaluated. A better frequency confined waveform may be transmitted over available narrowband spectrum holes which improves the bandwidth use efficiency and eases the resource allocation process. Besides, waveforms with improved side lobe rejection

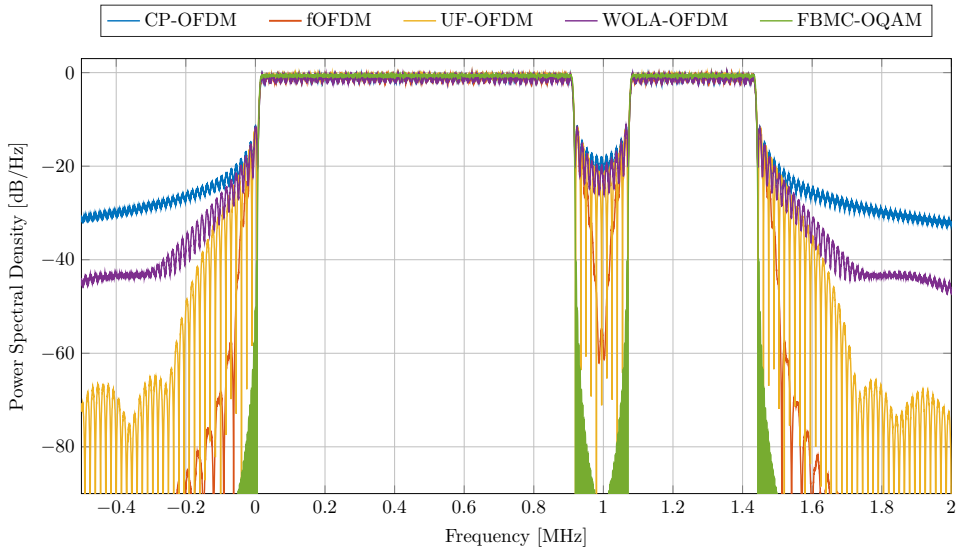

Figure 2.14: PSD of considered solutions with 5-RB and 2-RB allocations spaced by 1-RB guard band.

are expected to better behave in typical 5G NR where non-orthogonal adjacent subbands co-exist.

The results are depicted in Figure 2.14 for two allocated blocs (5 and 2 RBs) spaced by a 1-RB guard band. WOLA-OFDM and its windowing provides a slight side lobe rejection improvement with respect to legacy CP-OFDM. The performance gain is appreciable in the "far" OOB region (for frequencies further than 100 kHz from the allocated RBs) and increases with the distance from the allocated region. However, the performance gain is limited in the near OOB region (the 100 kHz adjacent to the allocated RBs) which does not improve the OOB emissions in narrow-band free spaces of the spectrum (*i.e.* the guard band).

The time-convolution based waveforms, fOFDM and UF-OFDM, outperform WOLA-OFDM. The fOFDM with its longer filter impulse response can provide a significant side lobe rejection improvement even in the near OOB region. Nonetheless, there is no rejection gain for the first three side lobes even for fOFDM.

The FBMC-OQAM and its subcarrier-wise filtering provides the best spectral confinement of the considered solutions. Even the first side lobes are highly attenuated w.r.t legacy CP-OFDM which provides clean spectrum holes.

2.5.2 Channel robustness

Two scenarios are considered for the channel performance evaluation: uncoded systems over double-ray Rayleigh channel and coded systems over Tapped Delay Line (TDL) channel. For the proposed scenarios, we assume a perfect Channel State Information (CSI) and ideal 1-tap ZF equalization for all the considered waveforms. Only the numerology $\mu = 0$ is considered with a 18 MHz frequency allocation.

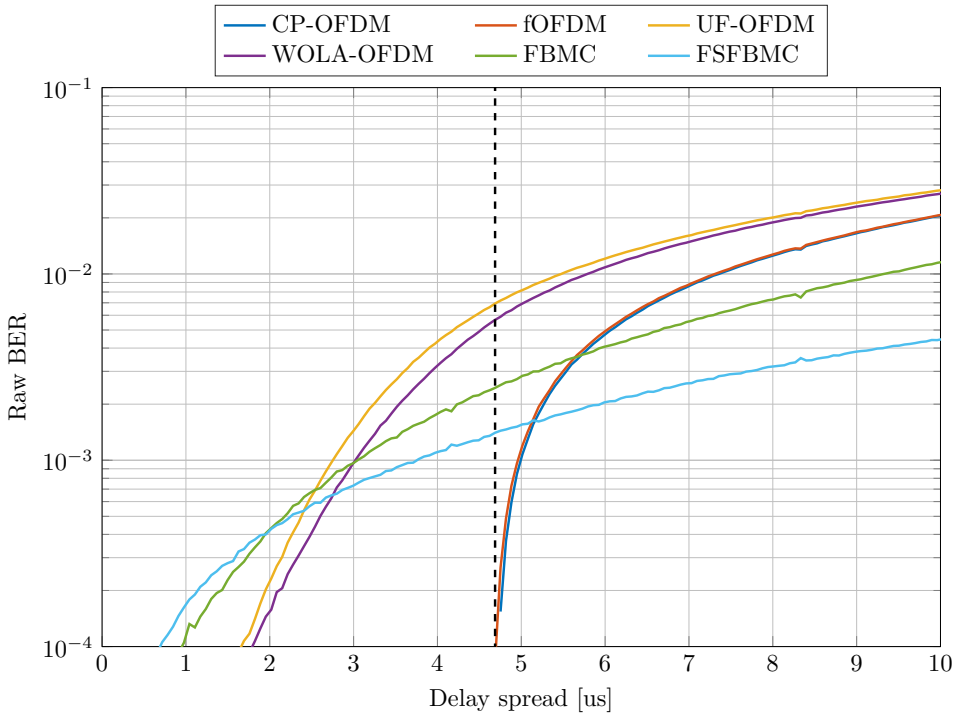

Figure 2.15: Impact of symbol spreading in time on delay spread robustness.

Double-ray channel

The first scenario aims at observing the impact of the symbol enlargement in time on delay spread resilience like in [69]. The channel model is defined in (2.34) with α_0 the Rayleigh distributed attenuation of the LOS (0 dB average power), α_1 the Rayleigh distributed attenuation of the echo (-2 dB average power) and n_{DS} the delay spread of the channel impulse response. No mobility and no additive noise are considered for this scenario. The results are obtained by averaging 10000 channels realisations per delay spread. The resulting Bit Error Rate (BER) as function of the channel delay spread is depicted in 2.15.

$$h[n] = \alpha_0 + \alpha_1 \delta\left[n - n_{\mathrm{DS}}\right] \tag{2.34}$$

For short delay spreads (*i.e.* shorter than CP length), CP-OFDM expectingly provides a perfect channel-induced distortion cancellation which results in ideal BER. For longer delay spreads, the BER of CP-OFDM increases with the delay spread. One can observe that fOFDM provides similar results. Indeed despite its very long filter response, the energy is distributed in time in a similar way as in CP-OFDM which leads to a non-appreciable performance difference.

UF-OFDM and WOLA-OFDM also share a similar behavior. ISI is generated even for short delay spreads mainly because of the joint action of time convolution and zero-adding for UF-OFDM and the overlapped structure for the WOLA-OFDM. The ISI energy increases with the delay spread of the channel which results in the worst performance for long delay spreads for the two solutions.

For very short delay spreads, the worst performance is obtained for the two FBMC waveforms as there is no CP. Nonetheless, as the symbols are much longer

than for the other waveforms, the FBMC-based solutions are less sensitive to long delay spreads and thus provide the best performance for long delay spread channels. Expectingly, a significant performance gain can be achieved with the FS-FBMC solutions thanks to the higher frequency resolution of its receiver.

As a first conclusion, the considered waveforms provide quite different results. On the one hand, fOFDM is interesting as it provides identical performance than CP-OFDM while significantly improving the spectral confinement. On the other hand, FBMC-OQAM, with both receiver schemes, outperforms CP-OFDM against long delay spread channels while providing the best spectral confinement and full symbol density. Generally speaking, solutions with large symbol enlargement (time convolution with long filter impulse response or filter-bank) are more appealing among the proposed contenders for the channel performance criterion. However, this scenario is rather simple and only aims at assessing the trade-off between spectral confinement and robustness to frequency selectivity. Performance for more realistic 5G NR scenarios are assessed in the next section.

TDL channels with mobility

TDL channel model are typical 5G NR channel model for non-MIMO systems working at maximum 100 GHz [70]. The specifications defines five TDL channel models but in this section we will only use TDL-A which is the non LOS Rayleigh-distributed channel with the longest channel delay spread. The TDL channels are scaled to achieve a desired RMS delay spread from very short delay spread (10 ns) to very long delay spread (1000 ns). In this thesis, the nominal RMS delay spread of 100 ns will be used.

A channel coding compliant with release 15 [71] is considered. The LDPC decoder is based on the Self-Corrected Min-Sum algorithm with maximum 50 iterations. The waveform performance evaluation is performed for three Modulation-Coding Schemes (MSC):

- MCS = 03: QPSK modulation with coding rate of about 25% (251/1024)
- MCS = 13: 16-QAM modulation with coding rate of about 50% (490/1024)
- MCS = 23: 64-QAM modulation with coding rate of about 70% (719/1024)

The results are depicted in Figure 2.16. Those results stress the impact of the coherence time of the channel on the performance of coded systems. For low mobility (50 km/h), FBMC/OQAM with both PPN and FS receiver schemes experience a performance penalty with respect to the other solutions. By the way, the two receivers provide exactly the same channel performance and their curves thus overlap. It is induced by its high symbol spreading (K times useful symbol duration) which does not guarantee constant channel response over a symbol. When the mobility increases to 150 km/h, the performance penalty becomes significant and FBMC-OQAM even exhibits an error floor for 16-QAM and 64-QAM. The FS receiver does not provide any performance gain in mobility scenario (but would for more frequency selective channels). With 64-QAM, fOFDM experiences a performance penalty with respect to the three other solutions for the same reasons.

As a conclusion, presented solutions somehow provide the same robustness level in mobility scenarios. Only waveforms with enlarged symbols in time are

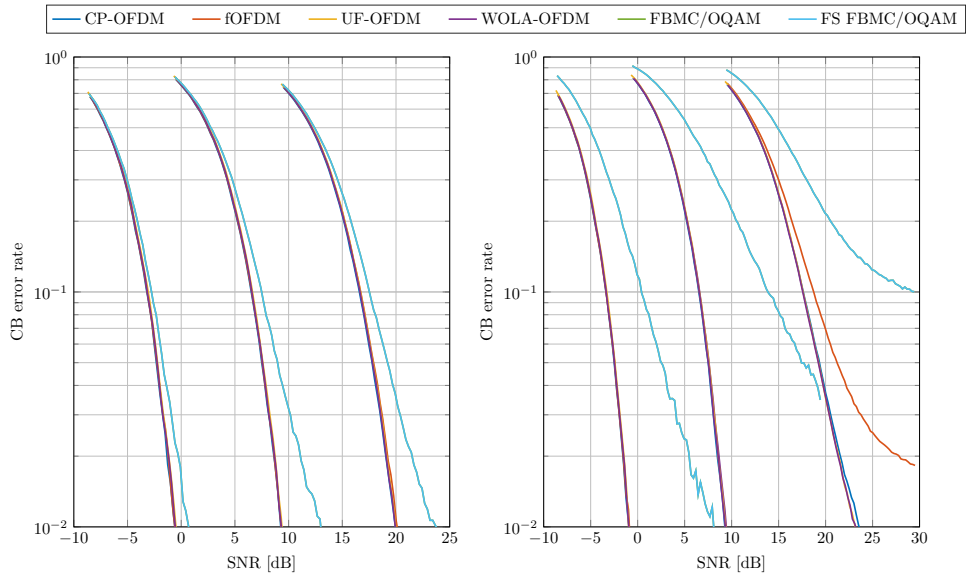

Figure 2.16: Evaluation of Code Block error rate over 100 ns TDL-A channels for 50 (left) and 150 (right) km/h with carrier frequency at 3.5 GHz.

weakened in mobility scenarios. FBMC-OQAM provides the worst performance in this scenario with a significant penalty gap with respect to the other solutions.

2.5.3 Complexity

In this section, a comparison of the computational complexity is performed. A more complex waveform requires more computation resource (*i.e.* logic units and processing time) which leads to a higher energy consumption. The complexity is evaluated by counting the number of real multiplications required to transmit a complex symbol.

It is assumed that one complex multiplication can be carried out with three real multiplications [72]. Besides, the split-radix algorithm is considered for the (I)DFT implementation.

CP-OFDM

The complexity of the transmitter (resp. the receiver) is reduced to a N-points IFFT (resp. N-points FFT) which leads to:

$$\mathrm{C}_{\mathrm{CP-OFDM,Tx/Rx}} = \frac{3N}{2}\log_2(N) \tag{2.35}$$

fOFDM

The complexity of this modulation scheme is induced by the (I)FFT and the filtering. The filter shape of length L is complex but symmetrical. The time convolution therefore requires $3\left(N+N_{\mathrm{CP}}\right)\left\lfloor\frac{L}{2}\right\rfloor$ real multiplications.

$$\mathrm{C}_{\mathrm{fOFDM,Tx/Rx}} = \frac{3N}{2}\log_2(N) + 3\left(N+N_{\mathrm{CP}}\right)\left\lfloor\frac{L}{2}\right\rfloor \tag{2.36}$$

UF-OFDM

The UF-OFDM transmitter provides a subband-processing at the RB level. It implies that the complexity of the transmitter depends on B the number of allocated RBs.

For each RB, the predistortion stage requires 12 complex multiplications, the transposition to the time domain $\frac{3N}{2}\log_2(N)$ and the convolution with the symmetrical filter (of length $L = N_{\text{CP}} + 1$) $3N\left(\left\lfloor\frac{N_{\text{CP}}}{2}\right\rfloor + 1\right)$.

At the receiver side, the $2N$-point FFT involves $3N\log_2(2N)$ real multiplications and the windowing $2 \times 2\,(N_{\text{CP}} + 1)$ extra multiplications.

$$\text{C}_{\text{UF-OFDM,Tx}} = B\left(2 \times 12 + 3\frac{N}{2}\log_2(N) + 3N\left(\left\lfloor\frac{N_{\text{CP}}}{2}\right\rfloor + 1\right)\right) \tag{2.37}$$

$$\text{C}_{\text{UF-OFDM,Rx}} = 3N\log_2(2N) + 4\,(N_{\text{CP}} + 1) \tag{2.38}$$

Reduced complexity schemes are been studied such as in [73]. They mainly aim at performing the filtering in the frequency domain which can be achieved at the expense of a slight performance penalty. Such schemes are not addressed in this thesis.

WOLA-OFDM

The WOLA-OFDM transmitter (resp. receiver) schemes requires $\frac{3N}{2}\log_2(N)$ real multiplications for the IDFT (resp.DFT) and $2 \times 2W_{\text{Tx}}$ (resp.$2 \times 2W_{\text{Rx}}$) real multiplications for the windowing.

$$\text{C}_{\text{WOLA-OFDM,Tx}} = 3\frac{N}{2}\log_2(N) + 4W_{\text{Tx}} \tag{2.39}$$

$$\text{C}_{\text{WOLA-OFDM,Rx}} = 3\frac{N}{2}\log_2(N) + 4W_{\text{Rx}} \tag{2.40}$$

FBMC-OQAM

The complexity of a PPN-based FBMC-OQAM transceiver is induced by the (I)FFT with $\frac{3N}{2}\log_2(N)$ real multiplications, the filtering adding $2NK$ real multiplications and the phase shift requiring $2N$ real multiplications (because the coefficient is either real or purely imaginary). Besides, because of the OQAM scheme, two FBMC symbols must be transmitted per complex symbols.

$$\text{C}_{\text{FBMC-OQAM,Tx/Rx}} = 2\left(\frac{3N}{2}\log_2(N) + 2NK + 2N\right) \tag{2.41}$$

The FS-receiver scheme is more complex. It relies on a KN-point FFT with $\frac{3KN}{2}\log_2(KN)$ real multiplications, the point-wise filtering applied in the frequency domain with $2(2K-1)N$ real multiplications and as for the PPN scheme the $2N$ real multiplications for the phase shift.

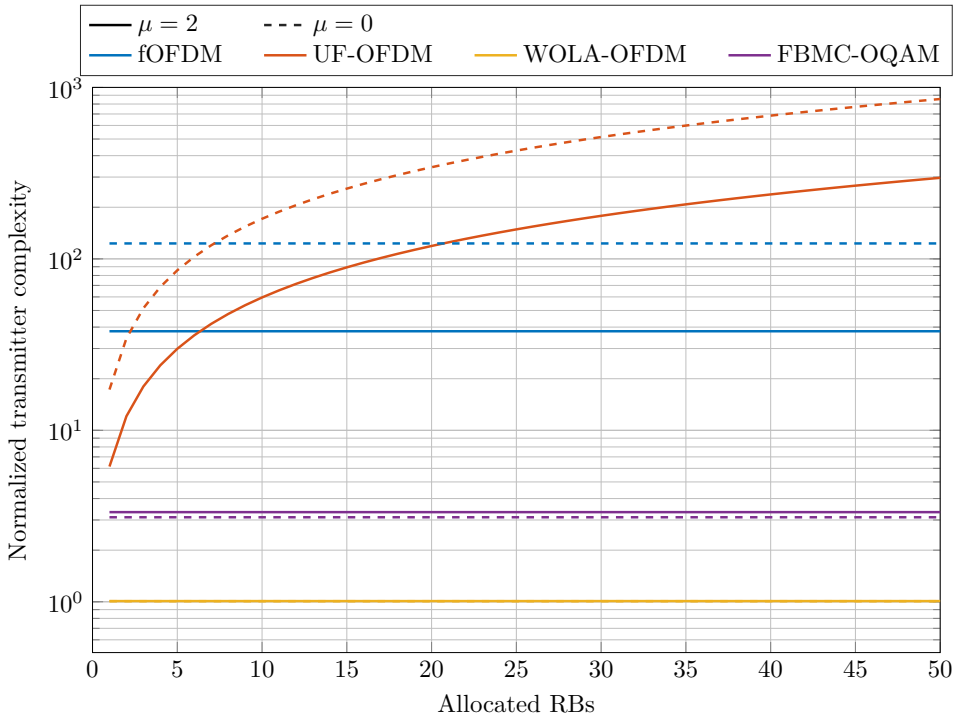

Figure 2.17: Transmitter complexity evaluation.

$$\mathrm{C}_{\mathrm{FS-FBMC-OQAM,Rx}} = 2\left(\frac{3KN}{2}\log_2(KN) + 2N(2K-1) + 2N\right) \tag{2.42}$$

Numerical evaluation

The complexity of the proposed schemes is normalized with respect to CP-OFDM. The results for the transmitter schemes are depicted in Figure 2.17 for numerologies $\mu = 0$ and $\mu = 2$.

The proposed solutions can be categorized into three different groups. The first group is composed of CP-OFDM and WOLA-OFDM and provides the most efficient implementations among the proposed waveforms. Then, FBMC-OQAM which requires a slight complexity increase ($\times 3$ w.r.t CP-OFDM). In the thirst group, there are fOFDM and UF-OFDM. Indeed, the two schemes are significantly more complex mainly because of they rely on filtering with time convolution. Nonetheless thanks to its RBs-based processing, UF-OFDM can achieve reasonable complexity increase w.r.t. CP-OFDM when only a few RBs are used.

There is not a significant difference between the two numerologies as only the most complex waveforms are impacted. Indeed, one can observe that the complexity difference w.r.t CP-OFDM increases with the number of subcarriers for fOFDM and UF-OFDM.

Results for receiver are depicted in Figure 2.18. CP-OFDM provides the least complex receiver scheme while fOFDM exhibits a significant complexity increase w.r.t. CP-OFDM because of the time convolution with its long filter impulse response. The two windowing-based receivers, WOLA-OFDM and UF-OFDM,

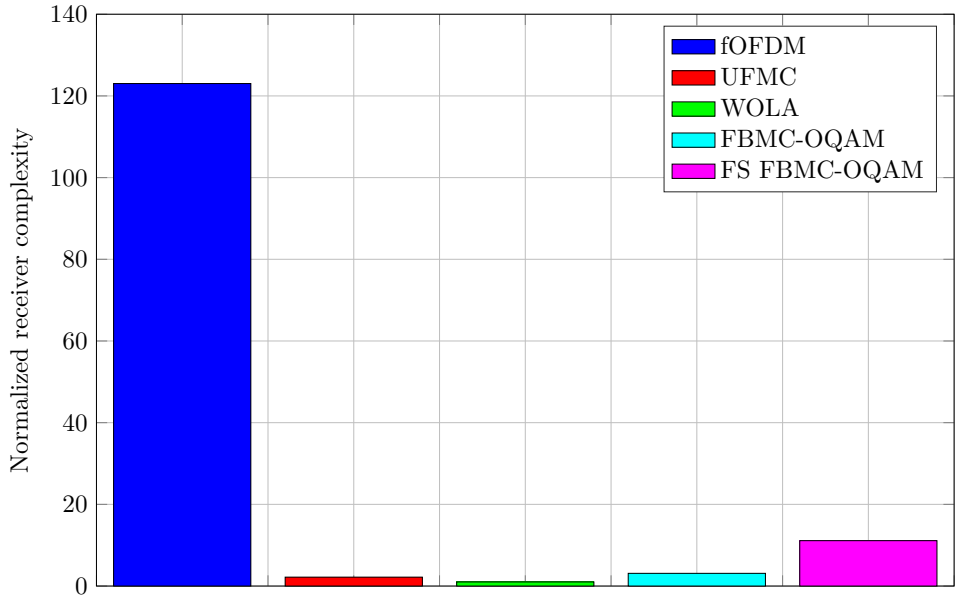

Figure 2.18: Receiver complexity evaluation.

exhibit a small complexity increase w.r.t. CP-OFDM receiver. It seems worth reminding that the UF-OFDM receiver can be implemented like a WOLA-OFDM receiver.

The two filter-bank based receivers provide a moderate complexity increase. The FS-scheme is the most complex among the two because of its higher frequency resolution.

Generally, the proposed solutions can be categorized into three different groups. The first group includes the transceivers based on filtering with time convolution (fOFDM Tx/RX and UF-OFDM Tx). Those transceivers require a large complexity increase w.r.t CP-OFDM. In a second group, the windowing-based solutions (WOLA-OFDM Tx/Rx, UF-OFDM Rx) can be brought together. They exhibit the least complex processing. Finally, there are the filter-bank solutions (FBMC-OQAM Tx/Rx) which provides in-between results.

Counting the number of multiplications and additions is a simple indicator to evaluate the complexity of a system. However, it may not reflect properly the difference at the hardware level. Some studies as [74] provide a hardware implementation comparison which is more relevant but require to have a hardware implementation of each solution.

It seems worth noticing that efficient implementations of UF-OFDM and fOFDM have been proposed in the litterature where the filtering is applied in the frequency domain like Fast-Convolution-based Filtered OFDM (FC-F-OFDM) [75].

2.5.4 Asynchronous multi-user uplink scenario

The scenario is the same as presented in Section 1.5.1 with two asynchronous users with 3 RBs each and no guard band between them. The distortion is measured at the subcarrier level to observe the distribution of the induced distortion over the band. The results are depicted in Figure 2.19.

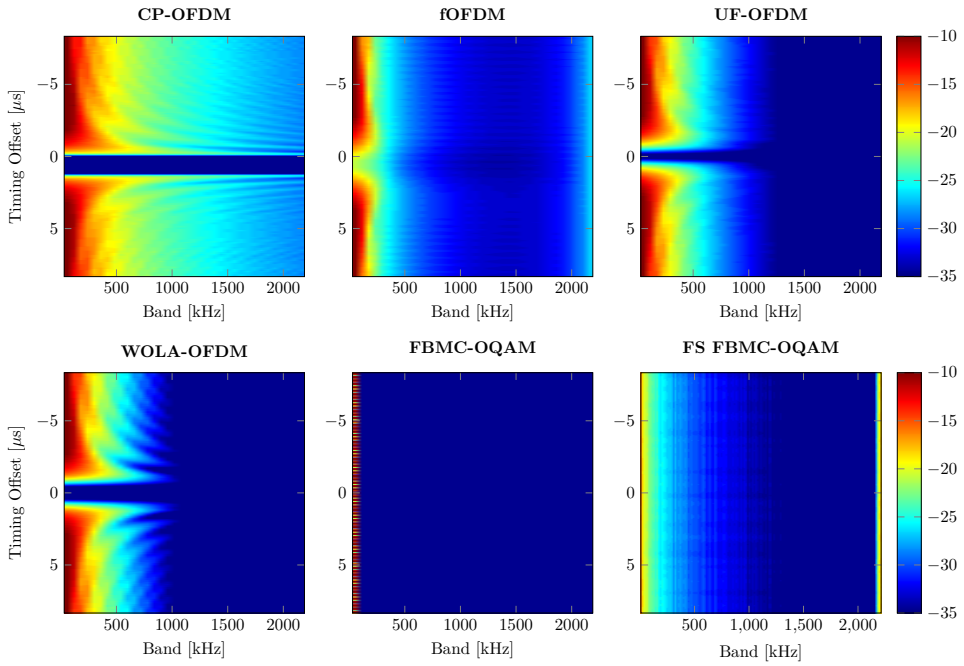

Figure 2.19: Mean Square Error per subcarrier [in dB] for multiple access schemes versus timing offsets [in μs] with no guard band.

The performance of the CP-OFDM has already been described in Section 1.5.1. fOFDM, UF-OFDM and WOLA-OFDM behave like CP-OFDM. Indeed, subcarriers just adjacent to the asynchronous user suffer from high interference power except from small timing offsets thanks to the CP or ZP for UF-OFDM. However, the three solutions are capable of fully cancel the interference induced by the relaxed synchronization for guard bands larger than 200 kHz which is a major difference with respect to legacy CP-OFDM. fOFDM provides the best interference rejection among the four solutions as a guard band of 50 kHz is enough to guarantee a MSE per subcarrier lower than -20 dB. The distortion appearing on the right side of the subband (after 500 kHz) is due to the filter and not by the scenario as discussed in Section 2.1. WOLA-OFDM and UF-OFDM exhibit similar performance by ensuring a MSE per subcarrier below -20 dB for guard band greater than 100 kHz.

The filter-bank based solutions provides better interference rejection than the four aforementioned techniques. Indeed, FBMC-OQAM with the PPN implementation is able to fully cancel the induced interference for guard band greater than a subcarrier. For the FS implementation, the distortion is evaluated at the input of the equalizer (like for the transmultiplexer response in Figure 2.10). The FS receiver appears less effective than its counterpart but it seems worth reminding than the distortion evaluation is performed prior to the receive filtering. Nonetheless, FS FBMC provides a significant interference rejection gain w.r.t to the OFDM-like waveforms for the subcarriers just adjacent to the interfering user.

In a second time, the performance will be assessed for 1) enhanced transmitters (*i.e.* transmitter schemes presented in Section 2) with a simple CP-OFDM receiver and 2) simple CP-OFDM transmitter with enhanced receivers (*i.e.* receiver schemes presented in Section 2). The goal of the study is to analyse the impact of

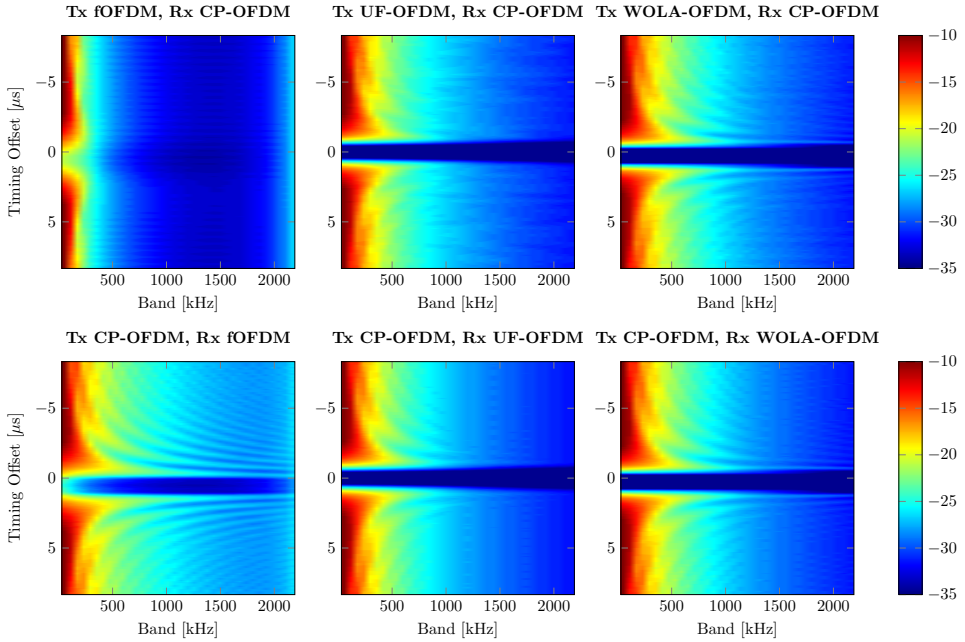

Figure 2.20: Study of performance gains depending on the proposed Tx and Rx processing schemes.

the proposed Tx and Rx processing on overall performance. Such scenario can not be applied to filter-bank based waveforms as the receiver configuration depends on the processing performed at the transmitter. The results for fODM, UF-OFDM and WOLA-OFDM are depicted in Figure 2.20.

One can observe that when one of the processing (either Tx or Rx) is not applied, the waveform robustness to timing offset is weakened. Regarding the first row, only fOFDM with only the Tx filtering provides significant performance gain and can achieve similar interference rejection level as presented in Figure 2.19. Otherwise, the performance gain w.r.t legacy CP-OFDM is limited. Indeed, even if the spectral confinement is improved, the amount of OOB emissions are still important (see Figure 2.14) which limits the performance gain.

The second row presents the results when only CP-OFDM waveform is used but with enhanced receiver schemes. The performance gains w.r.t to a simple FFT receiver are limited because of high OOB emission of CP-OFDM. However, unlike the first row, receivers performing windowing outperform the fOFDM receiver and its time convolution with a very long filter impulse response.

Co-existence between waveforms has been studied in recent literature [76]. The scenario is different as the one proposed in this thesis, as in [76] the users don't use the same waveform and receiver schemes. It has been observed that CP-OFDM and FBMC-OQAM can poorly co-exist because of the time structure of the signals are different. Even if the study scenario is different, the underlying reason is the same: the signals are dominated by OFDM-induced cardinal sine response [76, fig.3].

As a conclusion, spectrally confined waveforms can provide significant gain in terms of rejection of interference induced by timing offsets between users. The performance gain w.r.t. legacy CP-OFDM is mostly appreciable when both Tx

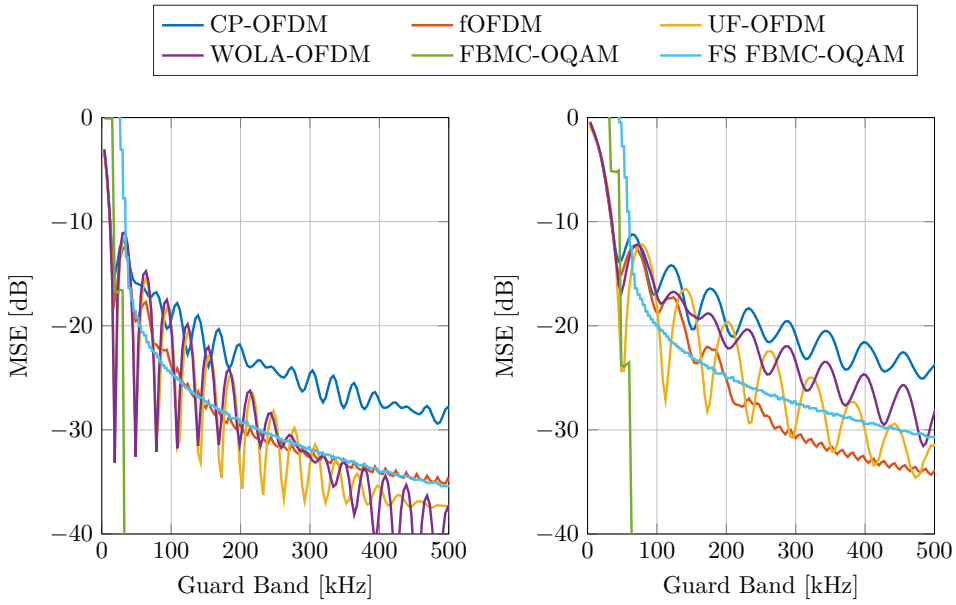

Figure 2.21: Mean Square Error per subcarrier [in dB] for multiple service schemes with $\mu = 1$ over $\mu = 0$ (left) and $\mu = 2$ over $\mu = 0$ (left) .

and Rx are applied. The enhanced interference cancellation can be used to improve the bandwidth use as guard bands between users could be shortened.

2.5.5 5G NR multi-service coexistence

The last study scenario to be considered is the multi-service co-existence as presented in Section 1.5.2. The distortion induced by 1-RB user of a different numerology is evaluated in this scenario. The cases $\mu = 1$ over $\mu = 0$ and $\mu = 2$ over $\mu = 0$ are addressed in this section. The results are depicted in Figure 2.21.

One can observe that FBMC-OQAM with its PPN receiver provides again the best performance. Indeed, a guard band of the maximum SCS among adjacent subbands (*i.e.* 30 kHz for left configuration and 60 kHz for right) is enough to completely avoid service-multiplexing induced interference. However the FS receiver does not perform as well as its counterpart.

PPN-based FBMC-OQAM aside, fOFDM and FS-based FBMC-OQAM provide the most interesting performance as they ensure −25 dB MSE per subcarrier with a guard band of 100 kHz in the left configuration and 200 kHz in the right.

WOLA-OFDM and UF-OFDM provide poor interference cancellation. Higher guard band are required to ensure −25 dB MSE per subcarrier: about 190 kHz for left configuration over 300 kHz for the right.

2.5.6 Synthesis

In this section, four solutions have been considered and compared as alternative to CP-OFDM. The considered solutions embody pragmatic processing solutions to 5G challenges. In the literature, more waveforms have been designed, studied and proposed as heir of the OFDM like Generalized Frequency Division Multiplexing [77], Lapped-OFDM [78] and many comparisons have been published [74, 79, 80,

81]. The proposed analysis in this thesis is limited to a few scenarios so as to stress the trade-off between the potential gains of the considered solutions in 5G scenarios and the penalties in channel performance and hardware implementation.

Efficiently multiplexing non-orthogonal subbands, which appears to be one of the major stakes of 5G and beyond technologies, can be ensured thanks to strong side lobe rejection techniques as noticed with fOFDM and filter-bank based waveforms. However, it seems essential to point out that spectral confinement is not the only criterion of interest and that the receiver processing matters as well [82] as observed by comparing the PPN and the FS receiver schemes for FBMC/OQAM.

Strong spectral confinement can be provided by relaxing the time localization of the transmitted signal. It can first be achieved by applying a time convolution with a long filter impulse response as proposed in fOFDM. This technique allows a flexible subband filtering as the pass band of the filter can be adapted to the allocated subband (*i.e.* user-level filtering) and it limits the energy spreading induced by the time convolution. Good robustness against fast fading induced effects (no penalty with respect to legacy CP-OFDM) is thus ensured. However, more computation resources are needed mostly to operate the time convolution which makes this solution less appealing.

It is possible to reduce the complexity induced by the time convolution by considering shorter filter impulse response. However passband flexibility can no longer be ensured and thus large subband must be processed by a bank of modulated filters of fixed passband which *in fine* requires high computation resource as well when multiple subbands are allocated.

It is also possible to consider a narrow-band shaping pulse instead of the conventional rectangular one. It can be efficiently implemented by means of a FBMC structure which exhibits a moderate complexity increase w.r.t the other considered solutions while providing excellent results in 5G scenarios. Nonetheless, it seems worth observing that the time structure of the signal significantly differs from legacy OFDM and "post-OFDM" waveforms that leads to distinct behavior in channel performance. On the one hand, as there is no cyclic prefix, the waveform is more sensitive to very short delay spreads. On the other hand, as the symbol duration is much more spread than with OFDM-like solutions, it provides an improved robustness to propagation channels with very long delay spread.

Windowing is another simple solution which provides moderate results in 5G scenarios but the most efficient implementation among the considered solutions. However, it suffers from strong ISI with channels with moderate delay spreads. It makes WOLA-OFDM poorly appealing for sub-6Ghz applications as fast fading is a strong impairment. Nonetheless, this technique is interesting for mmWave applications even if frequency localization could be improved.

2.6 Conclusion

In this chapter, four state-of-the-art solutions with enhanced spectral confined have been introduced and compared with legacy CP-OFDM. Enhanced spectral confinement provides suitable subband isolation in the frequency which is interesting for 5G applications. However it can be achieved with more complex

transceivers and weakened robustness to fast fading and mobility induced effects. It appears that FBMC/OQAM operates the best trade-off between the considered indicators. However, the reduction of the orthogonality to the real field prevents a straightforward backward compatibility with deployed technology which makes FBMC/OQAM poorly appealing for 5G. Despite, the waveform suffers from the largest performance penalty in mobility scenario because of its spread symbols.

There is still a need for sub-6GHz solution to 5G challenges. Indeed, even if the use of mmWaves can significantly improve the capacity of the network, sub-6GHz communications are still essential for 5G as low frequencies ensure a good spatial coverage and allow cost-effective radio systems. However, for sub-6 GHz communications the subband isolation can not be performed spatially because beamforming techniques are only envisioned for mmWave. That is why waveforms providing a confined spectrum are appealing for 5G sub-6 GHz applications.

FBMC/OQAM proves to be the best option for such applications regarding its performance but it is still unwanted because of the reduction of the orthogonality condition to the real field. That is why in the next chapter, alternatives to the OQAM signaling for FBMC waveform will be investigated and developed so as to design a filter-bank based waveform which demonstrates good performance results in 5G scenarios while ensuring full backward compatibility with LTE.

2.6.1 Contribution

The derivation of likelihood metrics for multiple antenna FS FBMC-OQAM systems has been published in [50]: D. Demmer, J.-B. Doré, D. Le Ruyet, and R. Gerzaguet, “Performance of soft-decision linear receivers for spatial-multiplexing FBMC/OQAM,” in *Proc. IEEE International Symposium on Wireless Communication Systems (ISWCS)*, (Poznan, Poland), pp. 404–408, 2016.

Some results related to the description and the analysis of ”post-OFDM” waveforms have been used for the WONG5 Project receiving funds from the French National Research Agency (ANR). A collaborative work giving a review of potential solutions for mMTC has been published [79]: Y. Medjahdi, S. Traverso, R. Gerzaguet, H. Shaïek, R. Zayani, D. Demmer, R. Zakaria, J.-B. Doré, M. B. Mabrouk, D. Le Ruyet, Y. Louët, and D. Roviras, “On the Road to 5G: Comparative Study of Physical Layer in MTC Context,” *IEEE Access*, vol. 5, pp. 26556–26581, 2017.

3 OFDM-based precoding for FBMC waveforms

A limitation of FBMC/OQAM is the orthogonality restricted to the real field. The intrinsic interference is difficult to cope with when transmitting over dispersive channels as pilot-based channel estimation process is not straightforward. The intrinsic interference also prevents a direct application of commonly used STBC MIMO schemes.

To alleviate this limitation, QAM-FBMC (FBMC with Quadrature Amplitude Modulations) has been proposed first in [83] and in [84, 85]. The first scheme [83] proposes to transform the two-dimensional intrinsic interference into a one-dimensional interference by alternating QAM symbols and padded symbols (and therefore preserving the same spectral efficiency). Nonetheless, the scheme suffers from performance degradation as interference terms are neglected but still distort the received signal. The second scheme [84, 85] relies on multiple filter-bank structures with a minimum of 2 filter-banks. The two filter-bank signals are ensured to be orthogonal one with the other by prototype filter design. However, residual interference among each filter-bank still exists.

The two aforementioned schemes proposed a solution to restore the complex orthogonality for filter-bank based transmission scheme. However the orthogonality is only partially ensured and intrinsic interference still impacts the transmission. In this chapter, an alternative which restores the complex orthogonality between any time/frequency position and for a unique filter-banks will be studied. The studied technique is entitled FBMC precoding. First, a solution based on Walsh-Hadamard precoding will be briefly reviewed. Then, a precoding scheme based on Fourier sequences is proposed. Two schemes based on the proposed scheme have been developed: Fast Fourier Transform FBMC (FFT-FBMC) which performs the reverse transmitter processing and Block-Filtered OFDM (BF-OFDM) which relies on a simple FFT receiver (*i.e.* a 4G/5G receiver).

3.1 CDMA-FBMC/OQAM

It has been proposed in [86] to combine FBMC/OQAM with Code Division Multiple Access (CDMA). The resulting scheme fitted with Walsh-Hadamard codes allows a complex transmission for a maximum number of users equal to half the number of possible codewords. Nonetheless, the system achieves maximal spectral efficiency [86]. The proposed scheme has then been used to combine Alamouti with

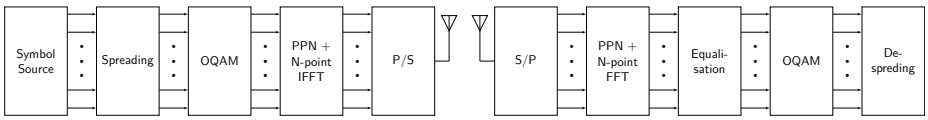

Figure 3.1: Tx and Rx CDMA FBMC/OQAM schemes.

FBMC/OQAM [87]. This same scheme has been studied in [88] where the authors consider double-dispersive channels for the channel performance estimation.

The overall Tx and Rx schemes are depicted in Figure 3.1. The schemes are similar to the FBMC/OQAM with the PPN implementation but encapsulated with the CDMA precoding (spreading stage) and decoding (despreading stage).

SIn [86] and [88], it is shown that only half of the possible CDMA sequence (Walsh-Hadamard sequences) can be used. Nonetheless the scheme achieves near full load. Indeed even if only of the sequences can be used as the scheme still relies on a FBMC/OQAM transmission the transmission rate is doubled. Consequently, the symbol density is maximized. However, a spectral density penalty occurs because the complex orthogonality is only ensured at the block level and therefore a subcarrier guard band must be considered between consecutive blocks. By considering block of 32 subcarriers as in [88], the induced spectral efficiency is limited to 3%.

As a consequence, the proposed scheme guarantees complex orthogonality for only a slight spectral efficiency penalty and channel performance over double-dispersive channels similar to CP-OFDM for the working SNR range of typical broadband communication devices [88]. On the one hand, the system is flexible as the subband can be adapted (as long as it is a power of two because of the Hadamard sequences). On the other hand, it is inflexible, as for each subband only half the possible sequences can be used and the system still requires Nyquist prototype filters.

3.2 FFT-FBMC

A possible improvement of the latter scheme is to consider a precoding scheme substituting the OQAM signaling instead of encapsulating it. Such idea has already been studied and is named Fast Fourier Transform FBMC (FFT-FBMC) [89].

First, let us recall the expression of received symbols with FBMC modulation (without OQAM signaling and phase offset) in (3.1) where A_g is the ambiguity function defined in (2.23) and Δ_p and Δ_n respectively the carrier index and time instant differences. The first term of (3.1) denotes the useful term and the second term is for the intrinsic interference.

$$y_{p_o}[n_o] = d_{p_o}[n_o]A_g(0,0) + \sum_{(p,n)\neq(p_o,n_o)} d_p[n]A_g\left(\Delta_n, \Delta_p\right) \tag{3.1}$$

In FFT-FBMC, the symbol to be processed by the filter-bank is first precoded by a IFFT stage at the transmitter side. We assume that a N_p-point IFFT is applied for each FBMC carrier. The FBMC carriers are thus assimilated to sub-

band carrying the active subcarriers of the OFDM modulator it is linked with. Therefore, the input symbol for the FBMC $d_p[n]$ can be expressed as in (3.2) where $a_{p,k}[n]$ denotes the QAM symbol transmitted over the p^{th} subband and the k^{th} subcarrier at time instant n. From now and for the rest of the work, the (I)DFT power normalisation coefficients will be omitted for sake of clarity.

$$d_p[l + nN_p] = \sum_{k=0}^{N_p-1} a_{p,k}[n] e^{j\frac{2\pi}{N_p}lk} \tag{3.2}$$

In practice, some redundancies are added to the precoded signal with the insertion of a CP of length N_{CP} and a cyclic suffix of length N_{CS} as shown in (3.3) with $N_e = N_p + N_{\text{CP}} + N_{\text{CS}}$. The purpose of the extra redundancy will be highlighted later on. The precoding stage can thus be described as a bank a cyclic prefix /cyclic suffix (CP/CS) OFDM modulators feeding the filter-bank.

$$d_p[l + nN_e] = \sum_{k=0}^{N_p-1} a_{p,k}[n] e^{j\frac{2\pi}{N_p}(l-N_{\text{CP}})k} \tag{3.3}$$

As a consequence, the output symbols coming from the analysis filter-bank are processed by N_p-point FFT.

$$r_{p,k}[n_o] = \sum_{l=0}^{N_p-1} y_p[l + N_{\text{CP}} + N_e n_o] e^{-j\frac{2\pi}{N_p}lk} \tag{3.4}$$

Because of the OFDM precoding, consecutive FBMC symbols (KN samples where K is the filter-bank overlapping factor and N the number of FBMC carriers) belong to the same precoded block as illustrated in Figure 3.2 where blue FBMC symbols represent the useful symbols, green symbol the redundancy brought by the CP/CS and red ones interfering symbols (*i.e.* adjacent symbols in time) The blocks are composed of N_e FBMC symbols.

3.2.1 Case with a unique active subband p_o

When a unique subband p_o is considered, there is no interference generated from subband multiplexing (*i.e.* sum over k in (3.1)). Therefore, the only interference comes from the symbol overlapping in the time domain operated by the filter-bank. For each FBMC symbol, the tails of the $2K-1$ symbols transmitted before and the beginning of the $2K-1$ symbols transmitted next overlap with the useful symbol as shown in line 1 of (3.6). Nonetheless if both the CP and CS added at the OFDM precoding stage are greater than $2K-1$, the beginning and tails of overlapping symbol belong to the same precoding block and thus the expression can be simplified as shown in (3.6).

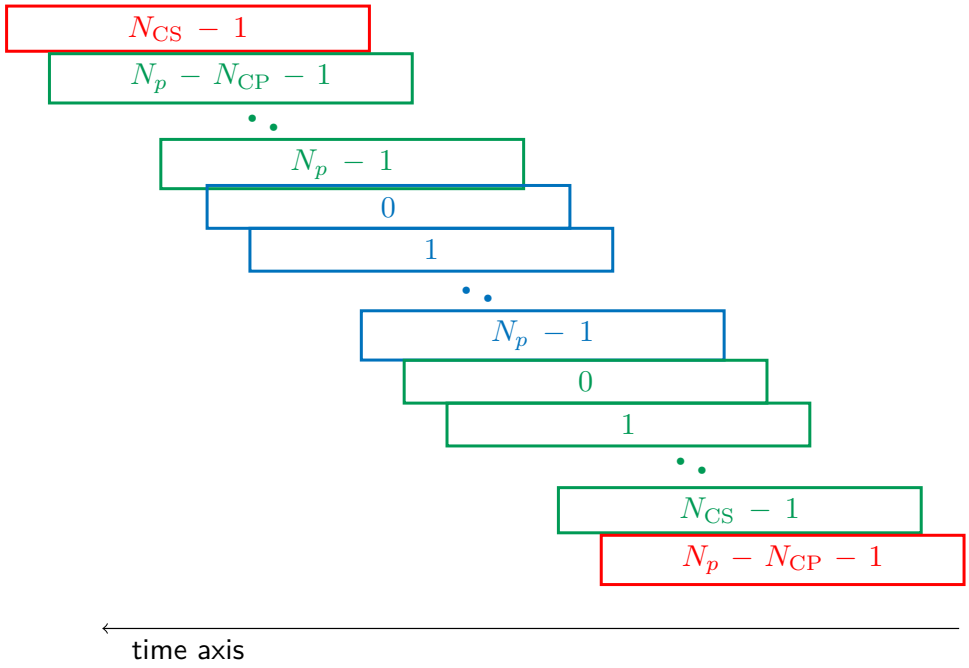

Figure 3.2: Time structure of the FFT-FBMC signal.

$$
\begin{aligned}
r_{p_o,k_o}[n_o] &= a_{p_o,k_o}[n_o] + \sum_{l=0}^{N_p-1} \sum_{\substack{i=-2K+1 \\ i\neq 0}}^{2K-1} A_g\left(i,0\right) d_p[l+i+N_{\text{CP}}+N_e n_o] e^{-j\frac{2\pi}{N_p} l k_o} \\
&= \sum_{l=0}^{N_p-1} \sum_{i=-2K+1}^{2K-1} A_g\left(i,0\right) \left(\sum_{k=0}^{N_p-1} a_{p_o,k}[n_o] e^{j\frac{2\pi}{N_p} lk} \right) e^{-j\frac{2\pi}{N_p} l k_o} \\
&= a_{p_o,k_o}[n_o] \sum_{i=-2K+1}^{2K-1} \left(\sum_{t=0}^{KN-1} g[t] g^*[t-iN/2] \right) e^{-j\frac{2\pi}{N_p} i k_o}
\end{aligned}
\tag{3.5}
$$

By letting $i' = iN/2$, one obtains:

$$
\begin{aligned}
r_{p_o,k_o}[n_o] &= a_{p_o,k_o}[n_o] \sum_{t=0}^{KN-1} g^*[t] \sum_{i'=-KN+N/2}^{KN-N/2} g[i'+t] e^{-j\frac{2\pi}{N_p N/2} i' k_o} \\
&= a_{p_o,k_o}[n_o] G^*(k_o) G(k_o) \\
&= a_{p_o,k_o}[n_o] \left| G(k_o) \right|^2
\end{aligned}
\tag{3.6}
$$

The transmitted QAM symbols $a_{p,k}$ can thus be recovered without intrinsic interference. The received symbols are affected by a coefficient $|G\left(k_o\right)|^2$ which correspond to the frequency response of the filter at the frequency $k_o/(NN_p/2)$. To ensure perfect reconstruction, there is a condition on CP and CS lengths expressed in (3.7).

$$\begin{cases} CP \geq 2K-1 \\ CS \geq 2K-1 \end{cases} \tag{3.7}$$

As a consequence, the spectral efficiency has to be penalised so as to ensure complex orthogonality according to the Balian-Low Theorem.

3.2.2 Case with multiple active subbands

In this paragraph, several active subbands are considered. The conditions on CP and CS lengths (3.7) are ensured. The expression of the received symbols for multiple active subbands is given in (3.8).

$$\begin{aligned} r_{p_o,k_o}[n_o] &= a_{p_o,k_o}[n_o]\left|G\left(k_o\right)\right|^2 \\ &+ \sum_{\Delta_p \neq 0} \sum_{l=0}^{N_p-1} \sum_{i=-2K+1}^{2K-1} A_g(i,\Delta_p) d_{p_o+\Delta_p}[l+i+N_{\mathrm{CP}}+N_e n_o] e^{-j\frac{2\pi}{N_p}lk_o} \\ &= a_{p_o,k_o}[n_o]\left|G\left(k_o\right)\right|^2 \\ &+ \sum_{\Delta_p \neq 0} a_{p_o+\Delta_p,k_o}[n_o] G^*(k_o+\Delta_p N/2) G(k_o) \end{aligned} \tag{3.8}$$

By comparing (3.8) with (3.6), one can notice the apparition of a new term. It represents the interference coming from the other subbands which powers depends on $|G^*(k_o+\Delta_p N/2)G(k_o)|$.

The precoded signal expression is given in (3.9) and the transmitted baseband signal can be expressed as in (3.10) with $N_{\mathrm{e}} = N_p + N_{\mathrm{CP}} + N_{\mathrm{CS}}$ and $g_k[m] = g[m]e^{-j\frac{2\pi}{NN_p/2}km}$.

From (3.3), we obtain:

$$\begin{aligned} d_p[i] &= \sum_n \sum_{k=0}^{N_p-1} a_{p,k}[n] \Pi_{N_{\mathrm{e}}}[i-nN_{\mathrm{e}}] e^{j\frac{2\pi}{N_p}(i-N_{\mathrm{CP}})k} \\ &= \sum_{k=0}^{N_p-1} \left(a_{p,k\uparrow N_{\mathrm{e}}} \star \Pi_{N_{\mathrm{e}}}\right)[m] e^{j\frac{2\pi}{N_p}(i-N_{\mathrm{CP}})k} \end{aligned} \tag{3.9}$$

and:

$$\begin{aligned}
s[m] &= \sum_{p=0}^{N-1} \sum_{i} d_p[i] g\left[m - iN/2\right] e^{j\frac{2\pi}{N}pm} \\
&= \sum_{p=0}^{N-1} \left((d_p)_{\uparrow N/2} \star g\right)[m] e^{j\frac{2\pi}{N}pm} \\
&= \sum_{p=0}^{N-1} \left(\left(\sum_{k=0}^{N_p-1} \left(\left(a_{(p,f)}\right)_{\uparrow N_e} \star \Pi_{\mathrm{N_e}} \right)[m] e^{j\frac{2\pi}{N_p}mk} \right)_{\uparrow N/2} \star g[m] \right) e^{j\frac{2\pi}{N}pm} \\
&= \sum_{p=0}^{N-1} \left(\left(\sum_{k=0}^{N_p-1} a_{(p,k)_{\uparrow N_\mathrm{e}}} \star \Pi_{N_\mathrm{e}}[m] \right)_{\uparrow N/2} \star g_f[m] \right) e^{j\frac{2\pi}{NN_p/2}m(pN_p/2+k)}
\end{aligned} \tag{3.10}$$

The frequency response of $\left(\left(a_{(p,k)_{\uparrow N_\mathrm{e}}} \star \Pi_{N_\mathrm{e}}\right)[m]\right)_{\uparrow N/2}$ and of $g_k[m]$ at frequency f are respectively $\sigma_a^2 \left| D_{N_p}^{N_e}(fN/2) \right|^2$ and $\left| G\left(f - \frac{k}{NN_p/2}\right) \right|^2$. The PSD expression can thus be derived from (3.10) as shown in [90]. The expression of the PSD $S(f)$ of the transmitted signal is given in (3.11).

$$S(f) = \sigma_a^2 \sum_{p=0}^{N-1} \left| G\left(f - \frac{p}{N}\right) \right|^2 \sum_{k=0}^{N_p-1} \left| D\left(fN/2 - k/N_p - p/2\right) \right|^2 \tag{3.11}$$

We assume that the prototype filter g admits a unitary roll-off, *i.e* $|G|$ has a main lobe width of $2/N$. Hence, there is an overlap between adjacent subbands leading to the interference term observed in (3.8). So as to alleviate this issue, only half the main lobe width of each subband will be used *i.e.* only $N_p/2$ subcarriers. The set of possible subcarriers is thus given in (3.12).

$$\Omega = \left\{ \left\lfloor -\frac{N_p}{4} \right\rfloor + 1, ..., \left\lfloor \frac{N_p}{4} \right\rfloor \right\} \tag{3.12}$$

Condition (3.12) prevents the overlap between consecutive subbands but does not ensure perfect complex orthogonality. Indeed, there is still interference coming from subbands with Δ_p even as $|D(fN/2 - l/N_p - k/2)|$ is N_p periodic. However this interference is highly attenuated because outside of the main lobe of the frequency response of the prototype filter.

The Signal-to-Interference Ratio (SIR) can be expressed as in (3.13) when the two aforementioned conditions are satisfied where σ_a^2 is the transmitted constellation mean energy.

$$\mathrm{SIR} = \frac{1}{N/2} \sum_{k \in \Omega} \frac{|G(k)|^4 \sigma_a^2}{\sum_{\epsilon \neq 0} \left| G^*(k + \epsilon N) G(k) \right|^2 \sigma_a^2} \tag{3.13}$$

The SIR is now evaluated for different CP/CS lengths in Figure 3.3. The system configuration is the following: $N = 16$, $N_p = 128$ and the conventional value of K used in FBMC/OQAM with a PHYDYAS prototype filter. It is a 5G

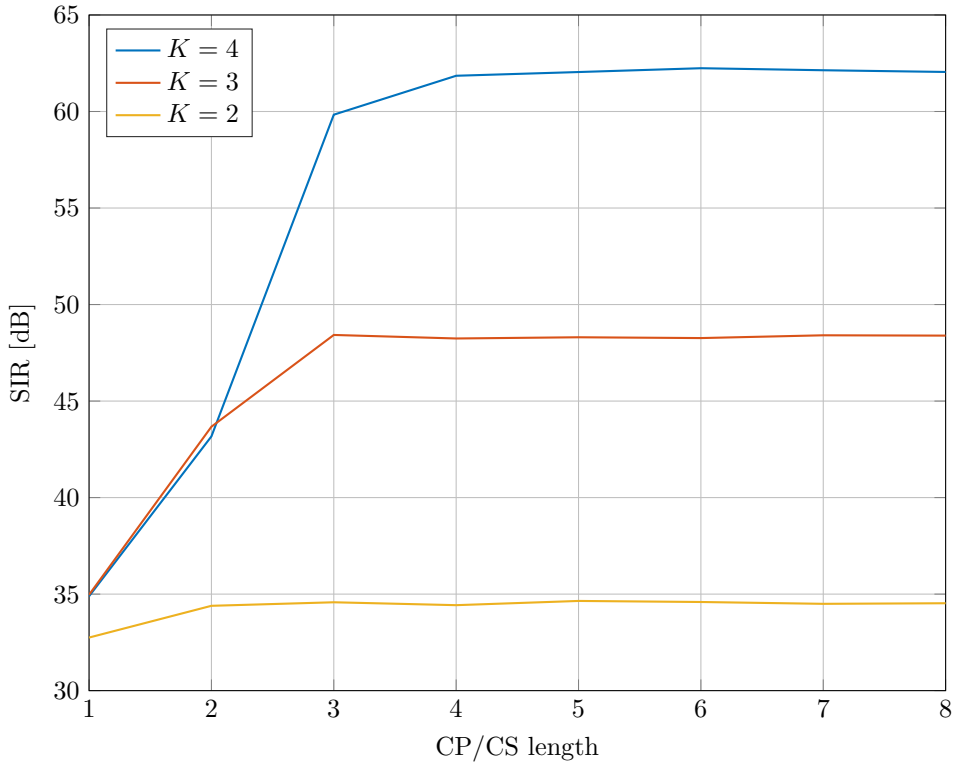

Figure 3.3: SIR evaluation for different CP/CS lengths and values of the overlapping factor K.

NR $\mu = 2$ configuration with 1024 available subcarriers. It is assumed here that the CP and the CS have both the same duration (*i.e.* symmetrical configuration). However for some values, the condition (3.7) may not be satisfied, meaning that the SIR expression (3.13) is not valid. For those values, the SIR level is estimated with numerical simulations of the systems. As a reminder, the estimation of the SIR is performed assuming an ideal channel response and a noiseless communication so as to stress on the level of intrinsic interference.

One may first observe that the value of the overlapping factor K has a significant impact on the power of the generated intrinsic interference. Indeed the higher K, the more attenuated the side lobes are which thus improves the SIR level as shown in (3.13).

Then one can also notice that not satisfying the CP/CS condition (3.7) may have a slight impact. The ideal value for the CP/CS lengths are respectively 3 for $K = 2$, 5 for $K = 3$ and 7 for $K = 4$. The SIR level starts leveling off with values just before the ideal values: 3 for $K = 3$ and 4 for $K = 4$. For those values, even if ISI is introduced because of shortened CP and CS, the power of the ISI is limited thanks to the time localization of the prototype filter.

3.2.3 Synthesis

The FFT-FBMC transmitter and receiver schemes are depicted in Figure 3.4. The OFDM subcarriers fed with 0 denote the inactive subcarriers imposed by (3.12). At the receiver side, as these subcarriers don't carry, they are not read. It seems worth reminding that there is no spectral efficiency penalty as the unused

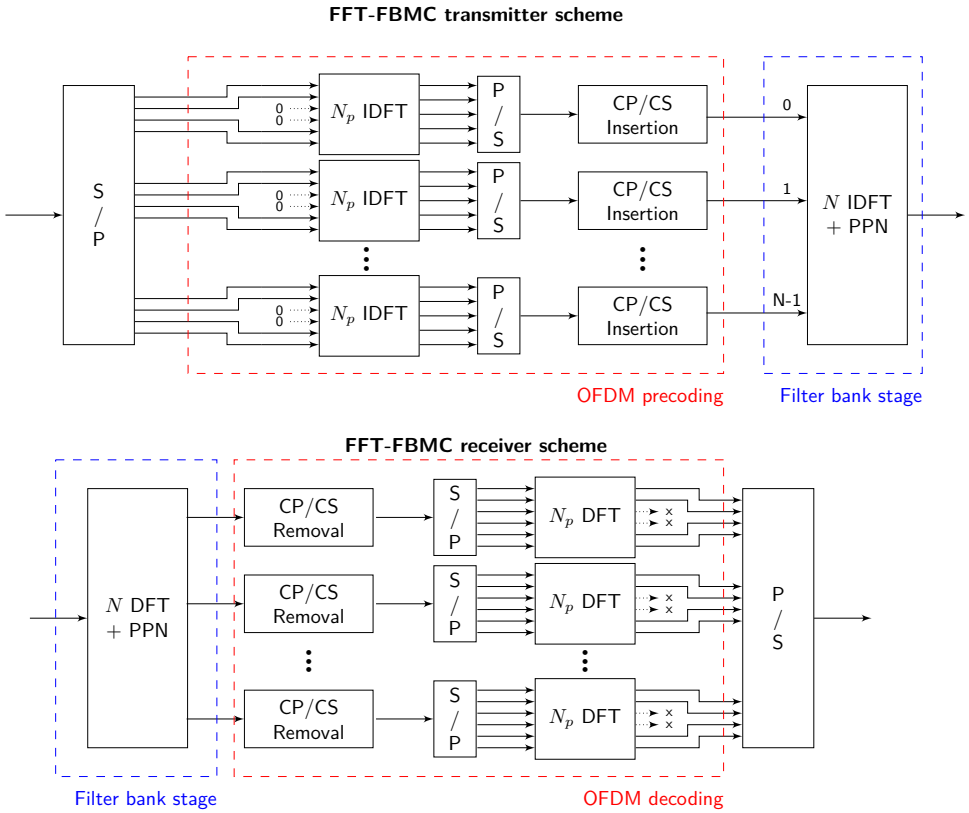

Figure 3.4: Tx and Rx FFT-FBMC scheme.

subcarriers compensate the subband overlap in the frequency domain. There is therefore no guard band between consecutive subbands.

The proposed OFDM-based precoding can ensure complex Near-Perfect Reconstruction for a FBMC waveform without OQAM signaling. However, two conditions have to be satisfied. The first condition given in (3.7) expresses the loosening of the symbol density (can be relaxed) and gives the minimum CP and CS length to prevent inter precoded blocks interference (strict condition). In [89], there is no CS and only a condition on the CP length which is doubled with respect to (3.7). The second condition is expressed in (3.12) and cancels consecutive subband overlap which prevents high-energy interference. Nonetheless, the waveform with the proposed receiver scheme is not purely complex orthogonal.

There are some similarities with CDMA-FBMC/OQAM scheme presented in the previous section. Indeed, for both schemes only half the possible sequences/subcarriers can be used. Besides, a power of two for the number of maximum sequences/subcarriers per subband is required as well (to be able to use (I)FFT-based OFDM modulators for FFT-FBMC and thus to benefit from a efficient hardware implementation). However, the spectral efficiency penalty for the FFT-FBMC is more critical as the symbol density must be relaxed to ensure complex NPR. Nonetheless, FFT-FBMC gains more design flexibility. First of all, there is no need to double the transmission rate as there is no longer OQAM signaling. Besides, there is no need of a Nyquist prototype filter (so far PHYDYAS filters are used but non-Nyquist filters will be studied later on). In a first time, the impact of the rate factor will be studied in the next section.

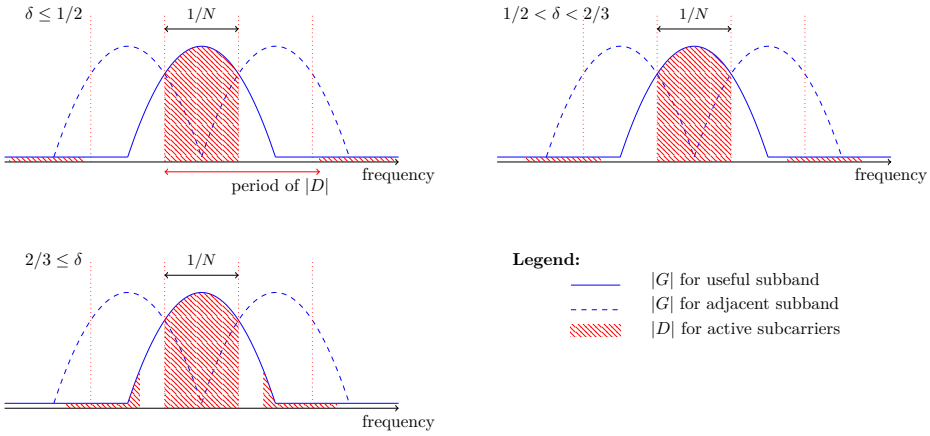

Figure 3.5: Interference distribution depending on the rate factor δ.

3.3 FFT-FBMC with a flexible rate factor of δ

In the previous section, the conventional narrowband signal rate of $2/N$ was considered. In FBMC/OQAM, it aims at compensating the rate penalty induced by the OQAM signaling. However in FFT-FBMC, there is no longer OQAM signaling and therefore no need for this specific rate factor. A generalized description of the FFT-FBMC with a narrowband signal rate of $1/(\delta N)$ is provided in this section. The following results are based on a collaborative work [91].

The baseband transmitted signal can thus be expressed as follows.

$$s[m] = \sum_{p=0}^{N-1} \left(\left(\sum_{k\in\Omega} a_{(p,k)_{\uparrow N_e}} \star \Pi_{N_e}[m] \right)_{\uparrow N\delta} \star g_f[m] \right) e^{j\frac{2\pi}{NN_p\delta}m(pN_p\delta+k)} \tag{3.14}$$

The PSD expression given in (3.11) can thus be generalised as in (3.15).

$$S(f) = \sigma_a^2 \sum_{p=0}^{N-1} \left| G\left(f - \frac{p}{N}\right) \right|^2 \sum_{k=0}^{N_p-1} \left| D\left(fN\delta - k/N_p - p\delta\right) \right|^2 \tag{3.15}$$

We may now distinguish three cases as presented below and illustrated with Figure 3.5.

- $\delta \leq 1/2$: the period $1/(\delta N)$ of $|D(fN\delta - k/N_p - p\delta)|$ is larger than the total main lobe width of $G(f)$ *i.e.* $2/N$. In the available main lobe width, *i.e.* $1/N$, we can activate at most $N_p\delta$ subcarriers $k \in \left\{ -\left\lfloor \frac{N_p\delta}{2} \right\rfloor + 1, ..., \left\lfloor \frac{N_p\delta}{2} \right\rfloor \right\}$. It is worth noticing that for this case, overlap with adjacent subbands is completely avoided.
- $1/2 < \delta < 2/3$: the period $1/(\delta N)$ of $|D(fN\delta - k/N_p - p\delta)|$ is larger than the available main lobe width of $G(f)$ and larger than $3/(2N)$ which corresponds to the distance between the furthest subcarrier and the cut-off frequency of the prototype filter. In the available main lobe width, we can still activate at most $N_p\delta$ subcarriers $k \in \left\{ -\left\lfloor \frac{N_p\delta}{2} \right\rfloor + 1, ..., \left\lfloor \frac{N_p\delta}{2} \right\rfloor \right\}$. However, limited-energy overlap between adjacent subbands occur.

- $2/3 \leq \delta$: the period of $|D(fN\delta - k/N - p\delta)|$ is smaller than $3/(2N)$. The inter-subband orthogonality can not be guaranteed because of high-energy overlap between adjacent subbands. The waveform then can not guarantee complex NPR. This case is not considered for the rest of the study.

As a consequence, the set of possible subcarriers preventing high energy ICI is given in (3.16).

$$\Omega = \left\{ \left\lfloor -\frac{N_p\delta}{2} \right\rfloor + 1, ..., \left\lfloor \frac{N_p\delta}{2} \right\rfloor \right\} \tag{3.16}$$

From now and for the rest of the manuscript, it is assumed that $N_p\delta \in \mathbb{N}$. It ensures that there is no loss of spectral efficiency induced by the floor operator in (3.16). As N_p is assumed to be a power of 2, $N_p = 2^{n_p}$ with $n_p \in \mathbb{N}$, $\delta = 1/2^\beta$ with $\beta \in \mathbb{N}$ and $\beta < n_p$.

FBMC symbols are now transmitted every $N\delta$ samples, it changes the number of overlapped symbols. Indeed now a useful FBMC symbol overlaps with the tails of the $\frac{K}{\delta} - 1$ previously transmitted symbols and the beginning of the $\frac{K}{\delta} - 1$ next symbols. The CP/CS condition given in (3.7) can be generalized as in (3.17).

$$\begin{cases} CP \geq \frac{K}{\delta} - 1 \\ CS \geq \frac{K}{\delta} - 1 \end{cases} \tag{3.17}$$

The SIR expression given in (3.13) can be generalised as well as shown below with $G(k)$ the frequency response of the prototype filter at frequency $k/(NN_p\delta)$:

$$\text{SIR} = \frac{1}{N_p\delta} \sum_{k\in\Omega} \frac{|G(k)|^4}{\sum_{\epsilon\neq 0} |G^*(k+\epsilon N)G(k)|^2} \tag{3.18}$$

As in the previous section, the SIR level will be evaluated for different values of the rate factor δ. The system configuration is the same with 1024 maximum subcarriers. However, as the rate factor changes, the number of subbands N is adapted to get 1024 subcarriers, *i.e* $N = 1024/(N_p\delta)$ with $N_p = 128$. The overlapping factor is fixed to 4 and the prototype filter is the PHYDYAS filter.

Decreasing the rate factor δ helps improving the achievable SIR. Indeed, decreasing the rate factor pushes the generated interference into further side lobes as shown in Figure 3.5 and is then more attenuated.

As a reminder, the CP/CS lengths do not directly represented the CP/CS length at the transmitted signal level. Indeed, the CP/CS are generated at the precoding stage and are therefore spread in time by the filter bank. We can define the effective CP (respectively CS) length by $N_{\text{CP}}N\delta$ (respectively $N_{\text{CS}}N\delta$). Therefore, for the three configurations studied in Figure 3.6, the effective CP and CS lengths remain the same. One can observe that changing the rate factor δ gives more flexibility as it is possible to reach higher SIR level even when the CP/CS condition is not satisfied.

The introduction of this new rate factor parameter δ gives more flexibility to the waveform design. Indeed, the number of possible subcarriers per subband is

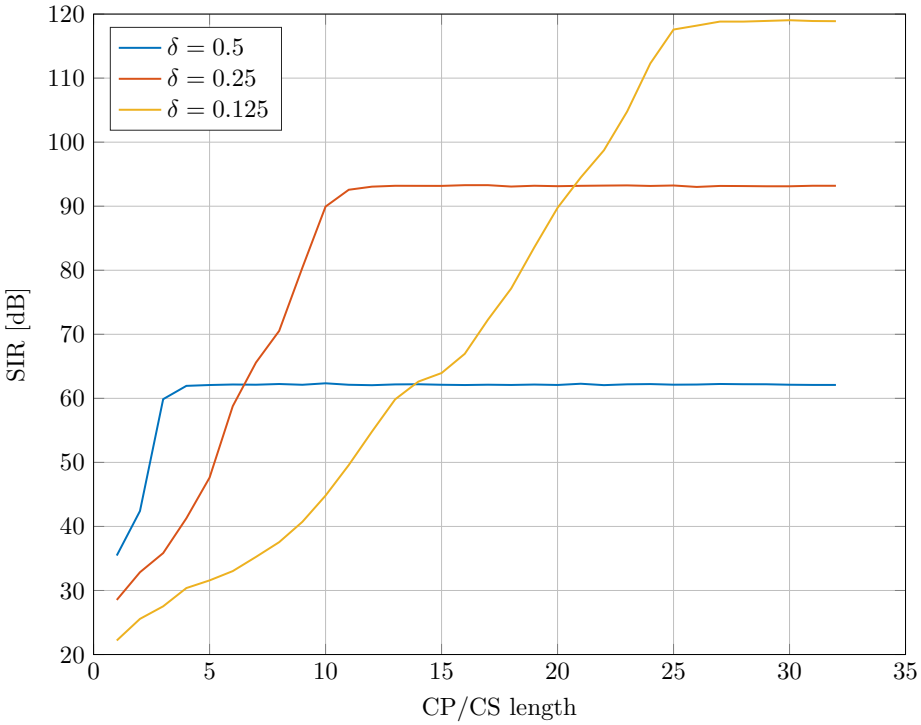

Figure 3.6: SIR evaluation for different CP/CS lengths and rate factor values.

no longer fixed to half the number of subcarriers but depends on δ. However, it has been observed that it is not possible to find a configuration where all the subcarriers can be used as $\delta \leq 2/3$.

The maximum number of subcarrier with this definition is $NN_p\delta$ where N corresponds to the number of subbands (*i.e.* FBMC carriers) and $N_p\delta$ the number of subcarriers per subband. Therefore, δ provides the possibility to balance the number of subbands and the number of subcarriers per subband with respect to the maximum number of subcarriers of the system.

3.4 BF-OFDM

In FFT-FBMC, the receiver performs the matched Tx processing. However, given that all the subcarriers are equally spaced in the frequency domain by a SCS of $\frac{1}{NN_p\delta}$, it is possible to rely on a simple $NN_p\delta$-point FFT receiver, similar to an OFDM receiver, to demodulate the signal. We propose then a new scheme named Block-Filtered OFDM (BF-OFDM)[92, 91]. The resulting Tx and Rx schemes are depicted in Figure 3.7.

Let $X[l, b]$ expressed the l^{th} sample of the $(b + N_{\text{CP}})^{\text{th}}$ FBMC symbol of the ${n_o}^{\text{th}}$ BF-OFDM transmitted symbol as defined in (3.19).

$$X_{n_o}[l, b] = g[l] \sum_{p=0}^{N-1} d_p[b + N_{\text{CP}} + n_o N_e] e^{j\frac{2\pi}{N}pl} \tag{3.19}$$

The FFT is synchronized with the beginning of the useful symbol. By applying

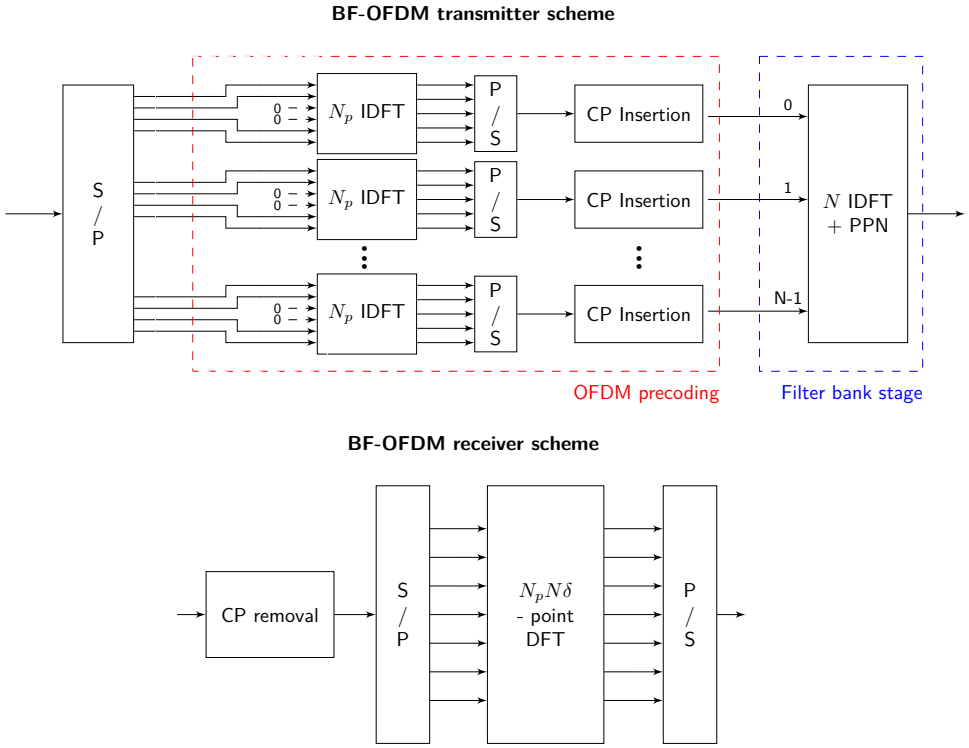

Figure 3.7: Tx and Rx BF-OFDM schemes.

the $NN_p\delta$-point FFT, several FBMC symbols are captured. Some of them are captured entirely (all their samples), for some of them just the tail is captured and for the remaining ones only the beginning. The $(b+N_{\text{CP}})^{\text{th}}$ FBMC symbol is entirely captured if

$$bN\delta + KN \leq NN_p\delta \tag{3.20}$$

Therefore by assuming from now that $K/\delta \in \mathbb{N}$, the number of entirely received symbols N_1 is

$$N_1 = N - \frac{K}{\delta} \tag{3.21}$$

The received symbol at frequency f_o and time instant n_o can thus be expressed as in (3.22).

$$\begin{aligned} r_{f_o}[n_o] &= \sum_{l=0}^{NN_p\delta-1} s[l + N_{\text{CP}}N\delta + n_oN\delta N_e]e^{-j\frac{2\pi}{MN\delta}lf_o} \\ &= \sum_{b=0}^{N_1-1}\sum_{l=0}^{KN-1} X_{n_o}[l,b]e^{-j\frac{2\pi}{NN_p\delta}(l-bN_p\delta)f_o} \\ &+ \sum_{b=-1}^{-K/\delta}\sum_{l=-bN\delta}^{KN-1} X_{n_o}[l,b]e^{-j\frac{2\pi}{NN_p\delta}(l-bN_p\delta)f_o} \\ &+ \sum_{b=N_1}^{N_1+K/\delta-1}\sum_{l=0}^{KN-(b-N_1+1)N\delta-1} X_{n_o}[l,b]e^{-j\frac{2\pi}{NN_p\delta}(l-bN_p\delta)f_o} \end{aligned} \tag{3.22}$$

It seems worth noticing that given that $N_1 + K\delta - 1 = N_p - 1$, only FBMC

symbols belonging to the $n_o{}^{\text{th}}$ transmitted BF-OFDM symbol are captured. There is not ISI coming from the following symbol.

However, if $N_{\text{CP}} \geq K/\delta - 1$ the following equation holds:

$$\forall b \in [-1, -K/\delta + 1], \quad X[l,b] = X[l, b+N_p] \tag{3.23}$$

By assuming the latter hypothesis, the expression (3.22) can be simplified:

$$\begin{aligned} r_{f_o}[n_o] = & \sum_{b=0}^{N_1-1} \sum_{l=0}^{KN-1} X_{n_o}[l,b] e^{-j\frac{2\pi}{NN_p\delta}(l-bN_p\delta)f_o} \\ & + \sum_{\substack{b'=N_p-K\delta \\ b'=b+N_p}}^{N_p-1} \sum_{l=-(b'-N_p)N\delta}^{KN-1} X_{n_o}[l,b'] e^{-j\frac{2\pi}{NN_p\delta}(l-b'N_p\delta)f_o} \\ & + \sum_{b=N_p-K\delta}^{N_p-1} \sum_{l=0}^{(N_p-b)N\delta-1} X[l,b] e^{-j\frac{2\pi}{NN_p\delta}(l-bN_p\delta)f_o} \\ & = \sum_{b=0}^{N_p-1} \sum_{l=0}^{KN-1} X_{n_o}[l,b] e^{-j\frac{2\pi}{NN_p\delta}(l-bN_p\delta)f_o} \end{aligned} \tag{3.24}$$

It implies that if (3.25) is satisfied, there is no ISI. This condition is highly similar to the CP/CS condition for FFT-FBMC given in (3.17). Besides, one can observe that the condition on the CP length is the same as it only depends on the number of overlapping FBMC symbol in time. However, for BF-OFDM with the FFT receiver, there is no need of a CS, therefore the symbol density in ideal condition is improved with respect to FFT-FBMC.

$$N_{\text{CP}} \geq \frac{K}{\delta} - 1 \tag{3.25}$$

As the transmitted signal is highly similar to the FFT-FBMC signal (there is no CS for BF-OFDM), the frequency response of the two signals is the same and corresponds to the one given in (3.15). As a consequence, the rule to avoid high-energy ICI given for FFT-FBMC (3.16) holds as well for BF-OFDM.

The conditions on CP length (3.25) and subcarrier allocation (3.16) are assumed to be satisfied for the rest of the study. It implies that a TX frequency tone f_o can be decomposed as shown in (3.26) with p_o the subband index and k_o the subcarrier index satisfying (3.16).

$$f_o = k_o + p_o N_p \delta \tag{3.26}$$

We can therefore express the demodulated symbol as follows:

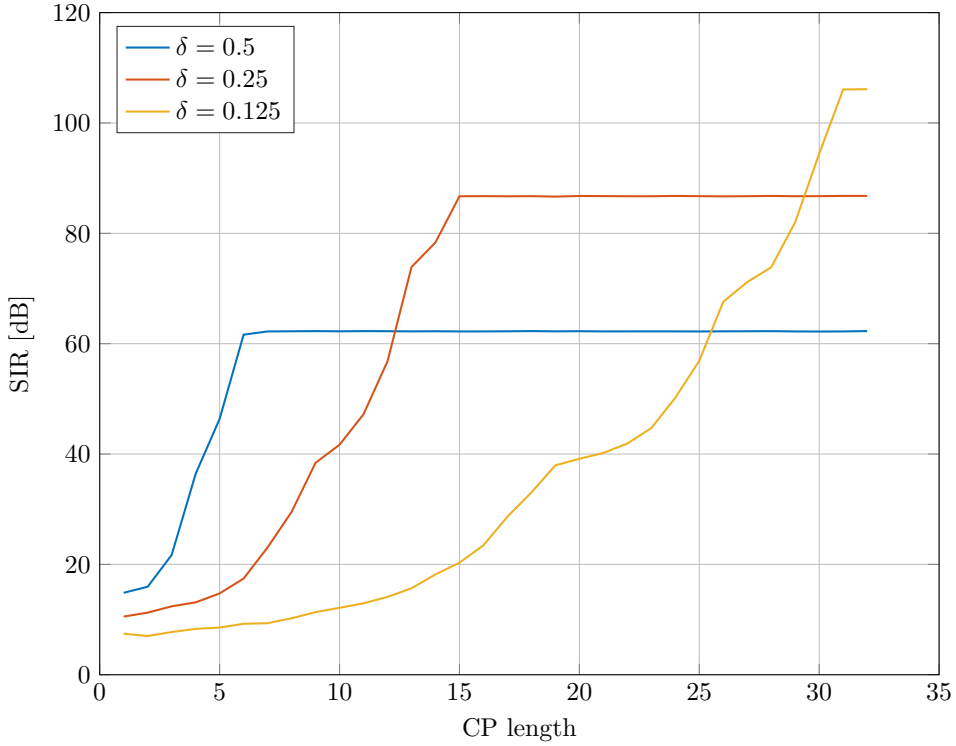

Figure 3.8: SIR evaluation for different CP lengths.

$$
\begin{aligned}
r_{k_o+p_oN_p\delta}[n_o] &= \sum_{l=0}^{KN-1} g[l] \sum_{p=0}^{N-1} a_{p,k_o}[n_o] e^{j\frac{2\pi}{N}pl} e^{-j\frac{2\pi}{NN_p\delta}l(k_o+p_oN_p\delta)} \\
&= a_{p_o,k_o}[n_o] G\left(k_o\right) + \sum_{\Delta_p \neq 0} a_{p_o+\Delta_p,k_o}[n_o] G\left(k_o + \Delta_p N_p \delta\right) \qquad (3.27)
\end{aligned}
$$

As in FFT-FBMC, an interference term appears even when the conditions (3.25) and (3.16) are satisfied. This intrinsic interference is generated by the OFDM precoding and can not be avoided.

We can nonetheless observe some significant differences between BF-OFDM and FFT-FBMC. First of all, as noticed in (3.25) there is no need of a CS for BF-OFDM which may improve the symbol density of the waveform. Then, the distortion induced by the prototype filter is different. The corresponding coefficient is the frequency filter response for BF-OFDM and its squared modulus for FFT-FBMC. The difference lies in the possible presence of a Rx filtering. For BF-OFDM, the SIR expression is thus slightly different and is given in (3.28).

$$
\text{SIR} = \frac{1}{N_p\delta} \sum_{k\in\Omega} \frac{|G(k)|^2}{\sum_{\Delta_p\neq 0} |G(k+\Delta_p N_p\delta)|^2} \qquad (3.28)
$$

The SIR evaluation is provided in Figure 3.8. The system configuration is the same as for FFT-FBMC with 1024 maximum subcarriers and $N_p = 128$. The overlapping factor is fixed to 4 and the prototype filter is the PHYDYAS filter.

One can observe that the maximum level of SIR corresponds to the one we obtained with FFT-FBMC (see Figure 3.6). However, shortened CP has a higher on SIR level because of the absence of receiver filtering.

It means that complex NPR can be ensured even with a simple FFT receiver without matched filtering. BF-OFDM provides the filtering capacity of the FFT-FBMC at the transmitter side but with a simple CP-OFDM receiver. This property is interesting especially for backward compatibility for OFDM-based system as 5G NR. Inded, it means that a BF-OFDM signal can be demodulated by a simple 5G NR receiver if the waveform numerology matches. However so as to provide good performance results in 5G typical scenarios, receiver windowing may be considered for BF-OFDM receiver.

3.5 Prototype Filter design

In FBMC/OQAM, PHYDYAS and IOTA prototype filters are commonly used. They are two low-pass filters with linear phase which satisfy the Nyquist criterion [41].

The SIR level can be evaluated for the two aforementionned prototype filters as explained in the previous section. We assume that the conditions on CP/CS lengths (3.17) and (3.25) are satisfied for both FFT-FBMC and BF-OFDM. A waveform configuration similar to the 5G NR $\mu = 2$ numerology with 1024 subcarriers is considered with:

- number of subbands: $N = 32$
- size of precoding OFDM blocks: $N_p = 128$
- rate factor: $\delta = 0.25$
- FBMC overlapping factor $K = 4$

The results of the SIR evaluation is given in Table 3.1. One can observe that the two prototype filters provide different SIR levels. Indeed, while the PHYDYAS filter ensures an excellent intrinsic interference rejection, the IOTA filter is less performant because of its relaxed stop band attenuation.

Table 3.1: SIR level obtained for typical FBMC/OQAM prototype filters with optimal CP/CS lengths.

	FFT-FBMC	BF-OFDM
Phydyas	≥ 250 dB	≥ 250 dB
IOTA	59.2 dB	66.6 dB

For FBMC-OQAM, the prototype filter has to satisfy the Nyquist criterion (*i.e.* meaning that $A_g(\Delta_n, \Delta_p) = 0$ for $\Delta_n + \Delta_p$ even). For FFT-FBMC and BF-OFDM, there is no need to satisfy this constraint according to the relations derived in previous paragraphs. Therefore, it is proposed now to consider non-Nyquist filter pulse and to optimise them on the SIR level. This prototype filter design method is detailled is the following paragraph.

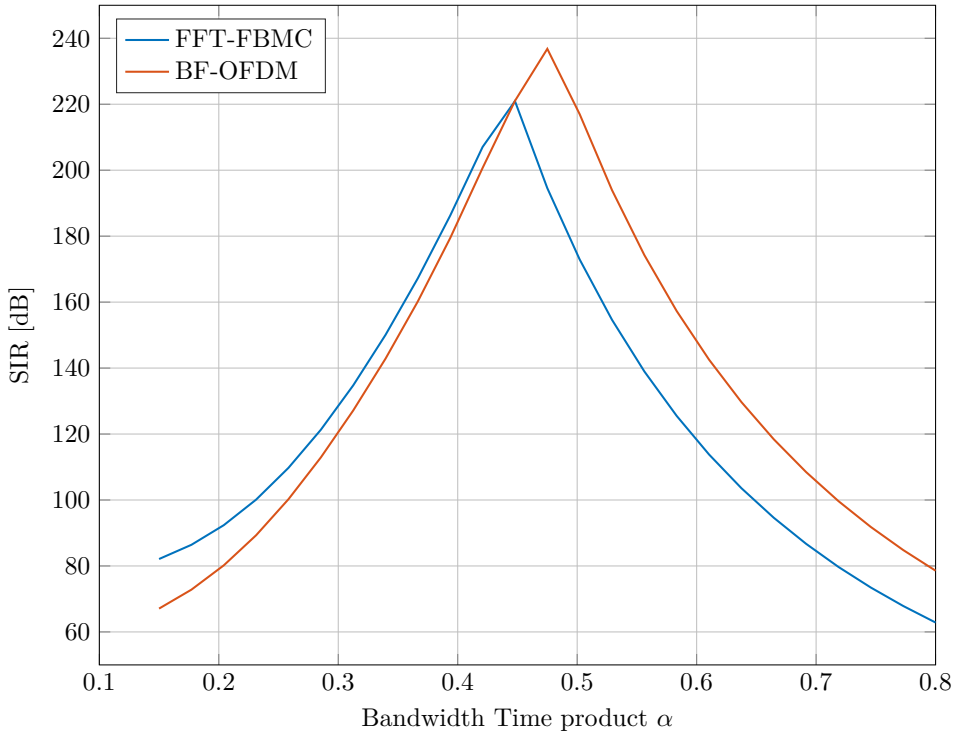

Figure 3.9: Prototype filter optimisation with Gaussian pulse for FFT-FBMC and BF-OFDM with ideal CP/CS lengths.

3.5.1 Optimisation on the intrinsic interference level

Considering non-Nyquist filter pulse gives more degrees of freedom in the filter design process. The filter pulses can thus designed to optimize some indicators such as the SIR level as proposed in [93] for BF-OFDM with $\delta = 1/2$ and applied on the generalized description of both FFT-FBMC and BF-OFDM in [91]. This method is described below.

Gaussian pulses will be thus considered as IOTA is a specific Gaussian pulse. Gaussian filters [24] are filters well localized in both time and frequency domains. The trade-off between the time and frequency localization is expressed by the Bandwidth-Time (BT) product α. The expression of the impulse response is given in (3.29).

$$g(t) = \alpha \sqrt{\frac{2\pi}{\ln(2)}} e^{-\left(\frac{\alpha\pi}{\sqrt{\ln(2)/2}}\right)^2} \tag{3.29}$$

For illustration, the optimization process for the Gaussian filter pulse is depicted in Figure 3.9 for both FFT-FBMC and BF-OFDM.

One can first observe that the two transmission schemes behave in a similar way. Indeed, they reach similar SIR level at a given BT α even if FFT-FBMC slightly outperforms BF-OFDM for $\alpha \leq 0.45$ and vice versa.

Besides, the effects of the trade-off between time and frequency localization on the intrinsic interference rejection can be analyzed. Indeed, when the Gaussian filter pulse is well localized in the frequency domain (low values of α), it

helps rejecting the intrinsic interference (thanks to its high stop band attenuation). However if the time localized is too relaxed, truncation-induced effects occur which weakens the intrinsic interference rejection. The optimal value of the BT parameter for the proposed configuration is thus $\alpha = 0.450$ for FFT-FBMC and $\alpha = 0.478$ for BF-OFDM which both provide a SIR level greater than 220 dB. However, for all the considered values of the BT parameter α, a SIR greater than 60 dB is achieved which guarantees NPR in the complex field.

We can therefore state that considering generalized filter pulses helps improving the intrinsic interference rejection of the two studied schemes. Indeed, the extra degrees of freedom can be use to perform an optimisation on the criterion of interest.

The proposed prototype design method can be adapted to any filter pulse. However, pulses that are defined by a small set of parameters (such as Gaussian pulses) are preferred to ease the optimisation process.

Besides, the proposed method may provide significant performance gain (depending on the waveform configuration), but satisfying the CP/CS length conditions (3.17) and (3.25) is not interesting at the system level (limited symbol density). The method will be therefore adapted to configurations with shortened CP/CS lengths in the next paragraph.

3.5.2 Shortened CP/CS

The waveform configurations considered in the previous paragraphs lead to a symbol density of 80.5% for FFT-FBMC and 89.5% for BF-OFDM. The obtained levels of symbol densities are lower in 5G NR (*i.e.* 93.4%). That is why, another configuration with shortened CP/CS will be considered to be able to satisfy the 5G NR spectral efficiency. Satisfying the 5G NR symbol density, brings the CP and CS lengths from 15 to 4.5 for FFT-FBMC and the CP length from 15 to 9 for BF-OFDM for the considered configurations.

However with shortened CP/CS, ISI coming from adjacent symbols in time occurs. As for WOLA-OFDM, the receiver demodulates the center part of the transmitted symbol to minimize the impact of ISI. For FFT-FBMC, it is already the case with the given definition as there are a CP and CS (therefore the useful symbol is centered with respect to the transmitted symbol). As the CP and CS lengths must be integers, we will consider a CP of 5 and a CS of 4 to have an average length of 4.5 as required. The useful symbol is assumed to be well centered even with the asymmetry CP/CS. When it comes to the BF-OFDM, the RX FFT will be shifted in time. A transmitted symbol is $KN + N\delta(N_e - 1)$ sample long. Therefore the shift in time can be expressed as follows [93]:

$$\begin{aligned} \Delta &= 0.5\left(KN + N\delta(N_e - 1) - NN_p\delta\right) \\ &= \frac{KN}{2} + N\delta\frac{N_{\text{CP}} - 1}{2} \end{aligned} \tag{3.30}$$

A phase offset is applied to compensate the shift in time:

$$\begin{aligned}\Theta &= -N\delta N_{\mathrm{CP}} + \frac{KN}{2} + N\delta\frac{N_{\mathrm{CP}}-1}{2} \\ &= \frac{KN}{2} - N\delta\frac{N_{\mathrm{CP}}+1}{2}\end{aligned} \tag{3.31}$$

The SIR for shortened CP/CS configurations and optimised BF-OFDM receiver is evaluated in Table 3.2.

Table 3.2: SIR level obtained for typical FBMC/OQAM with shortened CP/CS lengths.

	FFT-FBMC	BF-OFDM
IOTA	52.2 dB	59.8 dB
Phydyas	43.0 dB	53.8 dB

As first observation, not satisfying the conditions on CP and CS lengths worsen the intrinsic interference rejection as already observed in Figures 3.6 and 3.8. PHYDYAS pulse provides an interference rejection worst than the IOTA filter. The IOTA filter pulse is indeed more confined in the time domain than the PHYDYAS pulse as it can be observed with the transmultiplexer response comparison depicted in Figure 2.10.

The optimisation process will therefore be applied to this configuration by considering as well the FS pulses to improve the level of interference rejection of the PHYDYAS filter.

Considering FS filters is interesting as the number of degrees of freedom is higher than for Gaussian pulses. Indeed for FBMC/OQAM, the Nyquist constraint implies relations between the frequency coefficients G_k of FS prototype filters as shown in Appendix A. The FS coefficients are therefore all determined for $K = \{2, 3\}$ and there is only one degree of freedom with $K = 4$ (which is determined with an optimization on the stop band level for the PHYDYAS pulse[42]). For the two OFDM-precoded FBMC waveforms, there are always $K - 1$ degrees of freedom (assuming that $G_0 = 1$). The expression of the impulse response of a FS filter pulse is given in (2.25) and reminded below.

$$g[n] = \left(G_0 + 2\sum_{k=1}^{K-1}(-1)^k G_k \cos\left(\frac{2\pi}{KN}kn\right)\right)$$

The SIR for shortened CP/CS configurations for generalised filter pulses is evaluated in Table 3.3 with the corresponding filter parameters: BT α for the Gaussian filter and the frequency coefficients (G_1, G_2, G_3) for the FS filter.

The achievable SIR levels are lower than the ones obtained in the previous paragraph because of the induced ISI. By the way, one can observe that the optimised filter has an improved time localisation with respect to the previous case (*i.e.* BT parameter has increased) so as to limit ISI-induced power. Besides, BF-OFDM achieves better SIR level than FFT-FBMC. Indeed, BF-OFDM is closer to its ideal CP length which explains its better interference rejection. It is the reason

Table 3.3: SIR level obtained after optimisation of the prototype filters with shortened CP/CS lengths.

	FFT-FBMC	BF-OFDM
Gaussian	102.2 dB ($\alpha = 0.627$)	153.1 dB ($\alpha = 0.582$)
FS	54.4 dB $(0.876, 0.564, 0.218)$	81.3 dB $(0.794, 0.378, 0.084)$

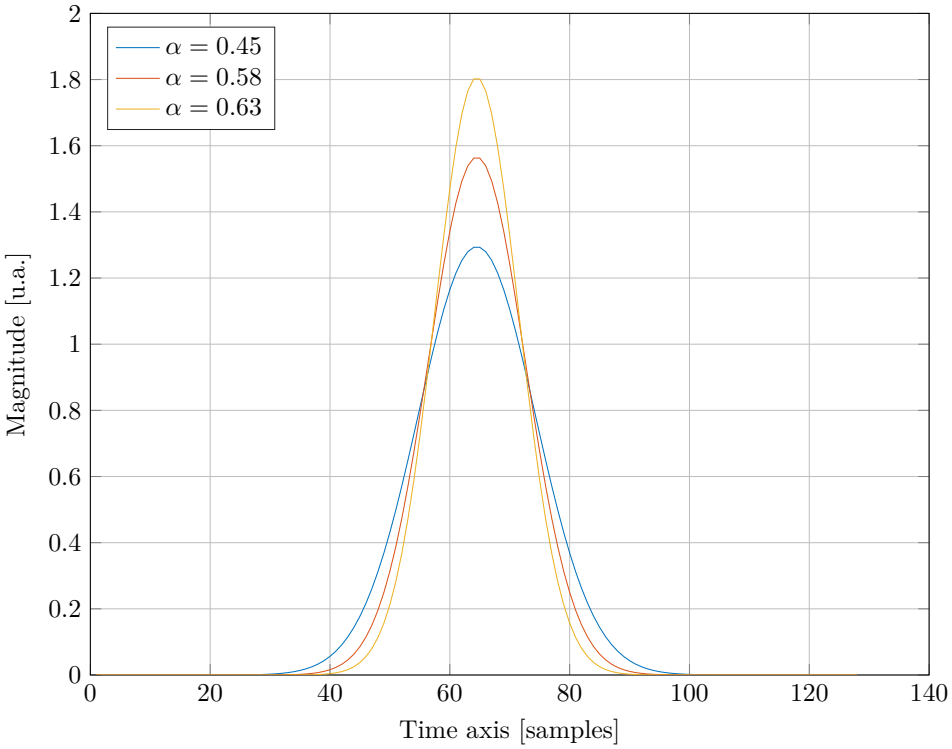

Figure 3.10: Impulse responses of the optimised Gaussian filter pulses.

why the optimised Gaussian pulse for the FFT-FBMC is even more confined in the time domain. The impulse responses of the optimised filters obtained for FFT-FBMC and BF-OFDM are compared with optimal Gaussian pulse for ideal CP/CS lengths ($\alpha = 0.45$) the in Figure 3.10.

Both FFT-FBMC and BF-OFDM can ensure complex NPR even when the conditions on CP/CS length are not met thanks to the propose prototype filter design method. The achieved SIR levels guarantee that the intrinsic interference has no impact on system performance as its in-band power is ensured to be significantly lower than any conventional impairments.

Reducing the achievable SIR level (and still ensuring complex NPR) can now be used as an extra degree of freedom for the filter design method so as to optimised the performance of another criterion such as the spectral confinement of the system.

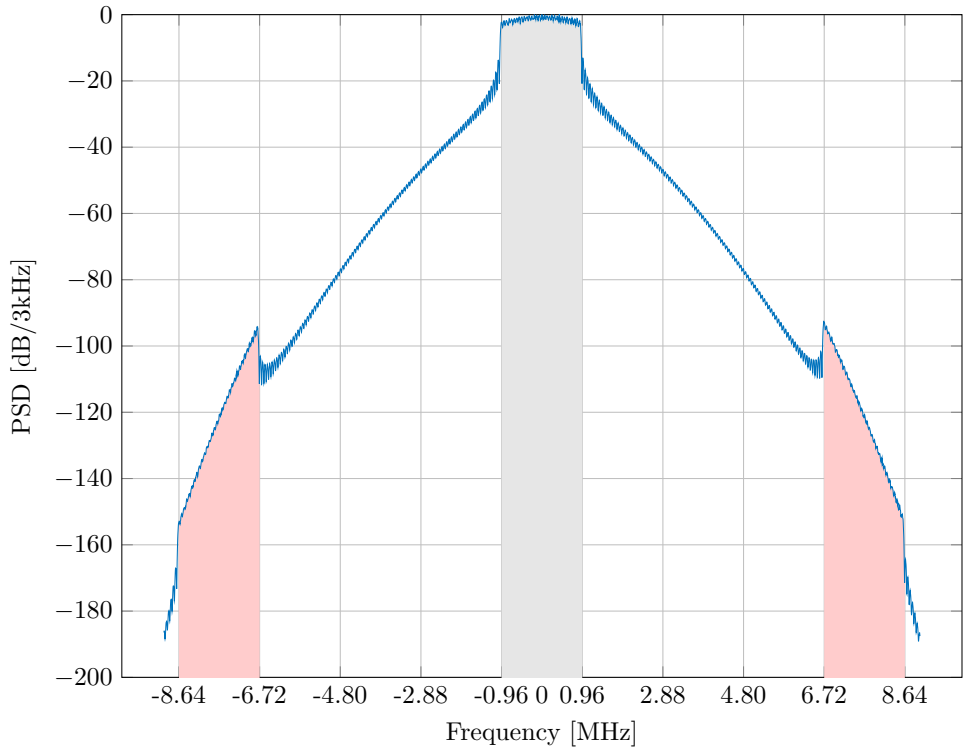

Figure 3.11: Frequency response of a subband for a Gaussian prototype filter ($\alpha = 0.627$).

3.5.3 Optimisation on the spectral confinement with a constraint on the intrinsic interference rejection

The SIR levels obtained in the previous paragraph are sufficient to ensure that the intrinsic interference has no impact on the overall system performance. The intrinsic interference rejection level can thus be degraded while still ensuring it has no impact on system performance so as to improve another criterion such as the spectral confinement of the system.

The filter design method studied in the previous section maximises the stop band attenuation of the frequency response of the prototype filter as shown in Figure 3.11 (red areas). However, by doing so the proposed method does not ensure a sharp transition band (between allocated subband and red areas) especially for low value of the rate factor δ.

It may be disadvantageous for wireless systems with a narrow SEM to satisfy such as systems working on unlicensed bands and cognitive radios. Besides, a more confined spectrum may lead to better performance in non-orthogonal subbands multiplexing as already observed in Chapter 2. The proposed method will be thus improved so as to obtain a more confined frequency response.

It is proposed now to relax the SIR level so as to improve the frequency localization of the frequency response of the prototype filter. The idea is to obtain a prototype filter with the most confined frequency response satisfying a target SIR level. It will be performed on Gaussian filter pulse as it is straightforward to derive the optimal BT parameter according to the new method. Indeed, as observed in Figure 3.9, the proposed method consists in finding the lowest value

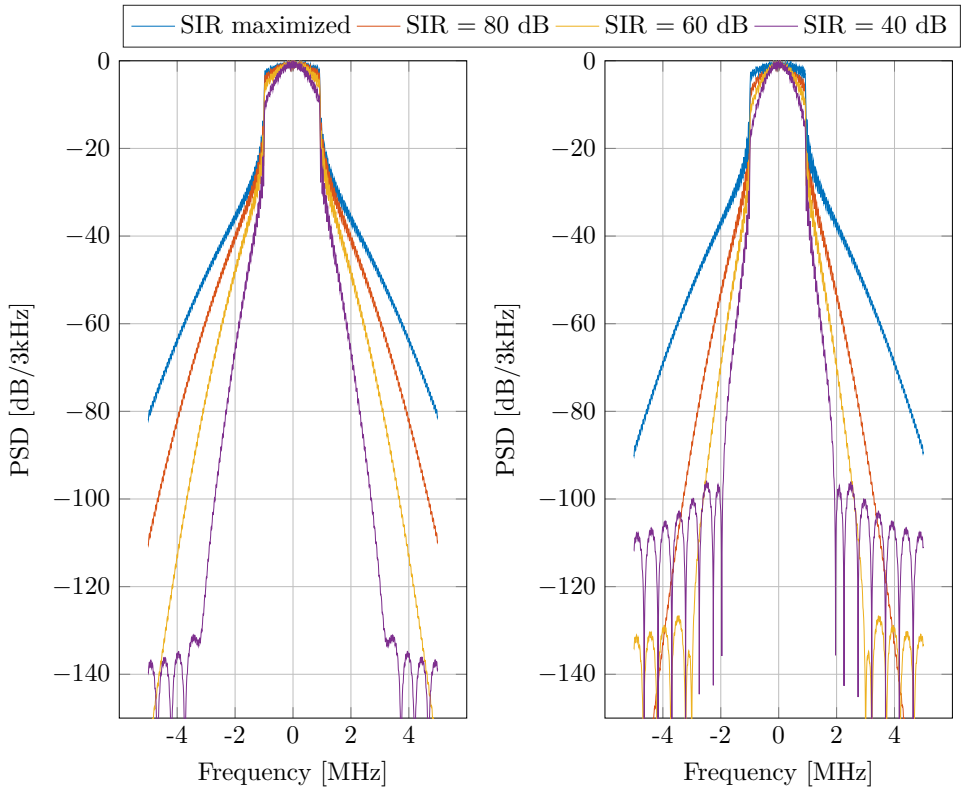

Figure 3.12: Subband spectrum of optimised spectrum response for different SIR targets for FFT-FBMC (left) and BF-OFDM (right).

of the BT parameter α satisfying a target SIR level.

$$\alpha_{\text{opt}} = \min\left(\alpha | \text{SIR}(\alpha) \geq \text{SIR}_{\text{target}}\right) \tag{3.32}$$

The optimisation results are given in Table 3.4 and the resulting spectrum in Figure 3.12. The SIR targets are arbitrary set to 80, 60 and 40 dB. The gain in side lobe rejection are significant even near the allocated subband.

Table 3.4: Optimal BT values for the optimisation on the spectral response giving some SIR targets.

SIR level	FFT-FBMC	BF-OFDM
80.0 dB	0.502	0.355
60.0 dB	0.396	0.277
40.0 dB	0.289	0.218

3.5.4 Concluding remarks

A prototype filter design method is detailed in this section. The filter pulses are optimised with respect to the intrinsic interference rejection levels as the main purpose of the OFDM-precoded is to allow QAM transmission with filter-bank. The design method has been extended to shortened CP configurations so as to be able to scale on target symbol density. The resulting SIR levels are degraded when CP length conditions are tough. However the proposed method can still

provided significant interference rejection as shown for the example considered in this section.

As the obtained SIR levels are very high even with shortened CP configurations, the intrinsic interference rejection can be relaxed and still guarantees complex NPR. By doing so, the filter design method gains some degrees of freedom that can be used to run a double-criteria optimisation. It is proposed to improve the spectral confined of the system. The observed gain in side lobe rejection is significant even for high SIR targets.

The proposed prototype filter design method is therefore flexible and allows FFT-FBMC and BF-OFDM to be adapted to any symbol density and SEM requirements.

3.6 Filter Predistortion

For both waveforms, the received symbols are distorted by the frequency response of the filter as shown in (3.8) for FFT-FBMC et (3.27) for BF-OFDM.

Several options exist to deal with those coefficients. The first option consists in ignoring them. The filter-induced distortion will be estimated by the channel estimation and considered as part of the channel response.

The second option is to pre-compensate those coefficients at the transmitter side. Indeed, the coefficients can be pre-computed and a pre-distortion stage can be pre-pended to the transmission chain. The predistortion coefficient to be applied on the k^{th} subcarrier of the p^{th} subband (at all time instants) $\mathcal{P}_{p,k}[n]$ is given in (3.33) for the two schemes. As already mentionned, this coefficient does not depend neither on the subband index p nor on the time intant n.

$$\begin{cases} \mathcal{P}_{p,k}[n] = \frac{1}{|G(k_o)|^2} & \text{for FFT-FBMC} \\ \mathcal{P}_{p,k}[n] = \frac{G^*(k_o)}{|G(k_o)|^2} & \text{for BF-OFDM} \end{cases} \tag{3.33}$$

The impact of the filter predistortion on the transmitted spectrum is observed in Figure 3.13 for the two schemes. For each scheme, the 40-dB prototype filter defined in Table 3.4 is used.

The addition of filter predistortion stage at the transmitter side, as it flattens the in-band transmitted spectrum at the expense of a slightly weakened side lobe rejection. The receiver can thus operate without any knowledge on the filtering performed at the transmitter side. Such receiver is said to be "transparent". The transparency condition allows a straightforward multiple access for the uplink. Indeed, if the uplink users have different configuration (such as prototype filter parameters), the receiver can demodulate the different signals without any information on the transmitter filtering.

For FFT-FBMC, the filter predistortion stage is not interesting as it is assumed that the receiver also uses the Tx prototype filter. Considering a filter predistortion stage for FFT-FBMC would be interesting when different TX and Rx prototype filters are considered. This case is not addressed in this thesis. The predistortion will thus not be considered in FFT-FBMC in the proposed study.

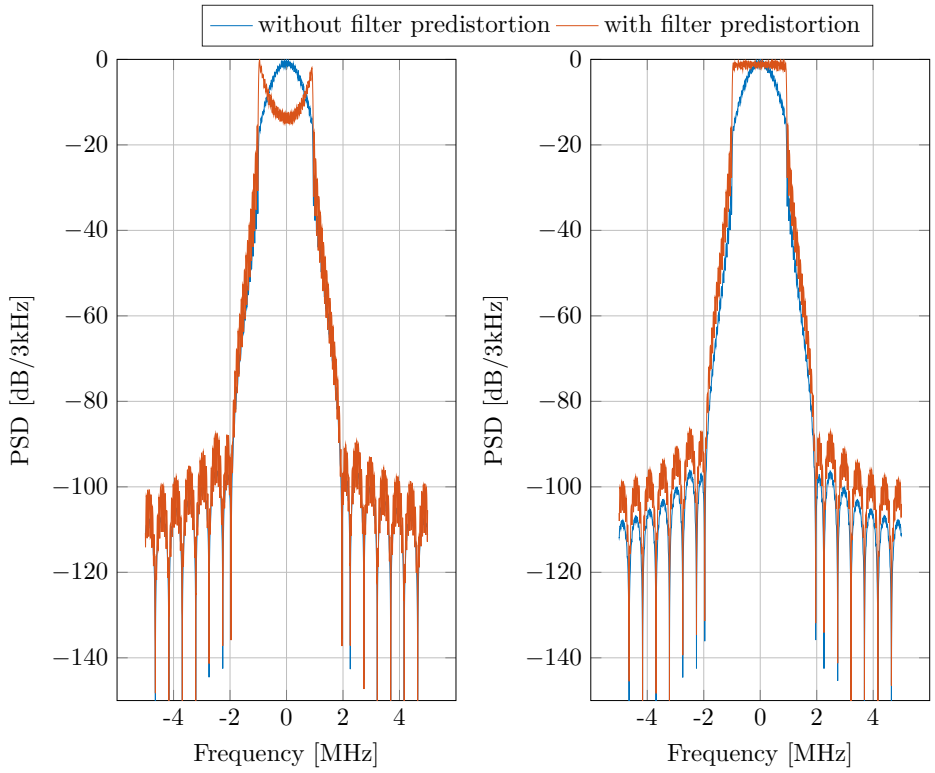

Figure 3.13: Impact of transmitter filter-predistortion for FFT-FBMC (left) and BF-OFDM (right).

It seems interesting noticing that the addition of the filter predistortion stage at the transmitter side has no impact of the SIR level after demodulation as it is verified for FFT-FBMC below. Same verification can be performed with BF-OFDM expression.

$$\begin{aligned} \mathrm{SIR} &= \frac{1}{N_p \delta} \sum_{k \in \Omega} \frac{\sigma_a^2}{\sum_{\epsilon \neq 0} \frac{|G^*(k+\epsilon N) G(k)|^2}{|G(k)|^4} \sigma_a^2} \\ &= \frac{1}{N_p \delta} \sum_{k \in \Omega} \frac{|G(k)|^4 \sigma_a^2}{\sum_{\epsilon \neq 0} |G^*(k+\epsilon N) G(k)|^2 \sigma_a^2} \end{aligned} \tag{3.34}$$

3.7 Conclusion

In this section, the OFDM precoding for FBMC-based waveforms has been proposed to allow NPR in the complex field.

The proposed precoding can restore the complex orthogonality of a filter-bank based waveform. Indeed, it prevents the subband overlapping (without compromising the spectral efficiency) which is a source of interference in FBMC-based waveforms. However, to ensure complex NPR, the frequency localisation is thus relaxed with respect to the commonly used OQAM signaling (from subcarrier-wise to subband-wise). Besides, the spectral efficiency of the scheme has to be relaxed as well with the insertion of CP ans CS according to the Balian Low Therorem.

Two schemes results from this study, namely FFT-FBMC with a FBMC-based receiver and BF-OFDM with a simple OFDM-based receiver. The working conditions for the two schemes have been established for any FBMC rate factor δ. The two complex orthogonal schemes are thus very flexible (in terms of subband bandwidth and precoding alphabet size) so that they can be easily adapted to any system requirements. The flexibility of the schemes is even improved by the proposed prototype filter design methods which allow to ensure complex NPR for any symbol rate and spectrum requirements.

The proposed schemes thus benefit from both complex orthogonality and a subband filtering performed by a filter-bank. The schemes are thus interesting for future mobile technologies. On top of that, BF-OFDM relies on a 5G NR receiver which makes it highly appealing for beyond 5G NR technologies. That is why in the next chapter, the two schemes will be now adapted to 5G NR numerologies and their performance evaluated for the scenarios considered in Chapter 2.

3.7.1 Contribution

This chapter represents the major contributions of the research work. First, the BF-OFDM scheme has been detailed in [92]: D. Demmer, R. Gerzaguet, J.-B. Doré, D. Le Ruyet, and D. Kténas, "Block-Filtered OFDM: a novel waveform for future wireless technologies," in *Proc. IEEE International Conference on Communications (ICC)*, (Paris, France), May 2017. The prototype filter design methods presented in Section 3.5.1 and 3.5.2 have been published in [93]: D. Demmer, R. Gerzaguet, J.-B. Doré, D. Le Ruyet, and D. Kténas, "Filter Design for 5G BF-OFDM Waveform," in *Proc. IEEE. European Conference on Networks and Communications (EuCNC)*, (Oulu, Finland), June 2017. However, the filter design optimising both the interference and side lobe rejection has not been published yet.

A first performance evaluation of BF-OFDM has been done in [94]: R. Gerzaguet, D. Demmer, J.-B. Doré, and D. Ktiénas, "Block-filtered OFDM: A new promising waveform for multi-service scenarios," in *Proc. IEEE International Conference on Communications (ICC)*, pp. 1–6, May 2017.

Then, the study has been extended to any FBMC rate factor δ in a collaborative work with the inventors of FFT-FBMC in [91]: D. Demmer, R. Zakaria, R. Gerzaguet, J.-B. Doré, and D. Le Ruyet, "Study of OFDM Precoded Filter-Bank Waveforms," *IEEE Transactions on Wireless Communications*, pp. 1–1, 2018.

4 Compatibility with 5G NR and analysis

In this chapter, the two schemes detailed in the third chapter, FFT-FBMC and BF-OFDM, are adapted to 5G NR systems. The two schemes are near complex orthogonal, meaning that the Nyquist condition is not satisfied but the intrinsic interference can be strongly attenuated. Two key indicators will be assessed to determine the best configuration to adopt: the intrinsic interference rejection and the hardware-implementation complexity. Three different configurations will be considered: one providing an excellent intrinsic interference rejection level and a low complexity, a second one with the same configuration but a prototype filter optimised to provide a more confined spectrum (and therefore a relaxed intrinsic interference rejection) and a last one with narrow subbands.

A multi-service transmission scheme is proposed which allows the simultaneous support of different numerologies with a unique filter-bank. Not only the multi-service transmitter scheme is interesting for an implementation point of view but it also favors multi-service coexistence for beyond 5G technologies.

The last section is dedicated to the performance evaluation and the analysis of the proposed schemes. The scenarios used in Chapter 2 will be considered to ease the comparison between the proposed configurations and the state-of-the-art waveforms.

4.1 Waveform configuration

4.1.1 Methodology

The aim of this section is to determine the best waveform configuration (*i.e.* the set of waveform parameters) to be compatible with the 5G NR numerologies. The configuration will depends on the numerology μ. We will therefore adopt the notations used in Chapter 1 where X^μ denotes the values of the parameter X for the numerology μ.

For the numerology μ, the total number of subcarriers must equal N_{FFT}^μ (where N_{FFT}^μ refers to the number of subcarriers presented in Table 1.1). It leads to the condition (4.1) with a sampling frequency of 61.44 MHz. As a reminder, N^μ corresponds to the number of subbands and $N_p^\mu \delta^\mu$ the number of subcarriers per subband. Ideally, the value of N^μ must be maximized (and thus $N_p^\mu \delta^\mu$ minimized)

to obtain narrow subbands and therefore an efficient filtering.

$$N^{\mu} N_p^{\mu} \delta^{\mu} = N_{\mathrm{FFT}}^{\mu} \tag{4.1}$$

A second condition is to satisfy the spectral efficiency of 5G NR (which is the same for all the numerologies). The analytical expression of the spectral efficiency is the same for the two proposed waveforms. Assuming, N_s the number of transmitted symbols, N_a the number of active subbands, r the modulation efficiency (including both the modulation order and the coding rate), the spectral efficiency can be expressed as follows:

$$\begin{aligned} \eta &= \frac{\delta^{\mu} N_p^{\mu} N_s N_a r}{K^{\mu} N^{\mu} + \delta^{\mu} N^{\mu} \left(N_s (N_p^{\mu} + N_{\mathrm{CS}}^{\mu} + N_{\mathrm{CP}}^{\mu}) - 1\right)} \\ &\xrightarrow{N_s \to \infty} r \frac{N_{\mathrm{a}}}{N^{\mu}} \frac{N_p^{\mu}}{N_p^{\mu} + N_{\mathrm{CP}}^{\mu} + N_{\mathrm{CS}}^{\mu}} \end{aligned} \tag{4.2}$$

As in CP-OFDM, the spectral efficiency is reduced because of the CP/CS insertions. However, one can observe that δ^{μ} has no impact on the spectral efficiency because the subband allocation has been adapted to the time structure of the signal. It implies that (4.3) must be satisfied so as to ensure the 5G NR symbol density (where 4096 is the number of subcarriers and 288 the CP length for service $\mu = 0$). As N_{CP}^{μ} and N_{CS}^{μ} are integer numbers, the minimum value of N_p^{μ} that still satisfies (4.3) is 128 (with $N_{\mathrm{CP}}^{\mu} + N_{\mathrm{CS}}^{\mu} = 9$).

$$\frac{N_p^{\mu}}{N_p^{\mu} + N_{\mathrm{CS}}^{\mu} + N_{\mathrm{CP}}^{\mu}} = \frac{4096}{4096 + 288} \tag{4.3}$$

As a consequence, if the typical rate factor $\delta^{\mu} = 1/2$ is considered then $N^{\mu} = 64$. In other words, there would be 64 subbands of 960 kHz. The subbands are therefore too wide (to be compared with a RB of 180 kHz for $\mu = 0$). To increase the number of subands and bring them closer to a 5G NR RB, lower values of the rate factor δ^{μ} will be considered thanks to the analytical analysis provided in the previous chapter.

Two Key Performance Indicators (KPI) will be used to determine the most suitable waveform configuration: the intrinsic interference rejection (SIR) and the complexity of the UE.

KPI 1: Intrinsic interference rejection

This KPI evaluates the orthogonality condition of the configuration to make sure it ensures complex NPR. It is based on the method described in the Section 3.5. The maximum SIR level will be estimated for the different configurations. Only Gaussian pulses will be considered and optimisation on the spectrum confinement will be performed as well.

KPI 2: Complexity

This KPI evaluates the hardware implementation complexity of the scheme which gives an estimation of the computation resource and energy consumption requirements as in Section 2.5.3.

As in Section 2.5.3, the complexity of a transceiver/receiver scheme is evaluated by counting the number of real multiplications required to transmit a symbol. The filter pre-compensation stage applies a complex coefficient on each frequency tone and therefore requires $3NN_p\delta$ real multiplications (only for BF-OFDM). The OFDM precoding scheme is composed of N N_p-point OFDM modulators set in parallel. However in our case, only a contiguous portion of the subcarriers are used: $N_p\delta$ out of N_p. Therefore the complexity of one OFDM modulator can be reduced to $N_p/2\log_2(N_p\delta)$. The polyphase-network filter bank needs $2KN$ real multiplications for the filtering and $3N/2\log_2(N)$ for the IFFT stage per block. The resulting complexity for the FFT-FBMC and BF-OFDM transmitter schemes are respectively given in (4.4) and (4.5).

$$\begin{aligned}\mathcal{C}_{\mathrm{FFT-FBMC,Tx}} &= 3NN_p/2\log_2(N_p\delta) \\ &\quad + N_p\left(3N/2\log_2(N) + 2KN\right)\end{aligned} \tag{4.4}$$

$$\begin{aligned}\mathcal{C}_{\mathrm{BF-OFDM,Tx}} &= 3NN_p\delta + 3NN_p/2\log_2(N_p\delta) \\ &\quad + N_p\left(3N/2\log_2(N) + 2KN\right)\end{aligned} \tag{4.5}$$

When it comes to the receiver schemes, FFT-FBMC performs the reverse Tx processing (without the pre-distortion stage) which results in (4.6). The BF-OFDM receiver is a WOLA-OFDM receiver (*i.e.* an OFDM receiver with windowing) which gives the complexity expressed in (4.8).

$$\mathcal{C}_{\mathrm{FFT-FBMC,Rx}} = \mathcal{C}_{\mathrm{FFT-FBMC,Tx}} \tag{4.6}$$

$$\mathrm{C}_{\mathrm{BF-OFDM,Rx}} = 3\frac{NN_p\delta}{2}\log_2(NN_p\delta) + 4W_{\mathrm{Rx}} \tag{4.7}$$

$$= \mathrm{C}_{\mathrm{WOLA-OFDM,Rx}} \tag{4.8}$$

As a consequence, only the complexity of the transmitter schemes will be evaluated and compared with the equivalent complexity of the CP-OFDM transmitter given in (2.35).

4.1.2 Support of non-integer CP values

As already mentioned, a configuration with a high number of subbands will be preferred as it eases the multiplexing of different services. Nonetheless, the condition (4.3) must still be ensured. Besides, to benefit from the efficient FFT implementation N_p must remain a power of two while the CP and CS lengths must remain integer. Therefore the minimum value possible for N_p is 128 which leads to $N_{\mathrm{CP}} + N_{\mathrm{CS}} = 9$. A possible solution to increase the number of subbands with $N_p = 128$ is to decrease the rate factor δ as described in the previous chapter.

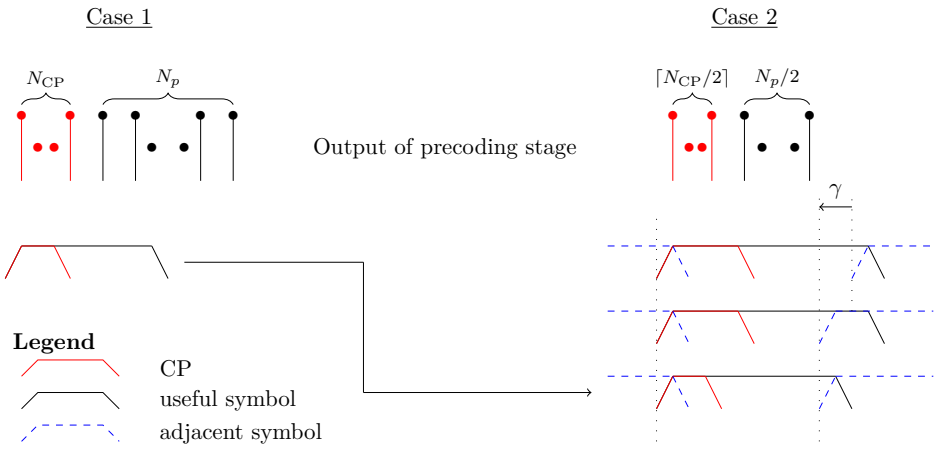

Figure 4.1: Transmitted frame with non-integer number CP/CS.

In this paragraph, another solution will be investigated which consists in supporting non-integer values of $N_{\text{CP}} + N_{\text{CS}}$ (and therefore values of N_p lower than 64). To do so, an enlarged value of CP/CS, $\widetilde{N_{\text{CP}} + N_{\text{CS}}}$ is defined in (4.9).

$$\widetilde{N_{\text{CP}} + N_{\text{CS}}} = \left\lceil \frac{9N_p}{128} \right\rceil \tag{4.9}$$

To restore the 5G spectral efficiency, the transmission scheme is slightly modified as depicted in Figure 4.1. Each FFT-FBMC or BF-OFDM symbol is advanced in time by a number of sample γ which expression is given in (4.10) .

$$\gamma = N\delta \left(\widetilde{N_{\text{CP}} + N_{\text{CS}}} - \frac{9N_p}{128} \right) \tag{4.10}$$

Indeed, the duration of the useful symbol (in black in Figure 4.1) is the same in the two case but the CP duration (in red in Figure 4.1) is slightly enlarged because of the ceil operator in the second case. The time offset γ between consecutive symbols (in blue dashed in Figure 4.1) compensates this extra CP duration.

It seems worth noticing that the same limitation on CP length has been observed for Fast-Convolution Filtered OFDM (FC-F-OFDM) presented in Chapter 2 as an efficient implementation of fOFDM. For FC-F-OFDM, the transmission scheme has been modified including CP extrapolation to adapt the scheme to the 5G time/frequency grid[95].

4.1.3 Multi-service scheme

A scheme enabling a straightforward service multi-service is proposed in this paragraph. The proposed transmission scheme is depicted in Figure 4.2 and can be adapted to both FFT-FBMC and BF-OFDM where the predistortion stage is only used in BF-OFDM.

The main idea is to rely on a simple PPN for all the numerologies for each frequency ranges (FR1 for sub-6 GHz and FR2 for above 6 GHZ) and to use the precoding stage to adapt to the numerology in use. The PPN parameters

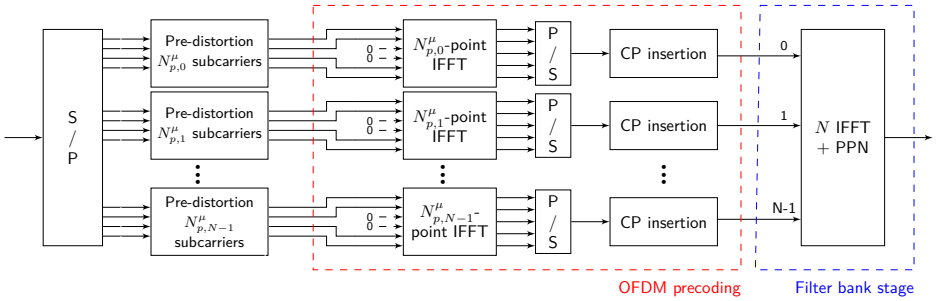

Figure 4.2: Multi-service transmission scheme.

(number of subbands N, overlapping factor K, rate factor δ and filter parameters) are thus independent from the numerology index. (4.1) can thus be simplified in (4.11) where $N^{\mu}_{p,k}$ denotes the size of the OFDM modulators for the k^{th} subband and numerology index μ. It means that the numbers of subcarriers from one numerology to another can be adapted only by updating the size of the OFDM modulators in the precoding according to the following expression $N^{\mu+1}_{p,k} = N^{\mu}_{p,k}/2$.

$$NN^{\mu}_{p,k}\delta = N^{\mu}_{\text{FFT}} \tag{4.11}$$

In this work, only FR1 systems will be addressed. However, the procedure can be directly applied for FR2 systems. With the proposed multi-service transmission scheme, a base station can provide simultaneously different services in the system bandwidth. At the UE side, it allows a dynamic change of numerology with a reduced hardware complexity.

4.1.4 Numerical Application

The best configuration for the two schemes will be now determined with a numerial evaluation of the considered KPIs. The evaluation is performed for numerology $\mu = 2$ which has the minimum number of subcarriers amongst the 5G NR numerologies (*i.e.* 256). With such low number of subcarrier, the modification of the transition schemes studied in Section 4.1.2 is likely to be interesting which thus may degrade the SIR level. Numerology $\mu = 2$ is therefore the most critical numerology that is why it is the one considered in the KPI evaluation.

The outputs of the numerical evaluation of the two KPIs are provided in Tables 4.1 and 4.2 for FFT-FBMC and in Tables 4.3 and 4.4 for BF-OFDM. Configurations with 'X', *i.e.* configurations with $(N_p, \delta) = (16, 0.125)$ are configurations which can not guarantee complex NPR and are therefore not evaluated.

One can observe that on the one hand decreasing the size of the precoding OFDM modulators N_p reduces the maximum achievable SIR level. Indeed, by the practical CP/CS lengths become significantly lower than the ideal CP/CS lengths which generates a large amount of ISI. In addition to that $N_p \leq 64$, the transition scheme is changed which brings even more ISI as described in Section 4.1.2. On the other hand, decreasing the rate factor δ which improve the rejection of the ICI.

Regarding the transmitter complexity, decreasing N_p slightly increases the complexity while decreasing δ significantly increases it. The complexity of BF-

Table 4.1: SIR level obtained after prototype filter optimisation (dB) for FFT-FBMC with Gaussian filter pulse.

K=4

δ \ N_p	128	64	32	16
0.5	91.7	55.7	38.1	34.6
0.25	101.2	62.4	42.4	38.0
0.125	104.8	64.8	43.6	X

K=3

δ \ N_p	128	64	32	16
0.5	78.3	60.0	38.0	34.3
0.25	101.1	62.3	42.4	38.0
0.125	101.8	64.7	43.6	X

K=2

δ \ N_p	128	64	32	16
0.5	59.1	58.3	39.2	35.0
0.25	102.9	63.1	42.6	38.1
0.125	105.2	65.0	43.7	X

K=1

δ \ N_p	128	64	32	16
0.5	38.7	38.8	33.2	30.7
0.25	63.1	61.4	43.2	38.4
0.125	106.3	64.9	43.6	X

Table 4.2: Complexity ratio w.r.t 5G NR CP-OFDM for FFT-FBMC.

K=4

δ \ N_p	128	64	32	16
0.5	2.6	2.7	2.8	3.0
0.25	4.8	5.2	5.5	5.9
0.125	9.8	10.7	11.6	X

K=3

δ \ N_p	128	64	32	16
0.5	2.3	2.4	2.5	2.6
0.25	4.1	4.5	4.9	5.3
0.125	8.5	9.4	10.3	X

K=2

δ \ N_p	128	64	32	16
0.5	1.9	2.0	2.2	2.3
0.25	3.5	3.8	4.2	4.6
0.125	7.2	8.0	8.9	X

K=1

δ \ N_p	128	64	32	16
0.5	1.6	1.7	1.8	2.0
0.25	2.8	3.2	3.6	3.9
0.125	5.8	6.7	7.6	X

Legend: $N_p\delta =$ 64 32 16 8 4

OFDM transmitter is slightly greater than for FFT-FBMC because of the filter pre-distortion stage. However, it seems worth reminding that BF-OFDM receiver is a simple WOLA-OFDM receiver while FFT-FBMC performs the reverse transmitter operation and therefore exhibits the same complexity level.

As a consequence, for a given number of subband (*i.e.* a given product $N_p\delta$), a configuration with a lower value for N_p to ease practical implementation of the system. Nonetheless, the configuration must satisfy a high enough SIR level to ensure complex NPR. Moreover, a configuration with a high value for the overlapping factor K will be preferred to benefit from a good side lobe rejection.

For the rest of the study, three configurations will be considered for each scheme. First, a configuration that filters group of 32 subcarriers (*i.e.* with $N_p\delta = 32$) is considered as it can provide a good level of SIR level. For both scheme, the configuration $(K, N_p, \delta) = (3, 64, 0.5)$ is preferred. Indeed, this con-

Table 4.3: SIR level obtained after prototype filter optimisation (dB) for BF-OFDM with Gaussian filter pulse.

K=4

δ \ N_p	128	64	32	16
0.5	117.7	76.2	40.5	24.5
0.25	146.9	77.8	43.6	25.7
0.125	147.2	80.1	44.8	X

K=3

δ \ N_p	128	64	32	16
0.5	87.3	76.9	40.5	24.0
0.25	147.5	77.9	43.5	25.6
0.125	148.2	80.2	44.8	X

K=2

δ \ N_p	128	64	32	16
0.5	60.8	61.9	40.6	24.0
0.25	117.7	78.0	43.6	25.7
0.125	148.4	80.3	44.8	X

K=1

δ \ N_p	128	64	32	16
0.5	32.9	33.1	32.1	25.1
0.25	63.5	60.9	44.0	25.6
0.125	117.3	80.3	44.9	X

Table 4.4: Complexity ratio w.r.t 5G NR CP-OFDM for BF-OFDM.

K=4

δ \ N_p	128	64	32	16
0.5	2.8	3.0	3.1	3.2
0.25	5.0	5.4	5.8	6.2
0.125	10	10.9	11.8	X

K=3

δ \ N_p	128	64	32	16
0.5	2.5	2.6	2.8	2.9
0.25	4.4	4.8	5.1	5.5
0.125	8.8	9.6	10.5	X

K=2

δ \ N_p	128	64	32	16
0.5	2.2	2.3	2.4	2.4
0.25	3.7	4.1	4.5	4.8
0.125	7.4	8.3	9.2	X

K=1

δ \ N_p	128	64	32	16
0.5	1.8	2.0	2.1	2.2
0.25	3.0	3.4	3.8	4.2
0.125	6.1	7.0	7.8	X

Legend: $N_p\delta =$ 64 32 16 8 4

figuration provide a good trade-off between SIR level and transmitter complexity. The achievable SIR level is high enough to optimise the prototype filter according to the side lobe rejection and the complexity ratio w.r.t. CP-OFDM is limited to 2.4 for FFT-FBMC and 2.6 for BF-OFDM. Therefore, for this configuration two prototype filter design methods will be addressed: a first one with SIR optimisation leading to the SIR results provided in the tables and another with a PSD optimisation with a SIR constraint at 40 dB.

A configuration with subband of 4 subcarriers is considered as well as it allows intrinsic RB-wise filtering which is highly appealing. The configuration $(K, N_p, \delta) = (3, 16, 0.25)$ is preferred for both scheme as it provides a good trade-off between overlapping factor K and complexity ratio.

All the selected configurations are summed in Table 4.5. As a reminder, the parameter set (K, N, δ, α) is the PPN configuration and remain the same for all

Table 4.5: 5G NR $\mu = 2$ FFT-FBMC and BF-OFDM configurations.

	FFT-FBMC			BF-OFDM		
Config	1	2	3	1	2	3
N	32		256	32		256
Subband [kHz]	1920		240	1920		240
Subband [RB $\mu = 2$]	2.67		0.33	2.67		0.33
Subband [RB $\mu = 0$]	10.67		1.33	10.67		1.33
K	3	3	3	3	3	3
(N_p^2, δ)	$(64, 0.5)$		$(16, 0.25)$	$(64, 0.5)$		$(16, 0.25)$
BT α	0.39	0.17	0.98	0.36	0.27	1.13

the numerologies. The parameter N_p^μ depends on the numerology in use and we have the following relation:

$$N_p^{\mu-1} = 2N_p^\mu \tag{4.12}$$

The configurations with 32 subbands are appealing because of the low value of the BT parameter (*i.e.* a prototype filter well localized in the frequency domain) while the configuration with 4 subbands allows an inherent RB-wise filtering. However for the latter configurations, the prototype filter is more localized in the time domain (high value of the BT parameter) to compensation the shortened CP/CS lengths.

4.2 Performance evaluation

The different configurations will be now evaluated by considering the scenarios introduced in Chapter 2. CP-OFDM will be used as reference in this section for sake of clarity. For some scenarios, other state-of-the-art solutions presented in Chapter 2 can be also used for comparison. To compare the performance of FFT-FBMC and BF-OFDM with the performance of the other state-of-the-art solutions, one should refer to the corresponding performance evaluation given in Chapter 2. As a reminder, the BF-OFDM receiver corresponds to a WOLA-OFDM receiver which is a windowing OFDM receiver. As for WOLA-OFDM, a BTRC window with a time-excess of half the CP length of CP-OFDM is considered.

4.2.1 Spectral Confinement

First, the spectral confinement is evaluated for two allocated blocs of 5 and 2 RBs spaced by 1-RB guard band. The PSD are depicted in Figure 4.3 for FFT-FBMC and in Figure 4.4 for BF-OFDM.

The spectrum of WOLA-OFDM is depicted as well for comparison. One can observe that FFT-FBMC and BF-OFDM globally provide a side lobe rejection comprised between CP-OFDM and WOLA-OFDM. It means that the two proposed schemes are the least spectrally confined among all the solutions studied in Chapter 2. Only BF-OFDM config 2 (32 subbands with PSD-optimised prototype filter) provides better side lobe rejection than WOLA-OFDM.

One can observe that the signal aliases for config 3 (both schemes) are less attenuated (because of the better time localisation of the prototype filter) which

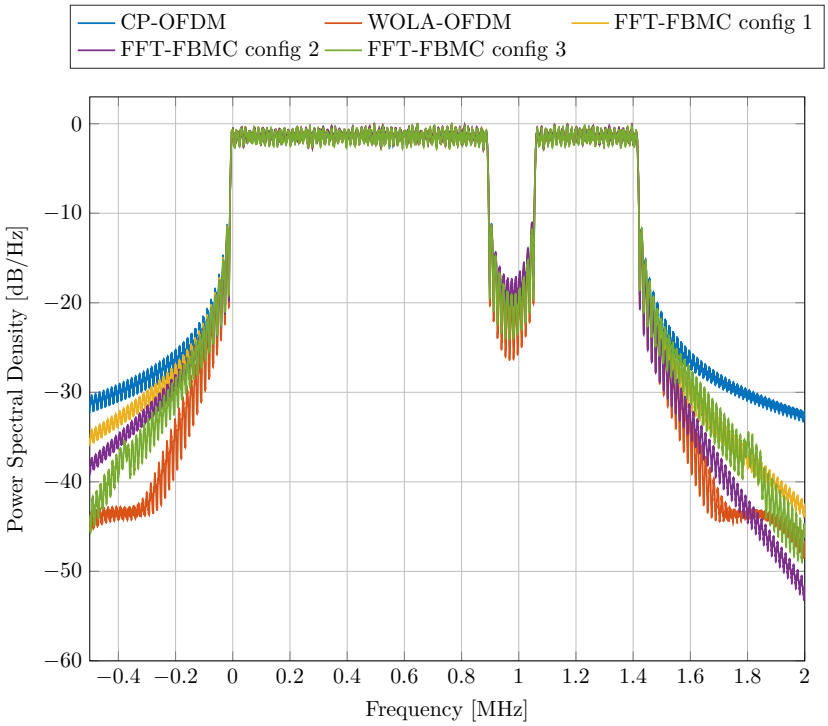

Figure 4.3: Spectral confinement of FFT-FBMC.

generates high ripples on the OOB region of the spectrum. Nonetheless, this ICI is attenuated enough to ensure complex NPR.

By observing the spectrums, one may expect that BF-OFDM outperforms WOLA-OFDM in 5G scenarios (*i.e.* asynchronous multi-user uplink and multi-service multiplexing) only with its configuration 2 (as they share the same receiver scheme). The performance provided by FFT-FBMC are harder to predict as no other solution uses the same receiver scheme.

4.2.2 Channel Performance

Double-ray channel

First, channel performance will be evaluated for uncoded systems over a two-ray Rayleigh channel. The channel model used for the simulations is described in Section 2.5.2. Perfect CSI and ideal 1-tap ZF equalization are assumed. Only the numerology $\mu = 0$ (longest CP length) is considered in the proposed evaluation. The results are depicted in Figure 4.5.

The proposed schemes exhibit a weakened robustness to delayspread with respect to CP-OFDM. Config 2 especially presents bad results. Indeed, this configuration is optimized on side lobe rejection. Therefore, the time localisation of the prototype filter is relaxed which makes the transmitted signal highly sensitive to delay spread. On the other hand, config 3 presents the best results. Indeed, the prototype filter is forced to be well localised in the time domain because of the shortened CP/CS length which makes the scheme more robust to delay spread induced effects.

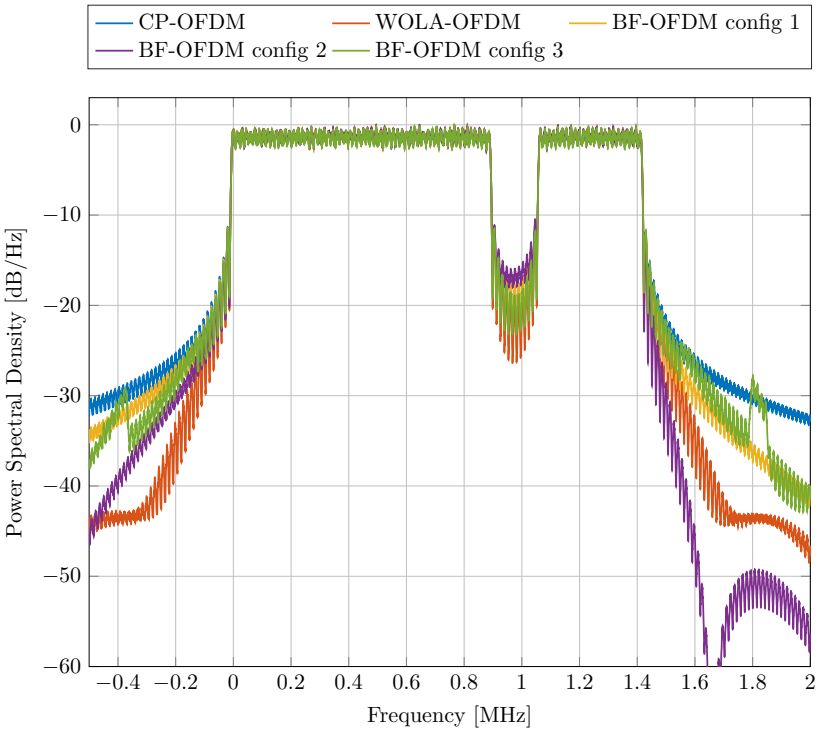

Figure 4.4: Spectral confinement of BF-OFDM.

TDL channels with mobility

In a second time, channel performance is evaluated by consideration 5G NR channel model for non-MIMO systems, *i.e.* TDL channels. As in the second chapter, only the TDL-A model and its average delay spread of 100 ns will be considered. A LDPC channel coding, compliant with 5G NR release 15, is considered. The decoder is based on the Self Corrected Min-Sum algorithm with a maximum of 50 iterations. Perfect CSI and perfect synchronization at the receiver side are assumed. As in chapter 2, three MCS are considered for the evaluation:

- MCS = 03: QPSK modulation with coding rate of about 25% (251/1024)
- MCS = 13: 16-QAM modulation with coding rate of about 50% (490/1024)
- MCS = 23: 64-QAM modulation with coding rate of about 70% (719/1024)

The results are depicted in Figure 4.6. It is interesting to notice that all configurations for both schemes performs as well as CP-OFDM. Indeed, in mobility scenario, the performance degradation mainly depends on symbol duration. As the scheme are perfectly adapted to the 5G NR time/frequency grid, there is no performance penalty with respect to CP-OFDM. Nonetheless, there is a slight SNR penalty for MCS 23 at 150 km/h induced by the accumulation of intrinsinc interference and channel distortion induced interference.

4.2.3 Complexity

The complexity of the scheme is evaluated by counting the number of real multiplications required to transmit a burst a symbol. Let the normalized complexity be the ratio between the complexity of a scheme and the complexity of CP-OFDM.

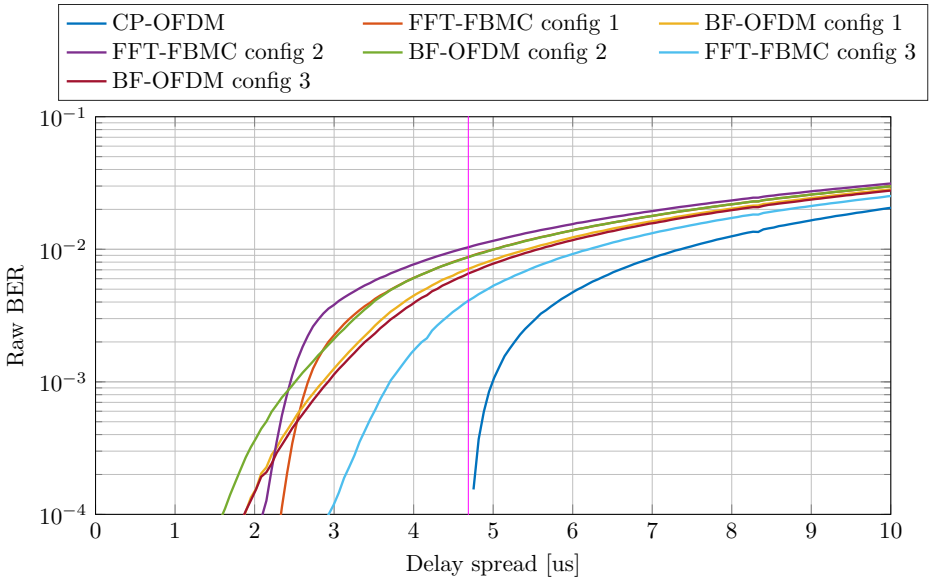

Figure 4.5: Impact of symbol spreading on delay spread robustness.

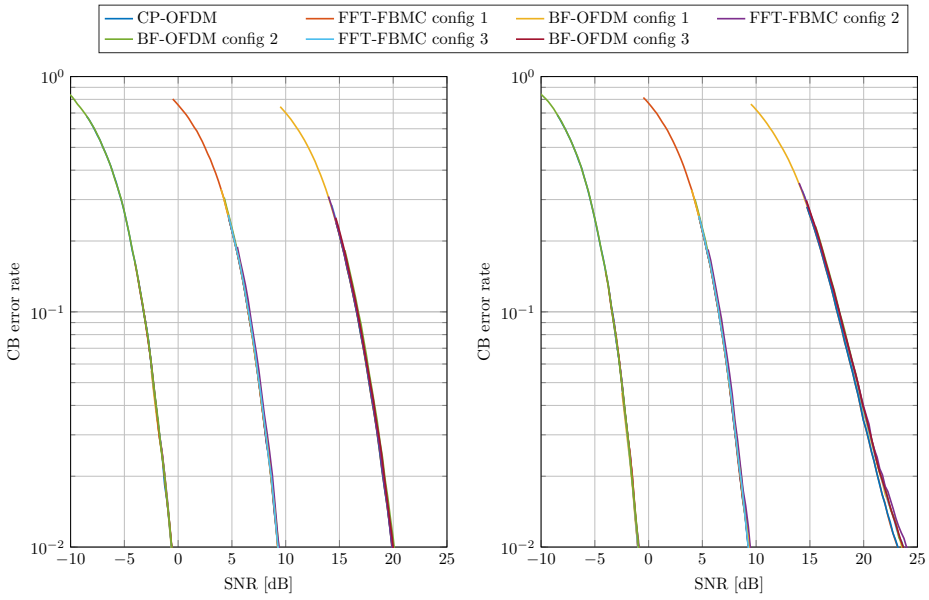

Figure 4.6: Evaluation of Code Block error rate over 100 ns TDL-A channels for 50 (left) and 150 (right) km/h with carrier frequency at 3.5 GHz.

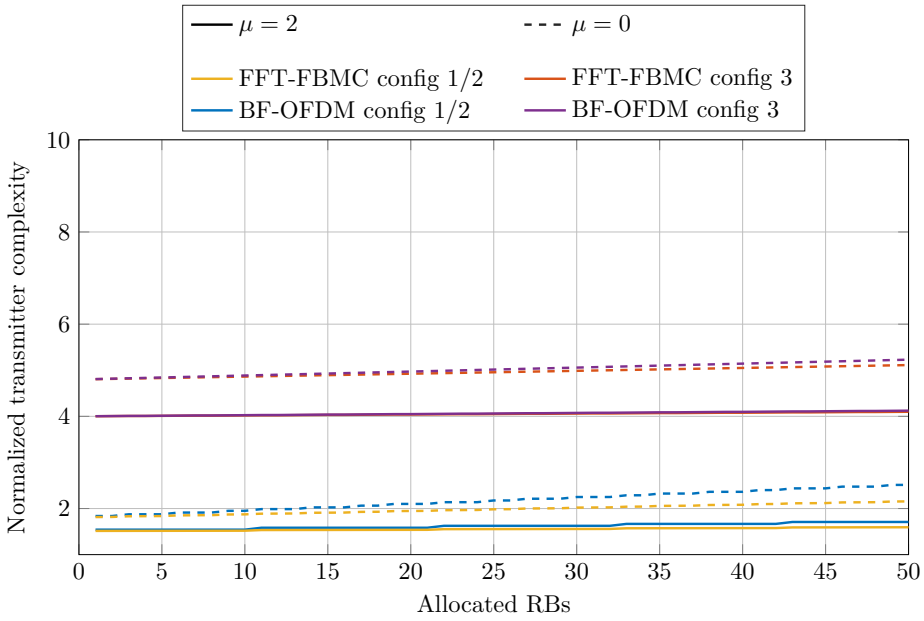

Figure 4.7: Transmitter complexity evaluation.

The complexity of the FFT-FBMC is given in (4.4) and for the BF-OFDM in (4.5).

The complexity evaluation for the transmitter schemes for numerologies $\mu = 0$ and $\mu = 2$ is depicted in Figure 4.7. As config 1 and 2 only differ from the prototype filter parametrization, they require the same complexity and are regrouped for this evaluation.

Thanks to its subband processing, the transmitter complexity depends on the number of active RBs. The number of active subbands nSB can be determined from the number of active RBs nRB by using the following expression:

$$nSB = \left\lceil \frac{nRB \times 12}{N_p \delta} \right\rceil \tag{4.13}$$

The number of active subbands has an higher impact for $\mu = 0$ as the OFDM modulators of the precoding stage are bigger ($N_p^0 = 4N_p^2$).

The proposed scheme are generally implementation-efficient with respect to the state-of-the-art solutions studied in Chapter 2 thanks to their filter-bank based schemes. Config 3 is slightly more complex because of the larger filter-bank it relies on.

The receiver complexity is only evaluated for numerology $\mu = 0$ and the results are shown in Figure 4.8.

As the receiver scheme is different for the two proposed schemes, we observe different results in terms of complexity. Indeed while FFT-FBMC receiver performs the reverse transmitter processing, BF-OFDM receiver is a simple WOLA-OFDM receiver (OFDM receiver with windowing). As a consequence, the complexity of the FFT-FBMC recevier is the same as the transmitter complexity while for BF-OFDM it is very close to 1 (but slightly higher because of the windowing).

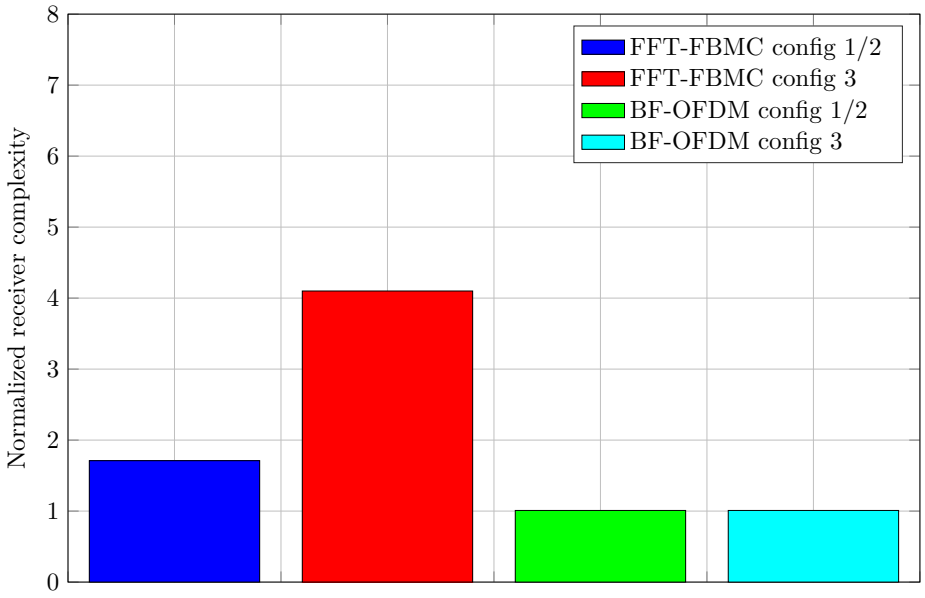

Figure 4.8: Receiver complexity evaluation.

4.2.4 Asynchronous multi-user uplink scenario

For this scenario, two users with 3 RBs and $\mu = 2$ and no guard band between them are considered. The two users are placed in adjacent subbands for both schemes. The result are depicted in Figure 4.9.

The proposed schemes provide excellent results in comparison with state-of-the-art solutions (see Figure 2.19). Indeed, both FFT-FBMC and BF-OFDM exhibits performance results similar to fOFDM which outperforms any other state-of-the-art solutions but FBMC/OQAM. Besides, FFT-FBMC and BF-OFDM both provide perfect interference cancellation for small timing offsets.

One can observe that FFT-FBMC outperforms BF-OFDM especially in the just adjacent zone (first kHz of the figure) which limits high energy interference. It results from its enhanced receiver scheme which performs a more selective filtering than a simple WOLA-OFDM receiver. For both schemes, the config 2 exhibits the best performance as only a spacing of few subcarriers between the two users are enough to strongly cancel timing offset induced interference.

The config 3 provide the worst performance despite its narrow-band filtering. Indeed as it has been observed with the spectral confinement evaluation, the prototype filter is too well localised in the time domain. Nonetheless, config 3 still outperforms UF-OFDM and provides similar results than WOLA-OFDM for FFT-FBMC. For BF-OFDM, the maximum interference rejection per subcarrier is limited to -25 dB MSE which corresponds to its SIR level (see Table 4.3).

4.2.5 5G NR multiservice coexistence

In this section, the multi-service co-existence is studied. A 1-RB interfering user using a different numerology is placed in adjacent band with respect to the useful user (with numerology $\mu = 0$). The case $\mu = 1$ over $\mu = 0$ and $\mu = 2$ over $\mu = 0$ are addressed for both proposed schemes. The results are depicted in Figure 4.10

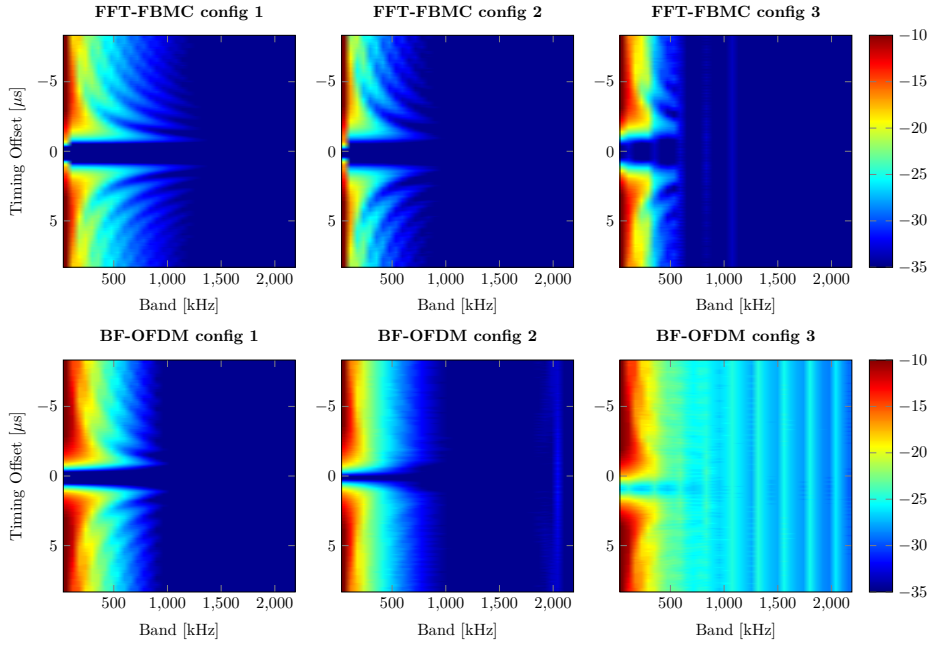

Figure 4.9: Mean Square Error per subcarrier [in dB] for multiple access schemes versus timing offsets [in μs] with no guard band.

for FFT-FBMC and in Figure 4.11 for BF-OFDM. fOFDM is added as reference in this section as it provides excellent results (see Figure 2.21).

Once again, config 2 provides the best results for both schemes. Indeed, config 1 only provides a slight interference mitigation with respect to CP-OFDM and therefore does not perform well. When it comes to config 3, it is interesting for guard bands greater than the subband size (*i.e* 240 kHz). For lower guard bands, the rejection of the interference due to the multi-numerology co-existence is very limited with respect to CP-OFDM.

One may observe that config 2 (both scheme) can even outperform fOFDM for small guard bands (lower than 100 kHz) which is interesting for bandwidth use efficiency. Regarding the difference observed between FFT-FBMC and BF-OFDM, it appears that FFT-FBMC slightly outperforms BF-OFDM for large guard bands (greater than 200 kHz) thanks to its enhanced receiver. Nonetheless, the performance obtained by BF-OFDM are good and close to fOFDM.

4.2.6 Synthesis

For each scheme, three configurations have been considered to be compared with the state-of-the-art solutions presented in Chapter 2:

- **Config 1:** maximizing the intrinsic interference rejection with a low complexity
- **Config 2:** same as config 1 but an more confined spectrum and a SIR level reduced to 40 dB
- **Config 3:** provides narrow-subband of 240 kHz (instead of 1920 kHz for the two other configurations).

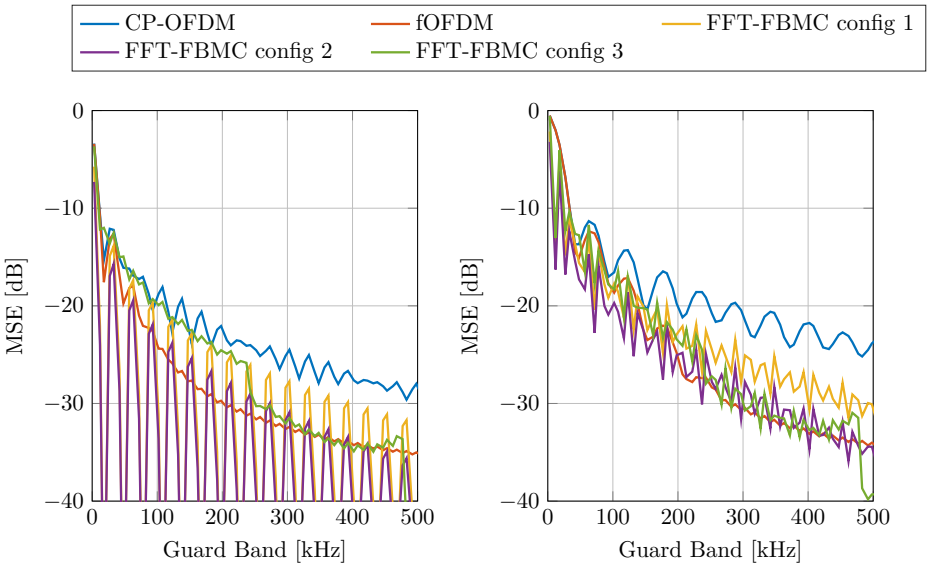

Figure 4.10: Mean Square Error per subcarrier [in dB] for FFT-FBMC with $\mu = 1$ over $\mu = 0$ (left) and $\mu = 2$ over $\mu = 0$ (right)

One can observe that the prototype filter design method plays a predominant role in system performance. Indeed, config 2 provides a moderate gain with respect to config 1 in 5G specific scenarios (asynchronous multi-user uplink and multi-service coexistence) while requiring the same complexity. Besides, the receiver processing has a small impact on system performance while windowing (BF-OFDM) is much less computation-hungry than a filter-bank (FFT-FBMC). However, the BER performance is degraded because of the time-relaxed prototype filter. Config 2 is therefore more sensitive to fast fading even if the performance penalty is canceled with LDPC channel coding.

On the other hand, config 3 which seems interesting with its narrow subband filtering does not provide excellent results in the considered evaluation scenarios. Indeed, the performance gain in 5G specific scenarios is not noticeable while the required complexity is twice as much.

4.3 Conclusion

In this chapter, FFT-FBMC and BF-OFDM has been configured according to 5G NR system parametrization. A multi-service scheme is proposed so that a unique filter-bank can serve all the numerologies of each of two frequency ranges. It limits the complexity at the base station side as a unique filter-bank can serve all the users regardless of the numerology in use. Complexity at the UE side is also limited thanks to the subband processing. Last but not least, the two schemes are complex orthogonal (at least in approximation) which allows a straightforward re-use of 5G NR known-how techniques.

Even if both schemes provide interesting performance gains with respect to legacy OFDM, they do not ensure the best trade-off between performance gain and complexity increase with respect to the other proposed solutions. Indeed, for instance WOLA-OFDM is a very simple solution and provides similar performance gain. Although the proposed scheme are made very flexible especially in time

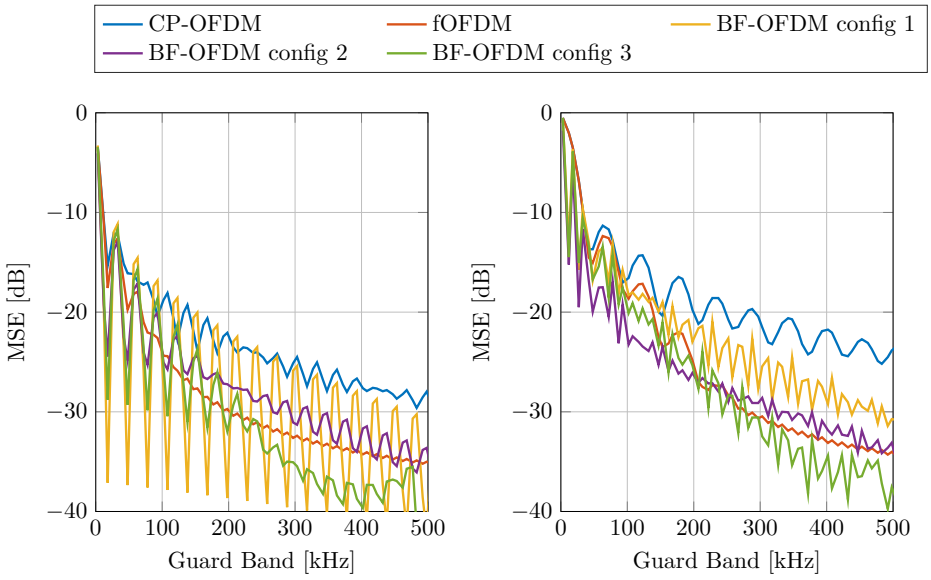

Figure 4.11: Mean Square Error per subcarrier [in dB] for BF-OFDM with $\mu = 1$ over $\mu = 0$ (left) and $\mu = 2$ over $\mu = 0$ (right)

by supporting any CP length thanks to the symbol time shifting, the 5G NR frequency/time grid is stringent and favors OFDM-based waveforms. It is indeed not easy to filter at the RB level because 12 is not a power of two. It thus forces to support subband of 4 subcarriers which poses high constraint on the time localisation of the prototype filter. Besides, considering subband larger than RBs as considered in the chapter reduces the bandwidth use efficiency which is undesirable.

Nonetheless, both FFT-FBMC and BF-OFDM exhibit appealing features. First, all techniques ranging from channel estimation to MIMO codes that are used in OFDM can be straightforwardly re-used for both scheme. Then, the proposed schemes simultaneously support different inter-subcarrier spacings and symbol durations with a low-complex transmission scheme based on a unique filter-bank. It allows dynamic adaption of link numerology depending on its needs and propagation impairments which is an appealing feature for future wireless technologies. Besides, BF-OFDM is backward compatible with OFDM-based systems which represents most of the wireless systems in use nowadays. In addition to that, the performance gain can be further improved by considering FFT-FBMC receiver. As a consequence, both FFT-FBMC and BF-OFDM demonstrates strong assets to be considered in future wireless technologies.

4.3.1 Contribution

A first adaption of FFT-FBMC and BF-OFDM to 3GPP 4G LTE with performance evaluation is studied in [91]: D. Demmer, R. Zakaria, R. Gerzaguet, J.-B. Doré, and D. Le Ruyet, "Study of OFDM Precoded Filter-Bank Waveforms," *IEEE Transactions on Wireless Communications*, pp. 1–1, 2018.

The adaptation of the proposed schemes to 5G NR systems is proposed in [96]:D. Demmer, R. Zakaria, J.-B. Doré, R. Gerzaguet, and D. Le Ruyet, "Filter-bank OFDM transceivers for 5G and beyond," in *Proc. Asilomar Conference on*

Signals, Systems, and Computers, Oct 2018.

5 Preliminary results on Lattice Reduction aided MIMO receivers

In the four first chapters, we concentrate on FR1-related challenges like maximizing the bandwidth use while multiplexing non-orthogonal subbands. Above 6-GHz communications come with its own challenges such as efficiently support large MIMO configurations (up to 8×8), beamforming or phase noise robustness. In this last chapter, the study of MIMO receivers is addressed.

The goal is to preserve an efficient implementation so as to support computation-hungry algorithm such as beamforming. It is the reason why Linear Detection (LD) is considered. However, the performance of linear MIMO receiver degrades with the number of antennas. Lattice-Reduction can be envisioned to assist linear receiver and improve their performance. Indeed, Lattice-Reduction-aided (LR-aided) MIMO receivers significantly outperform classical linear receivers schemes for uncoded systems. The results on LR-aided receivers are not only interesting for OFDM systems as they ensure a low-complex implementation for MIMO receivers but also for FBMC-OQAM. Indeed, LD can be straightforwardly applied on FBMC-OQAM receivers but lattice reduction can help attenuating the intrinsic interference and thus provides improved performance as observed in [97].

The adaptation of LR techniques to coded systems is nonetheless not straightforward. Indeed, the typical lattice demapping schemes used by LR-aided receivers is based on a round operation which acts like hard decoding and therefore prevents the proper determination of soft bits. In this chapter, a new lattice demapping algorithm, named Successive Interference Cancellation (SIC) is proposed. It guarantees a correct estimation of likelihood ratio metrics and even to re-use the simplifications used in the conventional linear systems. This chapter presents a preliminary work where only OFDM systems are addressed.

5.1 Introduction to lattice reduction

A lattice in $\mathbb{R}^n$ is the set of all linear combinations with integer coefficients of a given basis of $\mathbb{R}^n$. A typical lattice L in $\mathbb{R}^n$ can be expressed as in (5.1) where $V = \{v_1, v_2, .., v_n\} \in \mathbb{R}^{m \times n}$ is a basis of $\mathbb{R}^n$.

$$L = \left\{ \sum_{i=1}^{n} a_i v_i | a_i \in \mathbb{Z}^n \right\} \tag{5.1}$$

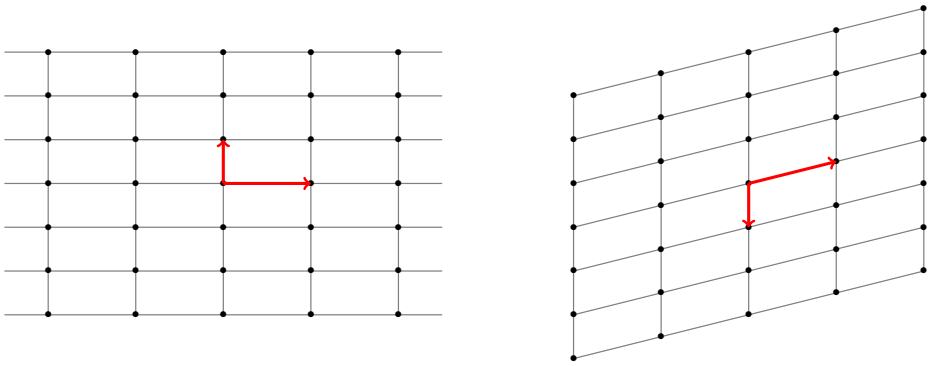

Figure 5.1: Lattice examples.

Examples of two-dimensional lattices are given in Figure 5.1 with the conventional basis in $\mathbb{R}^2$ and $\begin{pmatrix} 2 \\ 0.5 \end{pmatrix} \begin{pmatrix} 0 \\ -1 \end{pmatrix}$.

The same lattice can be generated by several distinct bases. Indeed if V is a basis, so is $\tilde{V} = VT$ for any unimodular matrix T[98]. T is called the basis changing matrix. However, the absolute value of the determinant of the basis vectors v_i is uniquely determined by L. This indicator is called the (co)volume of the lattice and is denoted by $\mathrm{vol}(L)$. In finite dimension, it can be defined as the square root of the determinant of the Gram Matrix of the basis as well.

$$\begin{aligned} \mathrm{vol}(L) &= |det(V)| \\ &= \sqrt{det(V^T V)} \end{aligned} \tag{5.2}$$

Reducing a lattice is searching for a "nice" basis having special properties. To achieve this goal, a suitable mathematical definition of such a basis and an algorithm to find it are required. A typical "nice" basis is close to be orthogonal and composed of short vectors. The orthogonality deficiency is used as indicator for the first property and is defined as follows. It measures the degree of orthogonality of the basis V. $\mathrm{od}(V)$ is always greater or equal to 1, with the equality satisfied only and only if V is perfectly orthogonal.

$$\mathrm{od}(V) = \frac{\Pi_{i=1}^{n} ||v_i||_2}{\mathrm{vol}(L)} \tag{5.3}$$

When it comes to the second property, the i^{th} Minkowski's successive minima $\lambda_i(L)$ is the radius of the smallest closed ball centered at the origin containing at least i independent lattice vectors. Hence, $\lambda_1(L)$ represents the Euclidean length of the shortest non-zero vector of L. For low dimensions, a basis of L is said to be reduced if it satisfies the minima $\lambda_i(L)$. However, for $n \geq 5$, such vectors do not necessarily form a basis.

Now that mathematical definitions are given, reduction algorithms can be introduced.

5.1.1 Hermite reduction

A lattice basis $V \in \mathbb{R}^{m\times n}$ is said to be Hermite-reduced (or size-reduced) if its R matrix of the QR decomposition satisfies the condition (5.4). The Algorithm 1 performs the size reduction and therefore ensures condition (5.4).

$$|r_{i,j}| \leq \frac{1}{2}|r_{i,i}|, \quad \forall\ 1 \leq i \leq j \leq n \tag{5.4}$$

Algorithm 1 Size-Reduction Algorithm

Inputs: $R \in \mathbb{R}^{n\times n}$, $T \in \mathbb{Z}^{n\times n}$
Outputs: R satisfying (5.4), T consequently updated

1: **for** $1 \leq i \leq j \leq n$ **do**
2: **if** $|r_{i,j}| > |r_{i,i}|/2$ **then**
3: $t \leftarrow \lfloor r_{i,j}/r_{i,i} \rceil$
4: $R(1:i,j) \leftarrow R(1:i,j) - tR(1:i,i)$
5: $T(:,j) \leftarrow T(:,j) - tT(:,i)$
6: **end if**
7: **end for**

5.1.2 HKZ reduction

A lattice basis V is called Hermite-Korkine-Zolotarev(HKZ)-reduced if it is size-reduced and its R matrix satisfies the property (5.5) where $L\left(R(i:n,i:n)\right)$ is the lattice generated by the basis $R(i:n,i:n)$. In other words, the diagonal elements of the R matrix are the shortest non-zero vector of the lattice generated by the submatrix.

$$r_{i,i} = \lambda_1\left(L\left(R(i:n,i:n)\right)\right), \quad \forall\ 1 \leq i \leq n \tag{5.5}$$

It has been proved that the length of the HKZ-reduced vectors can approximate the Minkowski's successive minima with a polynomial factor [99].

$$\frac{4}{i+1} \leq \frac{||v_1||_2^2}{\lambda_i^2(L)} \leq \frac{i+3}{4}, \quad \forall\ 1 \leq i \leq n \tag{5.6}$$

5.1.3 Minkowski reduction

A lattice basis V is said to be Minkowski-reduced if the norm of each v_i is the shortest over all lattice vector such as $\{v_1,..,v_i\}$ can be extended as a basis of L. A Minkowski-reduced basis always ensures the fourth first Minkowski's minima [99]. However, for higher dimensions the shortest length condition deficiency exponentially increases.

$$1 \leq \frac{||v_1||_2^2}{\lambda_i^2(L)} \leq \max\{1,(5/4)^{n-4}\} \quad \forall\ 1 \leq i \leq n \tag{5.7}$$

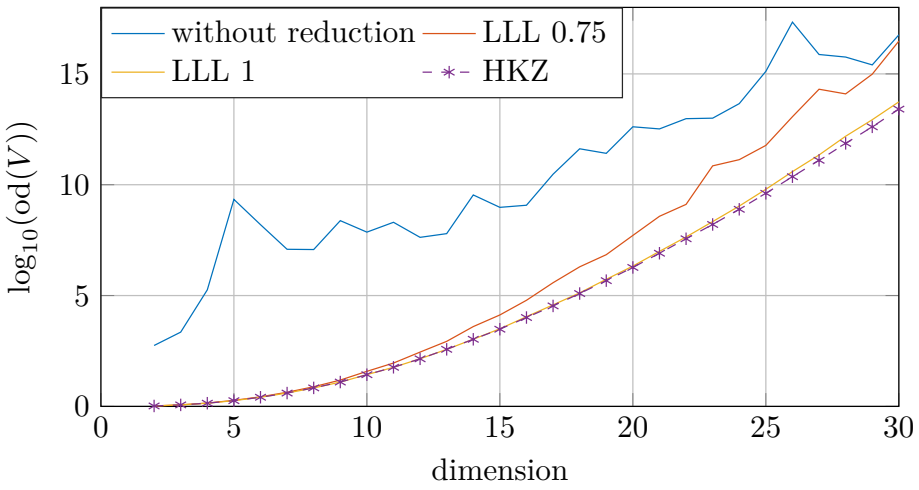

Figure 5.2: Performance analysis of HKZ, LLL 0.75 and LLL 1 reduction algorithms

5.1.4 LLL reduction

A lattice basis V is called Lenstra-Lenstra-Lovász(LLL)-reduced if it is size-reduced and its R matrix satisfies the condition (5.8) where $\delta \in]1/4, 1]$. Usually, $\delta = 1$ is not chosen as the algorithm does not guarante a polynomial running time [100].

$$r_{i,i}^2 + r_{i-1,i}^2 \geq \delta r_{i-1,i-1}^2 \tag{5.8}$$

LLL-reduced vectors approximate the Minkowski's minima with an exponential factor as well [99].

$$\left(\frac{1}{\delta - 1/4}\right)^{i-1} \leq \frac{||v_i||_2^2}{\lambda_i(L)} \leq \left(\frac{1}{\delta - 1/4}\right)^{n-1} \tag{5.9}$$

The LLL algorithms has also been extended to complex lattices providing similar error performance than the conventional version but with a reduced complexity [101].

5.1.5 Reduction algorithms performance

The reduction performance of the aforementioned reduction algorithms have been assessed. A random basis V is generated where the entries are independent real Gaussian random variables. Then, HKZ and LLL are applied and the orthogonality deficiency of the resulting matrices $\tilde{V}$ is measured. Minkowski performance is not evaluated because it is too computation resource hungry. The results are depicted in Figure. 5.2.

One can observe that for small dimensions the LLL behaves as an exact Shortest Vector Problem (SVP) algorithm. However, the performance degrades when the dimension of the basis increases.

5.2 Application to MIMO systems

5.2.1 System Model

A $N_T \times N_R$ MIMO system can be expressed as in (5.10) where s is the channel input (size $N_T \times 1$) and y the channel output ($N_R \times 1$). H is the channel matrix ($N_R \times N_T$) and n the additive noise ($N_R \times 1$). The constellation symbols are from a conventional 2^M-QAM constellation where each symbol can be expressed as $\alpha\left((2a+1)+i(2b+1)\right)$ where $(a,b) \in [-\frac{M}{2}, \frac{M}{2}-1]^2$ and α is the constellation normalization coefficient ensuring that the average power of the transmitted constellation is unitary (assuming equiprobable transmition of possible symbols).

$$y = Hs + n \tag{5.10}$$

The noise is assumed to be zero-mean white Gaussian with independent realisations. Hence, its covariance matrix R_n equals $\sigma_n^2 I_{N_R}$ where σ_n^2 is the noise variance and I_{N_R} is the identity matrix of size N_R. The channel inputs are assumed to be independent and taken from a normalized constellation. A uniform power allocation among all the streams is considered. Therefore, the covariance matrix of s is diagonal: $R_s = \frac{1}{N_T} I_{N_T}$. The channel matrix H is assumed to be composed of independent random variables.

For this study, only open-loop spatial-multiplexing is addressed with full Channel State Information (CSI) at the receiver. It is also assumed that $N_R \geq N_T$ and that a perfectly orthogonal waveforms is used. When it comes to MIMO detection, the Linear Detection (LD) is considered. It consists in separating the N_T incoming streams by means of linear combinations among the N_R received signals. It gives the model given in (5.11).

$$\begin{aligned} r &= Wy \\ &= WHs + Wn \end{aligned} \tag{5.11}$$

The detection matrix W is determined according the criterion in use. The zero-forcing (ZF) (5.12) entirely cancels the inter-stream interference. The minimum-mean-square-error (MMSE) (5.13) finds a better trade-off between inter-stream interference cancellation and noise enhancement. The MMSE can also be expressed as the pseudo-inverse of the channel matrix via a change in the system model [102][103]. And the matched-filter (MF) (5.14) avoids matrix inversion.

$$W_{\text{ZF}} = (H^H H)^{-1} H^H \tag{5.12}$$

$$W_{\text{MMSE}} = (H^H H + N_T \sigma_n^2 I_{N_R})^{-1} H^H \tag{5.13}$$

$$W_{\text{MF}} = \frac{1}{N_T} H^H \tag{5.14}$$

However, the performance of LD is limited by the orthogonality deficiency of the channel matrix H[102]. Therefore the fundamental idea behind lattice-reduction-aided LD is to reduce the channel basis H into $\tilde{H}$. The detection matrix W is then determined as a function of $\tilde{H}$ which is reduced. By considering a new

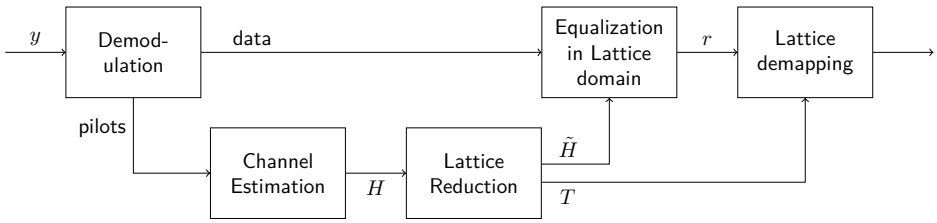

Figure 5.3: LR-aided MIMO receiver

channel input $z = T^{-1}s$ the system model becomes what follows:

$$\begin{aligned} r &= WHTT^{-1}s + Wn \\ &= W\tilde{H}z + Wn \end{aligned} \tag{5.15}$$

A MIMO LR-aided receiver scheme is depicted in Figure 5.3. The demodulation estimates the transmitted symbol sequence from the received signal and separates the pilots from the data symbols. With the pilot symbols, the conventional channel estimation is performed which estimates the channel matrix. The reduction of the channel matrix is then performed which determines the reduces channel matrix $\tilde{H}$ and the corresponding T matrix. The equalizer (assumed linear) determines the equalization matrix W from the reduced channel matrix and applies the correction matrix to data matrix. The lattice demodulation stage retrieves the estimated constellation symbols from the estimated and equalized lattice points r. The lattice demapping techniques will be further described later on. The estimated constellation symbol sequence can then bit demapping into the estimated bit sequence as in classic receivers.

The theoretical performance gain will now be studied through a capacity analysis.

5.2.2 MIMO ergodic capacity

The capacity of a channel corresponds to the maximum data rate that ensures an asymptotically small error probability[104]. Shannon defined it as the mutual information maximized over the transmitted signal distributions as shown in (5.16) where S and Y are respectively the channel input and output and $f(.)$ denotes the probability density function.

$$C = \max_{f(s)} I\left(S;Y\right) \tag{5.16}$$

The mutual information can be written as a function of the entropies in the channel output Y and the conditionnal output $Y|S$ as given in (5.17). By definition, the entropy $H(Y|S)$ corresponds to the entropy in the noise $H(N)$.

$$I\left(S;Y\right) = H(Y) - H(Y|S) \tag{5.17}$$

In [105], it is shown that the mutual information is maximized when the channel input s and the noise n are a zero-mean circularly symmetric Gaussian vari-

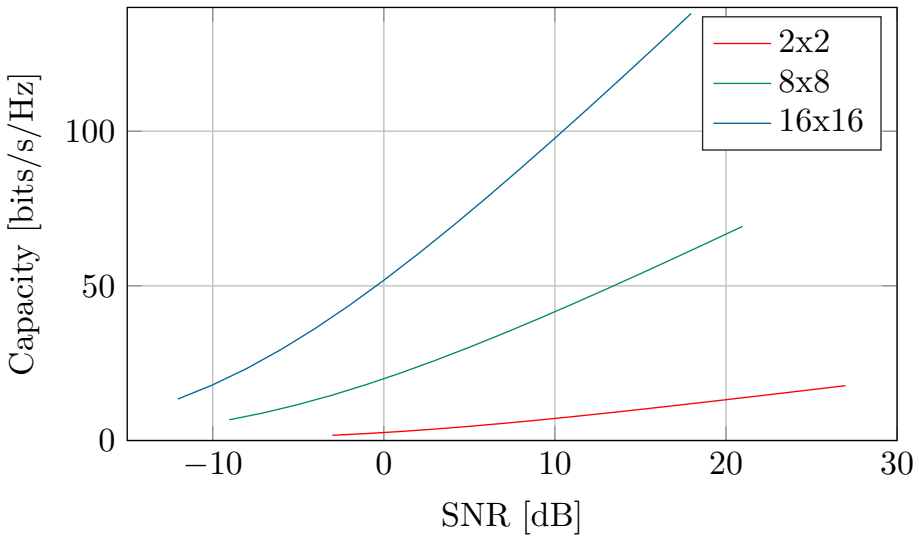

Figure 5.4: Ergodic capacity for different MIMO configurations for reduced Gaussian channels

ables. The resulting capacity is given in (5.18) where $R_x = E\left[xx^H\right]$ is the covariance matrix of the variable x and B is the band of the signal (in hertz).

$$C = B\log_2\left(\frac{\det(R_y)}{\det(R_n)}\right) \tag{5.18}$$

To determine the capacity, the power allocation among the antenna streams that maximized R_y needs to be found. As we assume that there is no CSI at the transmitter side, the best possible allocation is to uniformly distribute the power among all the available streams. It leads to the capacity expression given in (5.19). The resulting ergodic capacities for different MIMO system sizes and Gaussian channels are depicted in Figure 5.4.

$$\begin{aligned} C &= B\log_2\left(\frac{\det\left(\frac{1}{N_T}HH^H + \sigma_n^2 I_{N_T}\right)}{\det(\sigma_n^2 I_{N_T})}\right) \\ &= B\log_2\left(\det\left(\frac{1}{N_T}HH^H + \sigma_n^2 I_{N_T}\right)(\det(\sigma_n^2 I_{N_T}))^{-1}\right) \\ &= B\log_2\left(\det\left(\frac{1}{N_T}HH^H + \sigma_n^2 I_{N_T}\right)\det(\frac{1}{\sigma_n^2} I_{N_T})\right) \\ &= B\log_2\left(\det\left(\frac{1}{N_T\sigma_n^2}HH^H + I_{N_T}\right)\right) \end{aligned} \tag{5.19}$$

5.2.3 Linear receiver capacity

The study is dedicated to the ZF receivers (pseudo-inverse version [102][103]) receivers. Those detectors perfectly cancel the channel matrix (*i.e.* WH or $W\tilde{H}$ for LR-aided is the identity matrix). It greatly simplifies the expression of the system model (no inter-antenna interference). It leads to the straightforward capacity expression (5.20)[106] where $(\beta_N)_{i,i} = (WW^H)_{i,i}$. The given expression

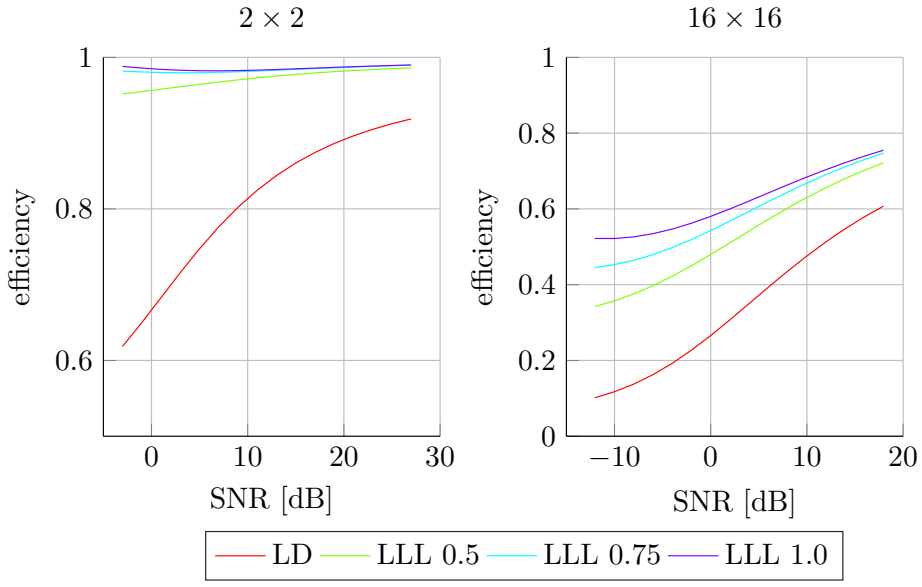

Figure 5.5: Receiver efficiencies for 2×2 and 16×16 MIMO configurations with ZF-based detection

holds for both LD and LR-aided LD receivers assuming that T is the identity matrix in non LR-aided configuration.

$$C = B \log_2 \left(\frac{\det(1/N_T T^{-1}(T^{-1})^H + \sigma_n^2 \beta_N}{\det(\sigma_n^2 \beta_N)} \right) \tag{5.20}$$

The receiver capacity needs to be compared with the ergodic capacity. To do so, the receiver efficiency, defined as the ratio between the receiver capacity et the ergodic capacity is defined. Figure 5.5 depicts the receiver efficiencies for LD and LLL-based LR-aided receivers. We can observe that the efficiency of a LD receiver decreases when the MIMO size increases. However LR-aided detection significantly improves the capacity of LD receivers.

The analysis that has been carried out in this section focuses on the theoretical performance of the lattice-reduction based receivers. We will now have a look at the practical performance results.

5.2.4 Lattice demapping techniques

The question now is how to make the symbol decisions in the lattice domain ? Indeed, it has been observed in the previous section that the decisions in the lattice domain are more reliable (higher capacity). However, the entries of z are dependent of each other which makes the decision complex to perform.

A first solution is simply to round the estimated symbols (after the application of the detection matrix W) and then to apply T in order to come back to the constellation domain [103][106].

$$\hat{s}_{\text{round}} = \alpha T \lfloor r/\alpha \rceil \tag{5.21}$$

The second proposed solution is to round according to the parity of the entries of z. Indeed, we know that the s entries are all odd. Therefore, z_i is even (resp. odd) only and only if $\sum_j (T^{-1})_{i,j}$ is even (resp. odd).

$$\hat{s}_{i,\text{round-par}} = \begin{cases} \alpha T \lfloor r_i/\alpha \rceil_{\text{odd}} & \text{if } \sum_j (T^{-1})_{i,j} \text{ odd} \\ \alpha T \lfloor r_i/\alpha \rceil_{\text{even}} & \text{otherwise} \end{cases} \tag{5.22}$$

A third and novel solution is proposed which is a successive noise cancellation algorithm. For this solution, real MIMO system model is used. The conversion for vectors and matrices is shown below where Re and Im respectively denote the real and imaginary parts. The subscript $_r$ denoting a real system model is omitted later now for sake of clarity.

$$y_r = \begin{bmatrix} \text{Re}(y) \\ \text{Im}(y) \end{bmatrix} \tag{5.23}$$

$$H_r = \begin{bmatrix} \text{Re}(H) & -\text{Im}(H) \\ \text{Im}(H) & \text{Re}(H) \end{bmatrix} \tag{5.24}$$

The algorithm is labeled Successive Interference Cancellation (SIC) is fuand lly described in Algorithm 2.

Algorithm 2 Successive Interference Cancellation algorithm

Inputs: $r \in \mathbb{R}^{2N_T \times 1}$, $T \in \mathbb{Z}^{2N_T \times 2N_T}$, $\mathcal{E} \in \mathbb{R}^{+*}$
Outputs: $\hat{s}_{\text{SNI}}$

1: $c \leftarrow Tr/\alpha$
2: $A \leftarrow TT^T$
3: **if** A is non diagonal **then**
4: $\quad I \leftarrow$ according to (5.25)
5: $\quad$ **while** $\exists i$ such as $c_i > s_{\max} + \mathcal{E}$ **do**
6: $\quad\quad k \leftarrow \arg\max_i (|c_i| - s_{\max} - \mathcal{E})$
7: $\quad\quad c \leftarrow c - A_k \text{sign}(c(k)) \mathcal{E}/I_k$
8: $\quad$ **end while**
9: **end if**
10: $\hat{s}_{\text{SNI}} \leftarrow \alpha \times c$

Indeed, by comparing the coordinates of $|Tr\alpha|$ with the $s_{\max}$ (which is the maximum real constellation amplitude), it is possible to detect a possible strong noise realisation. Unlike, in the conventional (i.e. constellation) domain, it is interesting to compensate this error in the lattice domain as it will impact (and therefore correct) possibly more than one symbol coordinates as the lattice basis may not be orthogonal.

The Gram matrix A is first computed (line 2). If the basis is orthogonal (i.e. all basis vectors are independent) then A is diagonal. However LRA often returns near-perfect basis. Hence A is likely to be non diagonal. As stated above, the proposed algorithm is specifically designed to run in the latter case. The vector I

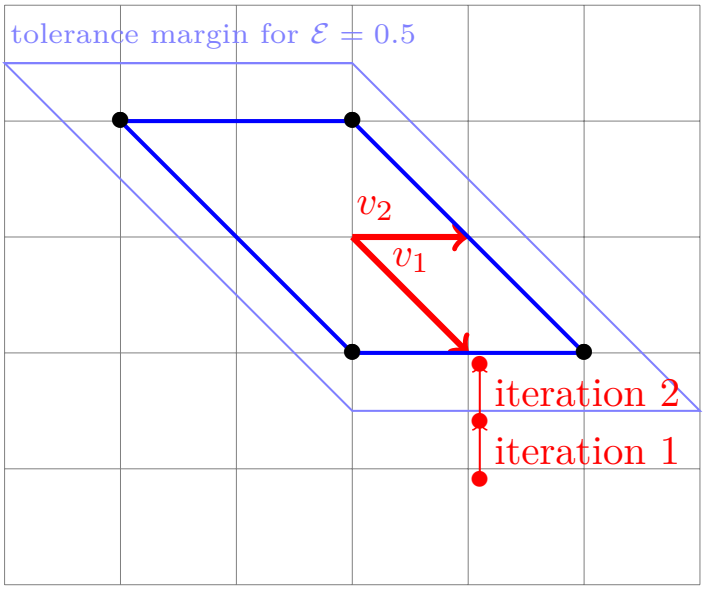

Figure 5.6: Example of realisation of SCI algorithm.

(size $2N_T \times 1$) stores the highest inner product for each basis vector, i.e.:

$$I_k = \max_j | < v_k; v_j > | \tag{5.25}$$

$\mathcal{E}$ is an input parameter of the algorithm that denotes the error tolerance. As long as one coordinate violates the tolerance, the error step projected over A_k is removed. When A is non diagonal then A_k may have more than one non-zero elements. Therefore cancelling the error for coordinate k corrects the other coordinates as well.

5.2.5 Illustration of SIC algorithm

The proposed algorithm will be illustrated with an example and the figure (5.6) to explain how it works.

Let consider a BPSK constellation $\mathcal{S} = [1, -1]$ and the real change of basis matrix $T = \begin{bmatrix} 0 & -1 \\ 1 & 1 \end{bmatrix}$. We can determine easily determine that $T^{-1} = \begin{pmatrix} 1 & 1 \\ -1 & 0 \end{pmatrix}$. Therefore, the basis of the lattice is $(v_1, v_2) = \begin{pmatrix} 1 \\ 0 \end{pmatrix} \begin{pmatrix} 1 \\ 1 \end{pmatrix}$. As a consequence, the 4 lattice points corresponding to the constellation symbols are the following :

$$\mathrm{L}(\mathcal{S}) = \begin{bmatrix} -1 & -1 & 1 & 1 \\ 0 & 2 & 0 & -2 \end{bmatrix} \tag{5.26}$$

The Gram matrix A is then computed which leads to (5.28). The matrix is not diagonal meaning that the lattice basis is not orthogonal. We can then determine the vector I storing the highest scalar product values as shown below:

$$A = \begin{bmatrix} 1 & -1 \\ -1 & 2 \end{bmatrix} \tag{5.27}$$

$$I = \begin{bmatrix} 1 \\ 2 \end{bmatrix} \tag{5.28}$$

A simple case is then presented:

- Let assume that the received lattice point is $r/\alpha = \begin{pmatrix} 1.1 \\ -2.1 \end{pmatrix}$ which is added to the figure (5.6).
- The coordinates in the constellation domain are first computed $c = Tr = \begin{pmatrix} 2.1 \\ -1 \end{pmatrix}$.
- A tolerance margin $\mathcal{E} = 0.5$ is considered. It leads to $|c| - \begin{pmatrix} 1+0.5 \\ 1+0.5 \end{pmatrix} = \begin{pmatrix} 0.6 \\ < 0 \end{pmatrix}$. There is an error exceeding the tolerance margin on the first coordinate.
- The algorithm cancels the exceeding error $c = \begin{pmatrix} 2.1 \\ -1 \end{pmatrix} - \begin{pmatrix} 1 \\ -1 \end{pmatrix} \times 0.5 = \begin{pmatrix} 1.6 \\ 0.5 \end{pmatrix}$. One can notice that the maximum coordinate correction is limited to $\mathcal{E}$.
- A second iteration occurs because the error still exceeds the tolerance margin. It lead to $c = \begin{pmatrix} 0.6 \\ -0.5 \end{pmatrix} - \begin{pmatrix} 1 \\ -1 \end{pmatrix} \times 0.5 = \begin{pmatrix} 1.1 \\ 0 \end{pmatrix}$.
- There is no longer error to correct. The algorithm stops.

As shown with this example, the coordinates may not be reliable in lattices to estimate distances because the basis is not orthogonal and thus noise/interference propagation may occur. The proposed algorithm corrects this issue when strong noise/interference is sensed.

5.2.6 Performance evaluation

The performance of the aforementioned demapping techniques are now assessed for an uncoded OFDM system and Rayleigh distributed channels. The results are depicted in Figure 5.7. The throughput is evaluated according to the expression (5.29) for codeblocks of Q bits and assuming perfect Modulation and Coding Scheme (MCS) swapping. One can observe that the simple "round" demapping (5.21) actually performs worse than the LD because of the naive lattice point selection. On the contrary, more intelligent demapping like the round according the parity (5.22) and the SIC algorithm (Algorithm 2) provides a significant performance gain. However, SIC does not significantly outperforms the parity-round lattice demapping techniques. Nonetheless, it allows a straightforward computation of likelihood metrics for coded systems. This case is addressed in the next section.

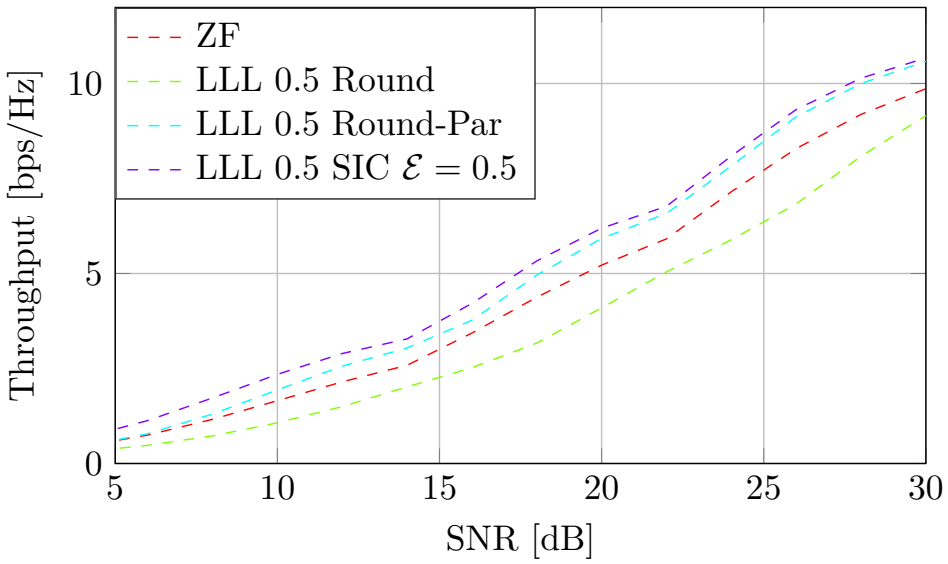

Figure 5.7: Throughput for MIMO 2x2 LD and LR-aided receivers with different demapping techniques.

$$\text{Throughput} = \text{TxRate} \times (1 - \text{BER})^{Q} \tag{5.29}$$

5.3 Extension to coded systems

5.3.1 Maximum Likelihood Detection

In this section, the lattice detection is applied to coded systems. It poses a new challenge: the soft output generation. Indeed in coded systems, soft information, or Log Likelihood Ratio (LLR), needs to be computed for each received bit. The sign of the LLR indicates the most likely bit value (positive for 1 and negative otherwise) and its absolute value indicates the reliability of the estimation (the higher the more reliable). The expression of the LLR can be expressed as shown in (5.30) assuming no priori information of transmitted bit sequence. Regarding the notations for the bits, $b_{m,q}$ represents the q$^{\text{th}}$ bits of s_m (time and frequency indices are omitted for sake of simplicity).

$$L(b_{m,q}) = \ln \frac{P(b_{m,q} = 1|y)}{P(b_{m,q} = 0|y)} = \ln \frac{P(y|b_{m,q} = 1)}{P(y|b_{m,q} = 0)} \tag{5.30}$$

The latter conditional probability can be written as the sum of probabilities as shown in (5.31) where $\mathcal{S}^X_{m,q}$ is the constellation symbol sets admitting $b_{m,q} = X$ (either 0 or 1).

$$p(y|b_{m,q} = X) = \sum_{u \in \mathcal{S}^X_{m,q}} p(y|s = u) \tag{5.31}$$

A common approximation known as the max log consists in considering only the largest of the elements of the sum. The expression therefore becomes as shown

in (5.32). It leads to the LLR expression given in (5.33). However, the max-log approximation still requires a search over the set $\mathcal{S}^X_{m,q}$. The solution thus becomes computationally complex for systems with large number of antennas and large constellation s.

$$p(y|b_{m,q} = X) \approx \max_{u \in \mathcal{S}^X_{m,q}} p(y|s = u) \tag{5.32}$$

$$L(b_{m,q}) = \frac{1}{2\sigma_n^2} \left(\min_{u \in \mathcal{S}^1_{m,q}} ||y - Hu||^2 - \min_{u \in \mathcal{S}^0_{m,q}} ||y - Hu||^2 \right) \tag{5.33}$$

5.3.2 Max-log LD

LD is a low complex alternative to MLD. The idea is to compute the soft information metrics on the received signal r after application of the LD matrix W as introduced in II.A. An approximation of the LLRs can be computed thanks to linear equations as shown in [14].

However, LD changes the noise statistics. Let $\sigma^2_{n,m}$ denotes the noise variance for r_m. Its expression is given in (5.34). Thus the LLR expression can be expressed as in (5.35).

$$\sigma^2_{n,m} = \sigma_n^2 \sum_{i=1}^{N_T} |W_{m,i}|^2 \tag{5.34}$$

$$L(b_{m,q}) = \frac{1}{2\sigma^2_{n,m}} \left(\min_{u \in \mathcal{S}^1_{m,q}} ||r - u||^2 - \min_{u \in \mathcal{S}^0_{m,q}} ||r - u||^2 \right) \tag{5.35}$$

However typical rectangular Voronoi regions are required to use the max-log LD. It can barely be adapted to LR-aided systems. Indeed, it is not possible to use the demapping techniques introduced in Section II.D as they rely on a round operator which must not be used in soft decoding (loose of information). Nonetheless, the SIC algorithm (Algorithm 2) can be used. Indeed it can be seen as an "update" of r without any round operator. It is sufficient to apply the unimodular T matrix after the execution of the algorithm to come back to the conventional Voronoi regions. By applying the SIC, the noise variance also changes at each iteration and becomes as expressed in (5.36) where m is the layer index and the second term corresponds to the correction factor of line 7 in Algorithm 2. The LLR expression is the same as in (5.35) when combined with the noise variance given in (5.36).

$$\sigma^2_{n,m} = \sigma_n^2 \sum_{i=1}^{N_T} |W_{m,i}|^2 + \sum_{\text{iterations}} (A(k,m)\text{sign}(c(k))\mathcal{E}/I_k)^2 \tag{5.36}$$

The results are depicted in Figure 5.8 for turbo-coded OFDM systems (with blocks of 6144 bits and 8 iterations) where the LR-aided receivers work with the proposed algorithm and compared with LD MAP receivers. The evaluation considers both perfect likelihood metrics (with circle marks) and the linear approximation [14] (with asterix marks). One can observe that the LR-aided with SIC algorithm provides a significant performance gain in both cases. It seems worth observing that LR-aided with approximated LLRs even outperforms ideal LD MAP systems.

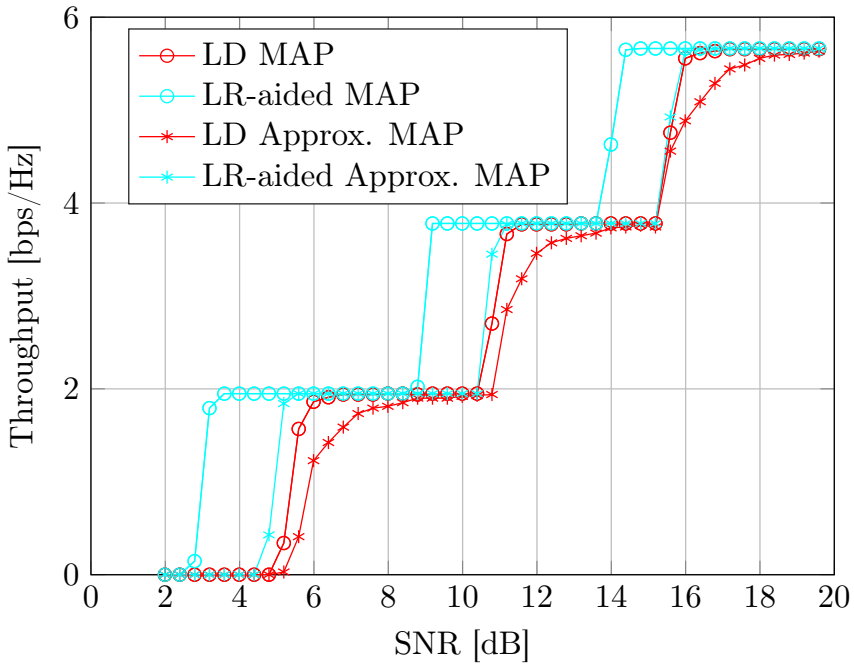

Figure 5.8: Thoughput for MAP 2x2 receiver for turbo-coded OFDM systems.

The other lattice demapping techniques can be not considered in this evaluation because of the round operation.

5.3.3 Suboptimal Algorithms for LR-aided LD

When it comes to LR detection, alternatives to MLD also exist. In order to reduce the complexity, the idea is to consider suboptimal algorithms when the candidate list χ is reduced [107].

$$p(y|b_{m,q} = X) = \begin{cases} \max_{u \in \mathcal{S}^X_{m,q} \in \chi} p(y|s = u) & \mathcal{S}^X_{m,q} \in \chi \neq \emptyset \\ \epsilon & \text{otherwise} \end{cases} \tag{5.37}$$

A simple suboptimal algorithm is the Fixed Perturbation (FP) [107]. First a lattice point is selected. Then the candidate set is composed of all the lattice points admitting a maximum perturbation of 1 for each coordinate with respect to the initial point. The reduced candidate set list is then composed of $4N_T + 1$ entries. It is an adaptation of sphere-decoding for LR-aided receivers.

Here the lattice demapping techniques are used to estimate the reference lattice point. Then the soft outputs are generated as in classic sphere-decoding systems.

The results are depicted in Figure 5.9 for the same turbo-coded OFDM systems. One can observe that the LR-aided with SIC algorithm provides a significant performance gain. The difference with respect to the parity-round techniques is increased than for uncoded systems.

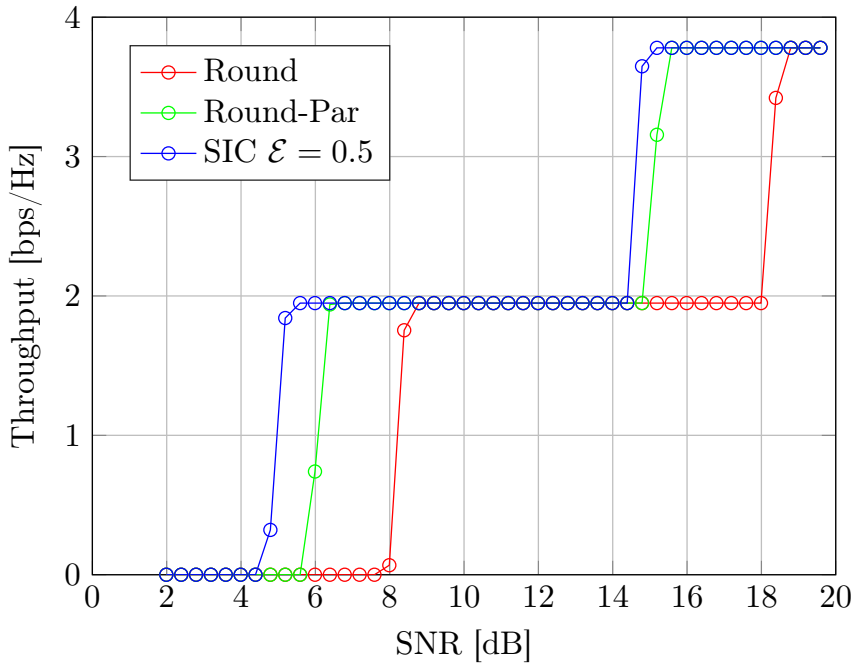

Figure 5.9: Throughput for FP 2x2 receiver

5.4 Conclusion

Lattice reduction can be used to improve the performance of linear MIMO receivers. However, it badly combines with soft decoding which prevents the use of channel coding. Some sub-optimal solutions exist and consist in extending the concept of sphere decoding for LR-aided receivers (*i.e.* like fixed perturbation technique).

A novel demapping algorithm, Successive Interference Cancellation (SIC), is proposed in this work. First, soft likelihood metrics can be easily estimated as the proposed algorithm does not include any round operator. And in addition to that, commonly used linear approximation for LLR estimation used in MAP receivers can be applied as well which further improve the performance of the latter receiver schemes.

The purpose of this chapter is twofold. First, the study of multiple antenna receiver for large MIMO configurations is addressed. As aforementioned, it may have positive consequence on 5G MIMO systems. However, this chapter also aims at providing enhanced MIMO receiver for FBMC/OQAM modulations with improved interference cancellation. However, the adaption to FBMC/OQAM receivers has not been addressed in this study and is proposed as thesis perspectives.

Contribution A patent has been granted for the proposed Successive Interference Cancellation algorithm at the French intellectual property protection agency INPI.

6 Conclusion

The development of forthcoming generations of wireless technology poses an important demand for air interfaces and waveforms with improved spectral confinement and increased flexibility. It is indeed required to efficiently and simultaneously serve the diverse requirements of the large range of supported applications. 5G initiates this transition from high data rate downlink traffic to heterogeneous networks.

OFDM has proven to be very effective for broadband systems. Indeed, by dividing large bandwidths into a set of narrow bands, OFDM provides an inherent and efficient robustness to selective fading channels. OFDM systems easily counteract channel-induced distortion with a simple 1-tap equalizer applied in the frequency domain when cyclic prefix is considered. Besides, the frequency division inherently provides frequency multiple access to users by assigning subsets of the total bandwidths to individual users. As a consequence, OFDM is a suitable solution to serve multiple high data-rate users thanks to its high spectral efficiency and implementation-efficient scheme. However, OFDM is not appealing when it comes to multiplex different types of signal. Indeed considering different signal configurations breaks the orthogonality of the OFDM which generates inter-user interference. Two solutions can be envisioned to alleviate this problem. First, spatial filtering, *i.e.* beamforming, can be considered. This solution is used in 5G NR above 6 GHz communications but requires the use of large MIMO configurations. The second solution is to ensure user isolation is the frequency domain. It is interesting for sub-6 GHz communications as no advanced multiple-antenna techniques is considered for those communications in 5G due to physical constraints. This solution can be efficiently implemented by jointly use frequency guard bands to space users and side lobe attenuation techniques. This solutions is studied in this work. It therefore requires an upgrade of the air interface technology.

Determining the most suitable heir of the legacy OFDM for this purpose is not straightforward. Indeed, the OFDM alternative has to ensure an ideal trade-off between performance gain, complexity increase and backward compatibility with already deployed solution. It lead to the development of so called "post-OFDM" waveforms presented in the second chapter of this manuscript. A first and pragmatic way to upgrade the 5G air interface is simply to upgrade the OFDM so as the new scheme provides enhanced side lobe rejection. The frequency filtering can be implemented in diverse way from time convolution as for fOFDM and UF-OFDM to windowing as for WOLA-OFDM. However the best trade-off

between performance gain and complexity increase is achieved by another scheme intrinsically different with the OFDM: FBMC-OQAM. A filter-bank is used as core element of the transmission scheme instead of a simple FFT which provides an efficient subcarrier-wise filtering. FBMC-OQAM provides excellent performance gain especially in 5G specific scenarios like multi-service multiplexing for a limited complexity increase. However, it exhibits two major drawbacks. First, the scheme is not complex orthogonal but its orthogonality condition is reduced to the real field. Pilot-based channel estimation must thus be adapted and STBC techniques can not be directly re-used which prevents backward compatibility with already deployed technologies.

In this work, OFDM-based precoding, an alternative of the OQAM signaling, is studied to alleviate the aforementioned drawbacks of FBMC. The proposed precoding scheme can restore the orthogonality in the complex field and thus the re-use of known-how 4G/5G techniques such as channel estimation and STBC for multiple-antenna systems. Two schemes using the proposed precoding are considered in this work: FFT-FBMC with a receiver performing the transmitter reverse processing and BF-OFDM with a simple 5G NR receiver (*i.e.* an OFDM receiver). Therefore, not only the proposed precoding ensures backward compatibility with 5G NR in terms of network techniques (channel estimation, multiple antenna schemes) but also at the receiver perspective with BF-OFDM. Indeed, BF-OFDM sastifies the receiver transparency condition. It implies that a BF-OFDM signal can be demodulated by any 5G NR receiver without any modification whatever the prototype filter parametrization in use. Different prototype filter design methods are proposed so as to increase the flexibility of the transmission schemes. Indeed, the prototype filter can be first optimised according to the intrinsic interference attenuation which ensures NPR in the complex field. However, the level of interference rejection can be strong enough to be slightly degraded so as to improve the side lobe rejection according to the Balian Low Theorem. In addition to that, a new degree of freedom has been unlocked in this study: the filter-bank rate factor. It corresponds to the ratio between the sampling rate used in the precoding stage and the sampling rate of the transmitted signal. Tuning this parameter allows to find a configuration providing a better trade-off between performance gain and complexity increase with respect to 5G NR system. The two schemes are thus highly flexible while ensuring NPR in the complex field which makes them appealing for forthcoming mobile technologies especially BF-OFDM for full backward compatibility with 5G NR receiver scheme.

The adaptation of the two studied schemes to 5G NR system specification results in interesting performance. A multi-service transmission is proposed so that an unique filter-bank can serve all the numerologies for each frequency ranges. It enables an efficient support of multi-service transmission as a base station can simultaneously serve different numerologies in the system bandwidth. The performance gain achieved by the schemes with the prototype filter providing enhanced side lobe attenuation is significant compared with 5G NR system for a limited complexity increase (ratio of 2). However, the proposed schemes do not ensure the best trade-off between performance gain and complexity increase with respect to the other proposed solutions. Indeed, even if the system models are highly flexible, the 5G NR time/frequency grid is stringent and efficiently supporting subbands of 12 subcarriers is not easy. Nonetheless, both FFT-FBMC and BF-OFDM exhibit appealing features. First, ensuring the complex orthogonality (even in approxi-

mation) allows a straightforward deployment as commonly used techniques can be directly re-used. Then, the proposed schemes simultaneously support different inter-subcarrier spacings and symbol durations with a low-complex transmission scheme based on a unique filter-bank. It allows dynamic adaption of link numerology depending on its needs and propagation impairments which is an appealing feature for future wireless technologies. Besides, BF-OFDM is backward compatible with OFDM-based systems which represents most of the wireless systems in use nowadays. In addition to that, the performance gain can be further improved by considering FFT-FBMC receiver. As a consequence, both FFT-FBMC and BF-OFDM demonstrates strong assets to be considered in future wireless technologies especially.

Another solution has been considered to adapt FBMC waveforms with multiple-antenna schemes in the last chapter. Instead of restoring the complex orthogonality, it is possible to improve the performance of FBMC linear MIMO receivers. Indeed, linear detection can be directly applied on FBMC MIMO receivers however its performance is limited because of the intrinsic interference. Linear MIMO receiver can be assisted by lattice reduction techniques to improve them and possibly reach near-ML performance. Besides, the results can be also re-used for OFDM-based receiver to improve the performance of linear detection while maintaining a low complexity. But lattice reduction techniques prevent a straightforward use of advanced channels coding. A novel demapping method, named Successive Interference Cancellation, has been introduced to jointly use lattice reduction with channel coding. Not only the proposed demapping method improves the performance with commonly used LR algorithms like fixed perturbation but it also properly combine LR-aided equalisation with MAP detection for OFDM systems. However, the extension on FBMC systems has not been addressed in this study and is left as perspective.

This work addresses two different approaches to consider filter-bank based waveforms for future wireless technologies. The first solutions focuses on mobile technologies and the FBMC waveforms is made complex orthogonal thanks to the OFDM-based precoding. The performance gain is improved with respect to state-of-the-art solutions but the margin of progression is limited because of the stringent 5G NR system requirements. The second approach deals with the interference cancellation for FBMC MIMO receiver. It is more interesting as it benefits from the subcarrier-wise filtering of the FBMC. However, the adaptation to FBMC receiver is not verified yet.

Contributions

- **Study of a precoding which ensures Near Perfect Reconstruction in the complex field for filter-bank based waveforms**
  The studied solution ensures complex orthogonality between any pair of transmitted symbols. As the precoding uses FFT, it is also possible to simplify the receiver scheme and to reduce it to a simple OFDM receiver without analysis filter-bank and decoding stage. However to do so, the filtered subband has been enlarged from a unique subcarrier as in FBMC/OQAM to a group of subcarriers.

- **Proposal of two prototype filter design methods**
  Optimising the prototype filter according to the intrinsic interference rejec-

tion criterion is logical as the first purpose of the proposed scheme is to ensure complex orthogonality (in approximation because perfect complex orthogonality can not be achieved). However, as the level of attenuation of the intrinsic interference can be strong enough, it can be slightly degraded to improve the side lobe rejection and then better confine the spectrum of the transmitted signal. The prototype filter design has been extended for any CP/CS lengths which gives the possibility to adapt the proposed schemes to any systems requirements.

- **Comparison with state-of-the-art solutions with 5G specific scenarios**
  The comparison of the proposed scheme with state-of-the-art solutions is based on multiple sub-6 GHz 5G scenarios like multi-service and channel performance over TDLC channel models for LDPC coded systems.

- **Proposal of a lattice-reduction demapping technique to ensure a proper interface with advanced channel coding**
  Existing solutions are sub-optimal as they only consider reduced candidate list. The proposed solution, named Successive Interference Cancellation, searches and corrects errors due to noise/interference enhanced so that the coordinates of the received point are reliable. The proposed solution demonstrates significant performance gain with respect to literature solutions.

Perspectives

- **Dynamic assignment of numerology depending on UE activity**
  The proposed schemes simultaneously support different inter-subcarrier spacings and symbol durations with a low-complex transmission scheme based on a unique filter-bank. It allows dynamic adaption of link numerology depending on its needs and propagation impairments which is an appealing feature for future wireless technologies.

- **Study the advantages of joint frequency and spatial filtering**
  Spatial filtering, *i.e.* beamforming, is considered in 5G NR above 6-GHz communications to isolate non-orthogonal subbands (like bandwidth parts of different numerologies). It may be interesting to assess the advantages of jointly considering air interfaces with confined spectrum and spatial filtering in order to determine an interesting trade-off to operate between the two solutions.

- **Extending the results on LR-aided receivers for non-ZF equalisation**
  It has been observed that LR-aided can greatly improve the performance of linear receivers. However, the proposed study is reduced to ZF receivers as the system model is simpler. It may be interesting to extend the results to non-ZF receivers like MMSE equalizers which would further improve the performance gain. It can be applied as well to MF equalizers which do not require channel matrix inversion which is interesting for large MIMO configurations.

- **Extending the results on LR-aided receivers for FBMC**
  In the presented work, only OFDM systems have been addressed. However LR-aided receiver are also envisioned for FBMC/OQAM MIMO linear receivers to improve their performance [97]. The SIC algorithm can be considered as well to deal with intrinsic interference generated by FBMC/OQAM modulations.

Dissemination

Patent

- **Simplified Max-Log Soft-Output Generation for LR-aided MIMO receivers**
  Méthode de détection pour récepteur de système MIMO aidé par réduction de réseau de points et suppression itérative de bruit
  Filed in February 2019

International Journal Communications

- **Study of OFDM Precoded Filter-Bank Waveforms**
  David Demmer, Rostom Zakaria, Robin Gerzaguet, Jean-Baptiste Doré, Didier Le Ruyet
  IEEE Transactions on Wireless Communciations, 2018
- **On the road to 5G: Comparative Study of Physical Layer in MTC Context**
  Yahia Medjadhi, Sylvain Traverso, Robin Gerzaguet, Hmaied Shaïed, Rafik Zayani, David Demmer, Rostom Zakaria, Jean-Baptiste Doré, Mouna Ben Mabrouk, Didier Le Ruyet, Yves Louët, Daniel Roviras
  IEEE Access, 2017

International Conference Communications

- **Filter-bank OFDM transceivers for 5G and beyond**
  David Demmer, Rostom Zakaria, Jean-Baptiste Doré, Robin Gerzaguet, Didier Le Ruyet
  Proc. Asilomar Conference on Signals, Systems and Computers (ASILOMAR), 2018
  invited paper
- **Analytical Study of 5G NR eMBB co-existence**
  David Demmer, Robin Gerzaguet, Jean-Baptiste Doré, Didier Le Ruyet
  Proc. International Conference on Telecommunications (ICT), 2018
- **Impact of Selective Channels on Post-OFDM Waveforms for 5G Machine Type Communications**
  Yahia Medjadhi, Yves Louët, Mouna Ben Mabrouk, Daniel Roviras, Rostom Zakaria, Hmaïed Shaiek, Didier Le Ruyet, Sylvain Traverso, Robin Gerzaguet, David Demmer, Jean-Baptiste Doré, Rafik Zayani
  Proc. International Symposium on Wireless Communication Systems (ISWCS), 2018
- **Block-Filtered OFDM: A novel waveform for future wireless technologies**
  David Demmer, Robin, Gerzaguet, Jean-Baptiste Doré, Didier Le Ruyet, Dimitri Kténas
  Proc. IEEE International Conference on Communications (ICC), 2017
- **Block-Filtered OFDM: A new promising waveform for multi-service scenarios**
  Robin Gerzaguet, David Demmer, Jean-Baptiste Doré, Dimitri Kténas

Proc. IEEE International Conference on Communications (ICC), 2017
Best paper award for wireless symposium

- **Filter Design for 5G BF-OFDM waveform**
  David Demmer, Robin, Gerzaguet, Jean-Baptiste Doré, Didier Le Ruyet, Dimitri Kténas
  Proc. IEEE European Conference on Networks and Communications (EuCNC), 2017
- **Comparison of promising candidate waveforms for 5G: WOLA-OFDM versus BF-OFDM**
  Robin Gerzaguet, Yahia Medjhadi, David Demmer, Rafik Zayani, Jean-Baptiste Doré, Hmaïed Shaiek, Daniel Roviras
  Proc. International Symposium on Wireless Communications Systems (ISWCS), 2017
- **Performance of soft-decision linear receivers for spatial multiplexing FBMC/OQAM**
  David Demmer, Jean-Baptiste Doré, Didier Le Ruyet, Robin Gerzaguet,
  Proc. International Symposium on Wireless Communications Systems (ISWCS), 2016

Appendices

A Nyquist relation applied to frequency-sampling prototype filters

The matrix-based transmitter model can be expressed as follows

$$\mathbf{S_n} = \mathbf{gDF^H\Theta_nA_n} + \sum_{p\neq 0, p=-2K+1}^{2K-1} \mathbf{Q_{p\frac{N}{2}}gDF^H\Theta_{n+p}A_{n+p}} \tag{A.1}$$

were $\mathbf{A_n}$ is the data symbol transmitted at time instant n (size N x 1), $\mathbf{F}$ the DFT matrix (size $N \times N$), $\mathbf{D}$ the duplication matrix (size $KN \times N$), $\mathbf{g}$ the filter impulse response matrix (size $KN \times KN$), $\mathbf{Q_{p\frac{N}{2}}}$ the delay matrix (size $KN \times KN$) with p the time instant difference, $\mathbf{\Theta_n}$ the phase offset matrix (size $N \times N$) and $\mathbf{A_n}$ the transmitted FBMC symbol at time instant n (size $N \times 1$).

$$\mathbf{g} = \begin{pmatrix} g[0] & 0 & 0 & 0 \\ 0 & g[1] & 0 & 0 \\ 0 & 0 & \ddots & 0 \\ 0 & 0 & 0 & g[KN-1] \end{pmatrix} \tag{A.2}$$

$$\mathbf{D} = \left.\begin{pmatrix} \mathbf{I_N} \\ \vdots \\ \mathbf{I_N} \end{pmatrix}\right\} \text{K Times} \tag{A.3}$$

$$\mathbf{Q_{x>0}} = \begin{pmatrix} \mathbf{0_{x,N}} \\ \mathbf{I_{N-x}} \quad \mathbf{0_{N-x,x}} \end{pmatrix} \tag{A.4}$$

$$\mathbf{Q_{x<0}} = \begin{pmatrix} \mathbf{0_{N-x,x}} \quad \mathbf{I_{N-x}} \\ \mathbf{0_{x,N}} \end{pmatrix} \tag{A.5}$$

The matrix-based receiver model can be expressed as follows.

$$\mathbf{R_n} = \mathbf{\Theta_n^H F D^H g^H Z_n} \tag{A.6}$$

where $\mathbf{R_n}$ is the received symbol vector at time instant n (size $N \times 1$).

Because of the symbol overlapping, the receiver captures with the useful symbol ($p = 0$) parts of symbols that are transmitted previously ($p < 0$) and after ($p > 0$).

The objective is the appendix is twofold. First, it gives an analytical expression of the transmultiplexer response (*i.e.* $\mathbf{FD^Hg^HQ_{p\frac{M}{2}}gDF^H}$ $\forall p$). Then, by considering a frequency-sampling prototype filter, the conditions to be satisfied by the frequency coefficients to ensure a Nyquist transmission will be derived.

First, we have

$$\mathbf{g^H Q_{p\frac{N}{2}} g} = \mathbf{Diag}\left[\underbrace{0\ldots0}_{pN/2 \text{ if } p>0} \quad g[0]g[p\tfrac{N}{2}] \quad \ldots \quad g[N-1-p\tfrac{N}{2}]g[N-1] \quad \underbrace{0\ldots0}_{pN/2 \text{ if } p<0}\right] \tag{A.7}$$

It leads to

$$(\mathbf{D^H g^H Q_{p\frac{N}{2}} g D})_{r,c} = \begin{cases} \sum_{l=0}^{N-1} g[r+lN]g[r+lN+p\frac{N}{2}] & \text{if } r=c \\ 0 & \text{otherwise} \end{cases} \tag{A.8}$$

We obtain

$$\begin{aligned} \sum_{l=0}^{N-1} g[i+lN]g[i+lN+p\frac{N}{2}] &= \sum_{k=0}^{K-1}\left[\left(\sum_{l=-K+1}^{K-1} H_l e^{j\frac{2\pi}{KN}l(i+kN)}\right)\right. \\ &\qquad \left.\times\left(\sum_{l'=-K+1}^{K-1} H_l e^{j\frac{2\pi}{KN}l'(i+kN+pN/2)}\right)\right] \\ &= \sum_{l=-K+1}^{K+1} H_l^2 e^{j\frac{4\pi}{KN}li} e^{j\frac{\pi}{K}pl}\left(\sum_{l=0}^{K-1} e^{j\frac{2\pi}{K}2lk}\right) \\ &+ \sum_{l\neq l'} H_l H_{l'} e^{j\frac{2\pi}{KN}(l+l')i} e^{j\frac{\pi}{K}pl'}\left(\sum_{l=0}^{K-1} e^{j\frac{2\pi}{K}(l+l')k}\right) \end{aligned} \tag{A.9}$$

The Dirichlet kernel can be simplified as shown below

$$\sum_{l=0}^{K-1} e^{j\frac{2\pi}{K}\alpha k} = \begin{cases} K & \alpha \equiv 0 \pmod K \\ 0 & \text{otherwise} \end{cases} \tag{A.10}$$

One obtains

$$\begin{aligned}
\sum_{k=0}^{N-1} g\left[i+lN\right] g\left[i+lN+p\frac{N}{2}\right] &= KH_0^2 + 2KH_{K/2}^2 \cos\left(\frac{2\pi}{KN}Ki\right)\cos\left(\frac{\pi}{2}p\right) \\
&+ K\left[\sum_{\substack{l=-K+1 \\ l\neq 0}}^{K-1} H_l H_{-l} e^{-j\frac{\pi}{K}pl} + \sum_{l=-K+1}^{K-1} H_l H_{K-l} e^{j\frac{2\pi}{N}i} e^{j\frac{\pi}{K}p(K-l)}\right] \\
&+ K\left[\sum_{l=-K+1}^{K-1} H_l H_{-K-l} e^{-j\frac{2\pi}{N}i} e^{j\frac{\pi}{K}p(-K-l)}\right] \\
&= K\sum_{k=-K+1}^{K-1} H_l^2 e^{-j\frac{\pi}{K}pl} + 2KH_{K/2}^2\cos\left(\frac{2\pi}{N}i\right)\cos\left(\frac{\pi}{2}p\right) \\
&+ K\sum_{\substack{l'=1 \\ l'=K-l}}^{K-1} H_{l'} H_{K-l'} e^{j\frac{2\pi}{N}i} e^{j\frac{\pi}{K}pl'} \\
&+ K\sum_{\substack{l'=-K+1 \\ l'=K+l}}^{-1} H_{l'-K} H_{-l'} e^{-j\frac{2\pi}{N}i} e^{-j\frac{\pi}{K}pl} \\
&= K\left(\sum_{k=-K+1}^{K-1} H_l^2 e^{-j\frac{\pi}{K}pl} + 2\cos\left(\frac{2\pi}{N}i\right)\sum_{l=1}^{K-1} H_l H_{K-l}\cos\left(\frac{\pi}{K}pl\right)\right)
\end{aligned} \tag{A.11}$$

Let $K_1(p) = \sum_{k=-K+1}^{K-1} H_l^2 e^{-j\frac{\pi}{K}pl}$ and $K_2(p) = 2\sum_{l=1}^{K-1} H_l H_{K-l}\cos\left(\frac{\pi}{K}pl\right)$. One gets:

$$(\mathbf{D^H g^H Q_{p\frac{N}{2}} g D})_{r,c} = \begin{cases} KK_1(p) + K_2(p)\cos\left(\frac{2\pi}{N}r\right) & r = c \\ 0 & \text{otherwise} \end{cases} \tag{A.12}$$

It means that the term $K_2(p) = 0$ is always null for frequency-sampling filters.

One gets:

$$(\mathbf{D^H g^H Q_{p\frac{N}{2}} g D})_{r,c} = \begin{cases} KK_1(p) + K_2(p)\cos\left(\frac{2\pi}{N}r\right) & r = c \\ 0 & \text{otherwise} \end{cases} \tag{A.13}$$

$$\mathbf{F D^H g^H Q_{p\frac{N}{2}} g D F^H} = KK_1(p)\mathbf{I_N} + K_2(p)\mathbf{F Diag}\left[\cos\left(\frac{2\pi}{N}r\right)\right]\mathbf{F^H} \tag{A.14}$$

By introducing $w = e^{-j\frac{2\pi}{N}}$ the primitive N$^{\text{th}}$ rooth of unity, it leads to:

$$\begin{aligned}
\left(\mathbf{Diag}\left[\cos\left(\frac{2\pi}{N}r\right)\right]\mathbf{F^H}\right)_{r,c} &= \cos\left(\frac{2\pi}{N}r\right)w^{rc} \\
\left(F\mathbf{Diag}\left[\cos\left(\frac{2\pi}{N}r\right)\right]\mathbf{F^H}\right)_{r,c} &= \sum_{k=0}^{N-1} w^{-rk}\cos\left(\frac{2\pi}{N}k\right)w^{kc} \\
&= \frac{1}{2}\left(\underbrace{\sum_{k=0}^{N-1} w^{k(c-r+1)}}_{\substack{=N \text{ for } r=c+1 \\ =0 \text{ otherwise}}} + \underbrace{\sum_{k=0}^{N-1} w^{k(c-r-1)}}_{\substack{=N \text{ for } r=c-1 \\ =0 \text{ otherwise}}}\right)
\end{aligned} \tag{A.15}$$

Let

$$\mathbf{U} = \begin{bmatrix}
0 & 1 & 0 & & 1 \\
1 & 0 & 1 & 0 & \\
0 & 1 & 0 & 1 & 0 \\
 & \ddots & \ddots & \ddots & \ddots \\
 & & & & \\
1 & & 0 & 1 & 0
\end{bmatrix} \tag{A.16}$$

Therefore, we obtain: $\mathbf{FD^H g^H Q_{p\frac{N}{2}} gDF^H} = KK_1(p)\mathbf{I_N} + \frac{K_2(p)N}{2}\mathbf{U}$. It leads to:

$$\left(\mathbf{\Theta_n^H U \Theta_{n+p}}\right)_{r,c} = \begin{cases} -j^{p+1}(-1)^{rn+c(n+p)} & r = c+1 \\ j^{p+1}(-1)^{rn+c(n+p)} & r = c-1 \\ 0 & \text{otherwise} \end{cases} \tag{A.17}$$

$$\begin{aligned}
\mathbf{R_n} &= KK_1(0)\mathbf{A_n} \\
&+ \underbrace{\sum_{\substack{p=-2K+1 \\ p\neq}}^{2K-1}\left(KK_1(p)j^p\mathbf{Diag}\left[(-1)^{pr}\right]_r\mathbf{A_{n+p}} + \frac{K_2(p)N}{2}\mathbf{\Theta_n^H U \Theta_{n+p} A_{n+p}}\right)}_{\text{interference terms}}
\end{aligned} \tag{A.18}$$

The interference is cancelled by taking the real part of (A.18). The set of frequency coefficients H_k must ensures that the real part of the interferences terms are null. Both $K_1(p)$ and $K_2(p)$ are real-valued. Therefore, the first term (with $K_1(p)$) is real when p is even and the second term (with $K_2(p)$) is odd. However, as shown in (A.19), $K_2(p)$ is null for any odd p. As a consequence, ensuring real orthogonality is equivalent to satisfying $K_1(p) \neq 0$ for any p even and non-null.

$$
\begin{aligned}
\forall p, K_2(p)/2 &= \sum_{l=1}^{<K/2} H_l H_{K-l} \cos\left(\frac{\pi}{K} pl\right) + H_{K/2}^2 \cos\left(\frac{\pi}{2} p\right) \\
&+ \sum_{l>K/2}^{K-1} H_l H_{K-l} \cos\left(\frac{\pi}{K} pl\right) \\
&= \sum_{l=1}^{<K/2} H_l H_{K-l} \left(\cos\left(\frac{\pi}{K} pl\right) + \cos\left(\frac{\pi}{K} p(K-l)\right)\right) \\
&= \sum_{l=1}^{<K/2} H_l H_{K-l} \cos\left(\frac{\pi}{K} pl\right) (1 + (-1)^p) \\
&= \begin{cases} 0 & p \text{ is odd} \\ \sum_{l=1}^{<K/2} H_l H_{K-l} \left(\cos\left(\frac{\pi}{K} pl\right) + \cos\left(\frac{\pi}{K} p(K-l)\right)\right) & p \text{ is even} \end{cases}
\end{aligned}
\tag{A.19}
$$

By solving the system, one obtains (assuming $H_0 = 1$):

- for $K = 2$: $H_1 = \frac{\sqrt{2}}{2}$ (no degree of freedom)
- for $K = 3$: $H_2 = \sqrt{1 - H_1^2}$ (1 degree of freedom)
- for $K = 4$: $H_3 = \sqrt{1 - H_1^2}$, $H_2 = \frac{\sqrt{2}}{2}$ (1 degree of freedom)
- for $K = 5$: $H_4 = \sqrt{1 - H_1^2}$, $H_3 = \sqrt{1 - H_2^2}$ (2 degrees of freedom)

Bibliography

[1] 3GPP TS 38.101-1 v15.2.0 release 15, "Technical Specifications Group Radio Access Network; NR: User Equipment (UE) radio transmission and reception; Part 1: Range 1 Standalone," standard, 3GPP, june 2018.

[2] B. Bertenyi, S. Nagata, H. Kooropaty, W. C. Xutao Zhou, Y. Kim, X. Dai, and X. Xu, "5G NR Radio Interface," *Journal of ICT Standardization, Combined Special Issue 1 & 2*, vol. 6, may 2018.

[3] 3GPP TS 38.213 v15.3.0 release 15, "Technical Specification Group Radio Access Network; NR; Physical layer procedures for control," standard, 3GPP, september 2018.

[4] 3GPP TS 38.101-2 v15.2.0 release 15, "Technical Specifications Group Radio Access Network; NR: User Equipment (UE) radio transmission and reception; Part 2: Range 2 Standalone," standard, 3GPP, june 2018.

[5] Miller II, Robert Raymond and Sonalkar, Ranjan V., "Power allocation scheme for DMT-based modems employing simplex transmission," december 2005. US Patent 6,973,122 B1.

[6] B. Hirosaki, "An Orthogonally Multiplexed QAM System Using the Discrete Fourier Transform," *IEEE Transactions on Communications*, vol. 29, pp. 982–989, july 1981.

[7] J. Cooley and J. Tukey, "An algorithm for the machine calculation of complex fourier series," *Mathematics of Computation*, vol. 19, no. 90, pp. 297–301, 1965.

[8] A. Peled and A. Ruiz, "Frequency domain data transmission using reduced computational complexity algorithms," in *Proc. IEEE International Conference on Acoustics, Speech, and Signal Processing (ICASSP)*, vol. 5, pp. 964–967, april 1980.

[9] 3GPP TS 36.211 v14.2.0 release 14, "LTE; Evolved Universal Terrestrial Radio Access (E-UTRA); Physical channels and modulation," standard, 3GPP, april 2017.

[10] "IEEE Standard for Information technology–Telecommunications and information exchange between systems Local and metropolitan area networks–Specific requirements - Part 11: Wireless LAN Medium Access Control (MAC) and Physical Layer (PHY) Specifications," december 2016.

[11] ETSI EN 300 401 V1.4.1, "Radio Broadcasting System; Digital Audio Broadcasting (DAB) to mobile, portable and fixed receivers," standard, ETSI, january 2006.

[12] ETSI EN 302 755 V1.4.1, "Digital Video Broadcasting (DVB); Frame structure channel coding and modulation for a second generation digital terrestrial television broadcasting system (DVB-T2)," standard, ETSI, july 2015.

[13] ETSI EN 302 769 V1.3.1, "Digital Video Broadcasting (DVB); Frame structure channel coding and modulation for a second generation digital transmission system for cable systems (DVB-C2)," standard, ETSI, october 2015.

[14] F. Tosato and P. Bisaglia, "Simplified soft-output demapper for binary interleaved COFDM with application to HIPERLAN/2," in *Proc. IEEE International Conference on Communications (ICC)*, vol. 2, pp. 664–668 vol.2, 2002.

[15] TS 38.300 v15.2.0 Release 15, "Technical Specifications Group Radio Access Network; NR; NR and NG-RAN Overall Description; Stage 2," standard, 3GPP, june 2018.

[16] J. Mietzner, R. Schober, L. Lampe, W. H. Gerstacker, and P. A. Hoeher, "Multiple-antenna techniques for wireless communications - a comprehensive literature survey," *IEEE Communications Surveys Tutorials*, vol. 11, pp. 87–105, Second 2009.

[17] S. Kutty and D. Sen, "Beamforming for Millimeter Wave Communications: An Inclusive Survey," *IEEE Communications Surveys Tutorials*, vol. 18, pp. 949–973, Secondquarter 2016.

[18] R. Balian, "Un principe d'incertitude fort en théorie du signal ou en mécanique quantique," *Compt. Rend. Acad. Sci. Ser. II*, vol. 292, no. 20, pp. 1357–1362, 1981.

[19] J. J. Benedetto, C. Heil, and D. F. Walnut, "Differentiation and the Balian-Low Theorem," *Journal of Fourier Analysis and Applications*, vol. 1, no. 4, pp. 355–402, 1994.

[20] D. Demmer, R. Gerzaguet, J.-B. Doré, and D. Le Ruyet, "Analytical study of 5G NR eMBB co-existence," in *Proc. IEEE International Conference on Telecommunications (ICT)*, pp. 186–190, June 2018.

[21] Huawei and HiSilicon, "f-OFDM scheme and filter design," TSG RAN WG1 Meeting 85, R1-165425, 3GPP, Nanjing, China, May 2016.

[22] J. Abdoli, M. Jia, and J. Ma, "Filtered OFDM: A new waveform for future wireless systems," in *Proc. IEEE International Workshop on Signal Processing Advances in Wireless Communications (SPAWC)*, pp. 66–70, June 2015.

[23] X. Zhang, M. Jia, L. Chen, J. Ma, and J. Qiu, "Filtered-OFDM - Enabler for Flexible Waveform in the 5th Generation Cellular Networks," in *Proc. IEEE Global Communications Conference (GLOBECOM)*, pp. 1–6, december 2015.

[24] A. Sahin, I. Guvenc, and H. Arslan, "A Survey on Multicarrier Communications: Prototype Filters, Lattice Structures, and Implementation Aspects," *IEEE Communications Surveys Tutorials*, vol. 16, pp. 1312–1338, Third 2014.

[25] V. Vakilian, T. Wild, F. Schaich, S. ten Brink, and J. Frigon, "Universal-filtered multi-carrier technique for wireless systems beyond LTE," in *Proc. IEEE Global Communications (GLOBECOM) Workshops*, pp. 223–228, december 2013.

[26] T. Wild, F. Schaich, and Y. Chen, "5G air interface design based on Universal Filtered (UF-) OFDM," in *Proc. IEEE. International Conference on Digital Signal Processing (DSP)*, pp. 699–704, august 2014.

[27] F. Schaich and T. Wild, "Relaxed synchronization support of universal filtered multi-carrier including autonomous timing advance," in *Proc. IEEE International Symposium on Wireless Communications Systems (ISWCS)*, pp. 203–208, august 2014.

[28] X. Wang, T. Wild, F. Schaich, and A. F. dos Santos, "Universal Filtered Multi-Carrier with Leakage-Based Filter Optimization," in *Proc. European Wireless Conference*, pp. 1–5, may 2014.

[29] X. Wang, T. Wild, and F. Schaich, "Filter Optimization for Carrier-Frequency- and Timing-Offset in Universal Filtered Multi-Carrier Systems," in *Proc. IEEE Vehicular Technology Conference (VTC Spring)*, pp. 1–6, may 2015.

[30] R. Zayani, Y. Medjahdi, H. Shaiek, and D. Roviras, "WOLA-OFDM: A Potential Candidate for Asynchronous 5G," in *Proc. IEEE Global Communications (GLOBECOM) Workshops*, pp. 1–5, december 2016.

[31] P. Tan and N. C. Beaulieu, "Reduced ICI in OFDM systems using the "better than" raised-cosine pulse," *IEEE Communications Letters*, vol. 8, pp. 135–137, March 2004.

[32] N. C. Beaulieu and P. Tan, "On the effects of receiver windowing on OFDM performance in the presence of carrier frequency offset," *IEEE Transactions on Wireless Communications*, vol. 6, pp. 202–209, Jan 2007.

[33] R. W. Chang, "Synthesis of band-limited orthogonal signals for multichannel data transmission," *The Bell System Technical Journal*, vol. 45, pp. 1775–1796, Dec 1966.

[34] B. Saltzberg, "Performance of an efficient parallel data transmission system," *IEEE Transactions on Communication Technology*, vol. 15, pp. 805–811, december 1967.

[35] P. Siohan and N. Lacaille, "Analysis of OFDM/OQAM systems based on the filterbank theory," in *Proc. Global Telecommunications Conference (GLOBECOM)*, vol. 4, pp. 2279–2284, december 1999.

[36] B. Farhang-Boroujeny, "OFDM Versus Filter Bank Multicarrier," *IEEE Signal Processing Magazine*, vol. 28, pp. 92–112, May 2011.

[37] M. Alard, "Construction of a multicarrier signal," 1996.

[38] B. L. Floch, M. Alard, and C. Berrou, "Coded orthogonal frequency division multiplex [tv broadcasting]," *Proceedings of the IEEE*, vol. 83, pp. 982–996, June 1995.

[39] C. Roche and P. Siohan, *Multi-Carrier Spread Spectrum*, pp. 179–186. Boston, MA: Springer US, 1997.

[40] P. Siohan and C. Roche, "Cosine-modulated filterbanks based on extended Gaussian functions," *Proc. IEEE Transactions on Signal*, vol. 48, pp. 3052–3061, november 2000.

[41] M. G. Bellanger, "Specification and design of a prototype filter for filter bank based multicarrier transmission," in *Proc. IEEE International Conference on Acoustics, Speech, and Signal Processing (ICASP)*, vol. 4, pp. 2417–2420 vol.4, May 2001.

[42] K. W. Martin, "Small side-lobe filter design for multitone data-communication applications," *IEEE Transactions on Circuits and Systems II: Analog and Digital Signal Processing*, vol. 45, pp. 1155–1161, Aug 1998.

[43] M. Bellanger, "FBMC physical layer: a primer," tech. rep., ICT-PHYDYAS Project, 2010. available on http://www.ict-phydyas.org.

[44] Y. Medjahdi, *Interference modeling and performance analysis of asynchronous OFDM and FBMC wireless communication systems*. PhD thesis, Conservatoire National des Arts et Métiers (CNAM), 2012. Thèse de doctorat dirigée par Terré Michel, Le Ruyet Didier et Roviras Daniel.

[45] M. Bellanger, G. Bonnerot, and M. Coudreuse, "Digital filtering by polyphase network:application to sample-rate alteration and filter banks," *IEEE Transactions on Acoustics, Speech, and Signal Processing*, vol. 24, pp. 109–114, April 1976.

[46] Y. Dandach and P. Siohan, "FBMC/OQAM Modulators with Half Complexity," in *Proc. IEEE Global Telecommunications Conference (Globecom)*, (Houston, USA), pp. 1–5, Dec 2011.

[47] A. Husam and Z. Kollár, "Complexity Comparison of Filter Bank Multicarrier Transmitter Schemes," in *Proc. IEEE International Symposium on Communication Systems, Networks Digital Signal Processing (CSNDSP)*, (Budapest, Hungary), pp. 1–4, July 2018.

[48] M. Bellanger, "FS-FBMC: An alternative scheme for filter bank based multicarrier transmission," in *Proc. IEEE International Symposium on Communications, Control and Signal Processing*, (Roma, Italy), pp. 1–4, May 2012.

[49] D. Mattera, M. Tanda, and M. Bellanger, "Frequency-spreading implementation of OFDM/OQAM systems," in *Proc. International Symposium on Wireless Communication Systems (ISWCS)*, (Paris, France), pp. 176–180, Aug 2012.

[50] D. Demmer, J.-B. Doré, D. Le Ruyet, and R. Gerzaguet, "Performance of soft-decision linear receivers for spatial-multiplexing FBMC/OQAM," in *Proc. IEEE International Symposium on Wireless Communication Systems (ISWCS)*, (Poznan, Poland), pp. 404–408, 2016.

[51] C. Lélé, J.-P. Javaudin, R. Legouable, A. Skrzypczak, and P. Siohan, "Channel estimation methods for preamble-based OFDM/OQAM modulations," *European Transactions on Telecommunications*, vol. 19, no. 7, pp. 741–750, 2008.

[52] S. Kang and K. Chang, "A Novel Channel Estimation Scheme for OFDM/OQAM-IOTA System," *ETRI Journal*, vol. 29, pp. 430–436, August 2007.

[53] C. Lele, P. Siohan, R. Legouable, and J.-P. Javaudin, "Preamble-based channel estimation techniques for OFDM/OQAM over the powerline," in *Proc. IEEE International Symposium on Power Line Communications and Its Applications (ISPLC)*, (Pisa, Italy), pp. 59–64, March 2007.

[54] C. Lele, P. Siohan, and R. Legouable, "2 dB Better Than CP-OFDM with OFDM/OQAM for Preamble-Based Channel Estimation," in *Proc. IEEE International Conference on Communications (GLOBECOM)*, (New Orleans, USA), pp. 1302–1306, May 2008.

[55] G. Garbo, S. Mangione, and V. Maniscalco, "MUSIC-based modal channel estimation for wideband OFDM-OQAM," in *IFIP Wireless Days*, (Duabi, United Arabs of Emirats), pp. 1–5, Nov 2008.

[56] E. Kofidis, "Preamble-Based Estimation of Highly Frequency Selective Channels in FBMC/OQAM Systems," *IEEE Transactions on Signal Processing*, vol. 65, pp. 1855–1868, April 2017.

[57] J. Doré, V. Berg, and D. Ktenas, "Channel estimation techniques for 5G cellular networks: FBMC and multiuser asynchronous fragmented spectrum scenario," *Transactions on Emerging Telecommunications Technologies*, vol. 26, no. 1, pp. 15–30, 2015.

[58] J.-P. Javaudin, D. Lacroix, and A. Rouxel, "Pilot-aided channel estimation for OFDM/OQAM," in *Proc. IEEE Semiannual Vehicular Technology Conference (VTC Srping)*, vol. 3, (Seoul, Korea), pp. 1581–1585 vol.3, April 2003.

[59] M. Bellanger, "FS-FBMC: A flexible robust scheme for efficient multicarrier broadband wireless access," in *Proc. IEEE International Conference on Communications (GLOBECOM)*, (Anaheim, USA), pp. 192–196, Dec 2012.

[60] J. Louveaux, M. Tanda, M. Renfors, L. Baltar, A. Ikhlef, T. Hidalgo-Stitz, M. Bellanager, and C. Bader, "D3-2 optimization of transmitter and receiver," tech. rep., FP7-ICT PHYDYAS project, 2009.

[61] J. C. Tu, "Optimum MMSE equalization for staggered modulation," in *Proc. IEEE Asilomar Conference on Signals, Systems and Computers (ASILOMAR)*, (Asilomar, USA), pp. 1401–1406 vol.2, 1993.

[62] E. Kofidis and D. Katselis, "Preamble-based channel estimation in MIMO-OFDM/OQAM systems," in *Proc. IEEE International Conference on Signal and Image Processing Applications (ICSIPA)*, (Kuala Lumpur, Malaysia), pp. 579–584, Nov 2011.

[63] J.-P. Javaudin and Y. Jiang, "Channel estimation for iterative MIMO OFDM/OQAM transceivers," in *IEEE European Wireless Conference*, (Prague, Czech Republic), pp. 1–6, June 2008.

[64] A. Ikhlef and J. Louveaux, "Per subchannel equalization for MIMO FBMC/OQAM systems," in *Proc. IEEE Pacific Rim Conference on Communications, Computers and Signal Processing (PRCCCSP)*, (Victoria, Canada), pp. 559–564, Aug 2009.

[65] R. Zakaria, D. Le Ruyet, and M. Bellanger, "Maximum likelihood detection in spatial multiplexing with FBMC," in *Proc. IEEE European Wireless Conference (EW)*, (Lucca, Italy), pp. 1038–1041, April 2010.

[66] R. Zakaria and D. Le Ruyet, "Partial ISI cancellation with viterbi detection in MIMO filter-bank multicarrier modulation," in *Proc. IEEE International Symposium on Wireless Communication Systems (ISWCS)*, (Aachen, Gernany), pp. 322–326, Nov 2011.

[67] H. Lin, C. Lele, and P. Siohan, "A pseudo alamouti transceiver design for OFDM/OQAM modulation with cyclic prefix," in *Proc. IEEE on Signal Processing Advances in Wireless Communications (SPAWC)*, (Perugia, Italy), pp. 300–304, june 2009.

[68] M. Renfors, T. Ihalainen, and T. H. Stitz, "A block-Alamouti scheme for filter bank based multicarrier transmission," in *Proc. European Wireless Conference (EW)*, (Lucca, Italy), pp. 1031–1037, april 2010.

[69] Y. Medjahdi, Y. Louet, M. B. Mabrouk, D. Roviras, R. Zakaria, H. Shaiek, D. Le Ruyet, S. Traverso, R. Gerzaguet, D. Demmer, J.-B. Doré, and R. Zayani, "Impact of Selective Channels on Post-OFDM Waveforms for 5G Machine Type Communications," in *Proc. IEEE International Symposium on Wireless Communication Systems (ISWCS)*, (Lisbon, Portugal), pp. 1–5, Aug 2018.

[70] 3GPP TS 38.901 v15.0.0 release 15, "Technical Specification Group Radio Access Network; Study on channel model from frequencies from 0.5 to 100 GHz," standard, 3GPP, june 2018.

[71] 3GPP TS 38.901 v15.3.0 release 15, "Technical Specification Group Radio Access Network; NR; Physical layer procedures for data," standard, 3GPP, october 2018.

[72] S. Krantz, "Handbook of complex variables," 1999.

[73] T. Wild and F. Schaich, "A Reduced Complexity Transmitter for UF-OFDM," in *2015 IEEE Vehicular Technology Conference (VTC Spring)*, pp. 1–6, May 2015.

[74] R. Gerzaguet, N. Bartzoudis, L. G. Baltar, V. Berg, J.-B. Doré, D. Kténas, O. Font-Bach, X. Mestre, M. Payaró, M. Färber, and K. Roth, "'the 5g candidate waveform race: a comparison of complexity and performance," *EURASIP Journal on Wireless Communications and Networking*, p. 13, Jan.

[75] A. Loulou, J. Yli-Kaakinen, and M. Renfors, "Efficient fast-convolution based implementation of 5G waveform processing using circular convolution

decomposition," in *Proc. IEEE International Conference on Communications (ICC)*, pp. 1–7, May 2017.

[76] Q. Bodinier, F. Bader, and J. Palicot, "Coexistence of filter banks and CP-OFDM: What are the real gains?," in *Proc. IEEE International Symposium on Wireless Communication Systems (ISWCS)*, (Poznan, Poland), pp. 628–632, Sept 2016.

[77] G. Fettweis, M. Krondorf, and S. Bittner, "GFDM - Generalized Frequency Division Multiplexing," in *Proc. IEEE Vehicular Technology Conference (VTC Spring)*, pp. 1–4, April 2009.

[78] M. Bellanger, D. Mattera, and M. Tanda, "Lapped-OFDM as an Alternative to CP-OFDM For 5G Asynchronous Access and Cognitive Radio," in *Proc. IEEE Vehicular Technology Conference (VTC Spring)*, pp. 1–5, May 2015.

[79] Y. Medjahdi, S. Traverso, R. Gerzaguet, H. Shaïek, R. Zayani, D. Demmer, R. Zakaria, J.-B. Doré, M. B. Mabrouk, D. Le Ruyet, Y. Louët, and D. Roviras, "On the Road to 5G: Comparative Study of Physical Layer in MTC Context," *IEEE Access*, vol. 5, pp. 26556–26581, 2017.

[80] J.-B. Doré, R. Gerzaguet, N. Cassiau, and D. Ktenas, "Waveform contenders for 5G: Description, analysis and comparison," *Physical Communication*, vol. 24, pp. 46–61, 2017.

[81] Y. Liu, X. Chen, Z. Zhong, B. Ai, D. Miao, Z. Zhao, J. Sun, Y. Teng, and H. Guan, "Waveform Design for 5G Networks: Analysis and Comparison," *IEEE Access*, vol. 5, pp. 19282–19292, 2017.

[82] Q. Bodinier, *Coexistence of communication systems based on enhanced multi-carrier waveforms with legacy OFDM Networks*. PhD thesis, École doctorale Mathématiques et sciences et technologies de l'information et de la communication (Rennes), 2017. Thèse de doctorat dirigée par Palicot, Jacques STIC – Télécommunications/Traitement du Signal Rennes 1 2017.

[83] R. Zakaria and D. Le Ruyet, "On Maximum Likelihood MIMO detection in QAM-FBMC systems," in *Proc. IEEE International Symposium on Personal, Indoor and Mobile Radio Communications (PIMRC)*, pp. 183–187, Sep. 2010.

[84] Y. H. Yun, C. Kim, K. Kim, Z. Ho, B. Lee, and J. Seol, "A new waveform enabling enhanced QAM-FBMC systems," in *Proc. IEEE International Workshop on Signal Processing Advances in Wireless Communications (SPAWC)*, pp. 116–120, June 2015.

[85] C. Kim, Y. H. Yun, K. Kim, and J. Seol, "Introduction to QAM-FBMC: From Waveform Optimization to System Design," *IEEE Communications Magazine*, vol. 54, pp. 66–73, November 2016.

[86] C. Lélé, P. Siohan, R. Legouable, and M. Bellanger, "CDMA Transmission with Complex OFDM/OQAM," *EURASIP Journal on Wireless Communications and Networking*, vol. 2008, p. 748063, Aug 2007.

[87] C. Lélé, P. Siohan, and R. Legouable, "The Alamouti Scheme with CDMA-OFDM/OQAM," *EURASIP Journal on Advances in Signal Processing*, vol. 2010, p. 703513, Jan 2010.

[88] R. Nissel, J. Blumenstein, and M. Rupp, "Block frequency spreading: A method for low-complexity mimo in fbmc-oqam," in *Proc. IEEE International Workshop on Signal Processing Advances in Wireless Communications (SPAWC)*, pp. 1–5, July 2017.

[89] R. Zakaria and D. Le Ruyet, "A Novel Filter-Bank Multicarrier Scheme to Mitigate the Intrinsic Interference: Application to MIMO Systems," *IEEE Transactions on Wireless Communications*, vol. 11, pp. 1112–1123, March 2012.

[90] R. Zakaria and D. Le Ruyet, "Theoretical analysis of the power spectral density for fft-fbmc signals," *IEEE Communications Letters*, vol. 20, pp. 1748–1751, Sep. 2016.

[91] D. Demmer, R. Zakaria, R. Gerzaguet, J.-B. Doré, and D. Le Ruyet, "Study of OFDM Precoded Filter-Bank Waveforms," *IEEE Transactions on Wireless Communications*, pp. 1–1, 2018.

[92] D. Demmer, R. Gerzaguet, J.-B. Doré, D. Le Ruyet, and D. Kténas, "Block-Filtered OFDM: a novel waveform for future wireless technologies," in *Proc. IEEE International Conference on Communications (ICC)*, (Paris, France), May 2017.

[93] D. Demmer, R. Gerzaguet, J.-B. Doré, D. Le Ruyet, and D. Kténas, "Filter Design for 5G BF-OFDM Waveform," in *Proc. IEEE. European Conference on Networks and Communications (EuCNC)*, (Oulu, Finland), June 2017.

[94] R. Gerzaguet, D. Demmer, J.-B. Doré, and D. Ktiénas, "Block-filtered OFDM: A new promising waveform for multi-service scenarios," in *Proc. IEEE International Conference on Communications (ICC)*, pp. 1–6, May 2017.

[95] J. Yli-Kaakinen, T. Levanen, M. Renfors, M. Valkama, and K. Pajukoski, "FFT-Domain Signal Processing for Spectrally-Enhanced CP-OFDM Waveforms in 5G New Radio," in *Proc. Asilomar Conference on Signals, Systems, and Computers (ASILOMAR)*, pp. 1049–1056, Oct 2018.

[96] D. Demmer, R. Zakaria, J.-B. Doré, R. Gerzaguet, and D. Le Ruyet, "Filter-bank OFDM transceivers for 5G and beyond," in *Proc. Asilomar Conference on Signals, Systems, and Computers*, Oct 2018.

[97] R. Zakaria, D. Silva, and D. Le Ruyet, "Lattice-Reduction-Aided Equalization for MIMO-FBMC Systems," *IEEE Wireless Communications Letters*, vol. 8, pp. 101–104, Feb 2019.

[98] C. P. Schnoor and M. Euchner, "Lattice Basis Reduction: Improved Practical Algorithms and Solving Subset Sum Problems," *Mathematical Programming*, vol. 66, pp. 181–191, 1994.

[99] W. Zhang, S. Qiao, and Y. Wei, "Practical HKZ and Minkowski Lattice Reduction Algorithms," 2011.

[100] P. Q. Nguyen and D. Stehlé, "An LLL algorithm with quadratic complexity," *Society for Industrial and Applied Mathematics*, vol. 39, no. 3, pp. 874–903, 2009.

[101] Y. H. Gan, C. Ling, and W. H. Mow, "Complex Lattice Reduction Algorithm for Low-Complexity Full-Diversity MIMO Detection," *IEEE Transactions on Signal Processing*, vol. 57, pp. 2701–2710, July 2009.

[102] X. Ma and W. Zhang, "Fundamental Limits of Linear Equalizers: Diversity, Capacity, and Complexity," *IEEE Transactions on Information Theory*, vol. 54, pp. 3442–3456, Aug 2008.

[103] D. Wubben, R. Bohnke, V. Kuhn, and K. D. Kammeyer, "Near-maximum-likelihood detection of MIMO systems using MMSE-based lattice- reduction," in *Proc. IEEE International Conference on Communications*, vol. 2, pp. 798–802 Vol.2, June 2004.

[104] J. Proakis, *Digital Communications 5th edition*. Electrical engineering series, McGraw-Hill, 2007.

[105] E. Telemar, "Capacity of Multi-Antenna Guassian Channels," 1999.

[106] X. Ma and Y. Kong, "Capacity analysis of lattice reduction aided equalizers for MIMO systems," in *Proc. IEEE Military Communications Conference*, pp. 866–871, Oct 2015.

[107] V. Ponnampalam, D. McNamara, A. Lillie, and M. Sandell, "On Generating Soft Outputs for Lattice-Reduction-Aided MIMO Detection," in *Proc. IEEE International Conference on Communications*, pp. 4144–4149, June 2007.

David Demmer

OFDM Precoding for Filter-Bank based Waveforms

De nouveaux usages des systèmes de communications sans fils, tels que les réseaux de capteurs ou les voitures autonomes, ont émergé au cours des dernières années. Ces usages sont fondamentalement différents des applications haut-débit actuelles des réseaux cellulaires. La future technologie mobile, la 5G New Radio, introduit donc le concept de numérologie du signal afin de pouvoir satisfaire aux besoin hétérogènes des multiples applications supportées. En effet en supportant différentes numérologies de signaux, l'allocation temps/fréquence des signaux devient plus flexible et le signal transmis peut être adapté en conséquence. Cependant, supporte simultanément différentes numérologies génère de l'interférence et donc distord les signaux. Les filtrages spatiaux, comme la formation de faisceaux, est envisagée en 5G pour limiter l'interférence générée mais pour les communications au-dessus de 6 GHz.

Il n'y a cependant pas de solutions proposées pour mes communications en-dessous de 6 GHz. Dans ce travail, des techniques d'atténuation des lobes secondaires sont étudiées pour faciliter le multiplexage des services pour les communications sous 6 GHz. L'interférence entre-utilisateurs est alors contrôlée mais la bande est également mieux utilisée. Une solution innovante, combinant bancs de filtres et orthogonalité complexe, est proposée. L'orthogonalité complexe est garanti grâce à un précodage OFDM qui remplace le précodage OQAM communément utilisé. De plus, le système développé, le Block-Filtered OFDM, utilise un récepteur 5G classique ce qui garantit la retro-compatibilité avec les techniques déjà déployée.

Le modèle du BF-OFDM est entièrement décrit et adapté aux normes des réseaux mobiles. De plus, de multiples méthodes de conception des filtres prototypes sont proposées afin de mieux répondre aux besoins des systèmes. La forme d'onde étudiée est également comparée avec les autres solutions de l'état de l'art sur des scénarios d'étude classiques mais également adaptés aux nouveaux enjeux des technologies sans fils.

Mots-clés: 5G, couche physique, OFDM, bancs de filtres, BF-OFDM

New use cases for wireless communications recently emerged ranging from massive sensor networks to connected cars. These applications highly differ from typical signals supported by already deployed mobile technologies which are mainly high data rate pipes. The forthcoming generation of mobile technology, 5G New Radio, introduces the new concept of signal numerology so as to properly serve the requirements of the diverse applications it will support. Indeed by considering different numerologies, the time/frequency signal allocation is made more flexible which allows to shape the transmitted signal according to its needs. However, multiplexing signals with different numerologies generates interference and therefore signal distortion. Spatial filtering, such as beamforming, is envisioned for 5G above 6-GHz communications to limit inter-user interference. However, this issue still holds for sub-6 GHz systems where spatial filtering is not considered in 5G.

In this work, we consider side lobe rejection techniques to ease service multiplexing in sub-6 GHz bands. Not only it provides inter-user interference mitigation but it also improves the bandwidth use efficiency. A novel solution, mixing filter-bank for confined spectrum and complex orthogonality for a straightforward re-use of known-how 4G/5G techniques, is proposed. The complex orthogonality is restored thanks to an OFDM precoding substituting the commonly used Offset-QAM signaling which limits the orthogonality to the real field. Moreover, the proposed solution, named Block-Filtered Orthogonal Frequency Division Multiplexing (BF-OFDM), relies on a simple 5G receiver scheme which makes it backward compatible with already deployed technologies.

The BF-OFDM system model is fully described and adapted to cellular standards. Besides, different prototype filter design methods are proposed to either improve the intrinsic interference attenuation or to better confine the spectrum of the transmitted signal. Last but not least, the proposed waveform will be compared with state-of-the-art solutions for both typical and 5G oriented evaluation scenarios such as multi-service coexistence.

Keywords : 5G, physical layer, OFDM, filter banks, BF-OFDM